





# **Nanomechanical Photothermal** Sensing

### DISSERTATION

submitted in partial fulfillment of the requirements for the degree of

### Doktor der Technischen Wissenschaften

by

Kostas Kanellopulos, M.Sc.

Registration Number 12038872

Institute of Sensor and Actuator Systems Technische Universität Wien

Advisor: Prof. Dr. Silvan Schmid Second advisor: Dr. Robert G. West



### Abstract

Over the past two decades, the field of nanomechanical resonators has seen remarkable growth, expanding its range of applications and pushing the boundaries of performance. To date, an extraordinary variety of sensors exploit these nanometer-size structures to detect mass, force, and temperature with exceptional sensitivity. Notably, measuring external stimuli by tracking shifts in a resonator's resonance frequency has led to groundbreaking achievements, such as detecting mass at the yoctogram scale — just three orders of magnitude heavier than a single proton.

This approach has also proven to be extremely powerful for detecting minute temperature changes, enabling imaging at the single-molecule level. Here, tensile stressed nanomechanical resonators exhibit frequency detuning upon photothermal heating, by means of a stress release via thermal expansion. Photothermal heating can originate from various processes, including electromagnetic radiation absorption, non-radiative heat transfer from single molecules, particle, and thin films. This simple yet sensitive method and its applications constitute the field of nanomechanical photothermal sensing. The present work aims to deepen the understanding of this detection technique while expanding its capabilities in microscopy and spectroscopy for single particles and molecules, and material optical characterization.

Along this thesis, a comprehensive analysis of the main figures of merit of the nanomechanical photothermal sensors is carried out, establishing a theoretical framework aimed at assessing their photothermal sensing performance. The analytical models developed herein highlight the critical interplay between sensor photothermal responsivity and its frequency stability. Different resonator designs are systematically compared theoretically and experimentally with respect to their sensitivity, response time, and practicality.

Label-free microscopy and imaging at room temperature has been one of the first applications of nanomechanical photothermal sensing. This work develops the state-of-the-art nanomechanical photothermal platform for spectroscopy and polarization-microscopy of individual nano-absorbers. This is showcased with the characterization of the absorption spectrum and the plasmonic properties of individual gold nanorods. This demonstrates the ability of nanomechanical photothermal sensing to resolve the heterogeneity within a single sample, with a reduced experimental complexity and higher signal-to-noise ratio compared to other label-free single-molecule optical techniques.

The field of applications of nanomechanical photothermal sensing is further expanded for the low optical loss characterization of materials exploited in nanophotonics and nanome-

chanics. In particular, it analyzes the dependence of the optical absorption of silicon nitride — a material of significant technological importance — on the film deposition and fabrication process. A direct correlation is identified between the deposition-related tensile stress and the extinction coefficient of silicon nitride, with the latter decreasing for increasing stress. This trend is attributed to a reduction in silicon-to-nitrogen ratio, which widens the material's energy bandgap. These findings pave the way for a precise, scattering-free, and fast optical characterization of materials.

The advancements in understanding and applicability of nanomechanical photothermal sensing presented in this work aim to establish a solid groundwork for the development and improvement of next-generation nanomechanical photothermal sensors, with the hope to offer valuable insights for researchers seeking to harness the full potential of this detection paradigm across a broad spectrum of applications.

## Zusammenfassung

In den letzten zwei Jahrzehnten hat das Gebiet der nanomechanischen Resonatoren ein bemerkenswertes Wachstum erfahren, das die Anwendungsmöglichkeiten erweitert und die Grenzen der Leistungsfähigkeit verschoben hat. Bis heute nutzt eine außergewöhnliche Vielfalt von Sensoren diese nanometergroßen Strukturen, um Masse, Kraft und Temperatur mit außergewöhnlicher Empfindlichkeit zu erfassen. Insbesondere die Messung externer Stimuli durch Verfolgung von Verschiebungen der Resonanzfrequenz eines Resonators hat zu bahnbrechenden Errungenschaften geführt, wie z. B. dem Nachweis von Masse auf der Yoktogramm-Skala - nur drei Größenordnungen schwerer als ein einzelnes Proton. Dieser Ansatz hat sich auch als äußerst leistungsfähig erwiesen, wenn es darum geht, winzige Temperaturänderungen zu erkennen, was eine Bildgebung auf Einzelmolekülebene ermöglicht. Hier zeigen zugfeste nanomechanische Resonatoren bei photothermischer Erwärmung eine Frequenzverschiebung durch Spannungsabbau über thermische Expansion. Die photothermische Erwärmung kann durch verschiedene Prozesse hervorgerufen werden, darunter die Absorption elektromagnetischer Strahlung und die nicht strahlende Wärmeübertragung von einzelnen Molekülen, Partikeln und dünnen Filmen. Diese einfache, aber empfindliche Methode und ihre Anwendungen bilden den Bereich der nanomechanischen photothermischen Sensorik. Die vorliegende Arbeit zielt darauf ab, das Verständnis dieser Detektionstechnik zu vertiefen und gleichzeitig ihre Möglichkeiten in der Mikroskopie und Spektroskopie für einzelne Partikel und Moleküle sowie die optische Charakterisierung von Materialien zu erweitern.

In dieser Arbeit wird eine umfassende Analyse der wichtigsten Leistungsmerkmale der nanomechanischen photothermischen Sensoren durchgeführt und ein theoretischer Rahmen für die Bewertung ihrer photothermischen Sensorleistung geschaffen. Die hier entwickelten analytischen Modelle heben das kritische Zusammenspiel zwischen der photothermischen Empfindlichkeit des Sensors und seiner Frequenzstabilität hervor. Verschiedene Resonatordesigns werden systematisch theoretisch und experimentell im Hinblick auf ihre Empfindlichkeit, Reaktionszeit und Praktikabilität verglichen.

Die markierungsfreie Mikroskopie und Bildgebung bei Raumtemperatur war eine der ersten Anwendungen der nanomechanischen photothermischen Sensorik. In dieser Arbeit wird eine hochmoderne nanomechanische photothermische Plattform für die Spektroskopie und Polarisationsmikroskopie von einzelnen Nanoabsorbern entwickelt. Dies wird anhand der Charakterisierung des Absorptionsspektrums und der plasmonischen Eigenschaften einzelner Goldnanostäbehen demonstriert. Dies zeigt die Fähigkeit der nanomechanischen photothermischen Sensorik, die Heterogenität innerhalb einer einzelnen Probe aufzulösen, und zwar mit einer geringeren experimentellen Komplexität und einem höheren Signal-Rausch-Verhältnis im Vergleich zu anderen markierungsfreien optischen Einzelmolekültechniken.

Der Anwendungsbereich der nanomechanischen photothermischen Sensorik wird für die Charakterisierung von Materialien mit geringem optischem Verlust, die in der Nanophotonik und Nanomechanik verwendet werden, weiter ausgebaut. Insbesondere wird die Abhängigkeit der optischen Absorption von Siliziumnitrid - einem Material von großer technologischer Bedeutung - von der Schichtabscheidung und dem Herstellungsprozess analysiert. Es wird ein direkter Zusammenhang zwischen der abscheidungsbedingten Zugspannung und dem Extinktionskoeffizienten von Siliziumnitrid festgestellt, wobei letzterer mit zunehmender Spannung abnimmt. Dieser Trend wird auf eine Verringerung des Verhältnisses von Silizium zu Stickstoff zurückgeführt, was die Energiebandlücke des Materials vergrößert. Diese Ergebnisse ebnen den Weg für eine präzise, streuungsfreie und schnelle optische Charakterisierung von Materialien.

Die in dieser Arbeit vorgestellten Fortschritte in Bezug auf das Verständnis und die Anwendbarkeit nanomechanischer photothermischer Sensoren zielen darauf ab, eine solide Grundlage für die Entwicklung und Verbesserung nanomechanischer photothermischer Sensoren der nächsten Generation zu schaffen, in der Hoffnung, den Forschern, die das volle Potenzial dieses Erkennungsparadigmas in einem breiten Spektrum von Anwendungen nutzen wollen, wertvolle Erkenntnisse zu bieten.

# Contribution to Original Knowledge

The research carried out during this PhD project represents a small, but important step forward in the field of nanomechanical resonators for photothermal sensing. Various original contributions to the knowledge of this field have been made, the most significant including:

- The advancement of nanomechanical photothermal sensing as a sensitive tool for microscopy and spectroscopy for single molecule and single particle analysis. This has been showcased with the measurements of the optical absorption spectrum of individual gold nanorods. The analysis has shown the advantages offered by nanomechanical photothermal sensing for the study of single nano-absorbers over the state-of-the-art single-molecule techniques. In particular, the superior signal-tonoise ratio and reduction in set-up complexity has been highlighted.
- The analysis of the electromagnetic dissipation and polarization properties of individual nanorods in the visible and near infrared spectral range, including their interaction with the underlying mechanical resonator.
- The advancement in the theoretical understanding of nanomechanical photothermal sensing through a comparative study of three resonator designs — namely strings. drumheads, and trampolines.
- The importance of photothermal back-action in nanomechanical photothermal sensing, showcasing this effect experimentally on trampoline resonators.
- The relation between optical extinction and process-related residual tensile stress in low-pressure deposition deposited silicon nitride thin films.



### List of Publications

### Journal publications

- Kostas Kanellopulos, Robert G, West, Stefan Emminger, Paolo Martini, Markus Sauer, Annette Foelske, Silvan Schmid, Stress-dependent Optical Extinction in LPCVD Silicon Nitride Measured by Nanomechanical Photothermal Sensing, Nano Letters 2024, 14, 36, 11262-1128
- Kostas Kanellopulos, Friedrich Ladinig, Stefan Emminger, Paolo Martini, Robert G. West, Silvan Schmid, Comparative analysis of nanomechanical resonators: Sensitivity, response time, and practical considerations in photothermal sensing, Submitted 2024
- Hajrudin Bešić, Andreas Deutschmann-Olek, Kenan Mešić, Kostas Kanellopulos, Silvan Schmid, Optimized Signal Estimation in Nanomechanical Photothermal Sensing via Thermal Response Modelling and Kalman Filtering, IEEE Sens. 2024, 24, 19, 30264-30274
- Kostas Kanellopulos, Robert G. West, Silvan Schmid, Nanomechanical Photothermal Near Infrared Spectromicroscopy of Individual Nanorods, ACS Photonics 2023, 10, 10, 3730–3739. DOI: 10.1021/acsphotonics.3c00937
- Robert G. West, **Kostas Kanellopulos**, Silvan Schmid, "Photothermal microscopy and spectroscopy with nanomechanical resonators, J. Phys. Chem. C 2023, 127, 45, 21915–21929. DOI: 10.1021/acs.jpcc.3c04361 (editor's choice)
- Jan N. Kirchfof, Yuefeng Yu, Denis Yagodkin, Nele Stetzuhn, Daniel B. de Araújo, Kostas Kanellopulos, Samuel Manas-Valero, Eugenio Coronado, Herre van der Zant, Stephanie Reich, Silvan Schmid, Kirill I. Bolotin, Nanomechanical absorption spectroscopy of 2d materials with femtowatt sensitivity, 2D Mater. 2023, 10, 035012. DOI: 10.1088/2053-1583/acd0bf
- Paolo Martini, Kostas Kanellopulos, Silvan Schmid, Towards Photon-Noise Limited Thermal IR Detection with Optomechanical Resonators, IEEE Sens. 2023, pp.1-4. DOI: 10.1109/SENSORS56945.2023.10325323

• Paolo Martini, Kostas Kanellopulos, Silvan Schmid, Towards an optomechanical photon-noise limited thermal IR detector, IEEE Nanotechn. Mater. Dev. Conf. (IEEE-NMCD) 2023, pp. 513 - 514. DOI: 10.1109/NMDC57951.2023.10343532.

### Conference contributions

- NEMS-based Photothermal Polarization Spectromicroscopy; Kostas Kanellopulos, Robert G. West, Miao-Hsuan Chien, Silvan Schmid; 27th International Workshop on Single Molecule Spectroscopy and Super-resolution Microscopy in the Life Sciences. PicoQuant (2022), Berlin, Germany (Poster)
- NEMS-based Photothermal Polarization Spectromicroscopy; Kostas Kanellopulos, Robert G. West, Miao-Hsuan Chien, Silvan Schmid; 18th International Workshop on Nanomechanical Sensing (NMC 2022), Bangalore, India (Poster)
- Nanomechanical Photothermal Near Infrared Spectromicroscopy; Kostas Kanellopulos, Robert G. West, Silvan Schmid; Frontiers of Nanomechanical Systems (FNS 2023), Delft, Netherlands (Poster)
- Comparative Analysis of Nanomechanical Resonators for Photothermal Sensing; Kostas Kanellopulos, Friedrich Ladinig, Stefan Emminger, Paolo Martini, Robert G. West, Silvan Schmid, 19th International Workshop on Nanomechanical Sensors (NMC 2024), Vienna, Austria (Poster)

## Acknowledgements

What I am writing on these pages will be what remains — a mark, a trace — of an experience far richer than these words can express. The acknowledgments I note here come from that inner depth, and as such, they are felt far more intensely than what might appear at first glance between these lines.

A lot of people have profoundly impacted my life and work throughout this journey, and though it is challenging to mention everyone, I will do my best to express my gratitude. First and foremost, I am deeply grateful to my advisor and mentor, Professor **Silvan Schmid**. This has been a long journey filled with ups and downs, and without his expertise, open-mindedness, and enthusiasm for science, I could never have overcome the obstacles I encountered. I am particularly thankful for the freedom he gave me to explore different research paths and his meticulous attention to detail, which has significantly shaped my scientific vision and skills. Thank you, Silvan, for your unwavering support over the years!

The whole MNS group, led by Silvan, has been both an inspiration and a second home to me. This incredible group is made up of amazing people who have shared so much with me, and I will never forget the experiences we've had together.

To **Robert West**, our countless discussions about literally everything have left an indelible mark in my mind. His experimental approach and open-mindness has been of utmost importance for my work. I am honored to have met you and grateful for all the support you have given to me. Thanks Robert!

To Paolo Martini and Johannes Hiesberger, with whom I've shared so many funny, stressful, and quiet moments since the beginning. Thank you for being there — you've been the best office neighbors I could have asked for! (Maybe one day you will fully experience a sphere!)

To my office mates, **Hajrudin Besic** (a.k.a. the Bro) and **Veljko Vukicevic**, I will always remember our jokes, laughs, and scientific discussions. Hvala for all the wonderful time spent together!

To **Jelena Timarac Popovic** and **Tatjana Penn**, thank you for the countless laughs during lunch, which were invaluable for recharging my energy before returning to work! To **Niklas Luhmann** and **Hendrik Kaehler**, with whom I shared a lot of interesting scientific discussions and parties. Thank you guys, for all those moments!

To Miao Hsuan-Chien, Markus Piller and Pedram Sadeghi, from who, directly or indirectly, I learned a lot. You have done an incredible scientific work and I am honored

to have met you at the beginning of the journey!

To the new members of the MNS group, Nicola Cavalleri, Thomas Tropper, Ariane Giesriegl, I have no doubt you will have a significant impact on the group's future research. I'm grateful to have shared the final part of my journey with you!

A lot of other people from ISAS have had a huge impact during these years. To **Davide Disnan**, for our lunches, discussions and supports during this time. Thank you for your lightness and optimism!

To Giorgio Scordo, for our discussions in front a good cup of coffee. I am honored to have met you!

To Matthias Wess, for his good vibes, irony, and open-mindness. Thank you for your lightness and all the funny moments spent together!

To Matthias Schlögel, for his support and our Sprachtandem. Thank you (don't climb too much)!

I am also deeply grateful to all the other people of ISAS. In particular, I extend my gratitude to Professor Ulrich Schmid for his dedication to managing ISAS and enabling the research. I also thank the cleanroom team Johannes Schalko, Sophia Ewert, Patrick Meyer, and Michael Buchholz, for their fundamental and invaluable work in the fabrication and characterization labs. A big thank to Martina Nuhsbaumer, Martina Bittner, Pia Da Silva Morais, and Andreas Astleitner for your vital support, which helped keep everything running smoothly.

What I wrote at the beginning of this acknowledgment assumes its deepest meaning here. I am forever indebted to my parents, who have always believed in me and stood by me through the toughest moments of this journey.

To my entire family for the constant support, whether direct or indirect, during these years.

To my friends, who have been there always for me, and have been a source of strength and bravery in all these years, far beyond this work.

Lastly, to my girlfriend, Marta Palomo Irigoyen: the ground beneath me, that supported me along this journey, in the toughest and lightest moments; the flower near me, whose fragrance enriches everything around it. Without her none of this would have been possible.

Φύσις κρύπτεσθαι φιλεί Ηράκλειτος ο Εφέσιος, 520 - 460 Β.C.

# Contents

$\mathbf{A}$	bstra	act	iii
Zι	ısam	menfassung	$\mathbf{v}$
C	ontri	bution to Original Knowledge	vii
$\mathbf{Li}$		Publications	ix
		rnal publications	ix
	Con	ference contributions	X
A	ckno	wledgements	xi
$\mathbf{Li}$	${f st}$ of	Figures	xvii
$\mathbf{Li}$	st of	Tables	xix
$\mathbf{Li}$	st of	Symbols	xxi
1	Intr	roduction	1
	1.1	Eppur si muove!	1
	1.2	Single-Molecule Spectromicroscopy	2
	1.3	Enhancing Nanomechanical Photothermal sensing	5
	1.4	Low-loss Optical Material Characterization	7
	1.5	Thesis Outline	9
2	Fun	damentals of Nanomechanical Resonators	11
	2.1	Lumped Element Models of Mechanical Vibrations	11
	2.2	Mechanical Dissipation Mechanisms	16
	2.3	Dynamic range	21
	2.4	Free Bending Vibration of Continuum Resonators	23
3	Fun	damentals of Nanomechanical Photothermal Sensing	31
	3.1	Nanomechanics for Thermal Sensing	31
	3.2	Summary	51

liothek	owledge hub
Die	The
Die approbierte g	approved
e gedruck	original ve
te Origi	ersion c
inalversion	of this doct
dieser D	toral thesis
issertation	s is availal
ı ist an	ole in p
der	rint

4	Exp	erimental and Computational Methods	53
	4.1	Silicon Nitride Sensing Platform	53
	4.2	Transduction	55
	4.3	Frequency Tracking Schemes	60
	4.4	Finite Element Method	62
5	Con	aparative Analysis of Nanomechanical Photothermal Sensors	71
	5.1	Strings	71
	5.2	Drumheads	75
	5.3	Trampolines	76
	5.4	Comparison	78
	5.5	Conclusions	81
6	Nanomechanical Photothermal NIR Spectromicroscopy		83
	6.1	Experimental Methods	84
	6.2	Photothermal Spectroscopy	89
	6.3	Overview on the State-of-the-Art	103
	6.4	Conclusions and Outlook	103
7	Nanomechanical Photothermal Sensing for Low-loss Material Charac-		
	teri	zation	107
	7.1	Characterization Procedure	107
	7.2	LPCVD SiN Thin Films	110
	7.3	Extinction Results	113
	7.4	Conclusions and Outlook	118
$\mathbf{A}$	Pho	tothermal back-action	119
	A.1	Experimental evaluation	119
В	Opt	ical characterization of LPCVD SiN - Appendix	121
	B.1	Compilation of state-of-the-art techniques for low-loss absorption charac-	
		terization	121
	B.2	XPS measurements	123
Bi	bliog	graphy	127



# List of Figures

xvii

1.1	Working principle of nanomechanical photothermal sensing
1.2	Overview on nanomechanical photothermal sensing
1.3	Nanomechanical photothermal sensing for optical loss measurements
2.1	Lumped element model of a mechanical mode
2.2	Driven damped vibrations
2.3	Gas damping
2.4	Surface friction losses
2.5	Dissipation dilution in SiN resonators
2.6	Duffing resonator
2.7	Vibrations of a string resonator
2.8	Vibrations of a drumhead resonator
2.9	Vibrations of a trampoline resonator
2.10	Fundamental resonance of a trampoline
3.1	Mean Temperature Framework
3.2	MTF: $G_{\text{cond}}$ vs $G_{\text{rad}}$
3.3	String's photothermal response
3.4	Heat localization in strings
3.5	Drumhead's photothermal response
3.6	Heat localization in drumheads
3.7	Trampoline's photothermal response
3.8	Heat localization in trampolines
3.9	Theory workflow
4.1	Comparison of materials for nanomechanics and photonics
4.2	Optical fiber-based Fabry-Perot interferometry
4.3	Laser-Doppler vibrometry
4.4	Influence of metals on the photothermal response
4.5	Frequency tracking schemes
4.6	Fractional frequency PSD and AD
4.7	Photothermal response FEM workflow
4.8	FEM thermal time constant
4.9	FEM of the nanorod's plasmonic response

Die app	The ap
<b>3ibliothek</b>	Your knowledge hub
P	EN

	$\Theta$	68
4.11	FEM plasmonic hotspots	69
5.1	String design	72
5.2	Laser power fluctuations	74
5.3	Drumhead design	76
5.4	Trampoline design	77
5.5	Performance summary	79
5.6	Specific detectivity	80
5.7		81
6.1	Schematics of the operating set-up	85
6.2	Sensor's power responsivity	87
6.3		88
6.4		88
6.5		89
6.6	• 9	90
6.7	1 1 0	92
6.8	•	93
6.9		93
		94
		95
		96
	<del>-</del>	97
		98
		99
	FEM intensity distribution at SiN-air interface	
	Polarization response of the plasmonic resonance	
	Polarization microscopy of individual nanorods	
	SNR comparison among single-molecule techniques	
7.1	Nanomechanical photothermal characterization of optical losses with strings 10	96 9
7.2	Nanomechanical photothermal responsivities	
7.3	SiN emissivity and interference factor	
7.4	Nanomechanical photothermal characterization of the extinction coefficient 1.	
7.5	Absorption coefficient in the band-fluctuations model	
7.6	Energy bandgap and Urbach energy	
7.7	Urbach energy versus Si/N ratio	
A.1	Experimental photothermal back-action	20
В.1	Refractive index of LPCVD SiN	22
B.2	XPS measurement positions	24

# List of Tables

2.1	Gas damping in SiN resonators	18
3.1 3.2	Low-stress LPCVD silicon nitride material parameters	35 47
4.1	Material comparison for nanomechanics	54
6.1	SNR comparison among single-molecule techniques	104
7.1	Strings physical properties	111
B.1	Comparison of SiN extinction coefficient	122

## List of Symbols

In the following a list of the most important and used symbols, with their description and the equation for they appear for the first time (when needed).

$\mathbf{Symbol}$	Description
A	Area $(m^2)$ , Eq. $(3.17)$
A	Surface scattering parameter, Eq. (4.17)
C	Thermal capacitance (J $K^{-1}$ )
$c_{ m p}$	Specific heat capacity at constant pressure (J $K^{-1} kg^{-1}$ )
$D^*$	Specific detectivity (cm $\sqrt{\text{Hz}} \text{ W}^{-1}$ )
E	Young's modulus (Pa)
$E_{ m g}$	Energy bandgap (eV)
f	Frequency (Hz)
F	Force (N)
$F_0$	Force amplitude (N)
G	Thermal conductance (W $K^{-1}$ )
$G_{ m cond}$	Conduction thermal conductance (W $K^{-1}$ )
$G_{ m rad}$	Radiation thermal conductance (W $K^{-1}$ )
h	Thickness (m)
$\hbar$	Reduced Planck constant, $1.0545 \cdot 10^{-34} \text{ J s}$
$H(\omega)$	Transfer function of a linear system
I	Intensity (W $m^{-2}$ )
L	Length (m)
m	Mass (kg)
$m_{ m eff}$	Effective mass (kg)
n	Modal number
n	Refractive index
NEP	Noise-equivalent power (W $Hz^{-1/2}$ )
p	Pressure (Pa)
P	Power (W)
Q	Quality factor
$\mathbf{r}, r$	Position vector
$\mathcal{R}_{\mathrm{T}}$	Relative temperature responsivity $(K^{-1})$
$\mathcal{R}_{ ext{P}}$	Relative power responsivity $(W^{-1})$

$S_x(\omega)$	One-sided power spectral density of a generic observable $x$
	in units $X$ ( $X^2$ Hz <sup>-1</sup> )
$s_{ m f}$	Shape factor
SNR	Signal-to-noise ratio
t	Time (s)
T	Temperature (K)
u	Displacement (m)
V	Volume $(m^3)$
w	Width (m)
$w_0$	Beam waist (m)
$\alpha_{ m abs}$	Absorptance
$ ilde{lpha}_{ m abs}$	Absorption coefficent $(m^{-1})$
$lpha_{ ext{eff}}$	Effective Duffing parameter (N m <sup>-3</sup> )
$lpha_{ m th}$	Linear coefficient of thermal expansion $(K^{-1})$
$\beta$	$\beta$ factor, Eq. (3.17)
$\beta$	Urbach slope, Eq. (7.10)
$\Gamma$	Linewidth (Hz)
$\Delta$	Difference operator
$\epsilon$	Dielectric function
$\epsilon_{ m rad}$	Emissivity
$\eta$	Absorptance correction factor, Eq. (7.2)
heta	Phase
k	Spring constant $(N m^{-1})$
$\kappa$	thermal conductivity (W $K^{-1} m^{-1}$ )
$k_{ m B}$	Boltzmann constant, $1.381 \cdot 10^{-23} \text{ J/K}$
$\kappa_{ m ext}$	Optical extinction coefficient
$\kappa_{ ext{eff}}$	Effective spring constant $(N m^{-1})$
$\lambda$	Wavelength (m)
$\nu$	Poisson's ratio
ho	Mass density $(kg/m^3)$
$\sigma$	Temperature dependent stress (Pa)
$\sigma_0$	Initial tensile stress (Pa)
$\sigma_y$	Allan deviation
$\sigma_{ m abs}$	Absorption cross-section (m <sup>2</sup> )
$\sigma_{ m sca}$	Scattering cross-section (m <sup>2</sup> )
$\sigma_{ m SB}$	Stefan-Boltzmann constant, $5.67 \cdot 10^8 \text{ W m}^2 \text{ K}^4$
au	Integration time (s)
$ au_{ m mech}$	Mechanical time constant (s)
$ au_{ m th}$	Resonator thermal time constant (s)
$ au_{ m PLL}$	PLL time constant (s)
1 111	

Filter time constant (s)

Angular frequency (rad/s)

Modeshape of the nth eigenmode



 $au_{
m L}$ 

 $\psi_n$ 

CHAPTER.

### Introduction

#### 1.1 Eppur si muove!

Any object with at least one dimension smaller than 1 µm falls under the definition of nano. At first glance, this definition seems straightforward, yet reducing an object's dimensions to the nanoscale brings more than just a spatial change. In fact, an entirely new class of physical phenomena emerges at this scale, which has been the subject of extensive study over the past century, leading to breakthroughs in both fundamental and applied science [1]. Fields like nanoelectronics, nanophotonics [2], and central for this work, nanomechanics [3], have pushed further the boundaries of our understanding of the surrounding world, simultaneously expanding the technological capabilities of our society. In particular, advancements in nanofabrication techniques, as well as the discovery of new materials, have enabled the development of increasingly more sensitive devices, capable of probing the quantum nature of matter [4, 5] and its interaction with light [6].

The classical study of an object's motion, known as mechanics, have revived over the past three decades with the advent of nanoelectromechanical systems (NEMS) [7]. These systems are characterized by the presence of one or more miniature mechanical components that are displaced from their equilibrium positions in response to external stimuli. Their small size makes them exceptionally sensitive to minute disturbances, enabling the quantum-limited detection of forces [8], single spin magnetic moment [9], and small masses [10–15] at an unprecedented sensitivity.

One of the earliest and most prominent applications of NEMS-based sensing has been in mass spectrometry, specifically for detecting single proteins and nanoparticles. These systems have achieved quantification down to the yortogram scale [11], measuring the target substance by monitoring the shift in resonance frequency caused by the added mass on the nanomechanical element. It is evident from this simple experiment that the response to mass can be improved by further reducing the size of the resonator. Consequently, mass sensing has been a primary driving force behind the continuous

miniaturization of electromechanical systems down to the nanoscale.

While detuning the resonator's frequency by altering its mass is a common method for detecting small signals—such as the landing of single proteins on its surface—another compelling and effective technique involves capturing frequency shifts caused by changes in stiffness. In tensile-stressed mechanical structures, this detuning can occur when the resonator absorbs heat, leading to a relaxation of the residual stress. Heat absorption may arise from electromagnetic radiation, or from energy released by a molecule adhering to the resonator's surface. This process, known as photothermal effect, has paved the way for a novel method of molecular and radiation characterization, which is the core focus of this work: nanomechanical photothermal sensing.

Like mass sensing, nanomechanical photothermal sensors have greatly benefited from the continuous device miniaturization, enhancing their responsivity to tiny amount of energy exchanges with the surrounding environment. Combined with the robustness of frequency-based measurements, this advancement has opened the door to a completely new method for detecting the optical absorption of minute samples [16–23], including single molecules [24], individual nanoparticles [25–31], two-dimensional (2D) material [32, 33], thin films [34, 35], as well as low-energy electromagnetic radiation [36–42].

#### 1.2 Single-Molecule Spectromicroscopy

#### 1.2.1 Overview

In recent decades, the development of techniques for characterizing individual particles and molecules has significantly advanced our understanding and control of nanoscale objects, of their functions and properties [43, 44]. The ability to probe individual nanoobjects offers the possibility to explore their heterogeneity within the same sample, along with their interaction with the surrounding environment [45].

The use of electron probes has brought about major breakthroughs in nanoscience, with the key advantage of electron microscopy being its ability to achieve exceptionally high spatial resolution, constrained only by the wavelength of the electrons. Likewise, scanning tunneling (STM) and atomic force (AFM) microscopy offer comparable capabilities [46. 47, though limited by their atomic-sized tips. In contrast, optical microscopy, while constrained by the diffraction limit, presents several benefits. Light is noninvasive in nature and can offer high throughput, easy integration with other methodologies, and applicability to a wide range of samples, from nanoparticles to living organisms [48]. Furthermore, the resonance of photons at optical frequencies with the electronic states of atoms and molecules facilitates spectroscopic observations, providing detailed insights into the structure and dynamics of matter at the molecular level [45].

Right after the first single-molecule detection via laser frequency modulation by Moerner and Kador [49], fluorescence microscopy demonstrated its superior signal-to-background ratio [50], quickly becoming a cornerstone tool in biology and condensed matter research. Significant efforts have also been made to develop super-resolution microscopy techniques to overcome optical diffraction limits [51].

Fluorescence microscopy fundamentally relies on the chemical contrast provided by fluorophores. However, this requires labelling the target molecule, which increases the experimental process complexity. Moreover, the stability of the fluorophore — affected by phenomena like photobleaching, photoblinking, and limited excited-state lifetimes directly influences the measurement results. The interaction between the fluorophore and the molecule of interest can also affect the system under study, depending on the nature of the labelling. These limitations have driven the development of fully label-free characterization methods, broadening the range of molecules that can be studied [52].

#### 1.2.2Label-free Spectroscopy

A wide range of non-fluorescent techniques rely on fully optical detection of single molecules through molecular extinction measurements, such as scattering and absorption [53]. Among these, absorption-based methods generally offer greater sensitivity than scattering-based approaches, due to the different scaling laws of their respective optical cross-sections. Specifically, while the scattering cross-section scales quadratically with the volume of the molecule ( $\sigma_{\rm sca} \propto V^2$ ), the absorption cross-section scales linearly with it  $(\sigma_{\rm abs} \propto V)$  [54].

As an example, surface-enhanced Raman scattering leverages the intense near-field enhancement at the nanoscale around plasmonic nanoparticles or nanostructures — referred to as hotspots — to improve the signal-to-noise ratio (SNR) of Stokes-shifted Raman scattering [55]. However, the complexity of the measurement process is increased by the challenges involved in the fabrication of these plasmonic nanostructures and the precisely positioning of the targeted particles or molecules at the desired sites.

Another example is offered by interferometric scattering microscopy (iSCAT), which measures the scattering of viruses, proteins and nanoparticles via a well balanced interference between the reference, transmitted light, and the field scattered by the system under study [48]. This enables accurate quantification of molecular absorption, but requires meticulous alignment of the interferometer's arms to reduce background noise from laser intensity fluctuations.

Another interesting solution to label-free detection of single molecules is given by groundstate depletion microscopy. In this method, two tightly focused laser beams at different wavelengths—both within the absorption band of the target molecule—are used. A strong saturating beam, the pump, excites the molecule, depleting its ground state and thus preventing absorption by the second probe beam. Single-molecule detection is achieved by modulating the transmitted probe beam, with the modulation depth directly linked to the molecule's absorption [56]. Synchronizing and aligning the shot-noise-limited beams is crucial for achieving high sensitivity in these measurements.

#### 1.2.3 Photothermal Spectroscopy

Unlike the previously mentioned methods, which measure the attenuation of light by a molecule, photothermal spectroscopy directly detects molecular absorption through the resulting photothermal heating [57]. One of the most prominent examples is thermooptic photothermal sensing [58]. This method also utilizes a dual-beam setup, similar to ground-state depletion microscopy, but with a key difference: only the pump laser operates within the molecule's strong absorption spectrum. This pump laser excites the target molecule, which then releases a portion of the absorbed electromagnetic energy as heat. The resulting temperature increase induces a local change in the refractive index of the surrounding medium, which is detected by a secondary probe laser via scattering modulation at the focal plane. To achieve a high signal-to-noise ratio (SNR), a medium with a large thermo-optic coefficient, such as glycerol, thermotropic liquid crystal, or near-critical Xe or  $CO_2$ , is essential [57]. As with other dual-beam techniques, precise alignment and synchronization of the lasers are crucial for sensitivity.

Another approach that exploits the photothermal effect involves the use of whisperinggallery modes (WGM) [59]. Here, the target molecule is positioned on an optical resonator. When the molecule absorbs light and heats up, the resulting temperature increase alters the refractive index, modulating the transmission of the optical cavity that forms the resonator.

#### Nanomechanical Photothermal Spectroscopy 1.2.4

A novel approach for single-molecule analysis has recently emerged: nanomechanical photothermal microscopy [24]. Here, a tensile-stressed nanomechanical resonator, rather than an optical one, is driven to vibrate at one of its resonance frequencies. A molecule placed on the resonator is then heated by a laser with a wavelength tuned to the molecule's absorption spectrum. The energy absorbed and released by the molecule through nonradiative processes increases the temperature of the nanomechanical resonator, causing a stress relaxation [60]. This results in a measurable frequency shift, as illustrated in Fig. 1.1. This method allows for the analysis of a wide range of samples, both fluorescent and non-fluorescent, without the need for a temperature-sensitive embedding medium or the precise laser synchronization required by conventional photothermal microscopy [61]. Previous studies have investigated optical absorption in a variety of small-scale samples [16–23], including thin films [34, 35], two-dimensional (2D) material [32, 33], single nanoparticles [25–30], and single molecules [24], in a wide range of the electromagnetic spectrum, from visible, near-infrared (NIR), to mid-IR [61]. However, amidst this extensive body of work, a comprehensive platform capable of localizing, and characterizing the spectroscopic and polarization features of a single nano-object has been not shown so far. This work aims to bridge this gap by advancing nanomechanical photothermal sensing into a robust technique for spectroscopy and polarization microscopy at the single-molecule level. By leveraging a silicon nitride (SiN) nano-optomechanical drum resonator as a precise temperature sensor, the spectral and polarization features of the longitudinal localized surface plasmon resonance of individual gold nanorods have been fully characterized in the NIR. In conjunction with finite element method (FEM) simulations, it is shown that the plasmonic damping is mainly limited by electron bulk and surface scattering. The polarization properties of the transversal surface plasmons are also studied, showing little dependence on the probing laser polarization. Additionally, the results demonstrate how the nanoresonator itself influences the absorption cross-section of the nanorods.

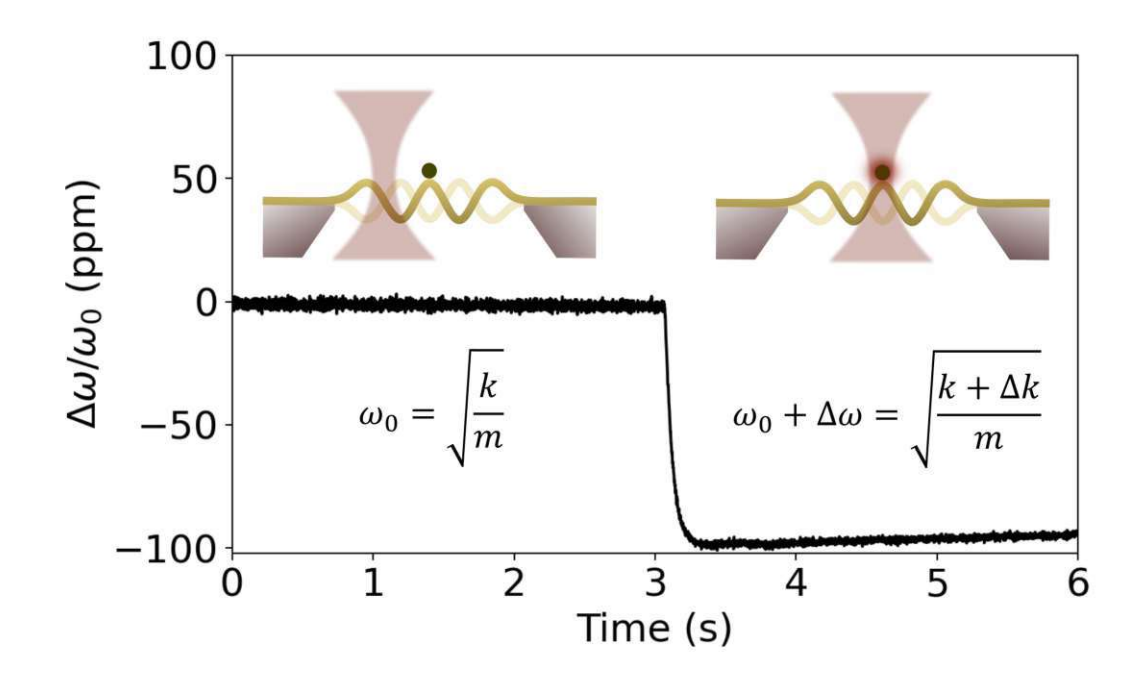


Figure 1.1: Working principle of nanomechanical photothermal sensing. The resonator is driven at one of its resonance frequencies  $\omega_0$ . A laser is scanned over the resonator surface. Far from the molecule (left), no photothermal heating is released to the resonator. When the laser impinges on the molecule (right), this heats up the resonator, leading to a stress reduction (here generalized in terms of spring constant change  $\Delta k$ ). This ultimately causes a detectable frequency shift  $\Delta\omega$ .

### 1.3 Enhancing Nanomechanical Photothermal sensing

In this detection paradigm, the nanomechanical resonator essentially functions as a thermometer. The detected heat can arise from various processes, including non-radiative energy transfer from low-abundance analytes or even single molecules, as discussed earlier, as well as electromagnetic radiation [36-42]. In this context, the field is making significant strides in bridging the terahertz (THz) gap with resonant micro- and nanomechanical thermal detectors, providing a novel approach for room-temperature operation [62, 63]. Additionally, light-sound interaction in nanoresonators has been successfully used for enthalpy measurements [64], detection of near-field heat radiation transfer [65, 66], and as a probe for phonon heat transfer via vacuum fluctuations [67]. Fig. 1.2 provides an overview of the various research areas being explored with nanomechanical photothermal sensing.

To date, a wide variety of mechanical photothermal sensors have been utilized to achieve these remarkable results, each tailored to specific experimental demands. For instance, SiN string resonators have been widely used in molecular microscopy and

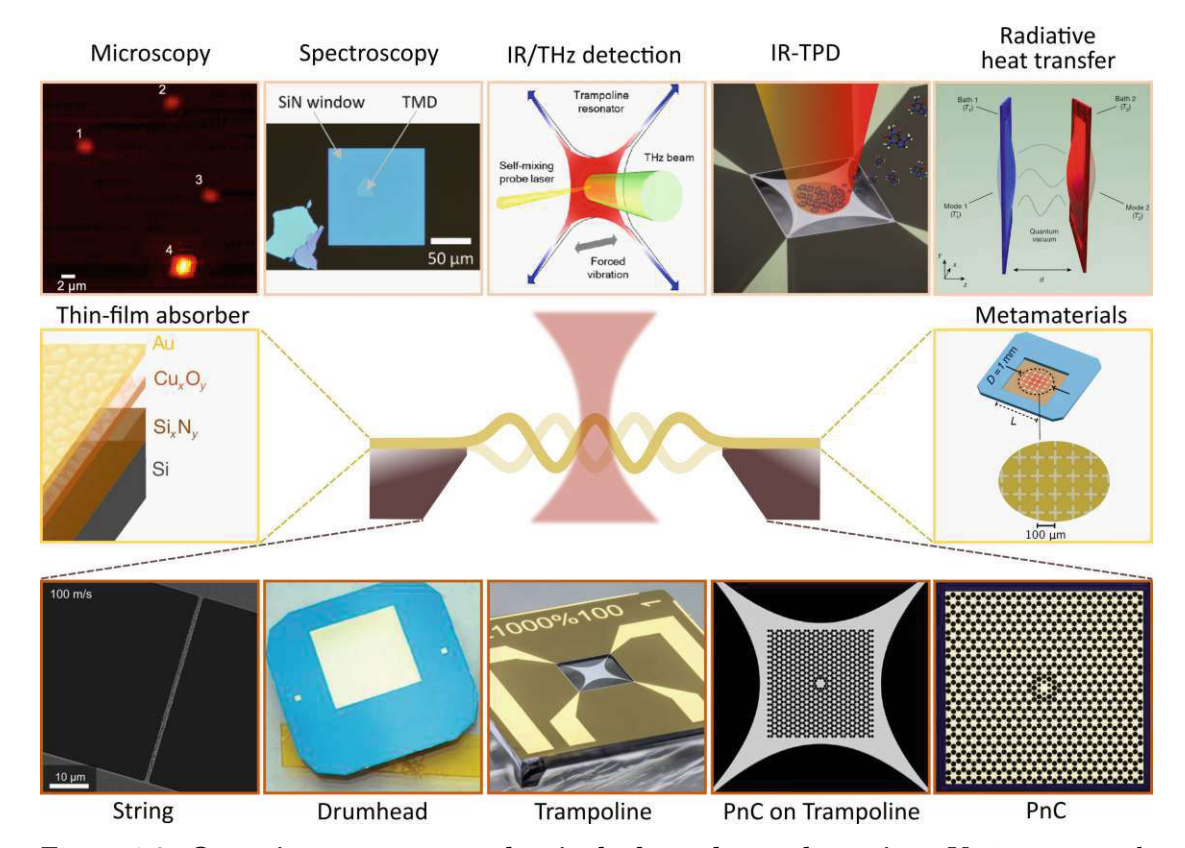


Figure 1.2: Overview on nanomechanical photothermal sensing. Various research fields have been explored so far (top row): microscopy for single particles and molecules (reproduced and cropped from ref. 24-Copyright author(s) 2018, licensed under CC BY-NC-ND 4.0), spectroscopy (reproduced and cropped from ref. 33-Copyright 2023 under a CC BY 4.0 license), IR/THz detection (reproduced and cropped from ref. 39-Copyright 2022 under a CC BY 4.0 license), IR-temperature programmed desorption (IR-TPD, reproduced and cropped from ref. 23-Copyright 2023 under a CC BY 4.0 license), and different mechanisms of radiative heat transfer (adapted with permission from ref. 67– Copyright 2019 by Springer Nature). Different resonator designs are also available (bottom row): strings (reproduced and cropped from ref. 19-Copyright 2016 under a CC BY-NC-ND 4.0 license), drumheads (adapted with permission from ref. 68–Copyright 2023 by AIP Publishing), trampolines (reproduced and cropped from ref. 40-Copyright 2023 under a CC BY 4.0 license), phononic crystal (PnC) geometries on trampolines (reproduced and cropped from ref. 69-Copyright 2020 under a CC BY 4.0 license), and PnC alone (adapted with permission from ref.70–Copyright 2017 by Springer Nature). Different applications further require the design of composite sensors. Two examples are (central row): resonators with thin-film absorbers (reproduced and cropped from ref. 71-Copyright 2020 under a CC BY 4.0 license), and metamaterials (reproduced and rearranged from ref. 42-Copyright 2024 under a CC BY 4.0 license).

spectroscopy [16–19, 21, 22, 25, 26, 28], as their small cross-sectional area, together with the exceptional material properties of SiN, makes them extremely sensitive to temperature changes [25]. Drumhead resonators, with their large surface area, have proven effective for nanomechanical photothermal spectroscopy, enabling studies of single nano-absorbers [24, 29, 30], 2D materials [32, 33], thin films [34, 35], and for IR/THz radiation [38, 42, 63]. More recently, trampoline resonators have been employed in various photothermal sensing studies [38–40, 72–74].

Despite this extensive body of research, a comprehensive comparison of these different resonator designs — evaluating their sensitivity, response time, and practicality — remains lacking.

A consistent part of this work aims to to develop a comprehensive theoretical framework for evaluating the photothermal sensing capabilities of nanomechanical resonators, with a focus on power sensitivity and response time. Analytical models are presented to provide insights into the relationship between sensor response to input signal power and frequency stability. Various noise sources affecting frequency stability, like additive phase noise, temperature fluctuation noise, and photothermal back-action noise are derived. These models are rigorously validated by comparison with experimental data and finite element method (FEM) simulations across various silicon nitride nanomechanical resonator designs, including strings, square drumheads, and trampolines. In all cases, the theoretical predictions show strong agreement with both experimental results and FEM simulations, demonstrating how the photothermal response of the resonance frequency is driven by the corresponding rise in mean temperature. The analysis also emphasizes the significant effect of photothermal back-action on frequency fluctuations. These findings not only clarify the comparative performance of different resonator designs but also establish a strong foundation for advancing the next generation of nanomechanical photothermal sensors.

### 1.4 Low-loss Optical Material Characterization

#### 1.4.1 Overview

Optical absorption is a fundamental phenomenon in nature, intimately connected to the electronic and structural properties of materials. Investigating absorption in solid-state materials is crucial for advancing both fundamental research and practical applications. In photonic integrated circuits (PICs), understanding the sources of optical absorption, and minimizing them to enable high-confinement waveguides [75], is of utmost importance for applications like quantum information processing [76, 77] and biosensing [78, 79]. Similarly, in cavity optomechanics [8, 80–83], minimal absorption of both the optomechanical resonator and the cavity mirrors is vital to prevent mechanical instability [83, 84] and cavity bistability [85]. In nanomechanical photothermal spectroscopy, low absorption is ideal to mitigate the photothermal back-action frequency noise introduced in the resonator, as discussed in this work. Conversely, in nanomechanical photothermal IR detection, maximum absorption is highly desired to enhance the sensor's specific

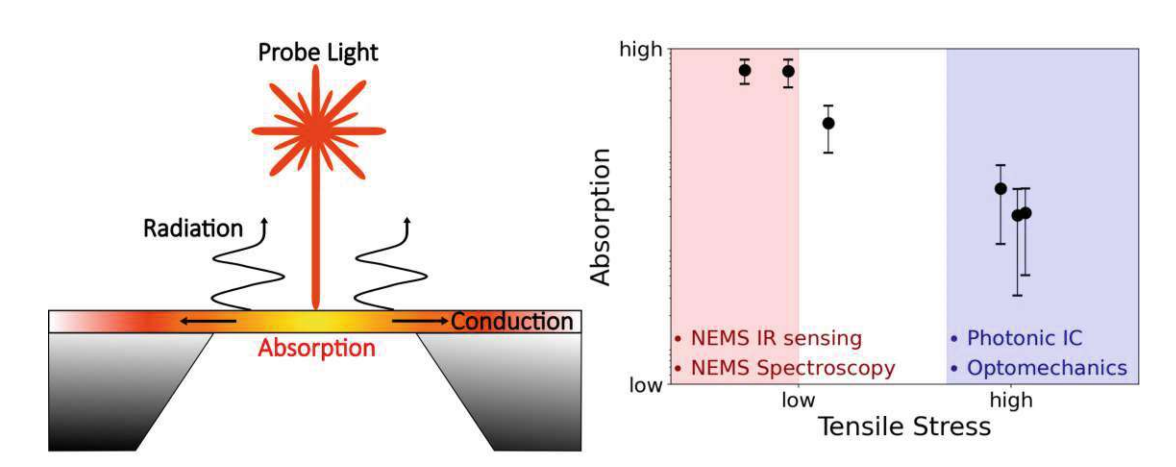


Figure 1.3: Nanomechanical photothermal sensing for optical loss measurements. Left: Schematics of the optical loss characterization with nanomechanical photothermal sensing. Right: Schematics of the SiN absorption as a function of the deposition-related tensile stress.

### detectivity [40, 86].

Among the various materials explored in these fields, silicon nitride (SiN) stands out due to its excellent optical, thermal, and mechanical properties [87, 88]. In particular, its widespread application in photonics stems from its broad transparency window  $(0.4-8 \mu m)$  [89], though this property can strongly depend on the film deposition and fabrication process, for which the underlying mechanisms are not fully understood. This has been observed by means of various techniques, such as ellipsometry [90–95], direct single-pass absorption spectroscopy [96], Fourier Transform IR (FTIR) interferometry [97, 98], cutback [99], outscattered light method [100–104], prism coupling [105], photoluminescence [106], photothermal common-path interferometry [107], and cavity-enhanced absorption spectroscopy [75, 88, 108, 109]. However, these approaches often suffer from scattering losses and slow measurement times, which obscure the true absorption of SiN and make analyses prone to parasitic heating of the surroundings.

### 1.4.2Optical Extinction Measurements with Nanomechanical Photothermal Sensing

Whitin this context, nanomechanical photothermal sensing offers a robust solution to these challenges [16, 18–20, 23, 74], as it directly detects absorption while being insensitive to scattering, as schematically illustrated in Fig. 1.3 (left). In the final part of this work, nanomechanical strings resonators made from low-pressure chemical vapour deposition (LPCVD) deposited SiN are utilized to investigate the relationship between the material absorption and the residual tensile stress (Fig. 1.3, right). The extinction coefficient of SiN at 632.8 nm wavelength reduces of two orders of magnitude when transitioning from low stress ( $\approx 200 \text{ MPa}$ ), relevant for nanomechanical photothermal spectroscopy and

IR sensing, to high stress (> 800 MPa), of relevance for cavity optomechanics and PIC design. Within the framework of the band-fluctuations model [110], this reduction is shown to be dictated by a blue-shift of the energy bandgap of the deposited SiN as the silicon-to-nitrogen ratio (Si/N) reduces. Hence, adjusting the Si/N ratio provides a way to tune the optical properties of SiN, advancing the understanding and application of this ubiquitous material.

#### 1.5 Thesis Outline

The primary goal of this thesis is two-fold. First, it seeks to advance the current understanding of nanomechanical photothermal sensing, leading to the development of a theoretical framework able to capture the core characteristics and key performance metrics of the state-of-the-art nanomechanical photothermal sensors. Second, it demonstrates the versatility and robustness of this sensing approach through two practical applications: single-particle spectromicroscopy and low-loss optical material characterization.

Given that this detection paradigm employs a mechanical element as the sensing core, made vibrate at one of its resonances, the fundamentals of nanomechanical resonators are introduced first (Chapter 2). It follows a detailed description of the theoretical framework for nanomechanical photothermal sensing (Chapter 3). Then, a detailed introduction to the methodologies employed for the acquisition of the results presented throughout this work is presented (Chapter 4). It follows the comparative experimental analysis of three different resonator designs (Chapter 5). Next, the description of the development of a platform for single-particle nanomechanical photothermal spectroscopy is given (Chapter 6). Finally, the effectiveness of nanomechanical photothermal sensing for low-loss material characterization is showcased (Chapter 7).

## Fundamentals of Nanomechanical Resonators

In this chapter, the basic theory of vibrations in nanomechanical resonators is outlined, with a particular emphasis on tensile-stressed structures. First, the general equation of motion for a lumped element model is reviewed, deriving the fundamental properties of resonant mechanical vibrations. Next, the most important mechanical damping mechanisms relevant to this work are introduced. Finally, the treatise shifts to continuum mechanical resonators, with a detailed analysis of three specific designs — namely, strings, drumheads, and trampolines. The theoretical background presented in the following is based on Ref. [60].

The results and associated discussions regarding the trampoline resonators presented in this chapter are based on Ref. [111].

### 2.1Lumped Element Models of Mechanical Vibrations

This section provides a reminder of fundamental concepts necessary to understand the motion in nanomechanical resonators and their interaction with the surrounding environment.

#### **Damped Linear Vibration** 2.1.1

A solid body subjected to the action of external forces, will experience changes in shape and volume, which are referred to as deformations [112]. Thus, each molecule within the solid is displaced from its equilibrium position  $\mathbf{r}$  to the new position  $\mathbf{r}'$  by an amount

$$\mathbf{u} = \mathbf{r}' - \mathbf{r},\tag{2.1}$$

known as displacement vector [112]. The special case of periodic deformations is referred to here as vibrations. The physics behind vibrations can be described with the simple yet

powerful approach of lumped element modelling. In a one-dimensional lumped element model, the whole mass m of the body is considered to be concentrated at a single point (see figure Fig. 2.1), and be displaced an amount u under the action of an external force F.

The kinetic energy introduced into the system by Fis partially stored as potential energy and partially dissipated to the environment. As the solid deforms, internal forces arise due to the rearrangement of its atoms and molecules, which act to restore their equilibrium positions [3]. For small displacements u, these internal forces can be described by the Hook's

$$F_{\mathbf{r}}(t) = -ku(t), \tag{2.2}$$

where k is the effective spring constant. Thus, the restoring force can be modeled as a massless spring with stiffness k.

The dissipative forces acting on the resonator, which represent energy lost to the environment, are assumed here to be proportional to the velocity of vibration  $\dot{u} = du/dt$ 

$$F_{\rm d}(t) = -c\dot{u}(t), \qquad (2.3)$$

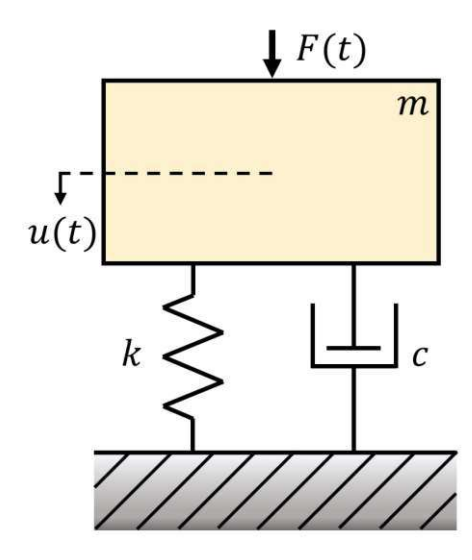


Figure 2.1: 1D lumped element model of vibrations in a driven damped mechanical resonator.

with c denoting the damping coefficient. This force is represented by a massless dashpot in the lumped element model. Balancing the forces acting on the mass, the 1D equation of motion is derived

$$m\ddot{u}(t) + c\dot{u}(t) + ku(t) = F(t), \tag{2.4}$$

with  $\ddot{u} = d^2u/dt^2$  denoting the acceleration, and F being the external driving force.

#### Free Undamped Vibration 2.1.1.1

In the special case where no energy dissipation (c=0) and driving force (F=0) are involved, the equation of motion simplifies to that of a simple harmonic oscillator. Such an undamped free mechanical system will oscillate endlessly at a frequency

$$\frac{\omega_0}{2\pi} = \frac{1}{2\pi} \sqrt{\frac{k}{m}},\tag{2.5}$$

known as eigenfrequency. In this condition, the system will never leave its dynamic state, with its constant mechanical energy swapping back and forth between kinetic and potential energy [60]. A similar scenario is observed in continuum mechanical structures for different vibrational modes, called *eigenmodes*, which, however, do experience dissipation. In the following sections, the focus will be on the dynamics of one such mode.

### 2.1.1.2Free Damped Vibration

For a system with a damping coefficient  $c \neq 0$ , the mechanical energy is no longer conversed, and the resonator will gradually lose its vibrational energy over time. The equation of motion (2.4) for an undriven damped resonator can be rewritten as

$$\ddot{u}(t) + 2\zeta\omega_0\dot{u}(t) + \omega_0^2 u(t) = 0 \tag{2.6}$$

with  $\zeta$  denoting the damping ratio, defined as

$$\zeta = \frac{c}{2\sqrt{km}}. (2.7)$$

In this work, only underdamped resonators are considered, whose vibrations are characterized by  $\zeta < 1$  [60]. A trial solution for Eq. (2.6) can be of the form

$$u(t) = u_0 e^{\gamma t}, \tag{2.8}$$

with  $u_0 \neq 0$  denoting the initial amplitude of vibration. Substituting Eq. (2.8) in (2.6), the expression of  $\gamma$  is found to be

$$\gamma = \omega_0 \left( \zeta \pm i \sqrt{1 - \zeta^2} \right). \tag{2.9}$$

Hence, solutions of Eq. (2.6) for a system left to freely oscillate for a time t > 0 are of the form

$$u(t) = u_0 e^{-\omega_0 \zeta t} \cos\left(\omega_0 \sqrt{1 - \zeta^2} t\right), \tag{2.10}$$

where the vibration occurs at a frequency

$$\frac{\omega_{\text{nat}}}{2\pi} = \frac{\omega_0}{2\pi} \sqrt{1 - \zeta^2},\tag{2.11}$$

called *natural frequency*, while its amplitude decays exponentially in time with a constant

$$\tau_{\rm mech} = \frac{1}{\omega_0 \zeta}.\tag{2.12}$$

The measurement of this time constant, known as ring-down, provides information about the coherence of the vibrational mode of interest.

### 2.1.1.3**Driven Damped Vibration**

Throughout this work, the most encountered scenario is that of a damped resonator driven at one of its eigenmodes  $(F, c \neq 0)$ . This section analyzes the steady-state mechanical response of the resonator when subjected to an harmonic driving force  $F(t) = F_0 \cos(\omega t)$ . With the use of the complex notation, the vibrational response can be expressed as

$$\hat{u}(t) = \hat{u}_0 e^{i\omega t} = u_0 e^{i(\omega t + \theta)}, \tag{2.13}$$

whose amplitude is given by [60]

$$u_0(\omega) = \frac{F_0/m}{\sqrt{(\omega_0^2 - \omega^2)^2 + 4\zeta^2 \omega_0^2 \omega^2}},$$
 (2.14)

while its phase relative to the driving force, also called phase lag, is

$$\theta(\omega) = \arctan\left(\frac{2\zeta\omega_0\omega}{\omega^2 - \omega_0^2}\right).$$
 (2.15)

Hence, the steady-state solution of Eq. (2.4) takes the form

$$u(t) = \mathcal{R}\{\hat{u}(t)\} = u_0 \cos(\omega t + \theta) = \frac{F_0/m}{\sqrt{(\omega_0^2 - \omega^2)^2 + 4\zeta^2 \omega_0^2 \omega^2}} \cos\left(\omega t + \arctan\left(\frac{2\zeta\omega_0\omega}{\omega^2 - \omega_0^2}\right)\right). \tag{2.16}$$

Normalizing Eq. (2.14) for the eigenfrequency  $\omega_0$ , gives

$$u_0(\omega) = \frac{F_0/k}{\sqrt{\left(1 - \left(\frac{\omega}{\omega_0}\right)^2\right)^2 + 4\zeta^2 \left(\frac{\omega}{\omega_0}\right)^2}} = u_s \delta u_0(\omega), \tag{2.17}$$

where  $u_s = F_0/k$  is the static deflection, and  $\delta u_0(\omega)$  is the frequency dependent relative amplitude

$$\delta u_0(\omega) = \frac{1}{\sqrt{\left(1 - \left(\frac{\omega}{\omega_0}\right)^2\right)^2 + 4\zeta^2 \left(\frac{\omega}{\omega_0}\right)^2}},$$
(2.18)

also called dynamic gain [60]. The phase lag can similarly be normalized as

$$\theta(\omega) = \arctan\left(\frac{2\zeta\left(\frac{\omega}{\omega_0}\right)}{\left(\frac{\omega}{\omega_0}\right)^2 - 1}\right). \tag{2.19}$$

Both expressions (2.18) and (2.19) are displayed in Fig. 2.2. It is worth noting that the dynamic gain for a slightly damped resonator exhibits a maximum near  $\omega_0$ . By differentiating Eq. (2.18) with respect to the driving frequency  $\omega$  and solving  $\partial \delta u_0/\partial \omega = 0$ , the frequency of maximum displacement is found to be

$$\frac{\omega_r}{2\pi} = \frac{\omega_0}{2\pi} \sqrt{1 - 2\zeta^2},\tag{2.20}$$

which is referred to as resonance frequency. For slightly damped resonators ( $\zeta \ll 1$ ), this simplifies to  $\omega_r \approx \omega_0$ . Moreover, at  $\omega = \omega_r$ , the phase lag is given by

$$\theta_r = \arctan\left(\frac{\sqrt{1-2\zeta^2}}{\zeta}\right),$$
(2.21)



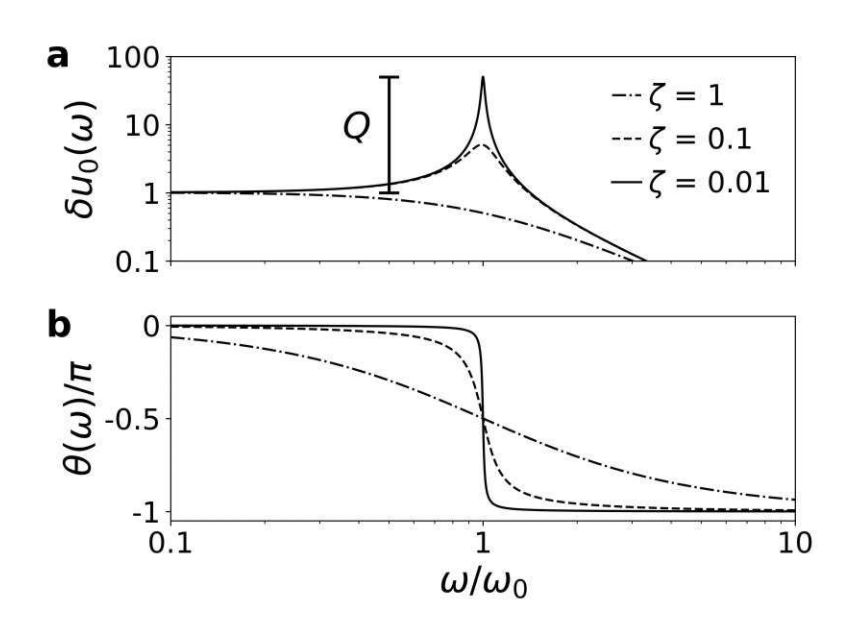


Figure 2.2: **Driven damped vibrations. a.** Dynamic gain (2.18) as a function of the normalized frequency  $\omega/\omega_0$ , for different damping ratios  $\zeta$ . b. Corresponding phase lag (2.19).

which approaches  $\theta_r \approx \pi/2$  for slight damping.

Hence, for low driving frequencies ( $\omega \ll \omega_r$ ), a slightly damped mechanical resonator vibrates with amplitudes equal to its static deflection  $u_s$ , in phase with the driving external force. As  $\omega$  approaches  $\omega_r$ , the resonator start to vibrate out-of-phase with respect to the force F, ultimately reaching a maximal value of

$$u_0(\omega = \omega_r) = \frac{F_0}{k} \frac{1}{2\zeta\sqrt{1-\zeta^2}} = \frac{F_0}{k}Q = u_s Q.$$
 (2.22)

The amplification factor appearing in Eq. (2.22) is called *quality factor* (Fig. 2.2a), and for slight damping can be written as

$$Q \approx \frac{1}{2\zeta}.\tag{2.23}$$

Hence, the smaller the damping ratio is, the higher is the Q factor of the resonator and its corresponding resonant vibrational amplitude (2.22). A higher Q also translates in stepper phase responses, with the slope at resonance given by

$$\frac{\partial \theta}{\partial \omega}(\omega = \omega_r) = \frac{1}{\omega_0 \zeta} = \frac{2Q}{\omega_0}.$$
 (2.24)

Notably, the phase slope at resonance (2.24) is equal to the mechanical time constant of the resonator  $\tau_{\text{mech}}$  (2.12). Therefore, for very slightly damped systems it results that

$$Q \approx \frac{1}{2}\omega_0 \tau_{\text{mech}}.$$
 (2.25)

By measuring the time it takes for the resonator to dissipate its mechanical energy, its quality factor can be extracted [60]. This method, known as ring-down, is especially useful for determining very high Q values and has been employed for all the Q measurements performed in this work. For other techniques used to measure Q, the reader can refer to [60].

### 2.2Mechanical Dissipation Mechanisms

As highlighted above, the quality factor expresses the amplification of the vibrational amplitude at resonance, as well as its sharpness. Physically, Q is defined as the ratio between the stored versus lost energy into the resonator during one vibrational cycle [60]. Various mechanisms can contribute simultaneously to the energy dissipation, leading to an overall damping [60]

$$\frac{1}{Q} = \frac{1}{Q_{\text{gas}}} + \frac{1}{Q_{\text{int}}} + \frac{1}{Q_{\text{rad}}} + \frac{1}{Q_{\text{other}}}.$$
 (2.26)

 $Q_{\rm gas}$  describes losses due to the interaction between the resonator and the surrounding gas,  $Q_{\rm int}$  refers to the losses occurring within the resonator (bulk and surface friction, thermoelastic damping etc.),  $Q_{\rm rad}$  denotes the losses due to energy radiation occurring at the clamping of the resonator, and  $Q_{\text{other}}$  includes all the other types of losses irrelevant for this work, such as electrical charge damping and Eddy current losses.

### 2.2.1Gas Damping

Gas damping belongs to the broader class of medium interaction losses, which includes the interaction between the resonator and its surrounding medium, such as gas or liquid. Here, only the resonator-gas interaction is briefly described. For a more comprehensive discussion of other scenarios, the reader can refer to [60].

The magnitude of gas damping is directly influenced by the gas pressure, as well as the geometry and frequency of the resonator itself [113]. In particular, the pressure defines two main operating regions, the *fluidic* and *ballistic regime*. The transition between the two regimes is expressed through the Knudsen number Kn, defined as ratio between the mean free path of the surrounding gas  $\lambda_f$  and the characteristic physical length of the resonator  $L_r$  [113]

$$Kn = \frac{\lambda_f}{L_r}. (2.27)$$

It depends on the gas pressure via  $\lambda_f$ , which, in turn, is given by

$$\lambda_f = \frac{k_B T}{\sqrt{2\pi} d_{\sigma_{BS}}^2} \frac{1}{p},\tag{2.28}$$

with  $k_B$ , T,  $d_{gas}$ , and p denoting the Boltzmann constant, the environmental temperature, the diameter of the gas molecule, and the gas pressure, respectively. For Kn < 1, the mean free path of the gas molecules is shorter than the resonator's characteristic length,

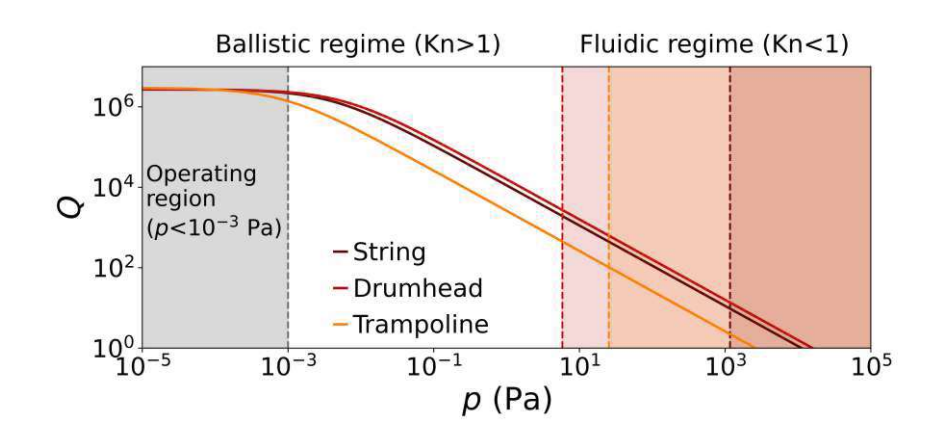


Figure 2.3: Gas damping. Theoretical Q factors as a function of the gas pressure p, for three different resonators (maroon, string; dark red, drumhead; orange, trampoline), made of low-stress (200 MPa) silicon nitride. The coloured dashed vertical lines refer to the pressure values for which Kn = 1 for the various geometries. The dimensions are summarized in Table 2.1.

and the gas behaves as a continuum fluid interacting with the resonator, dissipating energy via its viscous flow (fluidic regime). In contrast, for Kn > 1, where  $\lambda_f > L_r$ , the losses occur from the impact of non-interacting molecules onto the resonator (ballistic regime). Specifically, the net energy loss is caused by the imbalance in molecular collisions on the front and back surfaces of the resonator. In both regimes, energy losses can occur via squeezed-film and/or drag-force damping. The former arises from the interaction between the resonator and the gas trapped between this and the substrate, when present. The latter is caused by the collision of the gas molecules with the moving resonator. All the structures analyzed in this work are operated in vacuum, at pressures far below the fluidic region  $(p < 10^{-3} \text{ Pa})$ , where  $Q \ll Q_{\text{gas}}$ . This is clearly shown in Fig. 2.3 for three different resonators—namely, a string (Fig. 2.7a), a drumhead (Fig. 2.8a), and a trampoline (Fig. 2.9a). The specific geometrical properties chosen for the calculations are summarized in Table 2.1. The dashed vertical lines represent the corresponding transition pressure

$$p|_{Kn=1} = \frac{k_B T}{\sqrt{2}\pi d_{\text{gas}}^2} \frac{1}{L_r},$$
(2.29)

for a diameter  $d_{\rm gas}=0.362$  nm of air molecules, falling three orders of magnitude above the operating pressure (see Fig. 2.3 and Table 2.1). The linear p-dependence of Q for  $p > 10^{-3}$  Pa is due to ballistic drag-force damping, as no substrate is present. In this scenario, the damping reduces with the pressure p following the expression [114]

$$Q_{\rm gas} = \frac{\rho h \omega_0}{4} \sqrt{\frac{\pi}{2}} \sqrt{\frac{R_{\rm gas}T}{M_m}} \frac{1}{p} = \frac{1}{c_{\rm gas}} \frac{1}{p},$$
 (2.30)

Table 2.1: Gas damping in low-stress (200 MPa) LPCVD silicon nitride resonators of thickness h=50 nm. The length of the string, the side length of the drumhead, and the window side length of the trampoline are chosen to be equal to 1 mm. The SiN mechanical material parameters used are those summarized in Table 3.1. For  $c_{\rm gas}$ , T=300 K and  $M_{\rm m}=28.97$  g/mol are assumed. Moreover, only the fundamental out-of-plane flexural mode is considered.

Design	Characteristic length, $L_{\rm r}$	$p _{Kn=1}$ (Pa)	$c_{\rm gas}~({\rm Pa}^{-1})$
String	Width, 5 $\mu m$	1422	$8.94 \cdot 10^{-5}$
Drumhead	Side length, 1 mm	7	$6.32 \cdot 10^{-5}$
Trampoline	Central area side length, 230 $\mu \mathrm{m}$	31	$38.4 \cdot 10^{-5}$

where  $\rho$ , h, and  $\omega_0$  denote the resonator's mass density, thickness, and oscillation of vibration, respectively.  $R_{\rm gas}$ , T, and  $M_m$  refer instead to the universal molar gas constant, the temperature, and the molar mass of the gas, respectively. In the assumption that mechanical radiation losses can be neglected, the overall quality factor (2.26) is given by

$$Q^{-1} = Q_{\text{int}}^{-1} + c_{\text{gas}}p. (2.31)$$

(the corresponding values of  $c_{\rm gas}$  for the three design are given in Table 2.1). Hence, for  $p < 10^{-3}$  Pa, Q is independent of the pressure and limited by intrinsic losses  $Q_{\rm int}$  (see below). It is worth noting that resonators vibrating at higher frequencies  $\omega_0/2\pi$  will enter before the ballistic regime.

## 2.2.2 Radiation Damping

Radiation damping refers to the energy losses that occur due to radiation of mechanical energy from the vibrating resonator through the clamping points into the substrate [60]. While these losses strongly depend on the detailed anchor geometry, a general relationship can be expressed as

$$Q_{\rm rad} \propto \left(\frac{L}{h}\right)^a \eta^b,$$
 (2.32)

with  $\eta$  denoting the acoustic mismatch between a semi-infinite substrate and the resonator

$$\eta \approx \sqrt{\frac{E_s}{\rho_s}} \frac{\rho}{\sigma_0},\tag{2.33}$$

where  $\rho_s$  and  $E_s$  represent the mass density and the Young's modulus of the substrate, respectively. In Eq. (2.32),  $a \geq 1$  varies with the dimensionality of the structure, transitioning from 2D to 1D, while b = 0 for cantilevers and b = 3 for drumheads. Additionally, this type of loss also strongly depends on the chip mounting condition [115]. Slender beams and/or low-stress can mitigate this source of dissipation, as it occurs for the resonators studied in this work.

### 2.2.3 **Intrinsic Damping**

This type of damping encompasses all dissipation mechanisms occurring within the resonator itself. It can be categorized in friction losses and fundamental losses. The former arise from imperfections either within the bulk or on the surface of the resonator; the latter are inherent, even in an ideal, frictionless resonator. Since fundamental losses typically occur at very high frequencies, well beyond the range explored in this work, their effects are negligible and will not be discussed further. For additional information, the reader can refer to [60].

### 2.2.3.1Standard Linear Solid Model

Friction losses originate from irreversible atomic motion that occurs during the vibrations. They can be described within the standard linear solid (SLS) model, also known as Zener model, where the resonator is treated as an anelastic system with a single, frequencydependent friction loss mechanism [116, 117]. In this framework, the Young's modulus is expressed as

$$E(\omega) = E_{\text{real}}(\omega) + iE_{\text{imag}}(\omega), \qquad (2.34)$$

where  $E_{\text{real}}$  and  $E_{\text{imag}}$  denote the storage and the loss Young's modulus, respectively. The former expresses the energy W stored in the structure due to the applied strain; the latter expresses the energy  $\Delta W$  dissipated during one cycle of vibration. The damping associated to the friction losses is given by [60]

$$Q_{\text{friction}} = 2\pi \frac{W}{\Delta W} = \frac{E_{\text{real}}}{E_{\text{imag}}} = \tan^{-1}(\delta), \qquad (2.35)$$

where  $tan(\delta)$  is the loss tangent. For SiN,  $tan(\delta) \approx 10^{-5}$ . For more details, the reader can refer to [117].

### 2.2.3.2Surface Friction

As the mechanical structures are reduced in size, the surface-to-volume ratio increases, causing surface losses to dominate the dissipation within the resonator. This phenomenon is referred to as surface friction. Although surface loss is recognized as a significant source of dissipation in nanomechanical resonators, the precise contributions from different sources of surface friction remain unclear. Nonetheless, a general relationship can be written as [118, 119]

$$Q_{\text{surf}} = \beta h, \tag{2.36}$$

with h denoting the thickness of the resonator, and  $\beta$  the proportionality constant. In particular, Villanueva et al. investigated surface friction losses in SiN resonators [119], finding for the proportionality constant a value of  $\beta = (6 \pm 4) \cdot 10^{10} \text{ m}^{-1}$ . Fig. 2.4 illustrates the overall  $Q_{\rm int}$  as a function of h, as reported in [119]. For thicker resonators  $(h \ge 500 \text{ nm})$ , bulk losses dominates (where  $Q_{\text{vol}} \approx 28000 \text{ has been used})$ ; for h < 500nm, surface losses further reduce the ultimate intrinsic damping. The vertical, light shadowed region indicates the range of thicknesses characterized throughout this work.

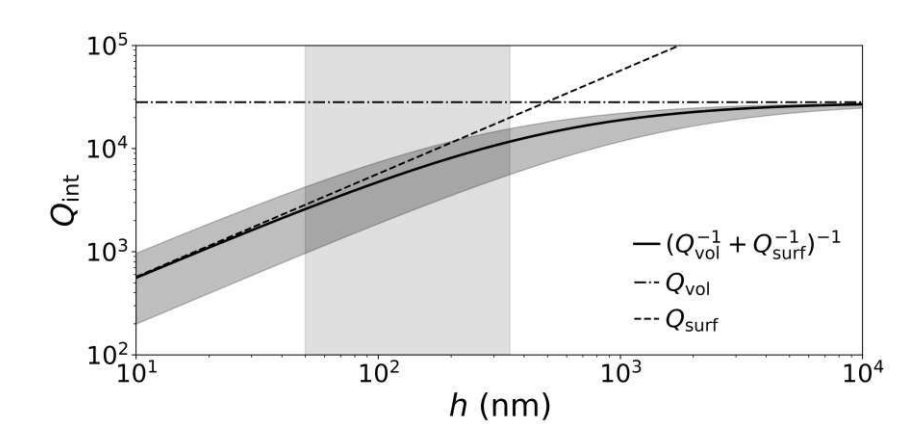


Figure 2.4: Surface friction losses. Intrinsic quality factor  $Q_{\text{int}} = (Q_{\text{vol}}^{-1} + Q_{\text{surf}}^{-1})^{-1}$  as a function of the resonator's thickness h. The horizontal, darker shadowed region accounts for the uncertainties in  $\beta$  [119], while the vertical, lighter region indicates the values of thickness considered in this work.

### 2.2.3.3Dissipation Dilution

The last element to be discussed relevant for this work, is the phenomenon of dissipation dilution, which has received significant attention in the last decades [120]. Here, only the essentials are covered. Additional details can be found in [60, 120].

In essence, dissipation dilution leads to an enhancement of the quality factor, exceeding the limits imposed by material intrinsic losses,  $Q_{\rm int}^{-1}$ . This arises from the presence of a quasi-lossless extra potential  $W_{lossless}$  contributing to the stored mechanical energy of vibration W of Eq. (2.35) [60, 120]

$$Q = 2\pi \frac{W + W_{\text{lossless}}}{\Delta W} = 2\pi \frac{W}{\Delta W} \left( 1 + \frac{W_{\text{lossless}}}{W} \right) = Q_{\text{int}} \alpha_{\text{DD}}. \tag{2.37}$$

Here,  $\alpha_{\rm DD}$  is the dilution factor, and quantifies the aforementioned Q enhancement. For stressed resonators, as those analyzed in this work, the lossless potential is given by the elastic energy stored during deformation against the static tensile force, and is of relevance for flexural modes [121]. A general expression for  $\alpha_{\rm DD}$  is given by [120]

$$\alpha_{\rm DD} = \left( a_{n(j)} \lambda_{\rm strain} + b_{n(j)} \omega_{n(j)} \lambda_{\rm strain}^2 \right)^{-1}, \tag{2.38}$$

with  $a_{n(j)}$  and  $b_{n(j)}$  being two mode-dependent factors (with n for 1D and nj for 2D structures),  $\omega_{n(j)}$  is the corresponding resonance frequency, and  $\lambda_{\text{strain}}$  is the strain parameter

$$\lambda_{\text{strain}} = \frac{h}{L} \sqrt{\frac{E}{12\sigma_{\text{avg}}}},\tag{2.39}$$

with E and  $\sigma_{\text{avg}}$  denoting the Young's modulus and average tensile stress of the resonator. Fig. 2.5 shows  $\alpha_{\rm DD}$  as a function of the resonator length L for a string and drumhead.

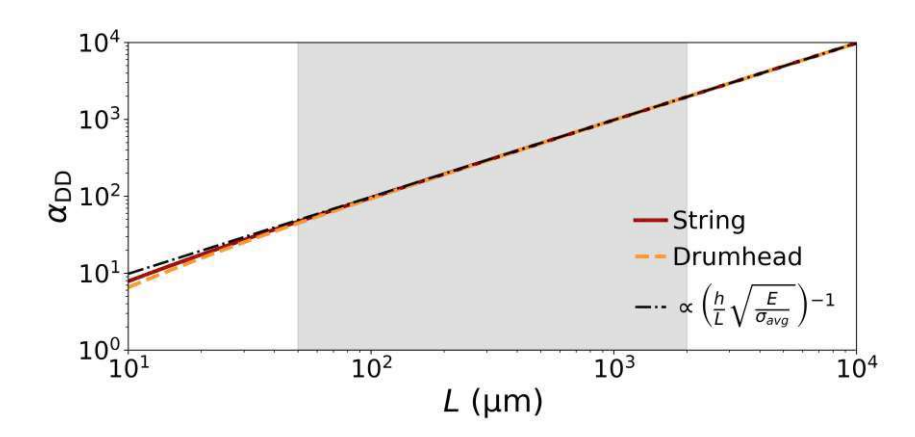


Figure 2.5: **Dissipation dilution.** Dissipation dilution factor  $\alpha_{\rm DD}$  as a function of the resonator length L. The calculations (2.38) are done for a string and drumhead with tensile stress  $\sigma_{\text{avg}} = 200 \text{ MPa}$ , made of SiN (see Table 3.1 for the material parameters used here). The shadowed region indicates the range of lengths considered in this work.

The shadowed region highlights the range of lengths explored in this work. In this regime, where  $\alpha_{\rm DD} \propto \lambda_{\rm strain}^{-1}$ , the dilution factor is constrained by the local bending near the clamping of the resonator [60].

At this stage, all the key parameters necessary for describing a single resonance mode in the linear regime using a lumped element model — namely, the resonance frequency  $\omega_r$  and the quality factor Q — have been covered.

### 2.3Dynamic range

Another crucial characteristic of nanomechanical resonators is their dynamic range (DR) of operation. The DR is defined by the amplitude range where the resonator's response  $u_0(\omega)$  to an external force  $F_0$  is independent of the amplitude itself [60]. Various nonlinearities set the upper limit on the achievable DR [60]. In flexural bending modes, geometrical nonlinearities arise from the effective elongation experienced by the structure during vibration. These can be modelled as an effective force that acts against the vibration and scales with  $\propto \alpha_{\rm eff} u^3$ , where  $\alpha_{\rm eff}$  is the effective Duffing parameter ( $\alpha_{\rm eff} > 0$ for materials like silicon nitride) and depends on the geometry of the resonator. Hence, the equation of motion for a slightly damped system (2.4) becomes

$$\ddot{u}(t) + \frac{\omega_0}{Q}\dot{u}(t) + \omega_0^2 u(t) + \frac{\alpha_{\text{eff}}}{m}u^3(t) = \frac{F(t)}{m},$$
(2.40)

known as Duffing equation, where the resonator exhibits an effective stiffness

$$k_{\text{eff}} = m\omega_0^2 \left[ 1 + \frac{\alpha_{\text{eff}}}{m\omega_0^2} u^2(t) \right].$$
 (2.41)

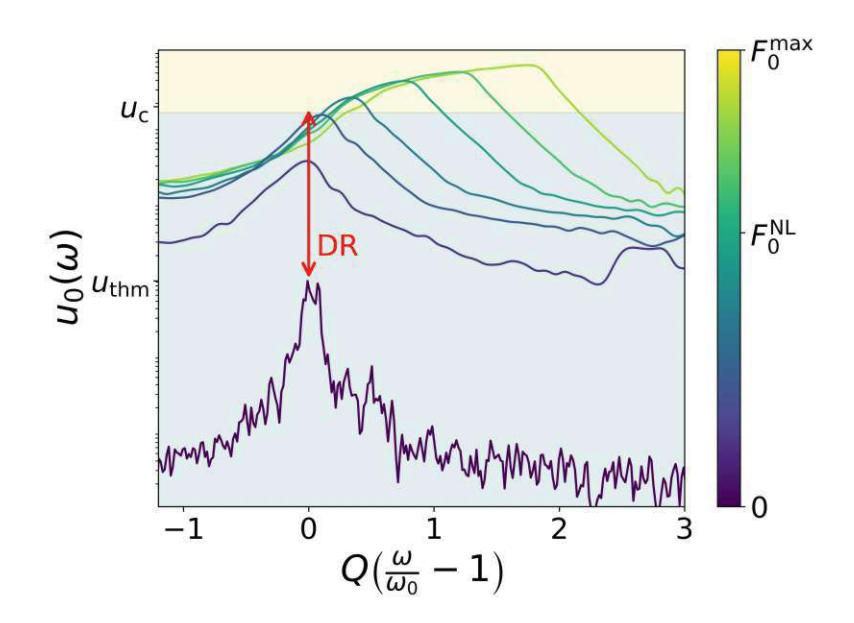


Figure 2.6: **Duffing resonator.** Amplitude of motion  $u_0(\omega)$  of a Duffing resonator as a function of the scaled frequency  $Q(\omega/\omega_0 - 1)$  for varying driving force  $F_0$ . The dynamic range (DR) is highlighted in red and goes from the amplitude peak driven by incoherent thermal energy  $(u_{\text{thm}})$  and the critical amplitude  $(u_{\text{c}})$ .

The first term corresponds to the stiffness of an harmonic oscillator as seen in Eq. (2.5); the second term becomes significant at high displacement, leading to two key effects: i) it shifts the resonance frequency  $\omega_0$  to higher values; ii) it reduces the amplitude peak

Fig. 2.6 shows both effects, where the amplitude of motion of a Duffing resonator is plotted as a function of a scaled driving frequency  $Q(\omega/\omega_0-1)$ , for varying magnitude of the driving force. For small forces (darker curves), the amplitude u is small enough that the second term in Eq. (2.41) can be disregarded, and the Lorentzian response (2.17) remains unaffected. For larger driving force (lighter curves), nonlinearities emerge beyond a critical amplitude  $u_c$  [60]

$$u_{\rm c} = \sqrt{\frac{8}{3\sqrt{3}}} \frac{1}{\sqrt{Q}} \sqrt{\frac{m\omega_0^2}{\alpha_{\rm eff}}},\tag{2.42}$$

which depends on Q and the ratio of the resonator's stiffness to the Duffing parameter. This value defines the upper bound of the DR, as illustrated in Fig. 2.6. Throughout this work, most experiments and theoretical analyses have been conducted at an amplitude  $u_0 = u_c$ , which ensures the highest signal-to-noise ratio to minimize frequency fluctuations (the details are provided in Chapter 3).

Next, the focus will shift to the discussion of each specific resonator design of interest in this work.

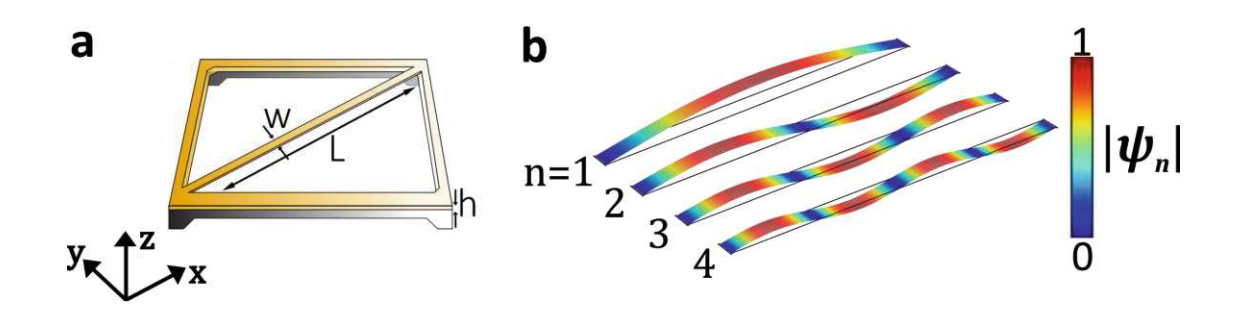


Figure 2.7: Vibrations of a string resonator. a. Schematics of a string resonator of length L, width w, and thickness h. b. FEM simulated mode shapes of the first four out-of-plane flexural modes of a string resonator.

### 2.4 Free Bending Vibration of Continuum Resonators

In this section, the bending modes of specific mechanical geometries — namely string, drumheads and trampolines — under initial tensile stress will be derived and discussed. In particular, the continuum nature of strings and drumheads will be taken into account in the mechanical description, while a lumped element model will be employed to describe the trampoline. Additionally, the expressions for the effective mass and Duffing parameters are given for completeness, as these parameters enters Eq. (2.42), essential for the theoretical analysis of the frequency stability in the three different designs as will be further discussed in Chapters 3 and 5.

### 2.4.1String

Strings are among the most explored mechanical resonators. The analytical model for their continuum mechanical description is based on the Euler-Bernoulli beam theory. Here, a beam is defined as a slender and long mechanical structure, such that its rotational inertia and shear deformation can be neglected [60]. The string is a special case of a beam fixed at both ends under a tensile stress  $\sigma_0$ . In the following, only strings with a rectangular cross-section are considered, with length L, width w, and thickness h (see Fig. 2.7a). Moreover, only out-of-plane flexural modes are discussed.

Under the assumption of a linear elastic material, no damping, and small deflections  $u(x,t) \ll h$ , the equation of motion of a string is similar to that of a doubly clamped beam subjected to an axial tensile force  $N = \sigma_0 wh$  along its length, and is given by

$$\rho w h \frac{\partial^2 u(x,t)}{\partial t^2} + E I_y \frac{\partial^4 u(x,t)}{\partial x^4} - N \frac{\partial^2 u(x,t)}{\partial x^2} = 0.$$
 (2.43)

 $\rho$ , E, and  $I_u$  denote the mass density, the Young's modulus, and the geometrical moment of inertia with respect to the y-axis, respectively. The latter is defined for a rectangular cross-section as

$$I_y = \frac{wh^3}{12}. (2.44)$$

The corresponding general solution to Eq.(2.43) is the superposition of the string's eigenmodes

$$u(x,t) = \sum_{n=1}^{\infty} \psi_n(x) u_n(t) = \sum_{n=1}^{\infty} \psi_n(x) u_{0,n} \cos(\omega_n t),$$
 (2.45)

where the separation of variables has been exploited.  $\psi_n$  represents the normalized modeshape of the nth eigenmode. For a simply supported string, where rotation at the clamping points is allowed, the boundary conditions are given by

$$\psi_n(0) = \psi_n(L) = 0, \tag{2.46}$$

$$\frac{\partial^2 \psi_n}{\partial x^2}(0) = \frac{\partial^2 \psi_n}{\partial x^2}(L) = 0. \tag{2.47}$$

Modeshapes of the form

$$\psi_n(x) = \sin(\beta_n x) \tag{2.48}$$

satisfy Eq. (2.46) and (2.47), with  $\beta_n$  denoting the wavenumber of the corresponding mode. Fig. 2.7b shows the first four out-of-plane flexural modes (n = 1 - 4). Substituting Eq. (2.48) and (2.45) into Eq. (2.43) yields the dispersion relationship

$$\frac{\omega_n}{2\pi} = \frac{1}{2\pi} \sqrt{\frac{EI_y}{\rho wh}} \beta_n^4 + \frac{\sigma_0}{\rho} \beta_n^2 = \frac{1}{2\pi} \sqrt{\frac{Eh^2}{12\rho}} \beta_n^4 + \frac{\sigma_0}{\rho} \beta_n^2 = \frac{\beta_n^2}{2\pi} \sqrt{\frac{Eh^2}{12\rho}} \sqrt{1 + \frac{12\sigma_0}{Eh^2}} \frac{1}{\beta_n^2}. \quad (2.49)$$

A wavenumber  $\beta_n$  that satisfies the boundary conditions (2.46) and (2.47) is given by

$$\beta_n = \frac{n\pi}{L}.\tag{2.50}$$

For the stress values used throughout this work, the following condition is always satisfied

$$\frac{12\sigma_0}{Eh^2} \frac{L^2}{n^2 \pi^2} \gg 1, \tag{2.51}$$

which implies that flexural rigidity of the beam  $D_E = Eh^3/12$  can be neglected, simplifying Eq. (2.49) to the form

$$\frac{\omega_n}{2\pi} = \frac{n}{2L} \sqrt{\frac{\sigma_0}{\rho}}. (2.52)$$

This is the dispersion of a pure string resonator, whose eigenfrequency is independent of the thickness h. All these results are valid for simply supported beams. For the case where the flexural rigidity at the clamping points is taken into account, the reader can refer to [60].

For completeness, the expressions for the effective mass and Duffing parameters are

provided here, as they define, together with the quality factor Q, the critical amplitude  $u_c$ of the resonator. To calculate them, an equivalent harmonic oscillator is used to describe the dynamics of a single resonance mode of a continuum structure [60]

$$\frac{\omega_n}{2\pi} = \frac{1}{2\pi} \sqrt{\frac{k_{\text{eff,n}}}{m_{\text{eff,n}}}},\tag{2.53}$$

with  $k_{\rm eff,n}$  and  $m_{\rm eff,n}$  denoting the effective stiffness and effective mass of the specified resonance mode, respectively. These effective parameters can be obtained by comparison between the energies of the lumped element model with those of the continuum counterpart. The resultant equivalence depends on the chosen amplitude normalization, i.e., the position along the continuum resonator must be defined. In the following, the choice falls in the position of the antinode of the fundamental mode. More details can be found in [60]. For a string resonator, the effective mass can be written as [60]

$$m_{\text{eff}} = \frac{1}{2}m_0,$$
 (2.54)

where  $m_0$  is the total mass of the string. It is interesting to notice that the effective mass is independent of the particular mode. In contrast, the effective Duffing parameter depends on the mode and is given by [60]

$$\alpha_{\text{eff,n}} = \frac{(n\pi)^4}{8} \frac{Ewh}{L^3},$$
(2.55)

presenting a strong dependence on the string's length.

### 2.4.2Drumhead

The drumhead resonators are the two-dimensional equivalence to strings, i.e. they are thin plates under tensile stress  $\sigma_0$ , which dominates their mechanical properties over the flexural rigidity. In the following, only squared membranes are discussed (see Fig. 2.8a). Assuming a linear elastic material, the equation of motion is given by [122]

$$\sigma_0 h \nabla^2 u(\mathbf{r}, t) - \rho h \frac{\partial^2 u}{\partial t^2} = 0. \tag{2.56}$$

 $\mathbf{r} = (x, y), (r, \theta)$  is the in-plane position vector in Cartesian and polar coordinates, respectively. The operator  $\nabla^2$  is given in Cartesian coordinates by

$$\nabla^2 = \frac{\partial^2}{\partial x^2} + \frac{\partial^2}{\partial y^2},\tag{2.57}$$

while in polar coordinates by

$$\nabla^2 = \frac{1}{r} \frac{d}{dr} \left( r \frac{d}{dr} \right). \tag{2.58}$$

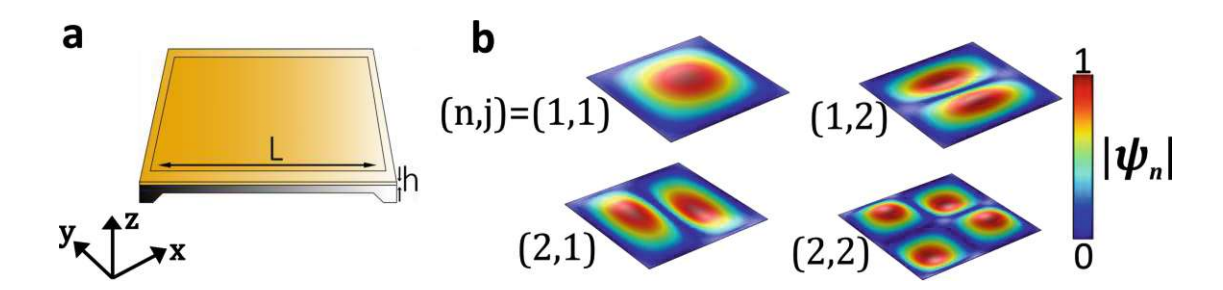


Figure 2.8: Vibrations of a drumhead resonator. a. Schematics of a drumhead resonator of side length L and thickness h. b. FEM simulated mode shapes of the first four flexural modes of a drumhead resonator.

In the assumption of simply supported drumheads, and by applying the separation of variables, the nth eigenmode solution of Eq. (2.56) will be in Cartesian coordinates of the form

$$u_{nj}(x, y, t) = \psi_{nj}(x, y)u_{0,nj}\cos(\omega_{nj}t),$$
 (2.59)

with a modeshape given by

$$\psi_{nj}(x,y) = \sin\left(\frac{n\pi}{L}x\right)\sin\left(\frac{j\pi}{L}y\right).$$
(2.60)

L is the side length of the drumhead, n and j the modal numbers, and  $\omega_{nj}$  the corresponding eigenfrequency. Fig. 2.8b shows the modeshape of the first four flexural modes. Substituting Eq. (2.59) into (2.56) yields to the dispersion relationship

$$\frac{\omega_{nj}}{2\pi} = \frac{\sqrt{n^2 + j^2}}{2L} \sqrt{\frac{\sigma_0}{\rho}},\tag{2.61}$$

as it has been shown for string resonators.

The effective mass for a drumhead resonator is [60]

$$m_{\text{eff}} = \frac{1}{4}m_0,$$
 (2.62)

and it is independent of the mode of interest. Its effective Duffing parameter is given by [60]

$$\alpha_{\text{eff,n,j}} = \frac{3\pi^4(n^4 + j^4)}{64} \frac{Eh}{L^2}.$$
 (2.63)

### 2.4.3 Trampoline

The third geometry analyzed here is the trampoline [29, 81, 82]. It consists of a central pad of area  $L^2$  and thickness h, anchored to the frame via four tethers of length  $L_t$  and



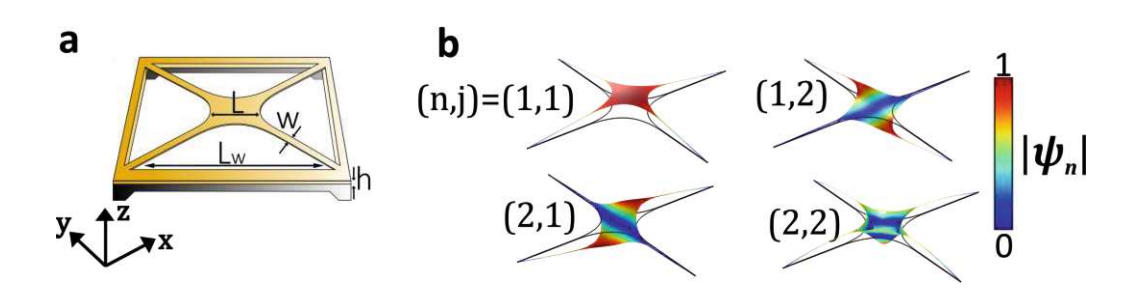


Figure 2.9: Vibrations of a trampoline resonator. a. Schematics of a trampoline resonator of side length L and thickness h. b. FEM simulated mode shapes of the first four out-of-plane flexural modes of a trampoline resonator.

rectangular cross-section  $w \cdot h$  under tensile stress, as shown schematically in Fig. 2.9a. The following analysis focuses specifically on the fundamental eigenfrequency of trampolines for a fixed window side length  $L_{\rm w}$  (mode (1,1) in Fig. 2.9b). To do that, the effective mass  $m_{\text{eff}}$  and effective spring constant  $k_{\text{eff}}$  are introduced (2.53). The theoretical model is compared to finite element method (FEM) simulations (for more details on the FEM, see Chapter 4).

The FEM simulations are performed for central pad with a square and Bezier profile (Fig. 2.10a). The former is an idealization of the latter, which has been characterized experimentally in this work (see Chapter 5). In both cases, the effective mass  $m_{\text{eff}}$  is connected to a fixed frame (a square window of side length  $L_{\rm w}$ ), via a spring of constant  $k_{\text{eff}}$  (representing the diagonal four tethers of Fig. 2.9a).

The spring constant is a function of the initial tensile stress, similar to what occurs in strings, which, however, varies along the diagonal length, as the structure's width is no longer constant. This variation stems from the balance of the tensile force N applied on the unsuspended thin film of thickness h. After the release process of the trampoline, the resulting strain  $\epsilon$  in the structure remains constant, since the distance between clamping points is unchanged, resulting in a force balance [121]

$$\frac{N}{hE} = \text{const} = \epsilon(x)w(x) = \frac{\sigma(x)}{E}w(x). \tag{2.64}$$

Here, w(x) denotes the local width of the geometry as a function of the coordinate x along the diagonal cut-line (Fig. 2.10a). From Eq. (2.64), it is evident that the tethers concentrate higher stress  $\sigma_t$  than the central pad due to a reduction in cross-section. This is clearly illustrated in Fig. 2.10b, where a cut-line along the x coordinate is shown for FEM simulated trampolines with a Bezier profile (T45 indicates a central pad side

length of  $L=45~\mu m$ ). Moreover, as the tethers shorten (for increasing values of L), this stress further increases. The FEM model includes also the chip to better show the stress distribution.

For clarity, additional FEM simulations have been performed for a trampoline with a central square pad of area  $L^2$  and effective mass  $m_{\rm eff,c}$ , connected to the frame via four tethers along its two diagonals, each of length  $L_{\rm t}$  and effective mass  $m_{\rm eff,t}$ . For such a trampoline oscillating at its fundamental resonance frequency  $\omega_0/2\pi$ , the effective spring constant  $k_{\text{eff}}$  can be modelled as that of a string of length  $L_{\text{t}}$ , under a prestress  $\sigma_0(1-\nu)$ , which is given by

$$k_{\text{eff}}(\sigma_0, L_{\text{t}}) = \frac{\pi^2}{2} \frac{wh}{L_{\text{t}}} \sigma_0 (1 - \nu)$$
 (2.65)

with  $\sigma_0$  denoting the nominal tensile stress of the unstructured thin film, and with the factor  $(1-\nu)$  accounting for the transverse strain relaxation upon release. From Eq. (2.65), it is possible to extract the stress concentrated at the tethers

$$\sigma_{\rm t} = \frac{2}{\pi^2} \frac{1}{wh} k_{\rm eff} \frac{\sqrt{2}L_{\rm w}}{2} = \frac{\sqrt{2}L_{\rm w}}{2L_{\rm t}} \sigma_0 (1 - \nu). \tag{2.66}$$

Hence,  $\sigma_t$  is directly proportional to the ratio of the trampoline diagonal length ( $\sqrt{2}L_w$ ) to the total length of the two parallel tethers  $(2L_t)$ . Fig. 2.10c displays this theoretical stress component (2.66) as a function of the central pad side length L (black curve), which closely aligns with the FEM results (red squares). As expected, the stress increases with L. The FEM results for the trampolines with a Bezier profile are displayed with black circles. Below a critical side length ( $L \le L_c \approx 500 \ \mu \text{m}$ ), the stress at the tethers grows faster with L than what observed for the square design. For  $L > L_c$ , the tethers' stress drops down, as predicted by Eq. (2.64). Indeed, their width increases for this range of L values, conversely to the square design case, for which w is constant. This increase in w compensates for the stress reduction, making the Bezier trampolines stiffer than the square design for  $L > L_c$  (Fig. 2.10d), consistent with the FEM simulated fundamental resonance frequency (see below, Fig. 2.10g). Fig. 2.10d clearly illustrates this compensation by plotting the product tethers' stress-width as a function of L.

Fig. 2.10e shows the corresponding effective spring constant  $k_{\text{eff}}$  (2.65) as a function of L. Different power laws are displayed to illustrate the change in spring constant with central area growth. For  $L^2 < 200^2 \,\mu\text{m}^2$ , the stiffness matches the case of a simple string resonator, as here the trampoline is a cross-string structure. For  $L^2 > 200^2 \ \mu\text{m}^2$ , the stiffness increases significantly, due to stress concentration at the tethers.

From the modeshape of the trampoline's fundamental resonance (mode (1,1) in Fig. 2.9b), its effective mass  $m_{\text{eff}}$  can be expressed as

$$m_{\text{eff}} = m_{\text{eff,c}} + m_{\text{eff,t}} = \rho h \left( L^2 + \frac{4wL_{\text{t}}}{2} \right).$$
 (2.67)

The tether's effective mass  $m_{\text{eff,t}}$  is the equivalent to that of the string,  $m_{\text{eff,s}} = 0.5 m_0$ , with  $m_0$  being the tether's total mass. For the central pad,  $m_{\rm eff,c}$  equals its full inertial mass as the entire pad is being displaced for the fundamental mode. Fig. 2.10f displays



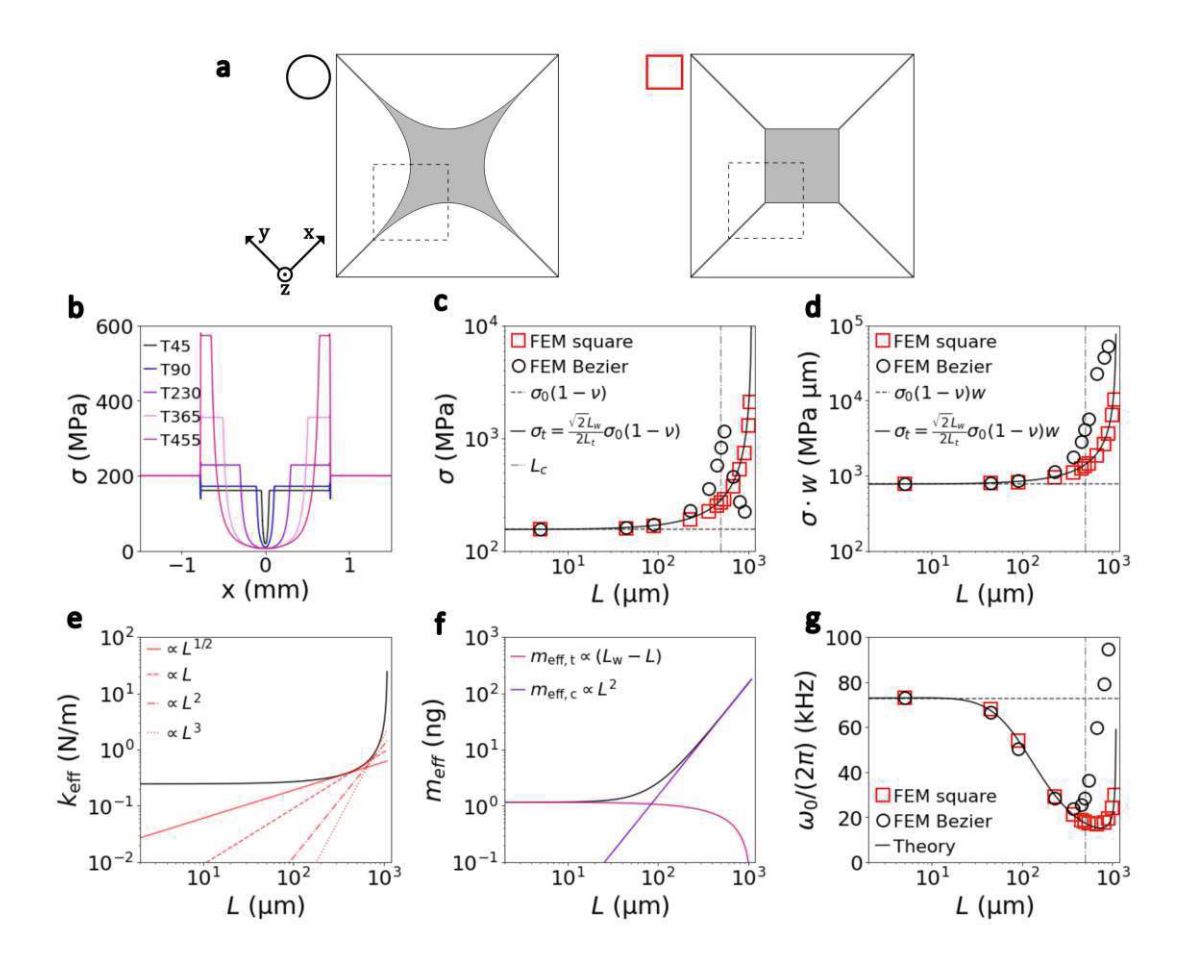


Figure 2.10: Mechanics of the trampoline. a. In-plane view of a trampoline with a Bezier (left) and square (right) profile of the central pad. The dashed squares highlight the major difference between the two geometries. b. X-cut stress profile in trampolines with a central pad with a Bezier curve profile. c. Tethers stress as a function of the central pad side length L. Red squares: FEM simulations for a trampoline with a square design of the central pad. Black circles: FEM simulations for a trampoline with a Bezier profile design for the pad. Black curve: theory (2.66). Vertical dashed dotted line: critical central pad side length  $L_c$ . For  $L > L_c$ , the tether width at the clamping points for a Bezier trampoline increases with L, changing the boundary conditions relative to the square design. d. Product tether's stress-width  $\sigma_t \cdot w$  as a function of L. For  $L > L_c$ , the reduction in stress is compensated by the increase in width at the clamping points. e. Square trampoline spring constant (2.65) as a function of L. Displayed are also different power laws  $L^{\zeta}$  for clarity. f. Trampoline effective mass as a function of L. Pink curve: tethers' effective mass. Purple: central pad's effective mass. g. Fundamental resonance frequency as a function of L. FEM and model parameters:  $\rho = 3000 \text{ kg/m}^3$ , E=250 GPa,  $\sigma_0=200$  MPa,  $\nu=0.23,\,h=50$  nm. For the square design,  $w=5~\mu\mathrm{m}$ always; for the Bezier design,  $w = 5 \mu \text{m}$  for  $L \leq L_c$ .

 $m_{\rm eff}$  as a function of the central pad side length L. Two regimes can be seen: for  $L^2 < 100^2 \ \mu \text{m}^2$ , the mass remains almost constant, as the reduction in tether length is counterbalanced by the growth of the central pad; for  $L^2 > 100^2 \ \mu \text{m}^2$ , the central pad fully defines the effective mass, growing here as  $m_{\rm eff} \propto L^2$ . It is worth noting that, in the range 100  $\mu$ m  $< L < 500 \mu$ m, the effective mass grows faster than the spring constant, reducing the overall resonance frequency in this region (Fig. 2.10g).

Fig. 2.10g compares the FEM results for square and Bezier trampolines with the theoretical predictions for the fundamental resonance frequency (2.53), showing excellent agreement.  $\omega_0$  increases faster with L for the Bezier design, due to an overall increase in tethers' stiffness, as shown above.

For trampolines, the effective Duffing parameter is determined by the tethers, as they primarly define the stiffness of these resonators. Hence, the expression of  $\alpha_{\rm eff}$  is given by

$$\alpha_{\text{eff}} = \frac{(n\pi)^4}{8} \frac{Ehw}{(2L_t)^3},\tag{2.68}$$

which is equivalent to the Duffing parameter of a string of length  $2L_t$ .



# Fundamentals of Nanomechanical Photothermal Sensing

In this chapter, the theory of photothermal sensing is introduced and discussed. The main figures of merit are presented and analyzed. The equations behind the photothermal detection are discussed in details for the three mechanical resonator's designs introduced in the previous chapter—namely, strings, drumheads, and trampolines. The theoretical models presented here are compared with the finite element method (FEM), whose details will be presented in Chapter 4.

The results and associated discussion of this chapter are based on the first part of the results presented in Ref. [111]. The general discussion also follows closely Ref. [60].

### Nanomechanics for Thermal Sensing 3.1

Nanomechanical photothermal sensors measure the power absorbed by the mechanical element, P. This is the fraction of irradiated or otherwise introduced power  $P_0$  that is converted into heat

$$P = \alpha_{\text{abs}}(\lambda)P_0,\tag{3.1}$$

with the absorber- and wavelength-dependent heat conversion factor  $\alpha_{abs}$  ( $0 \le \alpha_{abs} \le 1$ ). Therefore, the main figure of merit within this context is the minimum detectable power per unit bandwidth. This is denominated noise-equivalent-power (NEP), with units  $[W/\sqrt{Hz}]$ , and corresponds to the power level at which the signal from the sensor is equal to the noise — signal-to-noise ratio SNR= 1. It is defined for mechanical resonators as [60]

$$NEP = \frac{\sqrt{S_y(\omega)}}{\mathcal{R}_P(\omega)},$$
(3.2)

with  $S_y(\omega)$ ,  $\mathcal{R}_P(\omega)$ , and  $\omega$  denoting the one-side power spectral density (PSD) of the

fractional frequency fluctuations y, with units [1/Hz], the relative power responsivity with units [1/W], and the angular speed in units [rad Hz].

The relative responsivity is defined as the fractional shift of the resonator eigenfrequency  $\omega_0$  per absorbed power P and is given by [60]

$$\mathcal{R}_{P}(\omega) = \frac{\partial \omega_{0}}{\partial P} \frac{1}{\omega_{0}(0)} |H_{th}(\omega)| = \frac{\mathcal{R}_{T}}{G} |H_{th}(\omega)|, \qquad (3.3)$$

where  $\mathcal{R}_{\mathrm{T}}$  denotes the relative responsivity to temperature T, with units [1/K], G is the thermal conductance of the resonator [W/K], and  $H_{\rm th}(\omega) = (1 + i\omega\tau_{\rm th})^{-1}$  a low-pass filter transfer function accounting for the resonators' thermal response time [123]

$$\tau_{\rm th} = \frac{C}{G},\tag{3.4}$$

with C denoting the resonators' heat capacity [J/K].

More in general, the photothermal response depends on different parameters as listed below:

- it depends on the dimensions of the nanomechanical resonator, defining whether thermal conduction or radiation is the main thermal dissipation mechanism;
- it depends on the relative size of the heating source with respect to the resonator's dimensions. As it will be shown, very often localized heat enhances the response over uniform heating conditions;
- it depends on the position of the source relative to the center of the resonator's center, with the thermal dissipation increasing far from it.

All these features are captured within the mean temperature framework (MTF), as shown below.

### 3.1.1Temperature Responsivity

According to Eq. (3.3), nanomechanical photothermal sensors are, in essence, temperature sensors. The temperature responsivity is defined as

$$\mathcal{R}_{\mathrm{T}} = \frac{\partial \omega_0}{\partial T} \frac{1}{\omega_0(T_0)},\tag{3.5}$$

with  $T_0$  denoting the thermal bath temperature. Throughout all the present work, mechanical resonators with an initial tensile stress  $\sigma_0$  are analyzed, as introduced in Chapter 2. Their eigenfrequency is therefore a function of the temperature dependent stress  $\sigma(T)$ 

$$\omega_0 \propto \sqrt{\sigma(T)},$$
 (3.6)

while the effect of bending stiffness is neglected — this condition holds true for  $\sigma_0 \geq 1$ MPa. The rationale behind the choice of this subcategory of resonators will be clarified in a moment.

In the following, it is assumed that only the mechanical resonator is heated up to a temperature T, while keeping its frame at a fixed temperature  $T_0 < T$ . The resulting temperature increase  $\Delta T = T - T_0$  is responsible for the frequency shift experienced by the resonator.

### 3.1.1.1Strings

In a string with intrinsic uniaxial tensile stress  $\sigma_0$  and Young's modulus E, a mean temperature increase  $\langle \Delta T \rangle$  induces a thermal strain along the resonator's length L, resulting in a stress [60]

$$\sigma(T) = \sigma_0 - \alpha_{\rm th} E \langle \Delta T \rangle , \qquad (3.7)$$

with  $\alpha_{\rm th}$  being the material's linear coefficient of thermal expansion. For small temperature changes, the temperature responsivity (3.5) together with (3.6) and (3.7)approximately is given

$$\mathcal{R}_{\mathrm{T}} = -\frac{\alpha_{\mathrm{th}}}{2} \frac{E}{\sigma_{0}}.$$
 (3.8)

The factor  $E/\sigma_0$  is the photothermal enhancement factor and is a unique feature of resonators under tensile stress. For nanomechanical silicon nitride resonators, the photothermal enhancement factor can reach values between  $10^2 - 10^8$ . It is worth noting here that, for 10 kPa  $\leq \sigma_0 \leq 1$  MPa, the thermal stress (second addend in Eq. (3.7)) can be of the same order of magnitude of  $\sigma_0$ , making the temperature responsivity (3.8) nonlinear (such an effect can be observed in Ref. 24). For  $\sigma_0 \leq 10$  kPa, the resonator will behave as a beam, with a reduced temperature responsivity  $R_{\rm T} = (\alpha_{\rm th} + \alpha_{\rm E})/2$  ( $\alpha_{\rm E}$  being the Young's modulus softening coefficient). The same ranges of stress for the different regimes hold for drumheads.

### 3.1.1.2 **Drumheads**

For very thin  $(h \ll L)$  homogeneous isotropic drumheads, the assumption of thin shell holds, and the thermal stress is given by [20, 124]

$$\sigma(T) = \sigma_0 - \alpha_{\rm th} E \left[ \frac{1+\nu}{1-\nu} \frac{\langle \Delta T \rangle}{2} + \frac{1}{r^2} \int_0^r r' \Delta T(r') dr' \right]$$
 (3.9)

with  $\nu$  and r denoting the resonator's Poisson's ratio, and the size of the heating source in radial coordinates, respectively. An important feature of Eq. (3.9) is the explicit dependence of the thermal stress on the heating source's dimensions via the temperature profile  $\Delta T(r)$ . For the two extreme cases of uniform and point-like heating source, a simplified expression can be found. Specifically, for an uniformly distributed temperature, the integral becomes independent of r and equal to  $\langle \Delta T \rangle / 2$ , with Eq. (3.9) reducing to [122, 124]

$$\sigma(T) = \sigma_0 - \frac{\alpha_{\text{th}} E}{1 - \nu} \langle \Delta T \rangle. \tag{3.10}$$

This is particularly the case of large drumheads used for IR detection [86], where the main thermal dissipation is of radiative nature (see the discussion in the next section). Hence, the relative temperature responsivity is by

$$\mathcal{R}_{\mathrm{T}} = -\frac{\alpha_{\mathrm{th}}}{2(1-\nu)} \frac{E}{\sigma_0},\tag{3.11}$$

with the factor  $(1-\nu)$  accounting for the thermal expansion along the two in-plane directions. For a point-like heating source, the overall temperature responsivity is given by [20]

$$\mathcal{R}_T = -\frac{\alpha_{\text{th}}}{2(1-\nu)} \frac{E}{\sigma_0} [2 - \nu - 0.642(1-\nu)], \tag{3.12}$$

with the argument within the brackets representing an enhancement of  $\approx 27$  % compared to uniform heating conditions.

### 3.1.1.3**Trampolines**

The trampolines, as the one depicted in Fig. 3.7a, exhibit a thermal response similar to strings. For a central pad of area  $L^2$  and thickness h, anchored to the frame via four tethers of length  $L_{\rm t}$ , width w, and thickness h, its effective spring constant for the fundamental resonance mode can be expressed as that of string of length  $L_t$  (see Chapter 1) [111]

$$k_{\text{eff}}(T) = \frac{\pi^2}{2} \frac{wh}{L_t} (1 - \nu) \sigma_0 \left[ 1 - \frac{\alpha_{\text{th}} E}{\sigma_0} \left\langle \Delta T \right\rangle \right], \tag{3.13}$$

with the factor  $(1 - \nu)$  accounting here for the strain release along the directions perpendicular to the tether length. From the resonance frequency  $\omega_0(T) \propto \sqrt{k_{\text{eff}}}$ , it is easy to observe that the temperature responsivity is equal to

$$\mathcal{R}_{\rm T} = -\frac{\alpha_{\rm th}}{2} \frac{E}{\sigma_0},\tag{3.14}$$

underlining that the thermal expansion at the tethers is the main responsible for the temperature response.

### Thermal conductance 3.1.2

Besides the temperature responsivity, the power responsivity (3.3) also depends on the thermal conductance. The following thermal analysis is carried out based on the mean temperature framework (MTF) in the steady state that we introduce here. The model is derived first assuming a point-like heat source. The case of an evenly spread heat source is discussed at the end of each subsection. Theoretical models are compared with FEM simulations for SiN nanomechanical resonators (for the details about the FEM, see Chapter 4). For all the theoretical and FEM results presented here and in Chapter 5, a subset of SiN material parameters has been defined as given in Table 3.1.



Table 3.1: Low-stress LPCVD silicon nitride material parameters.

Parameter	Value	Reference
Mass density, $\rho$ [kg/m <sup>3</sup> ]	3000	24
Young's modulus, E [GPa]	250	87, 125
Poisson's ratio, $\nu$	0.23	25
Thermal conductivity, $\kappa$ [W/(m K)]	3	87
Specific heat capacity, $c_p$ [J/(K kg)]	700	87, 126

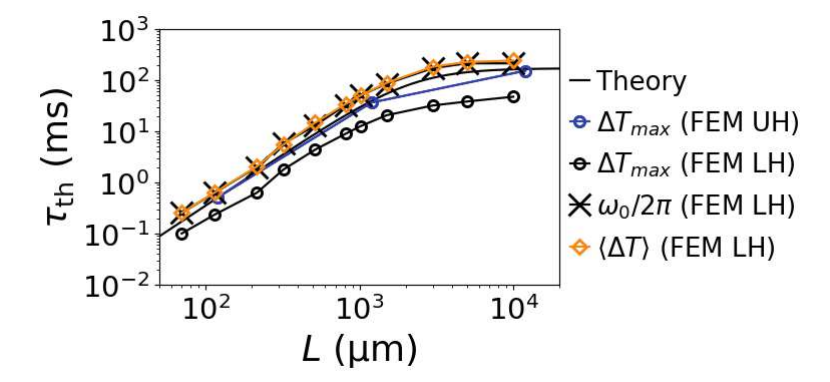


Figure 3.1: Mean Temperature Framework. Solid curve: theoretical thermal time constant as a function of the resonator length L (3.4). Blue circles: response time of the FEM peak temperature  $\Delta T_{FEM}$  for uniform heating (UH). Black circles: response time of  $\Delta T_{FEM}$  for local heating (LH). Orange diamondes: response time of the surface mean temperature  $\langle \Delta T_{FEM} \rangle$  for LH. Black crosses: response time of the resonance frequency  $\omega_{0_{FEM}}/2\pi$  for LH. FEM parameters: Table 3.1, resonator's thickness h=50nm, absorptance  $\alpha_{\rm abs} = 0.5 \%$ , emissivity  $\epsilon_{\rm rad} = 0.05$ .

### 3.1.2.1 Mean Temperature Framework

A resonator of thermal mass C absorbs a power P and dissipates it to the environment through its conductance G, resulting in a mean temperature rise  $\langle \Delta T \rangle$ 

$$\langle \Delta T \rangle = \frac{P}{G}.\tag{3.15}$$

In the MTF, all the resonator thermal properties are defined with respect to  $\langle \Delta T \rangle$ , as this temperature dictates the photothermal response of a nanomechanical resonator under tensile stress, rather than the local temperature variations  $\Delta T$ . This can be thought as a consequence of the fact that the resonance frequency is a global property of the resonator, depending on its material and geometry. This point is clarified in Fig. 3.1. It shows the FEM comparison of the thermal time constant of a drumhead resonator between two opposite heating conditions — namely, local (LH) and uniform heating (UH). The

theoretical predictions (3.4) are also displayed (black curve), closely aligning with the uniform illumination (blue circles), with  $\tau_{\rm th}$  derived from the temporal evolution of the resonator's maximum temperature increase  $\Delta T_{\rm max}$  ( $\approx \langle \Delta T \rangle$  for UH conditions). Notably, the thermal equilibrium is reached faster in the case of local heating (black circles)  $(\Delta T_{\rm max} > \langle \Delta T \rangle)$  in LH conditions). For the same scenario,  $\tau_{\rm th}$  has been additionally estimated through a transient study of the resonance frequency  $\omega_0/2\pi$  (black crosses), revealing a stronger agreement with the theory. Monitoring the mean temperature increase  $\langle \Delta T \rangle$  (orange diamonds) further supports this result and the rationale behind the use of the MTF: the two sets of FEM perfectly overlap, indicating that the resonance frequency is governed by the resultant mean temperature increase even in the presence of a local heating source.

In the MTF, C is given for an isotropic resonator by

$$C = c_{\rm p} \rho V, \tag{3.16}$$

where  $c_p$ ,  $\rho$ , and V are the specific heat capacity at constant pressure, mass density, and volume of the resonator, respectively.

As the resonator operates in a vacuum environment, only thermal conduction  $G_{\text{cond}}$  and radiation  $G_{\rm rad}$  contribute to the heat transfer [127]. In the MTF, the thermal conductance G is given by

$$G = G_{\text{rad}} + G_{\text{cond}} = 4A_{\text{rad}}\epsilon_{\text{rad}}\sigma_{\text{SB}}T_0^3 + \frac{s_f(\mathbf{r}, L, w_0)}{\beta(\mathbf{r}, L, w_0)}\kappa,$$
(3.17)

where  $A_{\rm rad}$ ,  $\epsilon_{\rm rad}$ ,  $\kappa$ , and  $\sigma_{\rm SB}$  are the resonator's radiating surface, its emissivity, thermal conductivity, and the Stefan-Boltzmann constant, respectively. For the thermal conduction term  $G_{\text{cond}}$ , a shape factor  $s_{\text{f}}$  is introduced to account for the design geometry via the resonator characteristic length L, the heat source position vector  $\mathbf{r}$ , and the heating radius  $w_0$  [127]. In this way, the dependence of G on the size of the probing heat source, as well as on its position with respect to the resonator, e.g. concentric or eccentric to it, captures within this formalism the aforementioned features of the resonators' photothermal response.

The product  $s_f(\mathbf{r}, L, w_0) \cdot \kappa$  in Eq. (3.17) is the thermal conduction with respect to the localized temperature field  $\Delta T$ . The factor  $\beta(\mathbf{r}, L, w_0)$  denotes the ratio between mean and peak temperature  $\beta = \langle \Delta T \rangle / \Delta T_{\text{max}}$ , ensuring the correct description of  $G_{\text{cond}}$  in the MTF. In contrast,  $G_{\rm rad}$  proves to be independent of the localization conditions of the laser and its position, and the resonator's full area must be considered. This is shown in Fig. 3.2 for a drumhead resonator heated up with a highly focused (LH — black circles) and uniformly distributed (UH — red crosses) laser. Fig. 3.2a shows the mean temperature as a function of the resonator side length L. For larger drumheads, no difference is observed between LH and UH conditions, where  $G \approx G_{\rm rad}$ . The corresponding  $G_{\rm cond}$  and  $G_{\rm rad}$  are displayed in Fig. 3.2b&c, respectively. It is shown that  $G_{\text{cond}}$  does depend on the size of the resonator and the heating condition; conversely,  $G_{\rm rad}$  depends on the resonator dimension, but it is independent of the heating conditions within the MTF.



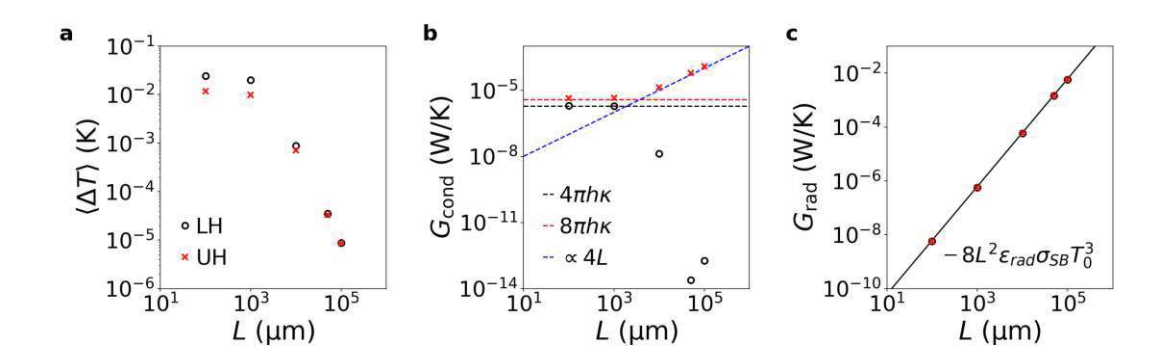


Figure 3.2: MTF:  $G_{\text{cond}}$  vs  $G_{\text{rad}}$ . FEM simulations of a drumhead resonator under localized (LH — black circles) and uniform (UH — red circles) heating. a Mean temperature as a function of the resoantor side length L. b Corresponding conductive thermal conductance  $G_{\text{cond}}$ . c Corresponding radiative thermal conductance  $G_{\text{rad}}$ . FEM parameters: Table 3.1, resonator's thickness h = 50 nm, absorptance  $\alpha_{abs} = 0.5$  %, emissivity  $\epsilon_{\rm rad} = 0.05$ .

### 3.1.2.2Strings

This design (Fig. 3.3a) represents the simplest geometry from a thermal transport standpoint. A string of length L, width w, and thickness h occupies a volume V = hwL, and, assuming  $h \ll w$ , radiates with an area  $A_{\rm rad} \approx 2wL$ . The factor of 2 accounts for the front and back surface radiation. This allows the direct evaluation of the thermal capacitance C and the radiative conductance  $G_{\rm rad}$ . For  $G_{\rm cond}$  instead, the shape  $s_{\rm f}$  and  $\beta$  factors have to be calculated. In this regard, it should be noted that the heating source can be in any position x along the string length, with the generated heat flowing along two paths of length x and L-x [61, 123]. Considering a localized heat source of power  $P_0$ , and given an absorptance  $\alpha_{\rm abs}$  (3.1), the Fourier law at steady-state gives [60]

$$P = \frac{4wh}{L}\kappa\Delta T_{\text{max}} = s_f(x, L, w_0)\kappa\Delta T(x), \qquad (3.18)$$

with  $\Delta T_{\text{max}} = T_{\text{max}} - T_0$  denoting the peak temperature rise with respect to the frame temperature  $T_0$ , occurring at the heat source position. For a string resonator, such as those analyzed in [111] (Chapter 5), a linear temperature profile is the solution of the heat diffusion equation in steady-state for short and intermediate length  $(L \leq 2 \text{ mm})$ 

$$\Delta T(x) = \Delta T_{\text{max}} \left( 1 - \frac{2}{L} |x| \right), \quad \text{for } -\frac{L}{2} \le x \le \frac{L}{2}, \tag{3.19}$$

as shown in Fig. 3.3b&c. The 1D temperature profiles for L = 0.1 mm (left) and 1 mm (right) have been obtained using FEM for different heating laser positions. For both strings, all profiles are linear. In the 1 mm long string, the thermal radiation plays a more significant role than in the 0.1 mm long one, causing the profile to deviate slightly

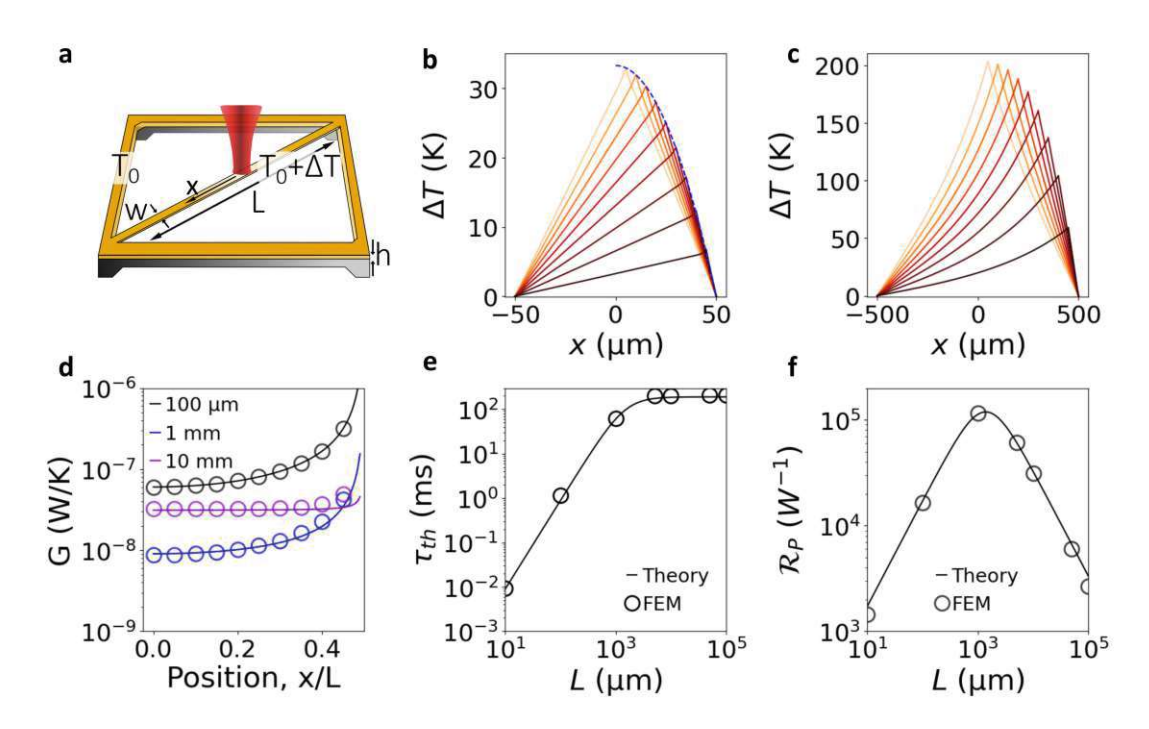


Figure 3.3: String's photothermal response a. Schematics of a string resonator illuminated by a light source (red) at the center. At steady-state, a temperature difference  $\Delta T$  from the frame temperature  $T_0$ , will arise upon photothermal heating. **b.** FEM simulated 1D temperature profiles of a 0.1 mm long string resonator, for different positions of the heat source. c. FEM simulated 1D temperature profiles for a 1 mm long string. Laser parameters: Gaussina beam with input optical power  $P_0 = 200 \,\mu\text{W}$ . d. String's thermal conductance G as a function of the point-like heat source relative position x/L, for three different lengths (0.1, 1, and 10 mm). Circles: FEM results of G in the mean temperature framework (MTF). Solid curve: MTF theoretical calculation (3.17). e. Comparsion between FEM results (circles) and model (solid curve) for the relative power responsivity (3.3) as a function of the string length. f. Comparison between FEM results (circles) and model (solid curve) for the thermal time constant (3.4) as a function of the string length. Model and FEM parameters: Table 3.1,  $\sigma_0 = 200$  MPa,  $\alpha_{\rm th} = 1.23$  ppm/K,  $w = 5 \mu \text{m}, h = 50 \text{ nm}, \epsilon_{\text{rad}} = 0.05, \alpha_{\text{abs}} = 0.5 \% [69, 128].$ 

from a purely linear trend. Nonetheless, as long as  $\Delta T$  can be treated as a linear function of the position r, even in the presence of thermal radiation losses, the shape factor can be phenomenologically found to be

$$s_{\rm f}(x) = \frac{4 w h}{L} \frac{1}{1 - \left(\frac{2 x}{L}\right)^2}.$$
 (3.20)

38

Its spatial dependence is shown in Fig. 3.3b by the dashed blue curve, properly following the behavior of the temperature peak.

The mean temperature within the string is

$$\langle \Delta T \rangle = \frac{1}{L} \int_{-L/2}^{L/2} \Delta T(x) dx = \frac{1}{L} \frac{L \Delta T_{\text{max}}}{2} = \frac{\Delta T_{\text{max}}}{2},$$
 (3.21)

which yields to  $\beta = 1/2$  for a string resonator.

Fig. 3.3d shows the overall thermal conductance G (3.17) as a function of the relative localized heating position for three different strings. The MTF model (solid curves) closely aligns with the FEM simulations (circles), where the conductance has been extract as  $G_{\text{FEM}} = P/\langle \Delta T_{\text{FEM}} \rangle$ . For strings measuring 0.1 mm (black curve) and 1 mm (blue curve) in length, G strongly depends on the heat source position, increasing as the latter approaches the frame, due to the enhanced thermal conduction. This effect is less pronounced for the 10 mm long string, where radiative heat transfer dominates. It is worth noting that the 1 mm long string shows the best thermal insulation, followed by the 10 mm long and 0.1 mm resonators, consistent with the theoretical and experimentally determined power responsivity  $\mathcal{R}_{P}$  (see Fig. 3.3e&5.1d).

For the case of an heating point source located at the string center (x=0),  $G_{\text{cond}}$  can be expressed as

$$G_{\text{cond}} = \frac{s_{\text{f}}(x=0)}{\beta(x=0)} \kappa = \frac{8 h w}{L} \kappa. \tag{3.22}$$

The MTF predicts a factor of 2 higher than what is reported in ref. 60, as  $\langle \Delta T \rangle$  is considered instead of the peak temperature, and is consistent with ref. 129.

Fig. 3.3e displays the comparison between FEM (circles) and theoretical response time (3.4). Short strings are dominated by conductive heat transfer, with  $\tau_{th}$  being a linear function of L. Conversely, long strings are dominated by radiative heat transfer and show a time constant independent of L, as both the thermal capacitance C and the conductance  $G \approx G_{\rm rad}$  grow linearly with L. As can be observed, the model accurately predicts the string's time constant.

Fig. 3.3f compares the theoretical power responsivity (3.3) to the FEM simulations, showing excellent agreement. For short lengths (L < 1 mm),  $\mathcal{R}_{P}$  increases linearly with L, until it reaches a maximum ( $L \approx 1$  mm). In this region, the string is mainly coupled to the thermal bath via thermal conduction ( $G \approx G_{\text{cond}}$ ). As the distance between the impinging and anchoring points increases, so does the power responsivity. For L > 1 mm, the string enters the radiation limited regime  $(G \approx G_{\rm rad})$ , resulting in a linear reduction of  $\mathcal{R}_{\rm P}$ , due to the increasingly larger emitting surface area  $A_{\rm rad} \propto L$ . These comparisons prove the validity of the time constant and responsivity model.

Nanomechanical photothermal sensing can be performed with tightly focused as well as uniformly distributed heat sources / beam diameters. Greater (lesser) localization of the heating yields higher (lower) temperature rises  $\langle \Delta T \rangle$ . Hence, two types of FEM simulations have been carried out to better understand the effect of the localization: i) local heating (LH) with a point heat source at the string's center; ii) uniform heating (UH) with the upper surface defined as the heating source. No Gaussian beam lasers are

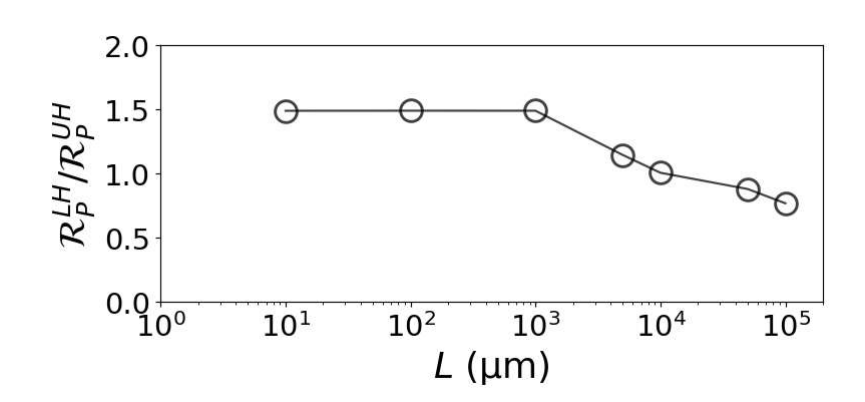


Figure 3.4: Heat localization in strings. Ratio between power responsivity for localized (LH) and uniform (UH) heating conditions. FEM parameters: Table 3.1,  $\sigma_0 = 200$  MPa,  $\alpha_{\rm th} = 2.2 \text{ ppm/K}, w = 5 \mu \text{m}, h = 50 \text{ nm}, \epsilon_{\rm rad} = 0.05, \alpha_{\rm abs} = 0.5 \%, P_0 = 10 \mu \text{W}.$ 

used in UH conditions, since part of the total input power would be lost perpendicularly to the string length. The ratio  $\mathcal{R}_P^{LH}/\mathcal{R}_P^{UH}$  between the LH and UH power responsivity is plotted as a function of the string length in Fig. 3.4. For  $L \leq 1$  mm, this ratio is constant at 1.5, indicating that localized heating provides a 1.5× improvement in power responsivity compared to uniform heating. For longer strings (L > 1 mm), the highly localized optical power at the center increases the radiation losses  $\propto (T^4 - T_0^4)$ , worsening the responsivity improvement.

For uniform illumination, all the points along the string length will contribute to the heat dissipation. Integrating  $G_{\text{cond}}$  in (3.17) for a string, for a concentric source gives

$$G_{\text{cond}} = \left(\frac{1}{\kappa} \frac{1}{L} \int_0^L \frac{\beta}{s_f(x)} dx\right)^{-1} = 12 \frac{wh}{L} \kappa.$$
 (3.23)

The overall conductance for a uniformly heated string is given by

$$G = 12 \frac{wh}{L} \kappa + 8wL\epsilon_{\rm rad}\sigma_{\rm SB}T_0^3. \tag{3.24}$$

Thus, localizing the heat source at the string center will lead to a  $1.5\times$  higher power

To conclude, it is worth noting the existing trade-off between power responsivity and thermal time constant: for  $L \leq 1$  mm higher responsivity corresponds to a slower thermal time response.

It is further worth highlighting that, for probing wavelengths  $\lambda > w$ , scattering phenomena have to be accounted for to extract the correct absorbed power P.

### 3.1.2.3 **Drumheads**

A square drumhead resonator of side length L and thickness h (Fig. 3.5a) has a volume  $V = hL^2$  and a radiating surface  $A_{\rm rad} = 2L^2$ . Given  $h \ll L$ , no thermal gradient is present along the thickness, and the eccentric shell model applies for the appropriate description of  $G_{\rm cond}$  [127], with the heat being dissipated isotropically to the frame. For simplicity, the model focuses on a circular drumhead of effective diameter  $D=2L/\sqrt{\pi}$ [20, 124], heated by a laser source of beam waist  $w_0$ , centered at position  $(r, \theta)$  relative to the drumhead's center (Fig. 3.5a). The expression of the shape factor is obtained starting from the eccentric shell scenario [127]. In these conditions, the temperature is assumed constant withing the source region (red dashed lines in Fig. 3.5b), with an overall spatial profile

$$\Delta T(r) = \begin{cases} \frac{P}{4\pi\kappa h} \ln\left(\frac{D^2}{4w_0^2}\right) & \text{for } 0 \le r < w_0\\ \frac{P}{4\pi\kappa h} \ln\left(\frac{D^2}{4r^2}\right) & \text{for } w_0 \le r \le \frac{D}{2}. \end{cases}$$
(3.25)

An analytical solution is available for the shape factor, namely [127]

$$s_f(r,\theta,D,w_0) = \frac{2\pi h}{\cosh^{-1}\left(\frac{D^2 + 4w_0^2 - 4r^2}{4Dw_0}\right)}.$$
(3.26)

At steady-state, the resulting dissipated heat is given by  $P = s_f \kappa \Delta T(w_0)$ . For a laser beam impinging on the drumhead, the resulting temperature profile is given by (dashed orange curve in Fig 3.5b)

$$\Delta T(r) = \begin{cases} \frac{P}{4\pi\kappa h} \left[ \left( 1 - \frac{r^2}{w_0^2} \right) + \ln\left(\frac{D^2}{4w_0^2}\right) \right] & \text{for } 0 \le r < w_0\\ \frac{P}{4\pi\kappa h} \ln\left(\frac{D^2}{4r^2}\right) & \text{for } w_0 \le r \le \frac{D}{2}. \end{cases}$$
(3.27)

Eq. (3.27) differs from (3.25) within the heated region, due to the different boundary conditions. In this case, the corresponding shape factor  $s_{\rm f}$  is obtained by rewriting  $\Delta T(w_0)$  as a function of the maximum temperature rise  $\Delta T_{\rm max}$ . For the simple case of concentric, conduction limited heat transport problem, this relation is given by [20]

$$\Delta T(w_0) = \frac{P}{4\pi\kappa h} \ln\left(\frac{D^2}{4w_0^2}\right) = \Delta T_{\text{max}} - \frac{P}{4\pi\kappa h}.$$
 (3.28)

Substituting Eq. (3.28) into Fourier's law gives

$$P = s_f(r, \theta, D, w_0) \kappa \Delta T(w_0) = \frac{2\pi h}{\cosh^{-1} \left(\frac{D^2 + 4w_0^2 - 4\mathbf{r}^2}{4Dw_0}\right)} \kappa \left(\Delta T_{\text{max}} - \frac{P}{4\pi \kappa h}\right).$$
(3.29)

Rearranging Eq. (3.29) as a function of the peak temperature rise  $\Delta T_{\text{max}}$  gives

$$P = \frac{4\pi h}{2\cosh^{-1}\left(\frac{D^2 + 4w_0^2 - 4\mathbf{r}^2}{4Dw_0}\right) + 1} \kappa \Delta T_{\text{max}} = s_f(r, \theta, D, w_0)\kappa \Delta T_{\text{max}}.$$
 (3.30)

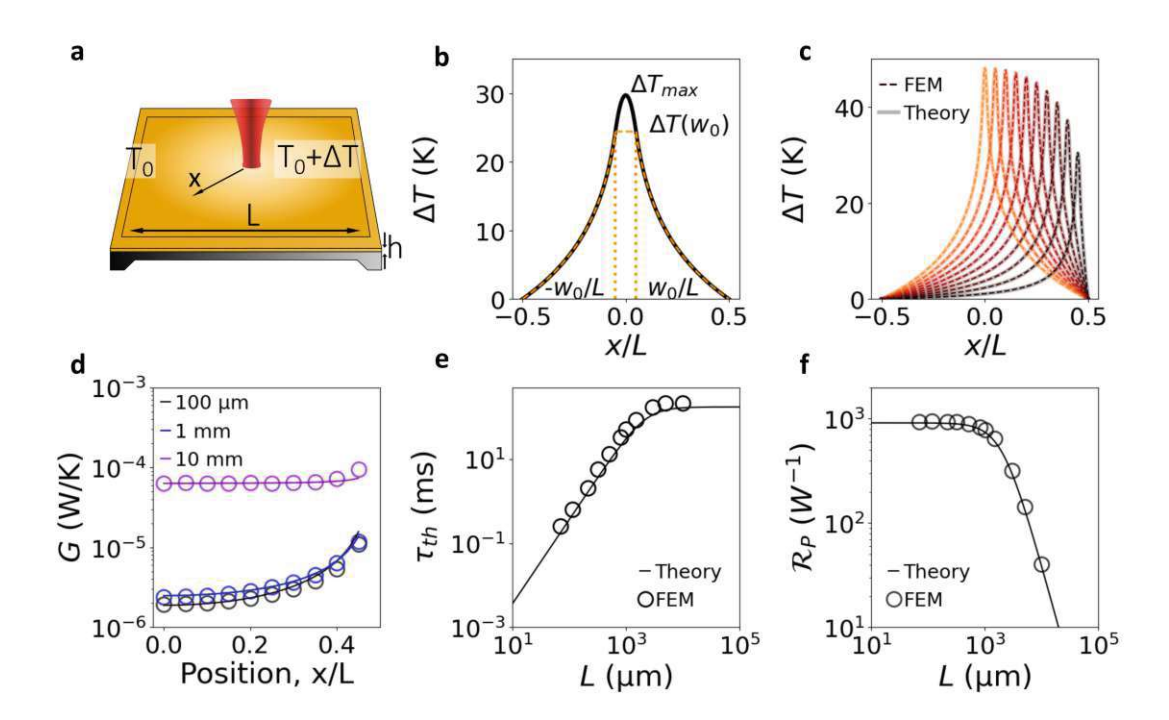


Figure 3.5: **Drumhead's photothermal response a.** Schematics of a drumhead resonator. For the comparison with the FEM, an equivalent circular geometry is used to reduce the problem complexity. **b.** 1D Temperature profile of circular membrane of diameter D, heated in the center by a top-hat disk beam of diameter  $2w_0$  (light blue solid curve). For comparison, the temperature distribution in the case of a eccentric cylinder, uniformly heated is shown (red dashed curve). c. Comparison between FEM (solid curves) and analytical (dashed curves) temperature profiles, obtained for a localized heat source of input power  $P_0 = 10 \mu W$  and beam waist  $w_0 = 1 \mu m$ , moving along a radial cut-line. d. Circular drumhead's MTF thermal conductance for 0.1, 1, and 10 mm side length, compared to the theory (black curve). e. Relative power responsivity comparison for drumheads. f. Thermal time constant comparison for drumheads. Model and FEM parameters: Table 3.1,  $\sigma_0 = 200$  MPa,  $\alpha_{\rm th} = 1.23$  ppm/K, w = 5  $\mu$ m, h = 50 nm,  $\epsilon_{\rm rad}=0.05,\,\alpha_{\rm abs}=0.5$  % [69, 128]. For all the FEM simulations, a Gaussian beam of waist  $w_0 = 1 \ \mu \text{m}$  has been used.

Eq. (3.30) describes the heat conduction losses with respect to the maximum temperature rise. The analytical solution (3.30) has been tested for different heat source positions against FEM simulations, showing excellent agreement. Fig. 3.5c shows the resulting FEM (solid curves) and analytical (dashed curves) temperature profiles. For the implementation of the MTF, the ratio between mean and peak temperature  $\beta$  must be found. Combining the two expressions of Eq. (3.27), it is possible to extract the peak temperature

$$\Delta T_{\text{max}} = \Delta T(0) = \frac{P}{4\pi\kappa h} \left[ 1 + \ln\left(\frac{D^2}{4w_0^2}\right) \right]$$
 (3.31)

Integrating Eq. (3.27) over the whole resonator area gives the mean temperature

$$\begin{split} \langle \Delta T \rangle &= \frac{1}{A} \iint_{A} \Delta T(r,\theta) dA = \frac{4}{\pi D^{2}} \left[ \int_{0}^{2\pi} \int_{0}^{w_{0}} \Delta T(r) r dr d\theta + \int_{0}^{2\pi} \int_{w_{0}}^{\frac{D}{2}} \Delta T(r) r dr d\theta \right] \\ &= \frac{4}{\pi D^{2}} \frac{P}{4\pi \kappa h} \left[ \int_{0}^{2\pi} \int_{0}^{w_{0}} \left[ -\frac{r^{2}}{w_{0}^{2}} + 1 + \ln\left(\frac{D^{2}}{4w_{0}^{2}}\right) \right] r dr d\theta - \int_{0}^{2\pi} \int_{w_{0}}^{\frac{D}{2}} \ln\left(\frac{4r^{2}}{D^{2}}\right) r dr d\theta \right] \\ &= \frac{4}{\pi D^{2}} \frac{P}{4\pi \kappa h} \pi \left[ \frac{w_{0}^{2}}{2} + w_{0}^{2} \ln\left(\frac{D^{2}}{4w_{0}^{2}}\right) + \frac{D^{2}}{4} - w_{0}^{2} - w_{0}^{2} \ln\left(\frac{D^{2}}{4w_{0}^{2}}\right) \right] \\ &= \frac{P}{4\pi \kappa h} \left( 1 - \frac{1}{2} \frac{4w_{0}^{2}}{D^{2}} \right). \end{split}$$

$$(3.32)$$

Hence, the  $\beta$  factor for the drumhead design can be written as

$$\beta(r,\theta,D,w_0) = \frac{1 - \frac{1}{2} \frac{4w_0^2}{D^2}}{1 + \ln\left(\frac{D^2}{4w_0^2}\right)} \left(1 - \frac{4r^2}{D^2}\right),\tag{3.33}$$

with the first term denoting the ratio between mean and maximum temperature rise, while the second term expressing the spatial dependence of the  $\beta$  factor. The latter follows by an heuristic approach, by fitting the FEM results.

Fig. 3.5d shows the overall conductance G as a function of a localized heat source position, for three different circular membranes (L = 0.1, 1, and 10 mm). The MTF model (solid curves) closely aligns with the FEM simulations for circular drumheads (circles). The two smaller drumheads (L < 1 mm, black and blue curves), primarily coupled to the environment via conduction, exhibit similar values. Conversely, the larger drumhead in the radiative heat transfer regime has a constant and worse thermal conductance.

For a focused heat source at the drumhead center  $(r=0, w_0 \to 0)$ , the conductance becomes

$$G_{\text{cond}} = \frac{s_{\text{f}}(r=0)}{\beta(r=0)} \kappa = 4\pi h\kappa, \tag{3.34}$$

recovering the same result as ref. 20. Even in the case of a localized heat source, thermal conduction in drumheads is independent of the side length L, contrary to what happens in strings (3.22).

Fig. 3.5f compares the theoretical and FEM modeling of the thermal time constant for localized heating, showing excellent agreement and a similar trend as the one observed in the strings.

Fig. 3.5e shows the comparison between the theoretical (black solid curve) and FEM power

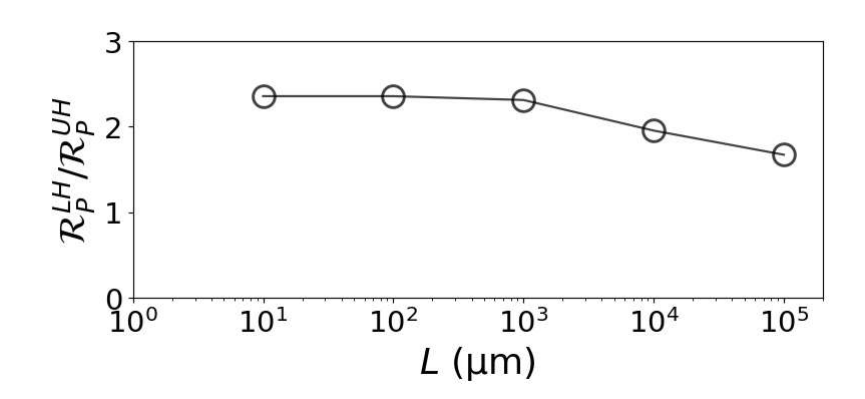


Figure 3.6: **Heat localization in drumheads.** Ratio between power responsivity for localized (LH) and uniform (UH) heating conditions. FEM parameters: Table 3.1,  $\sigma_0 = 200 \text{ MPa}, \ \alpha_{\text{th}} = 2.2 \text{ ppm/K}, \ h = 50 \text{ nm}, \ \epsilon_{\text{rad}} = 0.05, \ \alpha_{\text{abs}} = 0.5 \%, \ P_0 = 10 \ \mu\text{W}.$ 

responsivity (black circle), showing excellent agreement. Small drumheads (L < 1 mm) shows a responsivity independent of L, being  $G \approx G_{\text{cond}}$  exclusively a function of the material thermal conductivity  $\kappa$  and the resonator's thickness h (3.34). Large drumheads (L>1 mm) enter the radiative regime, and the responsivity drops down due to the increased surface area. This comparison confirms the validity of the theoretical responsivity model for drumhead resonators.

FEM simulations have also been conducted for the drumhead resonator to show the dependence of the power responsivity on the localization of the heating source. Drumheads show a different dependence on heat localization compared to strings. FEM simulations for a concentric Gaussian beam of varying waist  $w_0$  have shown that the power responsivity  $\mathcal{R}_P(w_0 = L/2) \approx \mathcal{R}_P(w_0 \ll 1)/2$ , i.e. for a uniform heating condition (see Fig. 3.6). Substituting Eq. (3.30) and (3.33) into equation (3.17) for a uniform  $(w_0 = D/2)$  heating concentric (r=0) to the drumhead gives

$$G_{\text{cond}} = \frac{4\pi h\kappa}{1 + 2\cosh^{-1}(1)} \frac{1 + \ln(1)}{1 - \frac{1}{2}} = 8\pi h\kappa, \tag{3.35}$$

meaning that the conductive contribution is doubled.

Hence, as a simple rule here, a point-like heat source offers a 2× improved photothermal responsivity compared to uniformly distributed heating.

To conclude, the most responsive drumheads show the fastest time response, opposite to what has been seen for strings.

### 3.1.2.4 **Trampolines**

A trampoline (Fig. 3.7a) occupies a volume  $V = h(L^2 + 4wL_t)$  and radiates through its central pad and tethers with an area  $A_{\rm rad} = 2(L^2 + 4wL_{\rm t})$ . The 2D heat conduction

problem simplifies here to a 1D scenario, as in strings. Indeed, heat generated in any position on the central pad conductively dissipates through the tethers. Since the heat flow is constricted by the tethers, the resonator can be modeled as a cross-string. The temperature profiles of five different trampolines are shown in Fig. 3.7b (the dimensions are of those characterized experimentally in Chapter 5), for a localized heating source. Each of them is composed of drumhead-like spatial distribution within the central pad (shadowed regions), and a linear, string-like distribution along the tethers. Since the temperature rise in the central pad is almost flat, and smaller than that at the tethers, it is possible to write the shape and  $\beta$  factors as

$$s_{\rm f}(x) = 2 \frac{4 w h}{2 L_{\rm t}} \frac{1}{1 - \left(\frac{x}{L_{\rm t}}\right)^2}, \text{ and}$$
 (3.36)

$$\beta(\mathbf{r}, L, w_0) = 1. \tag{3.37}$$

The factor of 2 in Eq. (3.36) accounts for the two crossing strings, while Eq. (3.37) is defined only with respect to the central pad, being the core sensing area.

Fig. 3.7c shows the FEM computed values for G for five trampolines of different central areas  $L^2$  (circles), together with the MTF predictions (solid curves). As the heat source moves from the center to the frame along a tether, the thermal conduction  $G_{\text{cond}}$  increases. Moreover, both  $G_{\text{cond}}$  and  $G_{\text{rad}}$  rise for increasing area—the former due to shorter tethers, the latter due to a larger surface. For a tightly focused beam at the center, the thermal conductance is

$$G_{\rm cond} = 4 \, \frac{h \, w \, \kappa}{L_{\rm t}},\tag{3.38}$$

recovering the results of a cross-string resonator of different tether lengths.

Fig. 3.7d shows the thermal time constant comparison between the model (solid curve) and the FEM simulations (circles), showing excellent agreement. For  $L < 50 \mu m$ , the trampoline behaves as a string. For 50  $\mu m < L < 230 \mu m$ , the resonator thermal capacitance grows faster than the conductance, increasing the overall response time. For  $L > 230 \ \mu \text{m}$ ,  $\tau_{\text{th}}$  reaches a plateau, to drop down for increasingly larger central pads. This is explained by the increase in conduction and radiation: the former, due to the shorter tether length; the latter, due to a bigger central area  $L^2$ . The interplay between thermal mass and conductance is the same one observed between the effective mass and the stiffness for the resonance frequency, as shown in Fig. 2.10f& 5.4a.

Fig. 3.7e displays the theoretical and FEM simulated power responsivity as a function of the central side length L. The model aligns closely with FEM simulations: resonators with small areas ( $L^2 < 100^2 \ \mu \text{m}^2$ ) show an almost constant  $\mathcal{R}_P$ ; for larger trampolines  $(L^2 > 100^2 \ \mu \text{m}^2)$ , it decreases linearly as the pad area grows. The trend is similar to the drumhead case (Fig. 3.5f). The difference in orders of magnitude compared to the drumheads relates to the improved thermal insulation (see Fig. 3.5f& 3.7e). As the window size is kept fixed, the growth of the central area corresponds to a reduction in tethers' length. For  $L < 100 \mu m$ , long tethers provide high thermal insulation, with  $\mathcal{R}_{P}$ converging to the cross-string case. As  $L^2$  approaches  $L_{\rm w}^2$ , thermal radiation, as well as

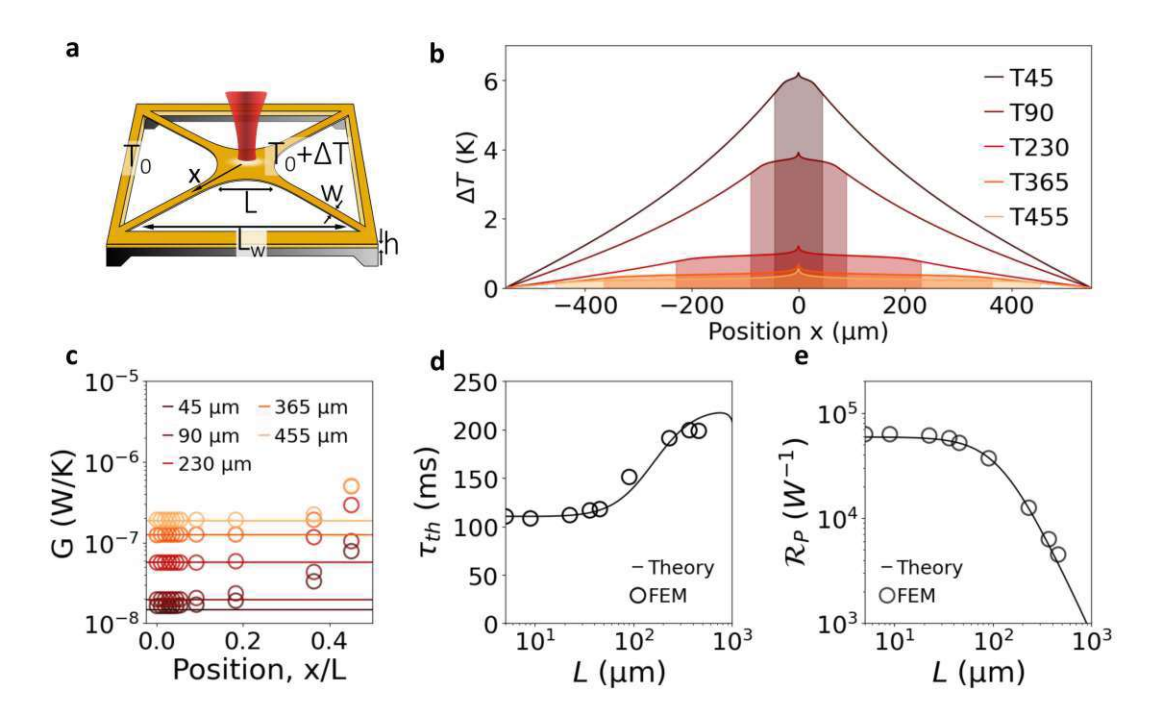


Figure 3.7: Trampoline's photothermal response a. Schematics of a trampoline resonator. b. FEM simulated temperature distribution along a X-cut line, for the five different trampoline dimensions analyzed experimentally in Chapter 5. The shaded regions denote the central sensing areas. c. Trampolines' MTF thermal conductance for a frame window side length of 1.1 mm and five different central pad side lengths. The model (solid curve) accounts here for a heat source impinging only in the central pad. d. Relative power responsivity comparison for trampolines. f. Thermal time constant comparison for trampolines. Model and FEM parameters: Table 3.1,  $\sigma_0 = 200$  MPa,  $\alpha_{\rm th} = 1.23 \ {\rm ppm/K}, \ w = 5 \ \mu{\rm m}, \ h = 50 \ {\rm nm}, \ \epsilon_{\rm rad} = 0.05, \ \alpha_{\rm abs} = 0.5 \ \% \ [69, 128].$  For all the FEM simulations, a Gaussian beam of waist  $w_0 = 1 \mu m$  has been used.



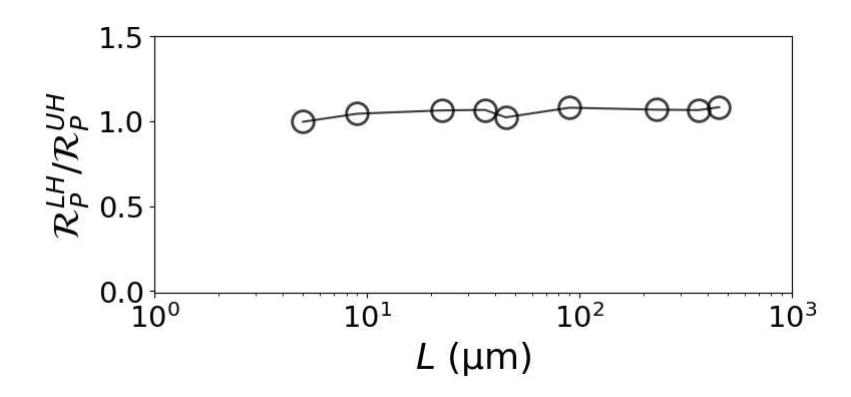


Figure 3.8: **Heat localization in trampolines.** Ratio between power responsivity for localized (LH) and uniform (UH) heating conditions as a function of the central area side length L. FEM parameters: Table 3.1,  $\sigma_0 = 200$  MPa,  $\alpha_{\rm th} = 2.2$  ppm/K,  $w = 5~\mu{\rm m}$ ,  $h = 50 \text{ nm}, \ \epsilon_{\text{rad}} = 0.05, \ \alpha_{\text{abs}} = 0.5 \ \%, \ P_0 = 10 \ \mu\text{W}.$ 

Table 3.2: Expressions for the relative temperature responsivity  $\mathcal{R}_T$  and thermal conductance G for the three designs. The two quantities are used to calculate the relative power responsivity (3.3), for localized (LH) and uniform (UH) heating.

	$\mathcal{R}_{\mathrm{T}}$ [1/K]	LH: $G$ [W/K]	UH: $G$ [W/K]
String	$-\frac{\alpha_{\rm th}}{2}\frac{E}{\sigma_0}$	$8\frac{wh}{L}\kappa + 8wL\epsilon_{\rm rad}\sigma_{\rm SB}T_0^3$	$12\frac{wh}{L}\kappa + 8wL\epsilon_{\rm rad}\sigma_{\rm SB}T_0^3$
Drumhead	$-\frac{\alpha_{\rm th}}{2(1-\nu)}\frac{E}{\sigma_0}$	$4\pi h\kappa + 4L^2\epsilon_{\rm rad}\sigma_{\rm SB}T_0^3$	$8\pi h\kappa + 8L^2\epsilon_{\rm rad}\sigma_{\rm SB}T_0^3$
Trampoline	$-\frac{\alpha_{\rm th}}{2}\frac{E}{\sigma_0}$	$8\frac{wh}{L_{\rm t}}\kappa + 4(8wL_{\rm t} + 2L^2)\epsilon_{\rm rad}\sigma_{\rm SB}T_0^3$	$8\frac{wh}{L_{\rm t}}\kappa + 4(8wL_{\rm t} + 2L^2)\epsilon_{\rm rad}\sigma_{\rm SB}T_0^3$

conduction increases due to the tethers shortening, with  $\mathcal{R}_{P}$  approaching the drumhead performances. This comparison shows the validity of the thermal model employed so far. As only the central pad is here the sensing area, uniform heating would result in an almost identical mean temperature rise  $\langle \Delta T \rangle$  for this geometry, leading to no reduction of the power responsivity  $\mathcal{R}_P(w_0 \to 0) \approx \mathcal{R}_P(w_0 = L/2)$  (Fig. 3.8).

To conclude, the most responsive trampolines exhibit the fastest time response, as observed for the drumheads.

A summary of the expressions of  $\mathcal{R}_{T}$  and G for the calculation of the power responsivity (3.3) is displayed in Table 3.2, for point-like source and even illumination.

### 3.1.3 Frequency stability

High photothermal sensitivity (3.2) requires also low fractional frequency noise y, as it defines the smallest resonance frequency shift that can be resolved. In nanomechanical photothermal sensing, the most relevant noise sources are: i) additive phase noise  $\theta$ , the sum of thermomechanical  $\theta_{\rm thm}$  and detection noise  $\theta_{\rm det}$ , with a frequency fluctuations PSD  $S_{y_{\theta}}(\omega) = S_{y_{\theta_{\text{thm}}}}(\omega) + S_{y_{\theta_{\text{det}}}}(\omega)$  [130, 131]; ii) temperature fluctuation frequency

noise  $y_{\rm th}$ , with PSD  $S_{y_{\rm th}}(\omega)$  [68]; and iii) photothermal back-action frequency noise  $y_{\delta P}$ , with PSD  $S_{y_{\delta P}}(\omega)$ 

$$S_y(\omega) = S_{y_{\theta}}(\omega) + S_{y_{\text{th}}}(\omega) + S_{y_{\delta P}}(\omega). \tag{3.39}$$

The experimental frequency fluctuations for all the designs are characterized by the Allan deviation  $\sigma_{\rm v}(\tau)$  (AD) [132]

$$\sigma_{y}(\tau) = \sqrt{\frac{1}{2(N-1)} \sum_{i=1}^{N} (y_{i+1,\tau} - y_{i,\tau})^{2}},$$
(3.40)

with  $y_i$  being the ith sample of the fraction frequency y(t) averaged over a time  $\tau$ 

$$y_{i,\tau} = \frac{1}{\tau} \int_{(i-1)\tau}^{i\tau} y(t)dt.$$
 (3.41)

The theoretical calculations of the AD are based on the analytical expression [130, 131, 133]

$$\sigma_{y}(\tau) = \sqrt{\frac{1}{2\pi} \frac{8}{\tau^{2}} \int_{0}^{\infty} \frac{\sin^{4}\left(\frac{\omega\tau}{2}\right)}{\omega^{2}} S_{y}(\omega) d\omega}.$$
 (3.42)

For the specific case of white frequency noise, i.e.,  $S_{\rm v}(\omega) = {\rm constant}$ , Eq. (3.42) reduces to

$$\sigma_{\mathbf{y}}(\tau) = \sqrt{\frac{S_{\mathbf{y}}(0)}{2\tau}}. (3.43)$$

### 3.1.3.1Additive phase noise

Additive phase noise originates from the conversion into phase noise of thermomechanical  $u_{\rm thm}$  and detection  $u_{\rm det}$  amplitude noise, with respective PSDs  $S_{u_{\rm thm}}(\omega)$  and  $S_{u_{\rm det}}(\omega)$ [131]. In the assumption of detection white noise, this contribution can be expressed with respect to the thermomechanical noise peak as [60]

$$S_{u_{\text{det}}}(\omega) = \mathcal{K}_{d}^{2} S_{u_{\text{thm}}}(\omega_{0}) = \mathcal{K}_{d}^{2} \left[ \frac{4k_{\text{B}}TQ}{m_{\text{eff}}\omega_{0}^{3}} \right]$$
(3.44)

with  $\mathcal{K}_{\rm d}$  < 1 for transduction systems able to resolve the thermomechanical noise.  $Q = \omega_0 \tau_{\rm mech}/2$  denotes the quality factor of the resonator, with  $\tau_{\rm mech}$  being the resonator's mechanical time constant. Assuming that the resonator is made to oscillate at an amplitude  $z_r$  by means of a closed-loop frequency tracking scheme, the resulting fractional frequency noise power spectral density (PSD) is [60]

$$S_{y_{\theta}}(\omega) = \frac{1}{2Q^2} \frac{S_{u_{\text{thm}}}}{u_{\pi}^2} \left[ |H_{\theta_{\text{thm}}}(i\omega)|^2 + \mathcal{K}_{d}^2 |H_{\theta_{\text{det}}}(i\omega)|^2 \right]. \tag{3.45}$$

 $H_{\theta_{\rm thm}}(i\omega)$  and  $H_{\theta_{\rm det}}(i\omega)$  are the loop-specific transfer functions for the thermomechanical and detection phase noise. The transfer functions for an open loop, phase-locked loop,



and self-sustaining oscillator are the same to a good approximation [131]. As an example, for a self-sustaining oscillator (SSO) scheme, as used in this work, the transfer functions are [131]

$$H_{\theta_{\text{thm}}}^{\text{SSO}}(i\omega) = H_{\text{L}}(i\omega),$$

$$H_{\theta_{\text{det}}}^{\text{SSO}}(i\omega) = \frac{H_{\text{L}}(i\omega)}{H_{\text{mech}}(i\omega)}.$$
(3.46)

 $H_{\rm mech}(i\omega)$  and  $H_{\rm L}(i\omega)$  are the low-pass filter transfer functions of the resonator and system filter, respectively

$$H_{\text{mech}}(i\omega) = \frac{1}{1 + i\omega\tau_{\text{mech}}},$$

$$H_{\text{L}}(i\omega) = \frac{1}{1 + i\omega\tau_{\text{L}}}.$$
(3.47)

with  $\tau_{\rm mech}=2Q/\omega_0$  and the filter time constant  $\tau_{\rm L}\equiv 1/(2\pi f_{\rm L})$ , being  $f_{\rm L}$  the filter bandwidth.

Additive phase noise (3.45) can be mitigated by actuating the resonator at the onset of nonlinearity  $z_{\rm r_c}$ ,

$$u_{\rm c} = \sqrt{\frac{8}{3\sqrt{3}}} \frac{1}{\sqrt{Q}} \sqrt{\frac{m_{\rm eff} \omega_0^2}{\alpha_{\rm eff}}},\tag{3.48}$$

with  $\alpha_{\rm eff}$  denoting the effective Duffing term [60]. For  $u_{\rm r} > u_{\rm c}$ , additional phase noise of nonlinear origin could enter the system, worsening the resonator frequency stability at the integration times of interest in this study [134].

#### 3.1.3.2Temperature fluctuation frequency noise

Thermal fluctuation fractional frequency noise can also be assumed to be white [123]. For a lumped-element model,  $S_{y_{\rm th}}(\omega)$  is given by [123, 135]

$$S_{y_{\rm th}}(\omega) = \frac{4 k_B T^2}{G_{\rm eff}} \mathcal{R}_{\rm T}^2 \left| \frac{1}{1 + i\omega \tau_{\rm th_{eff}}} \right|^2.$$
 (3.49)

Here,  $G_{\text{eff}}$  and  $\tau_{\text{th}_{\text{eff}}}$  represent an effective thermal conductance and time constant, accounting for the temperature fluctuations originating from the fluctuating radiant power exchange between resonator and surroundings [136]. Since this can occur at any position onto the detector, the radiant power sources are modelled as point-like heaters. Hence,  $G_{\text{eff}}$  is derived from the integration of the conductance G over all possible positions of a point-like heat noise source. Since radiation is heat source position-independent in MTF, only the integration of  $G_{\rm cond}$  is required. From  $G_{\rm eff}$ ,  $\tau_{\rm th_{eff}} = C/G_{\rm eff}$  can be evaluated.

In a resonator, thermal noise can enter the system at any point along its length L. For a

string, integrating Eq. (3.20) along L gives the effective conductance

$$G_{\text{eff}} = \left(\frac{1}{\kappa} \frac{1}{L} \int_0^L \frac{1}{s_f(x)} dx\right)^{-1} + 8wL\epsilon_{\text{rad}}\sigma_{\text{SB}}T_0^3$$

$$= \frac{6\kappa wh}{L} + 8wL\epsilon_{\text{rad}}\sigma_{\text{SB}}T_0^3.$$
(3.50)

Eq. (3.50) results in a higher conductance than (3.22), as the averaging includes noise sources closer to the clamping points, where  $G_{\text{cond}}$  increases exponentially (see Fig. 3.3d). For a circular drumhead, the integration is performed over its whole area, leading to

$$G_{\text{eff}} = \left(\frac{1}{\pi \left(\frac{D}{2}\right)^2 \kappa} \int_0^{2\pi} \int_0^{(D-d)/2} \frac{1}{s_f(r,\theta,D,d)} r dr d\theta\right)^{-1}$$

$$+ 8L^2 \epsilon_{\text{rad}} \sigma_{\text{SB}} T_0^3$$

$$\simeq 4\pi h \kappa + 8L^2 \epsilon_{\text{rad}} \sigma_{\text{SB}} T_0^3.$$

$$(3.51)$$

Here, the greatest noise contribution is in the central region, resulting in  $G_{\text{eff}} \simeq G(\mathbf{r} = 0)$ , since  $G_{\text{cond}}$  is less influenced by the position of the noisy heating source than in strings. For a trampoline, the integration is performed over its central pad and along its four tethers, resulting in

$$G_{\text{eff}} = \left(\frac{1}{\kappa} \frac{1}{\sqrt{2} L_{\text{w}}} \int_{0}^{\sqrt{2}L_{w}} \frac{1}{s_{\text{f}}(x)} dx\right)^{-1} + 4(8wL_{\text{t}} + 2L^{2})\epsilon_{\text{rad}}\sigma_{\text{SB}}T_{0}^{3}$$

$$= \frac{6\sqrt{2} \kappa w h}{L_{\text{w}}} + 4(8wL_{\text{t}} + 2L^{2})\epsilon_{\text{rad}}\sigma_{\text{SB}}T_{0}^{3}.$$
(3.52)

with  $L_{\rm w}$  denoting the window side length. While trampolines dissipate  $\sqrt{2}\times$  more than strings via conduction, the central pad will make this geometry extremely sensitive to temperature fluctuations ( $w < L \le \sqrt{4L_t w}$ , see also the theoretical curves in Fig. 5.4e). The temperature fluctuation noise (3.49) is shaped by the frequency tracking scheme employed in the measurements. To properly account for the noise propagation in the loop, Eq. (3.49) has to be filtered by the transfer function of the tracking system

$$S_{y_{\rm th}}^{\rm loop}(\omega) = S_{y_{\rm th}}(\omega) \left| \frac{1}{\tau_{\rm mech}} H_{\theta_{\rm thm}}(i\omega) \right|^2.$$
 (3.53)

The transfer function present in Eq. (3.53),  $H_{\theta_{\rm th}}(i\omega)$ , is expressed in terms of phase noise and must be divided by  $\tau_{\rm mech}$  to converted it in the frequency domain.

It is further interesting to notice that, for  $\tau_{\rm th} < \tau_{\rm PLL}$  or  $\tau_{\rm L}$  (in the SSO — see Chapter 4), part of the temperature fluctuation noise is filtered by the frequency tracking loop itself.



50

# Photothermal back-action frequency noise

Photothermal back-action frequency noise  $S_{y_{\delta P}}(\omega, \lambda)$  originates from the intensity fluctuations of the light source employed for photothermal sensing, as well as any other light source used for transduction, such as interferometric lasers. For a continuous wave (CW) source with an power fluctuation PSD  $S_P(\omega, \lambda)$  [W<sup>2</sup>/Hz] (see Fig. 5.2c), the resonator fractional frequency fluctuations are given by

$$S_{y_{\delta P}}(\omega, \lambda) = \alpha^2(\lambda) \mathcal{R}_{P}^2(\omega) S_P(\omega, \lambda),$$
 (3.54)

where  $S_P(\omega, \lambda)$  typically has the form

$$S_P(\omega,\lambda) = h_0 + h_{-1}f^{-1} + h_{-2}f^{-2}$$
(3.55)

for a generic laser source [137]. Here,  $h_0$  denotes the laser shot-noise limit  $S_{P,\text{sn}}(\lambda) =$  $2hc\langle P_0\rangle/\lambda$ , where  $\langle P_0\rangle$  is the average input power; the terms  $h_{-1}$  and  $h_{-2}$  express the flicker and random walk noise levels, respectively. It is worth noting that  $\lambda$  refers to the wavelength of the transduction laser, as well as all the wavelengths of the light source used as a probe for spectroscopy or radiation sensing applications.

Therefore, high optical absorption and responsivity (3.3) make the resonator more sensitive to laser intensity noise, highlighting a trade-off between responsivity and frequency fluctuations. This noise can be mitigated by selecting materials with low absorption in the targeted spectral range, or by operating the laser at its shot-noise limit  $S_{P,\mathrm{sn}}(\lambda)$ .

### 3.2Summary

This chapter introduced a theoretical model based on the mean temperature framework, which has been validated through comparison with FEM simulations. The model demonstrates excellent agreement with FEM results across all resonator designs.

To better clarify the theoretical calculation workflow for the power responsivity  $\mathcal{R}_{P}$ , thermal time constant  $\tau_{\rm th}$ , frequency noise  $S_y(\omega)$ , and the power sensitivity NEP, the process is displayed in chart 3.9. The first step involves defining the geometric and material parameters. From these, the effective mass  $m_{\rm eff}$ , resonance frequency  $\omega_0$ , Q factor, and the Duffing parameter  $\alpha_{\text{eff}}$  are determined as key mechanical parameters. These quantities serve as input parameters for the lumped element model of a single mechanical mode (Eq. (2.40)). Concurrently, the thermal conductance (Eq. (3.17)) and capacitance (Eq. (3.16)) are calculated to specify the thermodynamic properties. These thermal properties are then used to calculate the relative temperature responsivity  $\mathcal{R}_{\mathrm{T}}$ (Eq. (3.8), (3.11), and (3.14)) and the thermal time constant  $\tau_{\rm th}$  (Eq. (3.4)), ultimately leading to the evaluation of the relative power responsivity  $\mathcal{R}_{P}$  (Eq. (3.3)).

For the frequency noise, the thermomechanical noise  $S_{y_{\theta}}$  (Eq. (3.45)) is derived from the mechanical properties, while the thermal fluctuations noise  $S_{y_{\text{th}}}$  (Eq. (3.49)) is calculated using the thermal characteristics. The photothermal back-action noise (Eq. (3.54)) is obtained using the power responsivity and the material's optical absorption.

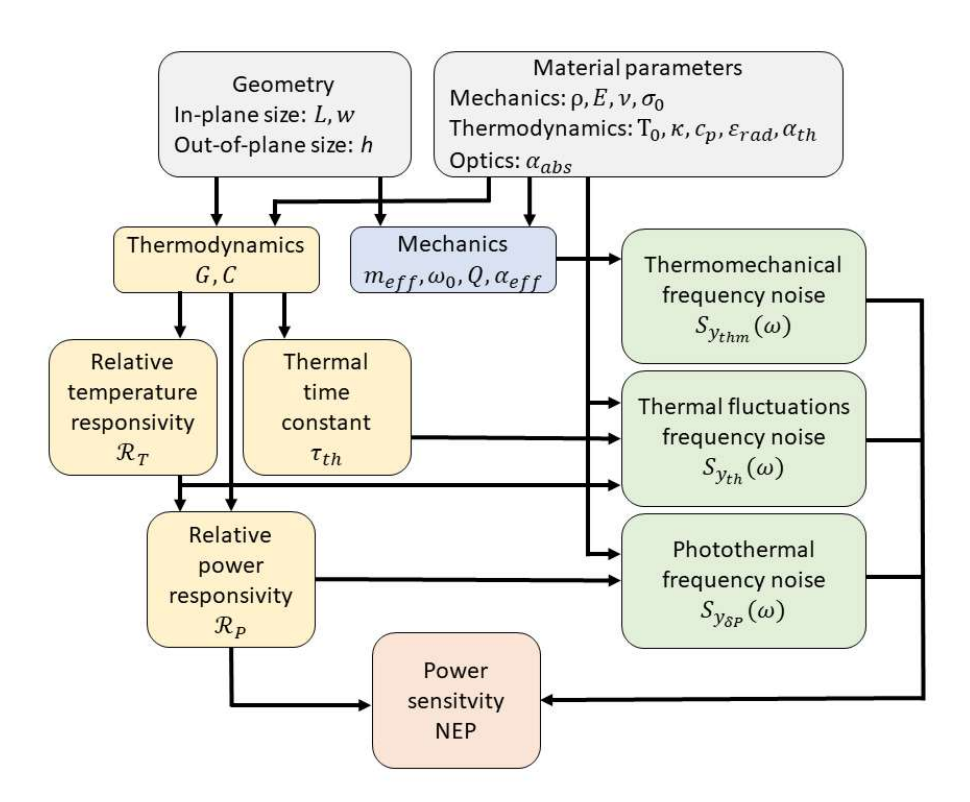


Figure 3.9: Theory workflow. Schematics of the workflow for the theoretical calculations of the power responsivity  $\mathcal{R}_{P}$ , thermal time constant  $\tau_{th}$ , frequency noise  $S_{y}(\omega)$ , and power sensitivity NEP.

Finally, the power sensivitiy NEP (Eq. (3.2)) is evaluated, completing the workflow for the theoretical analysis.

# Experimental and Computational Methods

This chapter introduces the experimental methodologies employed to actuate and measure the vibrations of nanomechanical resonators, as well as the techniques used to characterize their photothermal properties throughout this work. The discussion begins with the role played by silicon nitride for nanomechanical photothermal applications. It follows an introduction to Fabry-Perot interferometry and laser-Doppler vibrometry, along with a discussion about the measurement of other relevant physical observables central to this study. Next, two frequency tracking schemes—phase-locked loop and self-sustaining oscillator—are introduced. The chapter concludes with a detailed description of the finite element method (FEM) simulations performed for each investigation, including experimental approaches for determining the resonator's relative power responsivity and thermal time constant.

# 4.1 Silicon Nitride Sensing Platform

The rationale behind the use of SiN for photothermal sensing applications is the panoply of its mechanical, thermal, and optical properties. Table 4.1 compares these properties with other materials commonly employed in nanomechanics and photonics — silicon (Si), silicon carbide (SiC), lithium niobate (LN), and aluminum nitride (AlN).

For flexural out-of-plane modes operation, SiN resonators achieve among the best power sensitivity NEP, as highlighted in Fig. 4.1a for the case of string resonators. Among the materials considered here, LN achieves comparable performances. However, this high power sensitivity in SiN (like in LN) comes with the trade-off of slower response times, as shown in Fig. 4.1b.

SiN offers additional advantages over the other materials, including ease in fabrication, straightforward integration with other technologies [138], and a precise tunability of its

Table 4.1: Mechanical, thermal, electrical, and optical parameters comparison among various materials exploited in nanomechanics and photonics. All the paramters refer to a temperature T = 300 K. For anisotropic materials, one single direction is considered.

Parameter/Material	SiN	Si	SiC	LN	AlN
Mass density, $\rho$ [kg/m <sup>3</sup> ]	2700-3100 [87]	2330 [141]	3160 [142]	4650 [143]	3260 [144]
Young's modulus, E [GPa]	200-300 [87]	130-170 [145]	400 [146]	170 [147]	300 [148]
Poisson's ratio, $\nu$	0.23-0.28 [25, 87]	0.16-0.36 [145]	0.2 [149]	0.25	0.245 [148]
Stress tunability	Yes	Yes	Yes	Yes	Yes
Thermal conductivity, κ [W/(m K)]	3 [150]	130 [151]	280 [152]	4.6 [143]	170
Specific heat capacity, $c_p$ [J/(K kg)]	700 [87]	700 [145]	647 [152]	630 [143]	730 [153]
Thermal expansion coefficient, $\alpha_{\rm th}$ [ppm/K]	1-2.2 [139, 154]	2.6 [155]	4 [156]	14 [157]	4.2 [158]
Thermal softening coefficient, $\alpha_{\rm E}$ [ppm/K]	-87 [159]	-44 [160]	-25 [161]	-203 [162]	-
Piezoelectric coefficient, $c_{\rm pz}$ [pm/V]	=	-	-	6 [163]	5 [164]
Transmission window, $\lambda$ [ $\mu$ m]	0.4-8 [138]	1.2-8 [138]	0.37-12 [165]	0.32-5.2	0.2-6 [138]

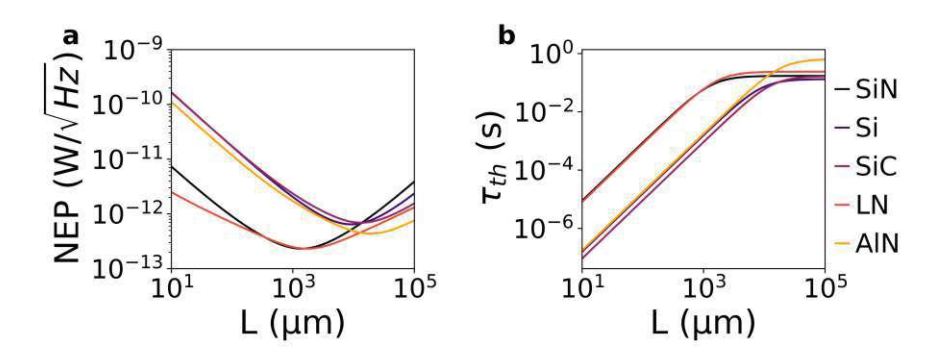


Figure 4.1: Comparison of materials for nanomechanics and photonics. a. NEP for the fundamental flexural out-of-plane modes of string resonators made of the materials listed in Table 4.1, as a function of the resonator's length. b. Corresponding thermal time constant. Parameters used:  $w = 5 \mu m$ ; h = 50 nm.

mechanical and optical properties [24, 139]. On the downside, SiN is isotropic and lacks piezoelectricity, making it challenging to excite high-frequency (< 100 MHz) mechanical modes. High-frequency modes represent a solution for reducing frequency fluctuations of thermomechanical origin. In this regard, piezoelectric materials such as AlN and LN provide promising alternatives, enabling the exploitation of GHz modes, such as Lamb waves [140].

#### 4.1.1 **Fabrication**

All the tensile stressed SiN resonators analyzed and used in this work are fabricated with a low-pressure chemical vapour deposition (LPCVD) process on a double-sided h(=50-340 nm) thick SiN on  $\langle 100 \rangle$  Si wafer. Photolithography is used to pattern the front and back sides of each chip according to the specific design. The structures are then released through a KOH etching process, which removes the underlying Si substrate [24, 69]. For a detailed overview of the cleanroom fabrication process of the

nanomechanical resonators employed here, the reader can refer to [166, 167]. For each design, the in-plane dimensions are characterized by optical microscopy, while ellipsometry is used to measure the thickness.

#### 4.2 Transduction

In its most general definition, transduction refers to the conversion of energy from one physical domain to another. Two types of transduction are particularly relevant for this work: the actuation of the resonator, where energy is converted from the electrical to the mechanical domain (a voltage is converted in mechanical vibrations), and the detection of its motion, where the mechanical energy is converted into an electrical signal. This section first discusses the actuation of flexural out-of-plane motion in the resonators, followed by a description of the optical detection schemes employed in this study.

#### 4.2.1Base Actuation

In this work, all mechanical resonators have been actuated piezoelectrically. In details, a piezoelectric element is placed beneath the resonator and supplied with a periodic external voltage to made it vibrate. The base vibrations at frequency  $\omega/2\pi$  are transferred to the mechanical structure above. Unlike direct force application, the base actuation imparts an acceleration to the resonator, resulting in a relative amplitude and phase response of the form [168]

$$\delta u_0(\omega) = \frac{\left(\frac{\omega}{\omega_0}\right)^2}{\sqrt{\left(1 - \left(\frac{\omega}{\omega_0}\right)^2\right)^2 + \left(\frac{\omega}{\omega_0 Q}\right)^2}} \tag{4.1}$$

and

$$\theta(\omega) = \arctan \frac{\frac{1}{Q} \frac{\omega}{\omega_0}}{1 - \left(\frac{\omega}{\omega_0}\right)^2}.$$
 (4.2)

Eq. (4.1) differs from (2.18) away from resonance due to the nature of acceleration-based actuation; however, both equations converge near resonance. Alternative non-integrated actuation schemes, such as photothermal drive and radiation pressure, are also viable and have been explored in related works [167].

#### 4.2.2Optical Detection

In this work, the displacement of nanomechanical resonators has been measured using fully optical detection techniques: Fabry-Perot inferferometry and laser-Doppler vibrometry. Both transductions are external to the resonator chip, ensuring flexibility while minimizing the interference with the resonator's thermal and mechanical properties [166]. In both cases, a laser serves as the core transducing element. Generally speaking, its key features, i.e., high spatial and temporal coherence, make interferometry one of the most precise

ways of measuring the motion of an object, whether it be a nanomechanical resonator [169] or a meter-scale test-mass [170]. In essence, an interferometer always consists of at least two beams — a reference beam and a measurement beam — of equal or different frequency. The relative phase relationship between these beams encodes the mechanical motion of the target object.

#### Fabry-Perot Interferometry (Setup I) 4.2.2.1

Fabry-Perot interferometry has been employed here for the spectroscopy and polarization microscopy of individual gold nanorods [31]. Specifically, a commercial fiber-based interferometer (IDS3010, Attocube systems AG) was used (Fig. 4.2).

Generally speaking, a Fabry-Perot interferometer is the simplest and most compact configuration for interferometric measurements, consisting of two parallel, partially transmitting mirrors (forming a cavity), spaced by a distance x [171], as illustrated in Fig. 4.2a. Light (with electric field  $E_0$ ) is sent to the input mirror (left) and is partially transmitted inside the cavity. Inside, the light undergoes multiple reflections between the mirrors, forming an infinite series of partial forward and backward waves. The portion of light reflected by the input mirror before entering the cavity constitutes the reference beam  $(E_{r0})$ , while the portion partially reflected by the target mirror (the movable reflector) and partially transmitted at the input mirror forms the measurement beam  $(E_{\rm rN}, \text{ with } N \neq 0).$ 

In the present setup (Fig. 4.2a), the cavity is formed between the cleaved end face of an optical fiber (left) and the nanomechanical resonator (right) [172–174]. The intensity reflected by the Fabry-Perot cavity can be expressed as [174]

$$I_{FP} = I_0 \frac{r_1^2 + (fr_2)^2 - 2r_1 f r_2 \cos(\Phi)}{1 + (r_1 r_2)^2 - 2r_1 r_2 \cos(\Phi)},$$
(4.3)

where

$$f = r_1^2 + \sqrt{\eta} t_1^2. (4.4)$$

 $I_0, r_1, t_1, r_2, \Phi = -k\Delta x$ , and  $\eta$  denote the input laser intensity, the reflection and transmission coefficients of the first mirror, the reflection coefficient of the second mirror, the relative phase of the interference intensity  $I_{FP}$  (where  $\Delta x = u$  is the motion of the mechanical resonator, while k the wavevector of the probing laser), and the fiber coupling coefficient of the system, respectively.

A schematics of the experimental configuration is given in Fig. 4.2b. The light beam is delivered to the cavity using a single-mode fiber (SMF) and fiber coupler (FC), and shaped with a high numerical aperture (NA) objective (Attocube Sensor Head D12/F2.8), with a resultant beam diameter of  $\approx 14 \ \mu \text{m}$  at the focal plane onto the resonator. The interference signal intensity  $I_{FP}$  is then sent to a photodetector via the FC. A key advantage of this type of interferometer, compared to traditional setups like Michelson interferometers, is its single-arm design. As a result, noise affecting the optical fiber impacts both the reference and measuring beams equally, reducing the need for stringent mechanical stability along the optical path.

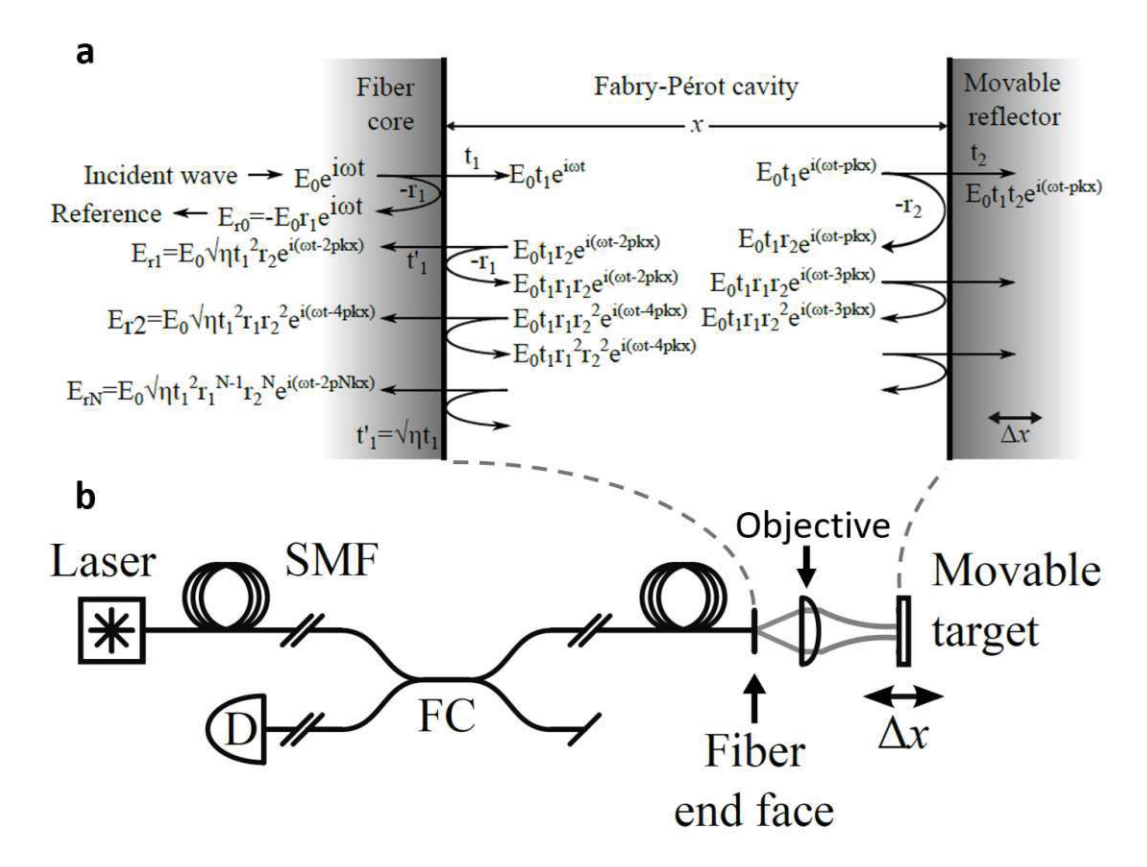


Figure 4.2: Optical fiber-based Fabry-Perot interferometry. a. Working principle of a Fabry-Perot interferometer. b. Schematics of the interferometer used in this work. SMF: single-mode fiber. FC: fiber coupler. D: photodetector. Adapted from Ref. [174]

For the spectroscopy measurements [31], the experiments are conducted in vacuum, at a pressure  $p < 10^{-5}$  mbar, to minimize gas damping [113] and thermal convection [127]. The optical fiber carrying the interferometric signal enters a custom-made vacuum chamber through an optical feedthrough. The input laser ( $\lambda = 1530$  nm) is focused on the backside of the resonator. The electrical signal generated upon photodetection is fed into a lock-in amplifier (HF2LI, Zurich Instruments) for frequency tracking measurements.

#### 4.2.2.2Laser-Doppler Vibrometry (Setup II)

In a laser-Doppler vibrometer, like the one used in two of the works described here (MSA-500, Polytec GmbH) [111, 139], the input laser (He-Ne,  $\lambda = 632.8$  nm) is split into two optical paths, as schematically shown in Fig. 4.3. One beam (left) is frequencymodulated via an acousto-optic modulator (represented by a Bragg cell in the schematics) to measure the Doppler shift

$$f_D = \frac{2}{\lambda} \frac{\partial u}{\partial t},\tag{4.5}$$

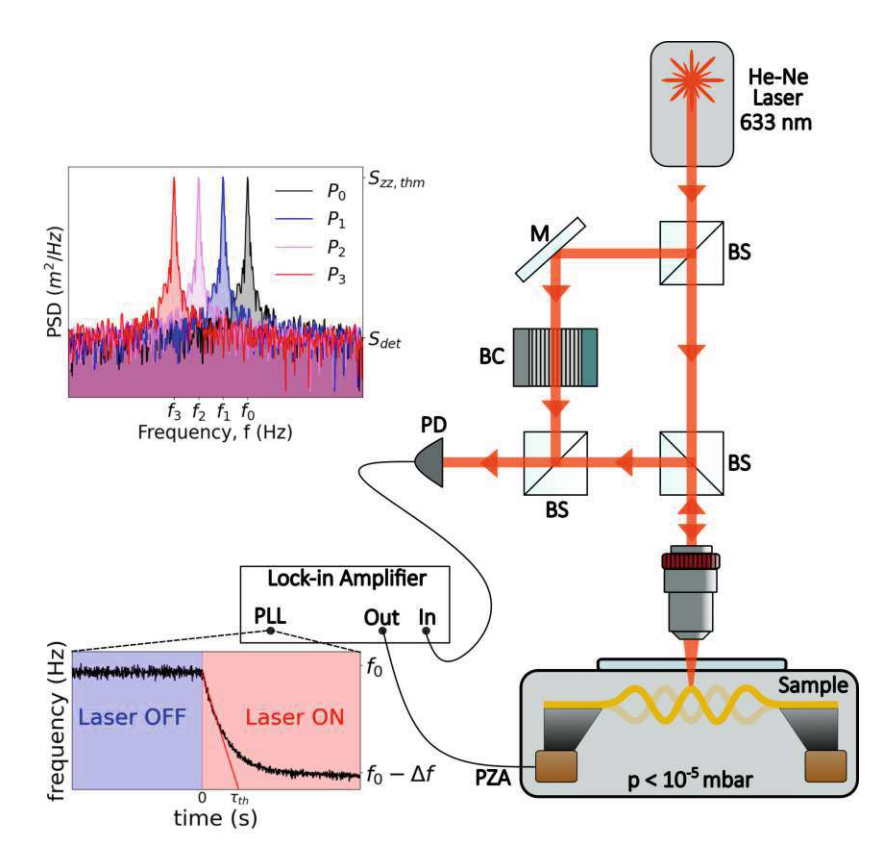


Figure 4.3: Lase-Doppler vibrometry. BC: Bragg cell. BS: beam-splitter. M: mirror. PD: photodetector. PZA: piezoelectric actuator. This setup alone enables the measurements of the power responsivity (top left plot). In conjunction with a frequency tracking device, the frequency noise and the thermal time constant can be measured (bottom left plot).

which corresponds to the frequency shift experienced by the input laser after reflecting off the mechanical resonator. Compared to the Fabry-Perot interferometer, this setup has two main differences: i) the laser-Doppler vibrometer directly measures the velocity of the nanomechanical resonator, relaxing the requirements of phase stabilization; ii) the signal is recorded with heterodyne detection, since signal and reference are now at two different frequencies.

In the experimental setup employed here, the laser is focused on the front surface of the resonator and enters the vacuum chamber in free space (Fig. 4.3). Similar to the Fabry-Perot setup, the optical interference is recorded by a photodetector. The photogenerated current is converted in a voltage signal, which is again fed into a lock-in amplifier for processing.

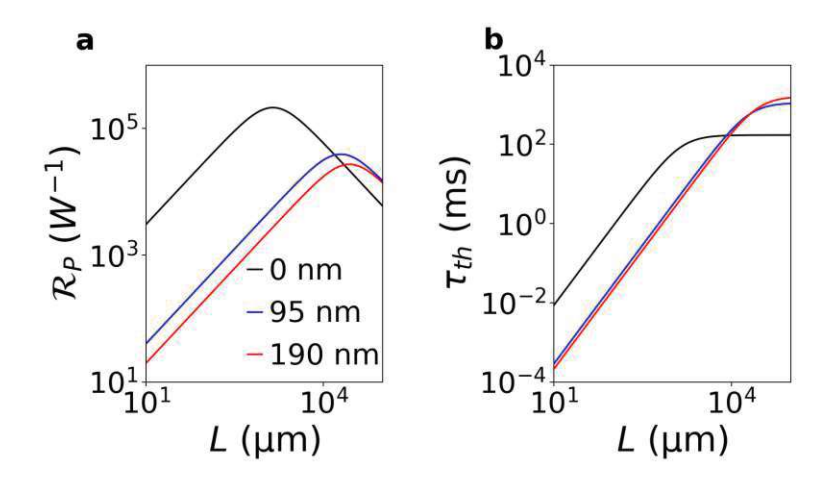


Figure 4.4: Influence of metals on the photothermal response. a. Relative power responsivity of a SiN string resonator without metal on its surface (black curve), with a 95 nm thick (blue) and 190 nm thick (red) Au layer. b. Corresponding thermal time constant. Parameters used:  $w = 5 \mu m$ ;  $h_{SiN} = 50 \text{ nm}$ ;  $h_{Cr} = 10 \text{ nm}$ . This combinantion of metals is inspired by [166].

#### 4.2.2.3Considerations on Optical Readout Schemes

Two important aspects underpin the choice of fully optical, off-chip displacement readout methods over integrated electrical approaches, such as electromotive readout [60, 166]. The first aspect concerns the power responsivity. The presence of metal traces, such as gold electrodes, significantly increases the thermal conductance, leading to a substantial reduction in the power responsivity of the sensor. For examples, as shown in Fig. 4.4a for the case of SiN string resonators, the addition of gold traces causes a reduction in  $\mathcal{R}_{P}$ by two order of magnitudes compared to bare SiN structures, for the lengths used in this work (L < 2 mm). This effect has also been observed in trampoline resonators [166].

The second aspect concerns the Johnson-Nyquist thermal noise introduced by free carriers in the electrodes, when an integrated electrical readout is employed. This type of thermal noise can dominate the output voltage noise, especially in nanoscale resonators, and often becomes the limiting factor in the system's performance, surpassing fundamental noise sources like thermomechanical or temperature fluctuation noise [40, 166].

However, the inclusion of electrodes does offer certain advantages, such as a practical reduction in the resonator's thermal response time, as shown in Fig. 4.4b. This effect arises from the increase in overall thermal conductance outweighing the increase in thermal capacitance introduced by the electrodes.

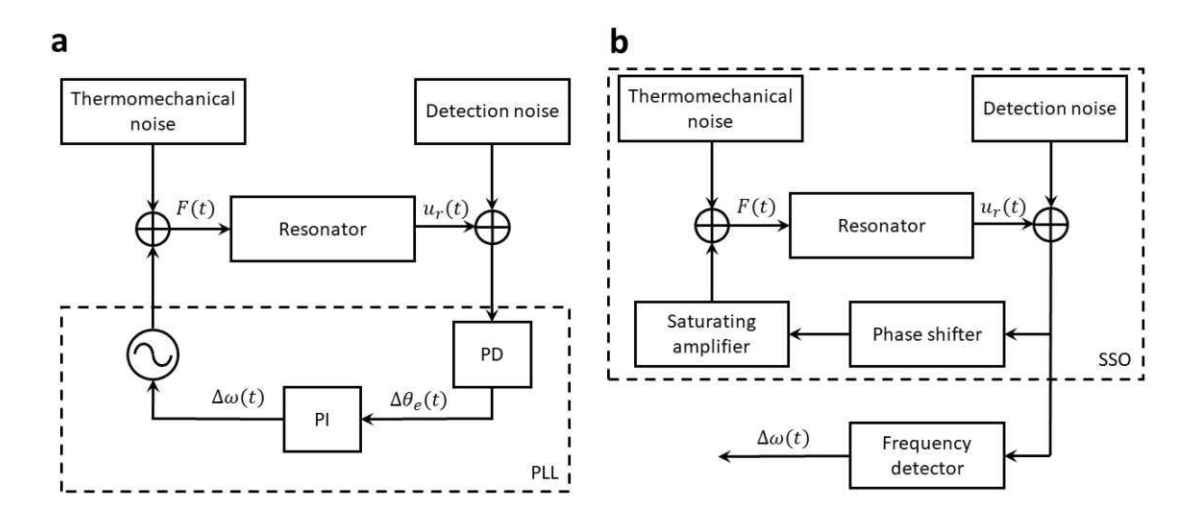


Figure 4.5: Closed-loop frequency tracking schemes. a Schematics of a PLL tracking scheme. b Schematics of an SSO tracking scheme. Figures are inspired by Figure 2 and 3 in [131].

## 4.3 Frequency Tracking Schemes

Precise and continuous monitoring of the mechanical resonance frequency is crucial in nanomechanical photothermal sensing, as it is the key observable used to detect small energy exchanges between the resonator and its environment. In this thesis, two different frequency tracking schemes have been employed: phase-locked loop (PLL) and self-sustained oscillator (SSO). Both are close-loop schemes, providing a larger dynamic range compared to open-loop approaches, as they can track frequency shifts larger than the resonator linewidth,  $\Delta\omega_0 > \omega_0/Q$  [60]. Below, the basic operation of both schemes is briefly described, followed by an introduction to their respective noise transfer functions. For a more comprehensive discussion, the reader can refer to [130, 131, 175]. In particular,  $Be\check{s}i\acute{c}$  et al. have shown that PLL and SSO offer the same performance in terms of noise [131].

## Phase-Locked Loop (PLL) 4.3.1

The PLL scheme has been employed for the acquisition of the results presented in Ref. [31], and for part of the data shown in Ref. [111]. A PLL is essentially a control system that adjusts the frequency of a voltage-controlled oscillator (VCO) to match the resonance frequency of the nanomechanical resonator. Using negative feedback, the VCO — also referred to as the local oscillator (LO) — is regulated by a proportional-integral (PI)

controller to minimize the phase error  $\Delta\theta_{\rm e} = \theta_0 - \theta(t)$  between a set-point phase,  $\theta_0$ (chosen to be the resonator phase at resonance,  $\theta_0 = \theta(\omega_0)$ ) and the resonator's measured phase  $\theta(t)$  (see Fig. 4.5a).

The resonator's phase is continuously monitored by a phase detector (PD), which compares the resonator's electrical output with the LO signal. The PD uses in-phase and quadrature (I/Q) demodulation to extract the phase information. It has a cutoff frequency  $f_{\rm L}$ , corresponding to a time constant  $\tau_{\rm L} = 1/2\pi f_{\rm L}$ , that suppresses the highfrequency components of both the signal and related additive phase noise, limiting the PD speed. The PI controller regulates the VCO at a frequency  $f_{\rm PLL} = 1/(2\pi\tau_{\rm PLL})$ , with  $f_{\rm PLL} \leq f_{\rm demod}/5$ . The PI coefficients can be chosen as follow to simplify the overall system transfer function [175, 176]

$$k_{\rm P} = 2\pi f_{\rm PLL} = \frac{1}{\tau_{\rm PLL}},\tag{4.6}$$

$$k_{\rm I} = \frac{k_{\rm P}}{\tau_{\rm mech}},\tag{4.7}$$

where  $k_{\rm P}$  and  $k_{\rm I}$  are the proportional and integral coefficients, respectively.

The noise processes that depend on the frequency tracking scheme are the thermomechanical and detection-amplitude noise, as already introduced in Chapter 3. The transfer functions of the PLL from the corresponding phase noise source to the frequency of the output signal are given by [175]

$$H_{\theta_{\text{thm}}}^{\text{PLL}}(i\omega) = \frac{1}{\tau_{\text{mech}}} \frac{(i\omega k_P + k_I)H_{\text{L}}(i\omega)}{-\omega^2 + i\frac{\omega}{\tau_{\text{mech}}} + (i\omega k_P + k_I)H_{\text{L}}(i\omega)}$$
(4.8)

$$H_{\theta_{\text{det}}}^{\text{PLL}}(i\omega) = \frac{1}{\tau_{\text{mech}}} \frac{1}{H_{\text{mech}}(i\omega)} \frac{(i\omega k_{\text{P}} + k_{\text{I}})H_{\text{L}}(i\omega)}{-\omega^2 + i\frac{\omega}{\tau_{\text{mech}}} + (i\omega k_{\text{P}} + k_{\text{I}})H_{\text{L}}(i\omega)}.$$
 (4.9)

 $H_{\text{mech}}(i\omega)$  and  $H_{\text{L}}(i\omega)$  represent the low-pass filter transfer functions of the resonator and system filter, respectively

$$H_{\text{mech}}(i\omega) = \frac{1}{1 + i\omega\tau_{\text{mech}}},\tag{4.10}$$

$$H_{\rm L}(i\omega) = \frac{1}{1 + i\omega\tau_{\rm L}}. (4.11)$$

These expressions provide a detailed description of how noise propagates through the PLL system and influences the tracking performance.

#### 4.3.2Self-Sustaining Oscillator (SSO)

The SSO scheme has been employed for the acquisition of part of the results shown in Ref. [111]. In this setup, the amplitude signal transduced from the vibrational motion of the resonator is fed back to the resonator after being amplified and appropriately phase-shifted (see Fig. 4.5b) [131, 177, 178]. The Barkhausen conditions must be satisfied for sustained oscillation: i) the loop gain must be equal to one, ensuring stable oscillation amplitude. This is achieved using a saturating amplifier, which stabilizes the resonator's motion by limiting the amplification when the amplitude exceeds a certain threshold. ii) The total phase around the feedback loop must be  $2\pi n$ , where n is an integer. This is managed by introducing a phase shifting element in the loop [131]. The noise transfer functions for thermomechanical and detection noise in an SSO are given by [131]

$$H_{\theta_{\rm thm}}^{\rm SSO}(i\omega) = \frac{1}{\tau_{\rm mech}} H_{\rm L}(i\omega),$$
 (4.12)

$$H_{\theta_{\text{det}}}^{\text{SSO}}(i\omega) = \frac{1}{\tau_{\text{mech}}} \frac{H_{\text{L}}(i\omega)}{H_{\text{mech}}(i\omega)}.$$
(4.13)

In this configuration, the frequency is measured using a frequency counter embedded within the SSO (PHILL, Invisible-Light Labs GmbH), as illustrated in Fig. 4.5b [131].

The transfer functions introduced so far for the PLL and SSO account for the loop dynamics of the thermomechanical and detection, as well as temperature fluctuation induced fractional frequency noise (see Chapter 3 for the detailed expressions). Thermomechanical and temperature fluctuation noise are white frequency noise sources, while the detection noise can give rise to flicker phase and / or white phase noise. In the power-law model used to describe the fractional frequency PSD [179]

$$S_y(f) = \sum_{i=-2}^{2} h_i f^i, \tag{4.14}$$

the thermomechanical noise, as well as thermal fluctuations, are characterized by a power-law  $h_0 f^0 = h_0$  (with  $h_i$  being the power-law coefficients). The detection noise follows instead  $h_1f + h_2f^2$ . Both components are shown in Fig. 4.6a, which presents an example of experimental fractional frequency PSD. Additionally, the figure shows other two noise sources commonly encountered in oscillators, i.e., flicker frequency (with power-law  $h_{-1}f^{-1}$ ) and random walk frequency (with power-law  $h_{-2}f^{-2}$ ).

In the time domain, the oscillator's frequency noise is characterized with the Allan deviation (see Eq. (3.40) and (3.42)). Fig. 4.6b shows the AD corresponding to the PSD of Fig. 4.6a, illustrating the different noise contributions as a function of the integration time  $\tau$ . The figure also includes the contribution from the frequency drift (orange line), which does not appear in the PSD. When limited by white frequency noise, the AD  $\sigma_{\nu}$ exhibits a characteristic slope  $\propto \tau^{-1/2}$  for increasing values of the integration time.

#### 4.4 Finite Element Method

This section provides an overview of the FEM simulations used to support the results presented in Ref. [31, 111]. This simulations were performed using COMSOL Multiphysics, a commercially available simulation software. The FEM simulations serve two primary purposes in this work, and they are divided into two main categories: i) photothermal



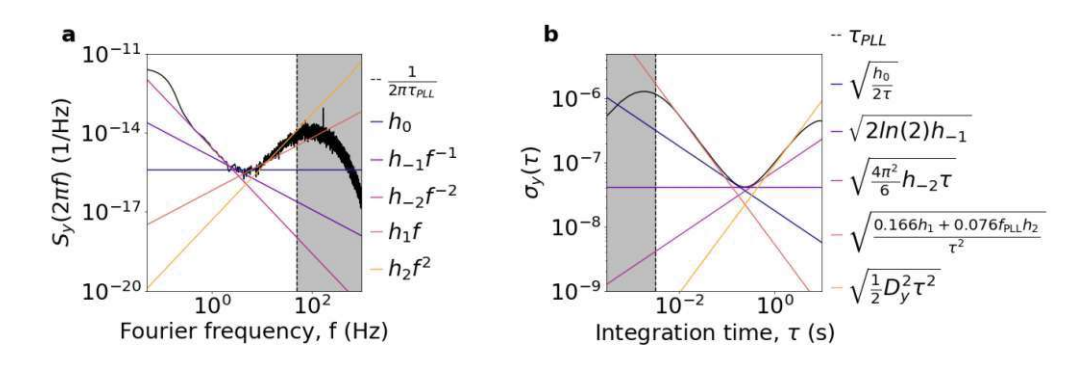


Figure 4.6: Fractional frequency PSD and AD. a Fractional frequency PSD. Noise components: white frequency (this includes thermomechanical, detection, and temperature fluctuation noise — blue); flicker frequency (dark purple); random walk frequency (purple); flicker phase (detection noise — red); white phase (detection noise — orange). **b** Corresponding AD. The orange curve represents the frequency drift component; the red curves is the sum of the flicker phase and white phase frequency noise components.

response of the various designs discussed throughout this thesis; ii) plasmonic response of the individual particles characterized in [31].

Each of these models will be discussed separately in the following sections to highlight their features.

#### 4.4.1 Photothermal Response

These simulations pertain to the results presented in Ref. [111] and focus on two key properties: the relative power responsivity  $\mathcal{R}_P$  and the thermal time constant  $\tau_{\rm th}$ , for each resonator's design. As both quantities depend on the interplay between mechanical and thermal properties of the resonator, two modules available in COMSOL are utilized — namely the Structural Mechanics Module and the Heat Transfer Module.

The Structural Mechanics Module is designed to solve problems of statics, eigenfrequency, and transients. The Heat Transfer Module is designed to solve problems of heat transfer, including conduction, convection, and radiation, in either transient or steady-state regimes. The two modules are coupled via thermal expansion occurring inside the resonator upon interaction with an heat source. All material input parameters are assumed constant over the range of simulated temperatures.

The common procedure for all simulations begins with defining the resonator's geometry and material properties (Fig. 4.7a). The designs all feature high aspect ratios  $(L/h > 10^3)$ , with h = 50 nm), which allows for the use of a shell interface. This reduces the computational problem from 3D to 2D, with the thickness h included as an input parameter in both the motion and heat transfer equations.

For the mechanical analysis, the material is assumed to be linear and elastic, with Young's modulus E, Poisson's ratio  $\nu$ , and mass density  $\rho$ ; a 2D uniform tensile stress is applied

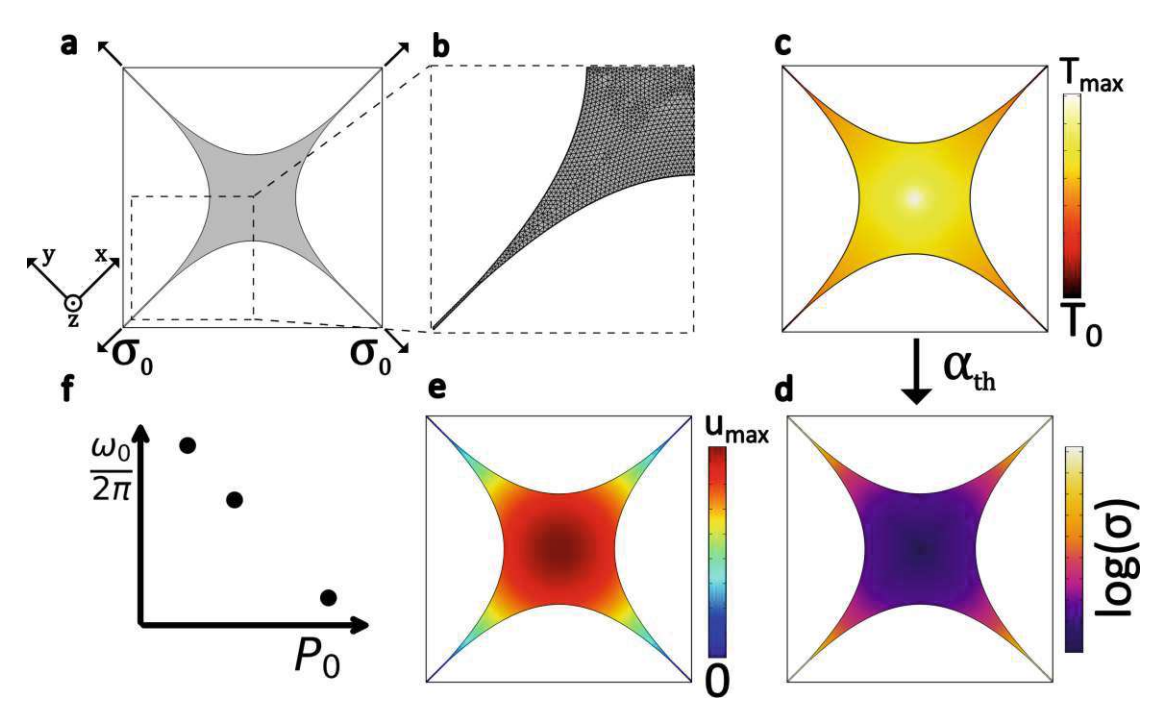


Figure 4.7: Photothermal response FEM workflow. a. Definition of geometry, material properties, and boundary conditions. b. Mesh configuration. c. Stationary study I: Steady-state temperature field T computed for a given input heat power  $P_0$ . d. Stationary study II: Resultant (steady-state) static stress field  $\sigma$ , derived from the temperature field in  $\mathbf{c}$ , which couples to  $\sigma$  via the thermal expansion (with the coupling strength determined by the thermal expansion coefficient  $\alpha_{\rm th}$ ). e. Eigenfrequency study: Modeshape of the fundamental out-of-plane flexural mode. f. Parametric study: The eigenfrequency is solved for varying input power  $P_0$ .

on the thin film,  $\sigma_{xx} = \sigma_{yy} = \sigma_0$ . Fixed constraints are applied at the clamping regions of the resonator, ensuring zero displacement at the edges. The thermal parameters are defined next, including the linear coefficient of thermal expansion  $\alpha_{\rm th}$ , the specific heat capacity  $c_p$ , the thermal conductivity  $\kappa$ , and the emissivity  $\epsilon_{\rm rad}$ . The heat source can either be a Gaussian laser beam with waist  $w_0$  and input power  $P_0$ , or a boundary heat source, like a point or surface with the same impinging power  $P_0$ . No convection is considered, as experiments are performed in vacuum. For the heat transfer problem, the temperature at the clamping regions is fixed to  $T_0 = 300$  K, modelling the connection of the resonator to its thermal bath.

It follows the meshing (Fig. 4.7b). Depending on the resonator design, a quadrilateral or triangular mesh is used. Mesh refinement is applied to the computational load, ensuring minimal memory usage while capturing the essential physics of the system.

#### 4.4.1.1 Power Responsivity $\mathcal{R}_P$

The first step in this study involves calculating the temperature profile T(x,y) within the resonator (Fig. 4.7c). This profile results from the thermal steady-state condition, where the input heat generated by the laser balances with the dissipative mechanisms of conduction and radiation.

The second step involves solving for the static stress field  $\sigma(x,y)$ , given T(x,y) as an input parameter (Fig. 4.7d). The coupling between the two physics is given by the thermal expansion (with the coupling strength given by the thermal expansion coefficient  $\alpha_{\rm th}$ ), which induces a stress relaxation.

The third and final step is to compute the eigenfrequency of interest (here the fundamental one, whose modeshape is shown in Fig. 4.7e) with the stress field serving as the input parameter. It is important to note that the measured quality factor  $Q = \mathcal{O}(10^4)$  [111] ensures that  $\omega_0 \approx \omega_r$ , justifying the use of the eigenfrequency study for this analysis.

These three steps are repeated for varying input laser powers  $P_0$ . From the eigenfrequency response to the power (Fig. 4.7f), the responsivity  $\mathcal{R}_P$  is extracted by fitting the FEM results with

$$\frac{\omega_0(P_0)}{2\pi} = \frac{\omega_0(0)}{2\pi} + \alpha_{\text{abs}}(\lambda) \mathcal{R}_P \frac{\omega_0(0)}{2\pi} P_0. \tag{4.15}$$

Here,  $\omega_0(0)/2\pi$  denotes the resonator eigenfrequency for zero impinging optical power  $(P_0 = 0 \mu W)$ , while  $\alpha_{abs}(\lambda)$  is the optical absorptance of the material.

Various studies have been conducted to examine how  $\mathcal{R}_P$  changes in response to different parameters. Specifically, the effects of the laser's position relative to the resonator's center and its beam waist have been analyzed, and the results are detailed in Ref. [111] (Chapter 3).

#### Thermal Time Constant $\tau_{\rm th}$ 4.4.1.2

Two types of simulations have been implemented to evaluate  $\tau_{\rm th}$ . Both simulations involve a transient thermal study where the laser is turned on time t=0 and the simulation solves for the temporal evolution of the temperature profile (Fig. 4.8). It is worth noting that the results are unchanged when the laser is initially on for t < 0 and then switched off at t=0.

The first study focuses on the evolution of the maximum and surface-averaged temperature of the resonator. This allows the analysis of how quickly the resonator's temperature reaches the steady-state. The second study extends this approach by using the evolving temperature profile as an input for mechanical simulation, as done for  $\mathcal{R}_P$ . For each time step t>0 the temperature field T(x,y) is updated, the corresponding tensile stress field is recalculated, and the temporal evolution of the eigenfrequency evaluated.

The results from both simulations are fitted with an exponential function of the form  $a(1-e^{-\frac{t-t_0}{\tau_{\mathrm{th}}}})+c,$  as depicted in Fig. 4.8.

The results indicate that the eigenfrequency stabilizes with the same time constant of the surface average temperature [111]. In contrast, the peak temperature reaches steady-state more rapidly.

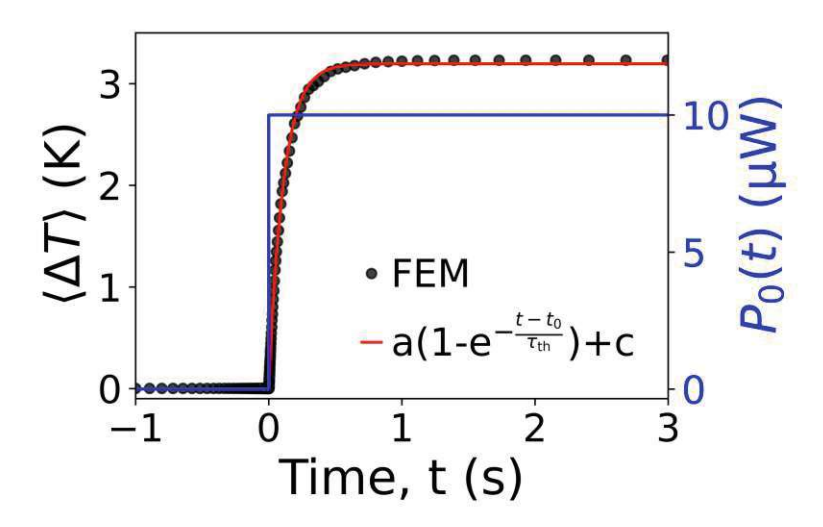


Figure 4.8: **FEM thermal time constant.** The FEM results (black dots) are fitted with an exponential function of the form  $a(1 - e^{-\frac{t-t_0}{\tau_{\text{th}}}}) + c$ .

### Plasmonic Response 4.4.2

The simulations described here pertain to the results in Ref. [31], focusing on the absorption cross-section  $\sigma_{abs}(\lambda)$  of single metal nanorods across the visible (VIS) to near-infrared (NIR) spectral range. In this range, absorption is dominated by localized surface plasmons (LSPR) within the metal core. Various techniques, such as Mie theory, Transition Matrix, discrete-dipole approximation, finite-difference time-domain method, and FEM, can be used to study this type of problem. Among these, FEM has the key advantage of supporting non-regular tetrahedral adaptive meshing, allowing for more accurate approximation of curved surfaces compared to other techniques [180, 181]. Furthermore, FEM is ideal for analyzing the electromagnetic interaction between the scatterer (nanoparticle) and the input field in the presence of an underlying substrate [181-183].

For this study, the *Electromagnetic Waves*, *Frequency Domain* interface was employed to investigate the optical properties of the nanorod both with and without the SiN substrate. The implementation of the simulations consists of two parts. The first one calculates the electromagnetic field within the simulation domain resulting from the interaction of a specific input field with the substrate, in the absence of the scatterer (the nanoparticle). The second step uses the resulting field from the first step as a background field and calculates the interaction between this field and the scatterer [184]. From this, the absorption cross-section can be determined as [185]

$$\sigma_{\text{abs}}(\omega) = \frac{1}{I_0} \iiint_{V_{\text{NR}}} Q_{\text{h}} d\mathbf{r} = \frac{1}{I_0} \iiint_{V_{\text{NR}}} \frac{1}{2} \omega \epsilon_0 \text{Im}(\epsilon_{\text{NR}}(\omega, \mathbf{r})) |\mathbf{E}(\mathbf{r})|^2 d\mathbf{r},$$
(4.16)

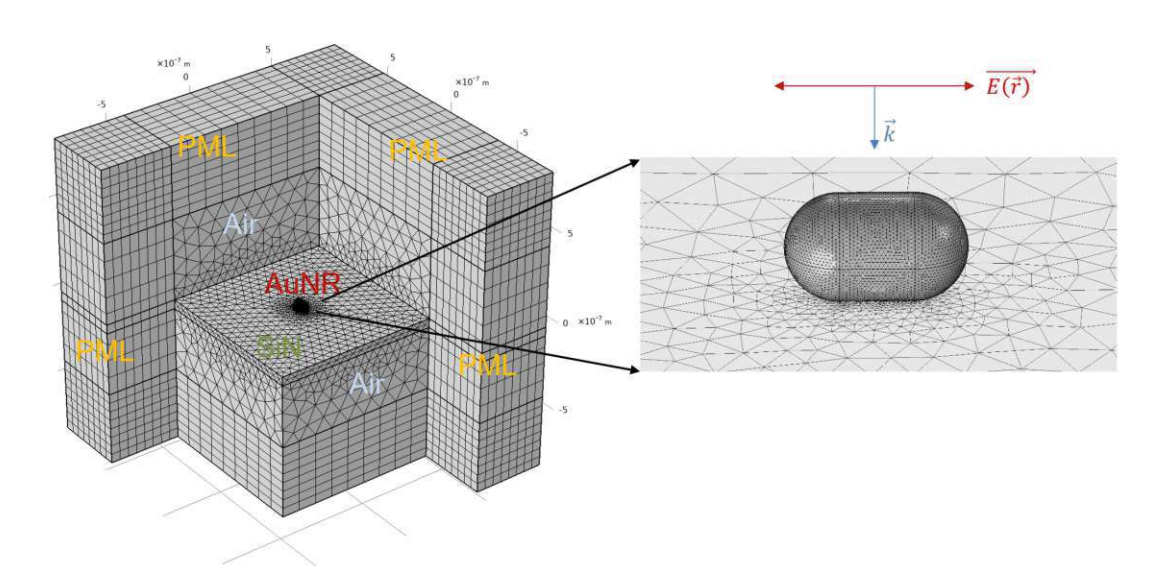


Figure 4.9: **FEM of the nanorod's plasmonic response.** FEM simulation domain, including the nanorod, the SiN substrate, the air/vacuum regions, and the PML regions. The meshing is adapted to the different region to preserve the physical problem, and save memory for the calculations. In particular, high-density meshes are used in the tiny regions characterized by strong electric field and high field gradients, while low-density meshes are used farer from the absorber. The input electromagnetic field enters the domain from top face of the whole domain, with a polarization parallel to the nanorod long-axis in the plot.

where the integral is evaluated over the nanorod's volume  $V_{\rm NR}$ .  $Q_{\rm h}$  is the total power dissipation density (as given in COMSOL),  $I_0$  is the impinging field intensity,  $\epsilon_0$  the vacuum dielectric permettivity,  $Im(\cdot)$  the imaginary operator applied on the dielectric function of the nanorod  $\epsilon_{NR}$ , and  $\mathbf{E}(\mathbf{r})$  the resulting electric field.

For each simulation, the geometry of the nanorod is defined first (inset of Fig. 4.9), with a particular focus on the aspect ratio, which is a key parameter due to its direct influence on both the peak absorption wavelength of the LSPR and the resonance amplitude [186-188. The aspect ratio is adjusted to align the FEM simulations with the experimental absorption spectra presented in Ref. [31], using size ranges provided by the vendor and confirmed through scanning electron microscopy (SEM). The nanoparticle's end caps are modeled as spherical, based on SEM imaging (see Chapter 6). This choice is crucial, as the absorption properties of elongated particles are highly sensitive to the shape of their tips, which strongly affects the local electric field in these regions [183, 189].

Next, the optical properties of the nanorod, i.e. its complex dielectric function  $\epsilon_{\rm NR}(\omega)$ , are set as input parameters for the FEM model (Fig. 4.10).  $\epsilon_{NR}(\omega)$  describes both the dispersive (real part, Fig. 4.10 top) and dissipative (imaginary part, Fig. 4.10 bottom) response of the nanoparticle to the external electromagnetic field. The base material is bulk gold, whose values  $\epsilon_{bulk}$  are taken from Ref. [190] and which accounts for the electron bulk scattering  $\gamma_0$ . However, due to the nanoscale dimensions of the analyzed

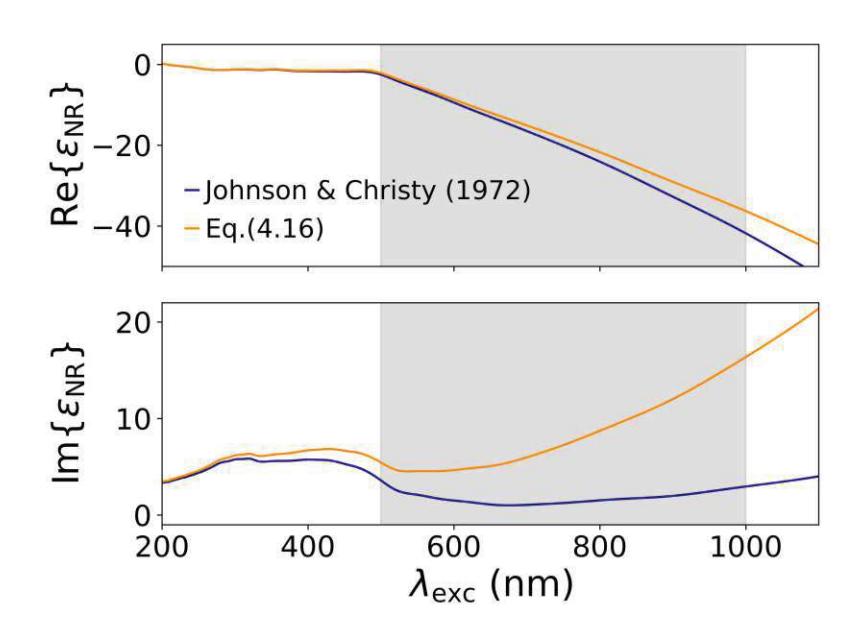


Figure 4.10: Dielectric function of the gold nanorod. Real (top) and imaginary (bottom) parts of the complex dielectric function of the gold nanorod as a function of the laser excitation wavelength. Two models are considered: the blue curve only considers electron bulk scattering (with the data taken from Ref. [190]); The orange curves further accounts for radiative damping and electron surface scattering (Eq. 4.17). The parameters used for the calculations are: A = 0.66,  $L_{\text{eff}} = 66$  nm, and  $V_{\text{NR}} = 5.24 \cdot 10^5$  nm<sup>3</sup>. The grey region indicates the explored range of wavelength.

nanorods, surface effects become more significant than in bulk samples, requiring an improvement in the description of in the dielectric response [182, 186, 188, 191]. Hence, both electron surface scattering and radiative damping are incorporated, described by the following expression

$$\epsilon_{\rm NR}(\omega, L_{\rm eff}) = \epsilon_{bulk} + \frac{\omega_p^2}{\omega^2 + i\omega\gamma_0} - \frac{\omega_p^2}{\omega^2 + i\omega(\gamma_0 + \frac{Av_F}{L_{\rm eff}} + \frac{\eta V_{\rm NR}}{\pi})}.$$
 (4.17)

Here,  $\omega_p$  denotes the plasma frequency of gold;  $v_F$  indicates the electron Fermi velocity; A is a dimensionless parameter describing the details of the electron surface scattering;  $L_{eff}$ , is the electron mean free path confined at the surface, which depends on the nanorod's size [182, 191, 192];  $\eta$  is an effective radiative damping rate [182]. The difference between the bulk dielectric function and Eq. (4.17) is shown in Fig. 4.10. While the dispersive response (top) remains largely unaffected by electron surface scattering, the dissipative component (bottom) shows an increase corresponding to greater electron surface channel losses.

The nanorod is coated with a silica (SiO<sub>2</sub>) layer with a thickness of 20 nm. Since the silica is transparent in the VIS and NIR, only the dispersive component is included in

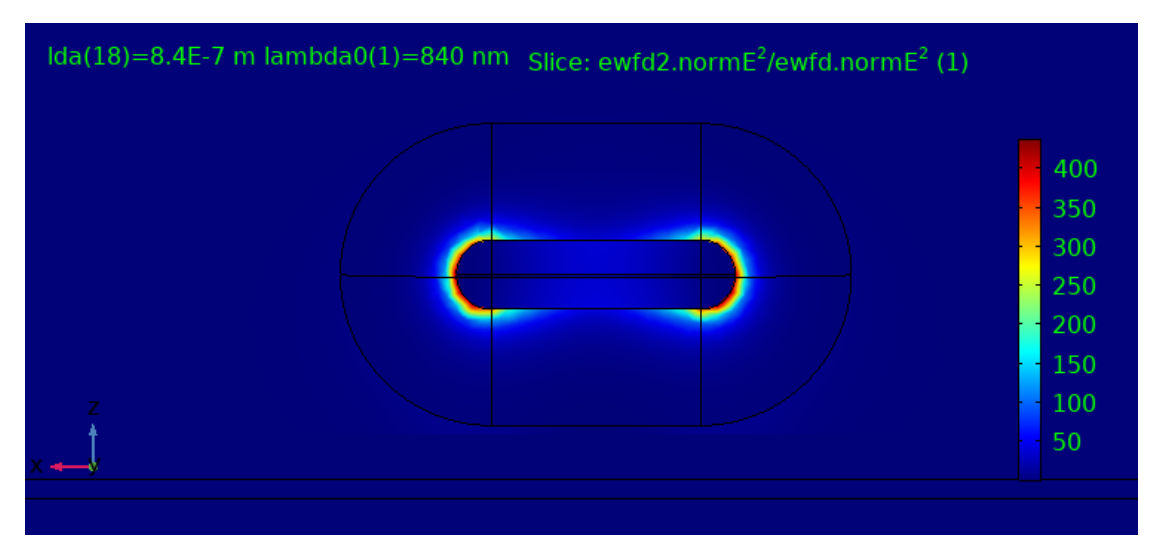


Figure 4.11: **FEM plasmonic hotspots.** FEM simulated field enhancement  $|\mathbf{E}|^2 / |\mathbf{E}_{inc}|^2$ for a light field polarized parallel to the long axis of the nanorod. The enhancement takes place in the region surrounding the hemispherical caps of the nanorod, of the order of the partical radial diameter [191, 193].

the modelling ( $\epsilon_{SiO_2} = 2.13$ ). The same is done for the SiN substrate, as its absorption in this spectral range is minimal compared to the nanorod ( $\epsilon_{SiN} = 4$ ). It follows the definition of the computational domain (Fig. 4.9).

Its sizes are chosen such that no interference phenomena occur within the vacuum regions, avoiding spurious results. To achieve this, the domain height is set equal to the maximum excitation wavelength used in the simulations ( $\lambda_{\text{max}} = 1 \, \mu \text{m}$ ). Perfectly matched layers (PML) are also defined at this stage, and used only in the second part of the simulation when the absorber is considered (see below, second step).

Next, the meshing process is conducted. Given the targeted physics, it is anticipated that strong electric fields will form around the tips of the nanorods due to the excitation of LSPR, leading to the emergence of hotspots [185, 191, 193]. These are shown in Fig. 4.11, around the hemispherical caps of the nanorod. Specifically, the resulting electric field enhancement  $|\mathbf{E}|^2/|\mathbf{E}_{inc}|^2$  arises for a light beam resonant with the central LSPR wavelength, and parallel to the long optical axis of the nanorod. Therefore, employing an adaptive mesh is crucial, enabling high-density element regions where high electric field gradients exist while maintaining lower density areas to minimize computational efforts [185], as illustrated in Fig. 4.9. For each subdomain, the maximum element size has been set to be  $\lambda_{\rm exc}/(6n_{\rm subdomain})$ , fulfilling the aforementioned physical requirements.

For the computation of the absorption cross-section (4.16), the Frequency Domain study is employed, where an electromagnetic field of given frequency, polarization and intensity  $I_0$  serves as the input for the system under investigation. As previously mentioned, the simulation consists of two distinct steps.

In the first step, the absorber is disregarded and only the interaction between the input field  $\mathbf{E}_{\mathrm{inc}}(\mathbf{r})$  and the substrate is computed. This step utilizes the full field formulation, yielding the resulting field as  $\mathbf{E}(\mathbf{r}) = \mathbf{E}_{\text{inc}}(\mathbf{r}) + \mathbf{E}_{\text{sca}}(\mathbf{r})$ . This represents the superposition of the input and scattered (transmitted and back-reflected) fields. This formulation offers the advantage to avoid the analytical derivation of the background electric field — at the basis of the background field formulation — and which is only used in the second step. To obtain the full field solution  $\mathbf{E}(\mathbf{r})$ , the simulation is configured with Port conditions. Given that all the nanorods are significantly smaller than the incident wavelengths, a plane wave is introduced as the input field on one of the ports (the upper face of the computational domain, not shown in Fig. 4.9), also allowing for specular reflection. The opposite (bottom face) absorbs the transmitted plane wave. Floquet conditions are applied to the side boundaries, imposing that the solution on one side of the geometry equals the solution on the opposite side, multiplied by a complex-valued phase factor. This effectively turns the model into a section of a geometry that extends infinitely in the xy-plane [184].

In the second step, the absorber is incorporated into the simulation, and PML boundaries are applied around the entire computational domain [194]. These are designed to avoid artificial reflections at the domain boundaries and function as an anisotropic absorbing layer. In this instance, the field solution of the previous step serves as the background field for the final computation.

The simulations implemented in this study have previously been validated for gold spherical nanoparticles, demonstrating excellent agreement with Mie theory.

# Comparative Analysis of Nanomechanical Photothermal Sensors

In this chapter, an experimental comparative analysis among the three resonator designs studied so far is carried out. For each design, the most important photothermal metrics are discussed in details for different resonator's in-plane dimensions. The experimental results focus on the fundamental out-of-plane flexural mode of low-stress SiN resonators, and are compared with the theoretical framework developed in Chapter 3. Firstly, the photothermal response to the probing laser is analyzed, which includes the discussion about the thermal time constant and relative power responsivity results. Secondly, the frequency stability is studied, followed by the evaluation of the photothermal sensitivity NEP. The measurement procedures for each metrics were described in Chapter 4.

All the results and related discussions are based on the second part of the study presented in Ref. [111].

# 5.1 Strings

The string resonators analyzed in the present work [111] are characterized for different lengths L, while keeping their width ( $w = 5 \mu m$ ) and thickness (h = 50 nm) fixed (the fabrication has been already introduced in Chapter 4). Fig. 5.1a shows the optical micrograph of a string resonator measured in this work. A tensile stress of  $\sigma_0 = 363$  MPa is extracted from the measurement of the fundamental resonance frequency for varying length L, as shown in Fig. 5.1b. The respective Q factors have also been measured for the theoretical calculations of the frequency stability, due to the Q dependence of the additive phase noise Eq. (3.45). The results are displayed in Fig. 5.1c, where the intrinsic

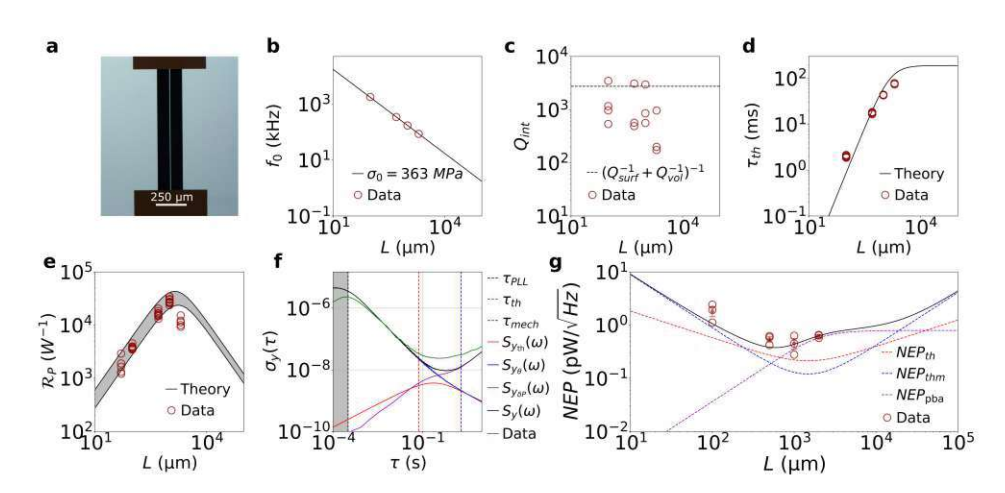


Figure 5.1: String design. a Optical micrograph of a string resonator. b Resonance frequency of 56 nm thick, 5  $\mu$ m wide string resonators of different lengths. From the measurements, a stress of 363 MPa is extracted. c Corresponding measured intrinsic Q factors. The dashed line represents the theoretical contribution from volume  $Q_{\rm vol}$ and surface losses  $Q_{\text{surf}}$  [119]. d Comparison between theoretical (black solid curve) and measured (dark red circles) thermal time constant  $\tau_{\rm th}$  for the same set of strings. e Comparison between theoretical (solid curves) and measured (dark red circles) relative power responsivity. The error bar indicates the uncertainties in  $\kappa$  (2.7 – 4 W/(m K)), E (200 – 300 GPa) [24]. For these structures,  $\alpha_{\rm th} = 1$  ppm/K has been measured following ref. [195]. f Allan deviation measured for a 2 mm long string (green solid curve), driven at the onset of nonlinearity  $z_{\rm r_c}$ , with low-pass filter bandwidth  $f_{\rm demod} = 2.5$  kHz, PLL bandwidth  $f_{\text{pll}} = 500 \text{ Hz}$  and optical input power  $P_0 = 6 \mu\text{W}$ . The comparison with the theoretical model is also shown (black solid curve), together with the single contributions (see main text). The grey region includes all the processes faster than the PID controller ( $\tau < \tau_{\rm th}$ ), which has a low-pass behavior, filtering all of them out. **g** Comparison between the theoretical (black solid curve) and experimentally extracted (black circles) NEP for strings. The theoretical curve is composed of two different noise contributions: temperature (red dashed curve) and thermomechanical (blue dashed curve) fluctuations-induced fractional frequency noise. For each string's length, three different resonators were characterized in terms of NEP. Average and standard mean error for the data points are also shown for each length.

 $Q_{\rm int}$  is plotted for all strings analyzed. As expected for this thickness, the mechanical dissipation is dominated by surface losses  $Q_{\rm surf}^{-1}$  (dashed black line — see Chapter 2) [119]. In the current setup, chip mounting constitutes another source of dissipation, as observed in the data scattering [115].

Next, the photothermal response has been characterized. The experimental thermal time constant shown in Fig. 5.1d (dark red circles) has been measured with an exponential fitting of the time signal, as discussed in Chapter 4. The results are also compared with the theoretical predictions (3.4) (solid curve), showing excellent agreement.

Fig. 5.1e displays the experimental relative power responsivity (dark red circles), and the corresponding comparison with the theoretical model (3.3) (black solid lines). The latter is calculated accounting for the uncertainty in material parameters  $\kappa$  and E. For these specific structures, the linear coefficient of thermal expansion  $\alpha_{\rm th}$  has been experimentally characterized following Ref. [195], and a value of  $\alpha_{\rm th} = 1$  ppm/K has been found. All data points fall within the uncertainty band except for L=2 mm. This discrepancy is consistent with the increased radiative losses caused by the high probing optical power  $(P_0 = 24 - 40 \ \mu\text{W})$ . Indeed, higher incident powers lead to elevated temperatures at the string's center, increasing the radiative heat flux  $\propto (T^4 - T_0^4)$  [167]. This results in a nonlinear reduction of  $\mathcal{R}_{P}$ , as well as a reduction in photothermal response time  $\tau_{th}$ , as the one observed in Fig. 5.1d.

It is worth noting at this point of the discussion that the power responsivity can be enhanced by reducing the resonator's thickness h (see Fig. 5.7) and width w. Indeed, thinner strings will improve the thermal insulation, due to a reduction in cross-sectional area, as well as in emissivity [196]. In contrast, narrower strings are not straightforwardly beneficial, since a smaller w will reduce the hosting area for particle and molecule spectroscopy, reducing the capture efficiency [197]. Hence, the width choice is critical for photothermal sensing.

The characterization continues with the resonators' frequency stability. Fig. 5.1f displays the Allan deviation (AD) for a string (green solid curve) [132]. All the acquired ADs have been compared with the theoretical model, accounting for the transfer functions (3.45) of the PLL and SSO tracking schemes [68, 131]. A good match is observed between measurements and theory (black solid curve) for integration times  $\tau < 0.1$  s, where the main noise source is additive in-phase (blue solid curve). For  $\tau > 0.1$  s, the data depart from the thermomechanical asymptote, with the presence of flicker frequency noise for  $0.1 \text{ s} < \tau < 1 \text{ s}$ , and frequency random walk for  $\tau > 1 \text{ s}$ , attributed to photothermal back-action (see below).

Fig. 5.1g presents the resulting NEP values, evaluated at  $\tau = \tau_{\rm th}$ . For each length, three different chips (black circles) have been analyzed. The results demonstrate strings' high photothermal sensitivity  $(0.28-2.5 \text{ pW/}\sqrt{\text{Hz}})$ . The plot also displays the theoretical NEP (black solid curve), closely aligning with the measurements. For clarity, the measurements' mean value and the standard error are plotted for each length, falling within the predicted values. The sensitivity is mainly limited by thermomechanical noise for almost all the lengths. The observed deviations are consistent with the photothermal back-action.

The positive correlation between noise level measured for long integration times ( $\tau > \tau_{\rm th}$ ) and power responsivity is evidence for photothermal backaction (3.54). To investigate this further, the laser relative intensity noise  $S_P(\omega,\lambda)$  has been characterized for all the optical powers employed in this study and  $S_{y_{\delta P}}(\omega, \lambda)$  evaluated. The intensity has been acquired for 1 minute with a silicon photodiode (Thorlabs GmbH S120C, 1  $\mu$ m response time) together with a digital power meter console (Thorlabs GmbH PM100D). The electrical signal is fed to the lock-in amplifier, with a filter bandwidth of  $f_{\rm L}=3$  kHz. The recorded intensity signal is then converted into frequency fluctuations, accounting

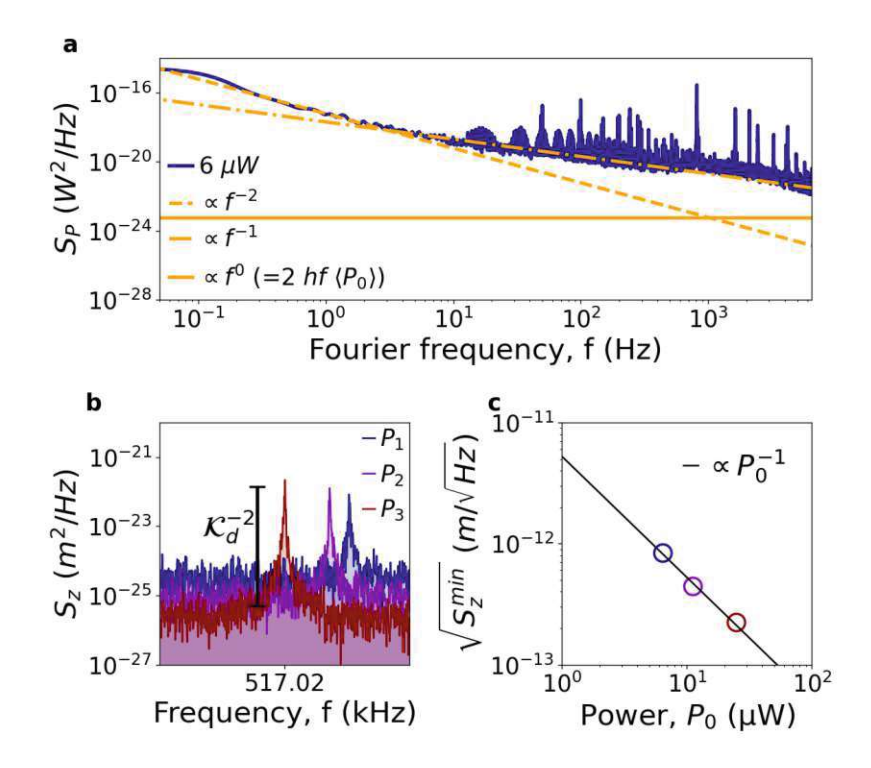


Figure 5.2: Laser power fluctuations. a Characterization of the intensity fluctuations for an average power  $\langle P_0 \rangle = 6 \,\mu\text{W}$  (smoothed with a Gaussian filter). The  $f^{-2}$ and  $f^{-1}$  noise contributions are shown (dashed orange and dashed-dotted orange lines, respectively). b Power spectral density of the thermomechanical noise for a drumhead resonator for different interferometer laser powers. c Corresponding measured displacement sensitivity  $\sqrt{S_z^{min}}$ , in units  $[m/\sqrt{Hz}]$ . It improves linearly with the laser power, with the effect of simultaneously introducing higher thermomechanical and laser power instability-induced frequency noise.

for the resonator's thermal response  $H_{\rm th}(\omega)$ , and the corresponding AD calculated (see Appendix A) [133]. The results are displayed in Fig. 5.1e with the purple solid curve, showing excellent agreement with the data for  $\tau > 0.1$  s. The observed flicker and random walk frequency noises are consistent with the intensity spectral distribution  $S_P(\omega,\lambda)$ , as clearly shown in Fig.5.2a, far above the ultimate laser shot noise limit  $S_{P,\text{sn}}(\lambda)$ .

Hence, photothermal back-action frequency noise imposes an upper limit on the probing power used for displacement transduction. On the one hand, high laser power improves the displacement sensitivity  $\sqrt{S_z^{min}}$  [m/ $\sqrt{\text{Hz}}$ ], as shown in Fig. 5.2b&c [198], reducing the detection coefficient  $\mathcal{K}_d$ . On the other hand, such a signal enhancement saturates at higher optical power due to the induced frequency noise [133], with any low-frequency intensity noise, such as mode hopping [199], directly impacting the resonator stability

[137].

Fig. 5.2c further shows that the displacement sensitivity is here inversely proportional to the optical power  $P_0$ , indicating that the laser noise has a classical (detector and technical noise) and not quantum shot noise origin [200]. Among the different approaches to mitigate laser classical noise, active intensity stabilization could offer a simple way to push the laser to its shot-noise limit [201]. A simpler approach to reduce the transducing laser-induced photothermal back-action is the use of another wavelength, for which SiN absorption is reduced (e.g. 1550 nm as shown in Ref. 68), along with employing a more stable lasing source.

#### 5.2Drumheads

Fig. 5.3a shows the optical micrograph of a drumhead resonator measured in this study. Fig. 5.3b&c show the resonance frequency corresponding to the drumheads characterized experimentally, and the respective intrinsic quality factors  $Q_{\rm int}$ . As for the strings, the main dissipation mechanisms are the surface and chip mounting losses. Regarding the thermal time constant of drumhead resonator, no experimental results are presented here, as the photothermal response time of SiN drumheads has been already experimentally studied elsewhere [86, 128].

Fig. 5.3d compares the theoretical predictions (3.3) (solid curves) with the experimental data (dark red circles) for the relative power responsivity. The uncertainty band, defined by the uncertainties in  $\kappa$ , E, and  $\alpha_{\rm th}$ , encompasses all the experimental points, indicating a strong agreement between theory and experiments.

Fig. 5.3e illustrates the AD for a drumhead. In detail, two regimes can be recognized for different integration times: i)  $\tau < 0.01$  s, the AD is limited by additive phase noise  $S_{y_{\theta}}(\omega)$ (blue solid curve); ii)  $\tau > 0.01$  s, the noise is dominated by photothermal backaction  $S_{y_{\delta P}}(\omega)$ . Notably, in the absence of photothermal back-action, temperature fluctuation frequency noise would dominate. This condition, where a mechanical resonator interacts with the environment at the single shot noise level, is of significant interest for micromechanical thermal detectors [40, 42, 68, 123, 202].

Fig. 5.3f presents the experimental NEP evaluated at  $\tau = \tau_{\rm th}$ , alongside the theoretical sensitivity (black solid curve), closely aligning to each other. The experimental results of 1-20 pW/Hz are one order of magnitude lower than previously characterized, electrodynamically transduced drumhead resonators [40], showing the outstanding performances of pristine SiN structures over integrated nanoelectromechanical systems (NEMS), where electrodes are an important part of the design [29, 40, 72]. The use of pure SiN for photothermal sensing applications is enabled by noninvasive transduction approaches, such as interferometry. In particular, pure optical transduction offers two key advantages: i) the absence of metal traces increases the thermal insulation, improving the responsivity (3.3); ii), the sensor is not limited by Johnson noise, which usually degrades the frequency stability (3.39) of a vast group of NEMS resonators [40]. Conversely, bare SiN drumheads are mainly affected by temperature fluctuations noise (dark red dashed curve), as shown for  $L > 50 \ \mu m$ . Moreover, as the resonator enters the radiation-limited regime, thermal



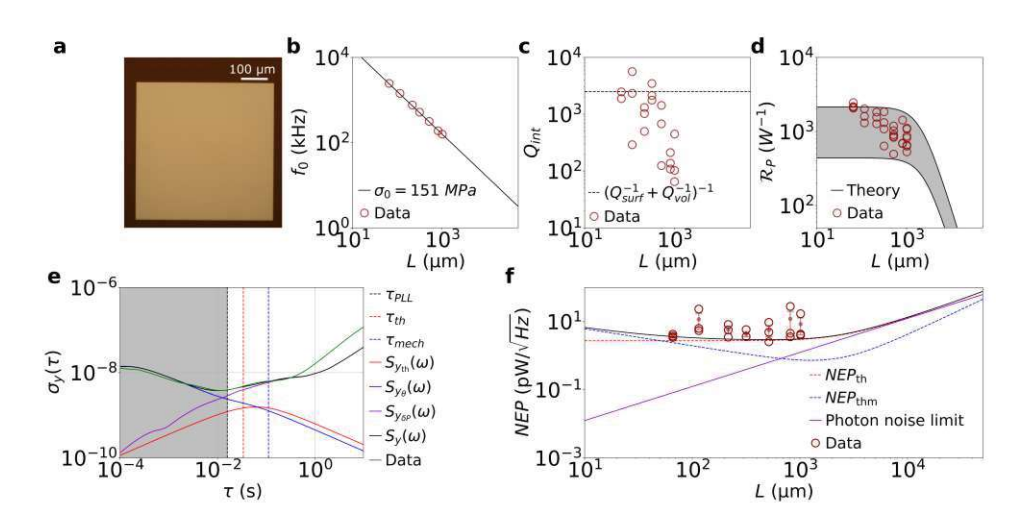


Figure 5.3: **Drumhead design.** a Optical micrograph of a drumhead resonator. b Resonance frequency for 50 nm thick square drumhead resonator of different side length. From the measurements, a stress of 150 MPa is extracted. c Corresponding measured intrinsic quality factors,  $Q_{\rm int}$ . d Comparison between theoretical (solid curves) and measured (dark red unfilled dots) relative power responsivity. The error bar indicates the uncertainties in  $\kappa$  (2.7 – 4 W/(m K)), E (200 – 300 GPa), and  $\alpha_{\rm th}(1-2.2~{\rm ppm/K})$ [24]. e Allan deviation measured for a 1 mm<sup>2</sup> square membrane (green solid curve), driven at the onset of nonlinearity  $z_{\rm r_c}$ , with low-pass filter bandwidth  $f_{\rm demod} = 2.5$  kHz, PLL bandwidth  $f_{\rm pll} = 10$  Hz and optical input power  $P_0 = 6 \mu W$ . The comparison with the theoretical model is also shown (black solid curve), together with the single contributions (see main text). f Comparison between the theoretical (black solid curve) and experimentally extracted (black unfilled dots) NEP for membranes. Temperature (red dashed curve) and thermomechanical (blue dashed curve) fluctuations-induced fractional frequency noise are also shown, together with the single photon noise limited NEP. For each membrane's length, three different resonators were characterized in terms of NEP.

photon shot noise becomes dominant (dark violet solid curve) [86, 123].

# 5.3 Trampolines

The experimental analysis has been carried out for trampoline resonators with central pads designed using a Bezier profile (see Fig. 5.4a) [39, 40, 72–74], a thickness h of 50 nm, a tethers' width w of 5  $\mu$ m, and tether's length  $L_{\rm t}$  ranging from 460 to 756  $\mu$ m. Fig. 5.4b presents the resonance frequency as a function of the central area  $L^2$ . For small areas  $(L^2 < 50^2 \ \mu \text{m}^2)$ ,  $\omega_0$  can be approximated with that of a string [60]. In the intermediate range ( $50^2 \ \mu \text{m}^2 < L^2 < 500^2 \ \mu \text{m}^2$ ) the effective mass  $m_{\text{eff}}$  grows faster  $(\propto L^2)$  than the tethers' effective stiffness  $k_{\rm eff}$  ( $\propto L^{\zeta}$ , with  $\zeta < 2$ ), leading to a reduction in resonance frequency  $\omega_0$ . For larger areas  $(L^2 > 500 \ \mu\text{m}^2) \ k_{\text{eff}}$  increases more rapidly

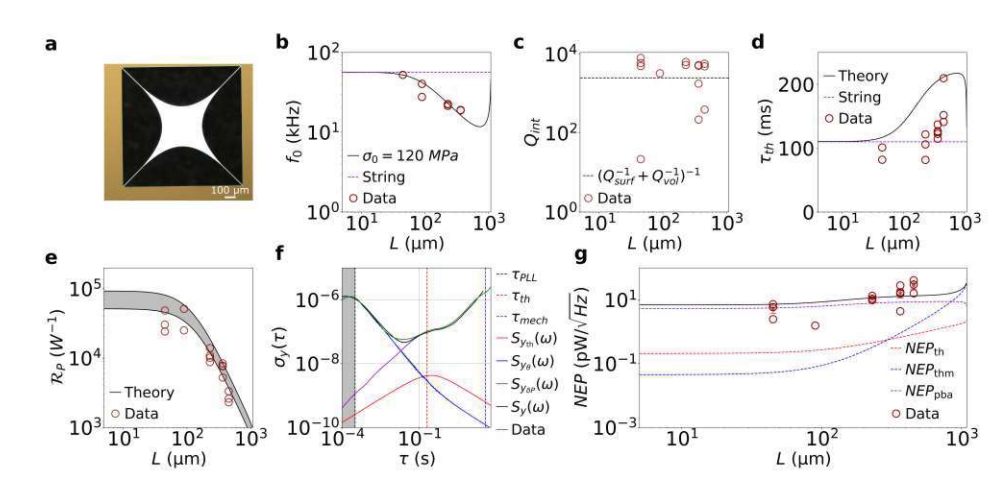


Figure 5.4: **Trampoline design.** a Optical micrograph of a trampoline resonator. b Resonance frequency for 50 nm thick trampoline resonators of different central area side lengths. The window side length is fixed to  $L_{\rm w} \approx 1$  mm, while the tether width is to  $w=5~\mu\mathrm{m}$ . From the measurements, a stress of 120 MPa is extracted. c Corresponding intrinsic  $Q_{\rm int}$ . d Comparison between theoretical (black solid curve) and experimental thermal time constant  $\tau_{th}$ . e Comparison between theoretical (solid curves) and measured (dark red circles) relative power responsivity. The error bar indicates the uncertainties in  $\kappa$  (2.7-4 W/(m K)), E (200-300 GPa), and  $\alpha_{\rm th}$  (1-2.2 ppm/K) [24]. **f** Allan deviation measured for a  $230^2 \mu m^2$  central area trampoline (green solid curve), driven at the onset of nonlinearities  $z_{\rm r_c}$ , with low-pass filter bandwidth  $f_{\rm demod} = 2.5$  kHz, PLL bandwidth  $f_{\rm pll} = 500 \; {\rm Hz}$  and optical input power  $P_0 = 11 \; \mu {\rm W}$ . The comparison with the theoretical model is also shown (black solid curve), together with the single contributions (see main text). g Comparison between the theoretical (black solid curve) and experimentally extracted (dark red circles) NEP. For each trampoline's central length, three different resonators were characterized in terms of NEP.

than  $m_{\rm eff}$  ( $\zeta > 2$ ), causing  $\omega_0$  to rise beyond the string value (see Chapter 2). Again, the main sources of mechanical dissipation are here the surface losses (see Fig. 5.4c).

Fig. 5.4d compares the theoretical thermal response time (black solid curve) with the experimental measurements (dark red circles). Discrepancies between the model and experimental data may stem from variations in material parameters, as supported by findings in the literature [87]. For instance, differing values of specific heat capacity and mass density from those used in the model would affect the heat capacitance C. while variations in emissivity and thermal conductivity would influence the thermal conductance G. Nevertheless, a positive correlation between  $\tau_{\rm th}$  and L is evident. This slow thermal response significantly impacts the frequency noise in the experimental setup employed here.

Fig. 5.4e shows the comparison between the theoretical and measured power responsivity, exhibiting excellent agreement. As for the other designs, the shaded band represents

uncertainties in  $\kappa$ , E, and  $\alpha_{\rm th}$ .

Fig. 5.4f shows the AD for a trampoline. Also here, two regimes can be recognized: an additive phase noise-limited region for integration times  $\tau < 0.02$  s, and a fully photothermal back-action frequency noise-dominated region for  $\tau > 0.02$  s. The sum of all the contributions (black solid curve) is a good match with the experimental data (green solid). It is worth noting that  $\tau_{\rm th}$  lies far in the photothermal back-action dominated region (red dashed vertical line), meaning that, during the time the resonator takes to reach a new thermal equilibrium, e.g. upon energy relaxation by a molecule, intensity fluctuations of the probing laser increase the frequency noise. Conversely, with a shotnoise limited laser, the temperature fluctuation frequency noise would dominate for

Fig. 5.4g displays the experimental sensitivities evaluated at  $\tau = \tau_{\rm th}$  (dark red circles) compared with the theoretical calculations (blue and red dashed curves). The plot reveals that the photothermal back-action (dark violet dashed curve) has degraded the sensitivity by one order of magnitude compared to the theoretical expectations. Moreover, this effect is much more pronounced for this design than for the others. Indeed, the slow thermal response time of trampolines makes them more sensitive to the laser relative intensity noise (3.55), where flicker and random walk noise are present, worsening the corresponding sensitivity

$$NEP_{\text{pba}} = \alpha_{\text{abs}} \sqrt{h_0 + 2\pi \tau_{\text{th}} h_{-1} + (2\pi \tau_{\text{th}})^2 h_{-2}}.$$
 (5.1)

However, the data follow the theoretical trend, with the sensitivity worsening for increasingly larger central areas  $L^2$ . As for the  $\tau_{\rm th}$  (Fig. 5.4d), the observed discrepancies between model and data may arise from variations in material parameters. Similar to drumheads, temperature fluctuations represent the ultimate theoretical limit of the photothermal sensitivity in the absence of photothermal back-action.

# 5.4Comparison

In summary, a theoretical comparison among the three resonator designs of comparable dimensions is illustrated in the radar chart shown in Fig. 5.5. The metrics used for this comparison are the NEP, the thermal time constant  $\tau_{\rm th}$ , and the sensing area  $A_{\rm sens}$ , each normalized to the best-performing value.

The string demonstrates the highest photothermal sensitivity due to its superior thermal insulation, albeit with the smallest sensing area. It presents an intermediate thermal response time compared to the other geometries. The fundamental frequency noise limit for this design is likely dominated by thermomechanical phase noise. These features make strings an excellent workhorse for nanomechanical photothermal spectroscopy [61]. Conversely, the drumhead exhibits the lowest sensitivity but offers the largest sensing area and the fastest thermal response. In particular, the combination of high speed and optimal sensitivity for this design makes drumheads ideal for applications requiring quick measurements. Furthermore, temperature fluctuations are expected to be the ultimate frequency noise limit.

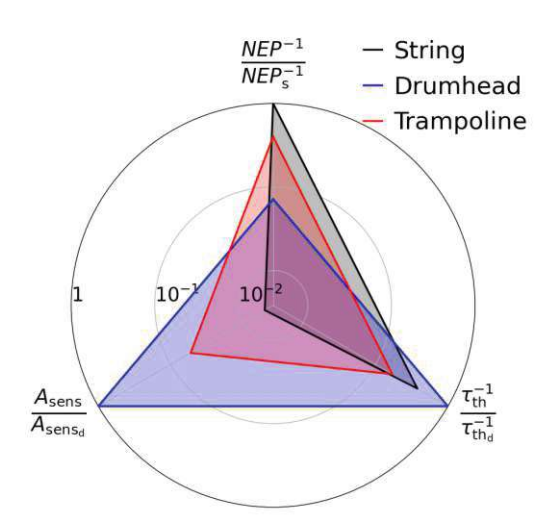


Figure 5.5: **Performance summary.** Radar chart of the nanomechanical photothermal performances. The chart accounts for the normalized NEP, thermal response time  $\tau_{\rm th}$ , and sensing area  $A_{\rm sens}$ . The highest value for each metric has been used for normalization, with the subscripts referring to the corresponding design (s, string; d, drumhead; t, trampoline). The string length, the membrane side length, and the trampoline window side length are all 1 mm long. The trampoline has a central area  $L^2 = 230^2 \ \mu \text{m}^2$ . All the structures are assumed to be 50 nm thick.

Drumheads are good candidates for scanning spectromicroscopy, as well as a promising platform for room-temperature IR/THz detection. In particular, in the case of singlephoton noise-limited detection, the large sensing area  $A_{\text{sens}}$  could enable drumheads to achieve the room-temperature specific detectivity limit  $D^* \equiv \sqrt{A_{sens}}/NEP \approx 1.8$ .  $10^{10} \text{ cm}\sqrt{\text{Hz}}/W$  [40, 86, 202]. It is important to note that in the regime limited by temperature fluctuations, where  $S_y(\omega) \approx S_{y_{\text{th}}}(\omega) \propto A_{\text{sens}}^{-1/2}$ , the NEP increases with the sensing area, following the relationship NEP $\propto \sqrt{A_{\rm sens}}$ 

$$NEP \approx NEP_{th} = \frac{\sqrt{4A_{sens}\epsilon_{rad}\sigma_{SB}k_{B}T_{0}^{5}}}{\alpha_{abs}(\lambda)},$$
(5.2)

reducing the sensitivity of the resonator. Consequently, in this regime the specific detectivity  $D^*$  for a single side coupled to the environment reaches its maximum and becomes independent of the area  $A_{\text{sens}}$ 

$$D^* = \frac{\sqrt{A_{\text{sens}}}}{\text{NEP}_{\text{th}}} = \sqrt{\frac{\alpha_{\text{abs}}^2(\lambda)}{16\epsilon_{\text{rad}}\sigma_{\text{SB}}k_{\text{B}}T_0^5}}.$$
 (5.3)

For a black-body,  $\alpha_{\rm abs}(\lambda) = \epsilon_{\rm rad} = 1$ , it results indeed  $D^* \approx 1.8 \cdot 10^{10} \, {\rm cm} \sqrt{{\rm Hz}}/{\rm W}$ . In the case where both sides are radiating to the environment, but only one is absorbing light,

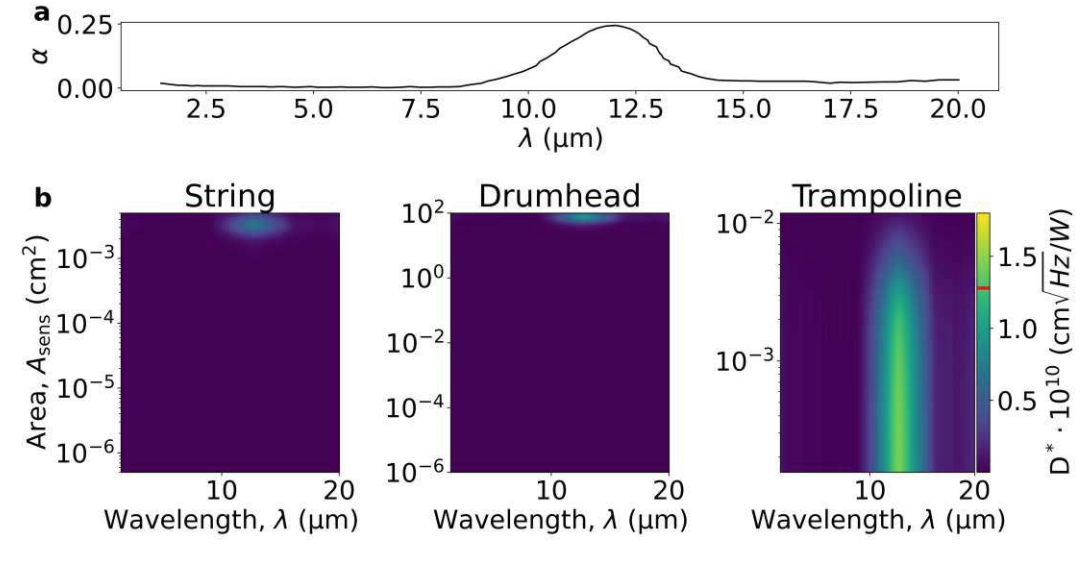


Figure 5.6: Specific detectivity. a Absorption spectrum  $\alpha_{abs}(\lambda)$  for 50 nm thick SiN thin film, taken from [128]. **b** Specific detectivity  $D^*$  as a function of the optical wavelength and the resonator's sensing area.

 $D^* \approx 1.28 \cdot 10^{10} \text{ cm} \sqrt{\text{Hz}}/\text{W} \text{ (red line in Fig. 5.6b)}.$ 

Hence, strings and drumheads operating in the temperature fluctuations limited regime will present similar performances in terms of specific detectivity. This is shown in Fig 5.6b, where theoretical calculations of  $D^*$  as a function of the optical wavelength and the resonator's sensing area are presented for 50 nm thick SiN resonators (with its absorption spectrum given in Fig. 5.6a). For all design, a region of maximum specific detectivity is found, which is independent of the sensing area (yellowish regions). However, drumheads and trampolines offer the advantage of less stringent optical requirements, needing less precise focusing of the incoming IR light. The drumheads have the further advantage of a reduced influence from photothermal back-action.

Trampolines present a compromise between the highly sensitive strings and the drumheads with a larger sensing area. As such, trampolines show intermediate values in terms of power sensitivity and sensing area. Their only drawback is the slow thermal response, which makes them more susceptible to photothermal back-action frequency noise than the other designs, as confirmed by experimental observations. Despite this, their high sensitivity makes this design a good candidate for photothermal spectroscopy. Moreover, temperature fluctuations are expected to be the ultimate limiting frequency noise, therefore making them a promising alternative for IR/THz thermal detection and a potential competitor for drumheads.

The present study has examined the three main resonator designs exploited so far in nanomechanical photothermal sensing. Various optimization methods are available to

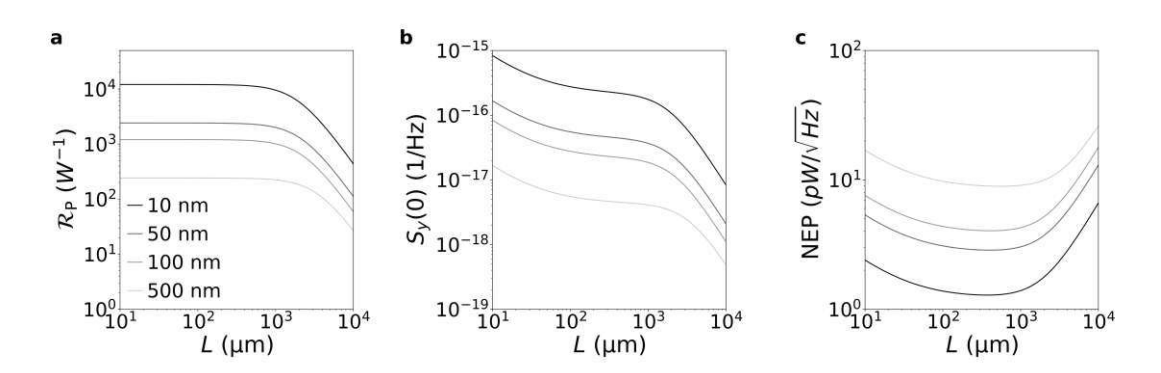


Figure 5.7: **Thickness optimization.** a Relative power responsivity of a drumhead resonator as a function of the side length L, for different thicknesses h. b Corresponding maximum fractional frequency noise  $S_y(0) = S_{y_{\theta}}(0) + S_{y_{\text{th}}}(0)$ . c Corresponding power sensitivity NEP.

improve the current state-of-the-art photothermal sensitivity. A straightforward approach is the reduction of the resonator's thickness h, as the NEP =  $S_y^{1/2}(\omega)/\mathcal{R}_P \propto \sqrt{h}$ . On the one hand, the power responsivity scales with the thickness as  $\mathcal{R}_{\rm P} \propto G^{-1} \propto h^{-1}$ , as shown in Fig. 5.7a, since both  $G_{\rm cond}$  and  $G_{\rm rad}$  are  $\propto h$  (for  $h = \mathcal{O}(10 \, \rm nm)$ ), the emissivity can be approximated as  $\epsilon_{\rm rad} \propto h$  [196] — this can be observed in Fig. 7.3a). On the other hand, the fractional frequency noise scales as  $S_y(\omega) \propto h^{-1}$ , as shown in Fig. 5.7b, since both the additive phase noise  $S_{y_{\theta}}(\omega) \propto \alpha_{\text{eff}} m_{\text{eff}}^{-2} \propto h^{-1}$  and the temperature fluctuations frequency noise  $S_{y_{\text{th}}}(\omega) \propto G^{-1} \propto h^{-1}$  scale in the same manner. Fig. 5.7c shows the resulting improvement in NEP for thinner resonators. Beyond thickness optimization, new designs routinely employed in other fields of nanomechanics, e.g., in optomechanics, could be explored for photothermal sensing. For instance, phononic crystal (PnC) engineering could be easily integrated within the sensor, enhancing the resonator thermal response, as well as its thermal properties. In particular, the use of PnC defect flexural modes for sensing applications would boost the power responsivity due to the increased overlap between the photothermally induced temperature field and the mechanical mode volume, as already shown [69]. Exploring resonance modes beyond flexural modes (0.1-100)MHz), which usually lie at higher frequencies (> 100 MHz), offers an intriguing direction for further research. High-frequency oscillations could improve the frequency stability of the resonator, especially against thermomechanical noise. This approach would likely involve materials other than SiN, such as lithium niobate, which additionally supports design integration capabilities [140] (see Chapter 4).

#### Conclusions 5.5

In summary, the comparative analysis conducted on three distinct resonator designs utilized in photothermal sensing — namely strings, drumheads, and trampolines — has



elucidated the relationship between the resonator's photothermal sensitivity and its mechanical and thermal properties. Across all scenarios, the theoretical framework has shown remarkable consistency with both experimental data and FEM simulations, demonstrating how the resonance frequency photothermal response is governed by the resultant mean temperature rise. Overall, strings emerge as the most sensitive design, followed by trampolines and drumheads. Conversely, drumheads exhibit the fastest thermal response, followed by strings and trampolines. The analysis has also highlighted the critical role of photothermal back-action, particularly its impact on the trampolines' frequency fluctuations, due to their slowest thermal response. Therefore, high photothermal sensitivity can be achieved with low-tensile-stressed, thin resonators, especially when combined with low-noise detection methods like interferometry. For optical readouts particularly, utilizing low-intensity lasers and low-absorption materials will be crucial in minimizing photothermal back-action.

The findings reported here not only clarify the relative performance of the resonator designs investigated but also establish a solid groundwork for the development of nextgeneration nanomechanical photothermal sensors. This study contributes to the advancement of nanomechanical sensing technology, offering valuable insights for researchers seeking to harness the full potential of photothermal sensing in diverse applications.

# Nanomechanical Photothermal NIR Spectromicroscopy

This chapter introduces the development of a room-temperature near-infrared (NIR) spectroscopy and polarization microscopy approach. The capabilities of nanomechanical photothermal sensing are leveraged here to study the plasmonic properties of individual nanorods. Specifically, square SiN nano-optomechanical drumhead resonators are employed to localize these nano-scale absorbers, enabling the spectral and polarizationresolved characterization of their longitudinal localized surface plasmon resonances (LPSR) in the NIR range. Additionally, the transverse localized surface plasmon resonances (TSPR) in the visible (VIS) spectrum are investigated, focusing on their polarization characteristics.

With the interplay of experiments, theory and FEM simulations, the study provides an in-depth analysis of the different dissipation mechanisms that contribute to plasmondriven absorption. The primary sources of electromagnetic dissipation are identified as bulk and surface electron scattering. The interaction between the nanoabsorber and the underlying mechanical resonator is further examined using FEM modeling to offer a more comprehensive understanding of this coupling.

Finally, the chapter compares nanomechanical photothermal spectroscopy with other state-of-the-art techniques for single-molecule and single-particle detection, highlighting the superior signal-to-noise ratio performance of nanomechanical sensors.

The whole results and discussions presented in this chapter are based on Ref. [31].



### 6.1Experimental Methods

#### Working Principle 6.1.1

The working principle of nanomechanical photothermal imaging and spectroscopy relies on the frequency shift of a mechanical resonator (the sensing core) caused by the photothermal heating of a molecule or particle absorbing at a specific excitation wavelength,  $\lambda_{\rm exc}$ . Imaging is achieved by scanning a probe laser across the resonator's surface. When the laser reaches the nano-absorber under study, the absorber takes in part of the electromagnetic energy, by an amount quantified by its extinction cross-section  $\sigma_{\text{ext}}(\lambda_{\text{exc}})$ . A portion of this energy is re-emitted via radiative processes, like scattering, by an amount given by the scattering cross-section  $\sigma_{\rm sca}(\lambda_{\rm exc})$ . The remaining part is converted into heat and quantified by the absorption cross-section  $\sigma_{abs}(\lambda_{exc})$ . This last contribution is responsible for the temperature rise in the nanomechanical resonator, leading to a measurable frequency shift.

For a Gaussian laser with input power  $P_0$  and beam waist  $w_0$ , impinging on an absorber, the power dissipated due to absorption is given by

$$P_{\rm abs} = \sigma_{\rm abs}(\lambda_{\rm exc})I_0, \tag{6.1}$$

where  $I_0$  denotes the input irradiance of the probing laser

$$I_0 = \frac{2P_0}{\pi w_0^2},\tag{6.2}$$

which is a function of the input power and beam waist.

Nanomechanical photothermal spectromicroscopy enables the direct measurement of the absorbed power  $P_{abs}$  via the resonator's frequency detuning

$$P_{\rm abs} = \frac{1}{\mathcal{R}_{\rm P}} \frac{\Delta f}{f_0},\tag{6.3}$$

with  $f_0$ ,  $\Delta f$ , and  $\mathcal{R}_P$  denoting the original mechanical resonance frequency, the experienced frequency shift, and the relative power responsivity of the nanomechanical resonator. Eq. (6.3) assumes full thermalization, which refers here to steady-state conditions: at each new position of the scanning laser, the resonance frequency is recorded for an interval of time longer than the slowest transient present in the measurement apparatus (here, the thermal response time of the nanomechanical resonator, see Eq. (6.4)).

In essence, by combining Eq. (6.1) and (6.3), the absorption cross-section  $\sigma_{abs}$  of the system under study can be determined for a given wavelength, thereby enabling spectroscopy characterization of individual absorbers.

#### 6.1.2 Platform for Spectroscopy and Microscopy

The complete experimental apparatus is illustrated in Fig. 6.1. The core sensor in this system is a 50 nm thick, square SiN nano-optomechanical drumhead resonator of 1 mm

84

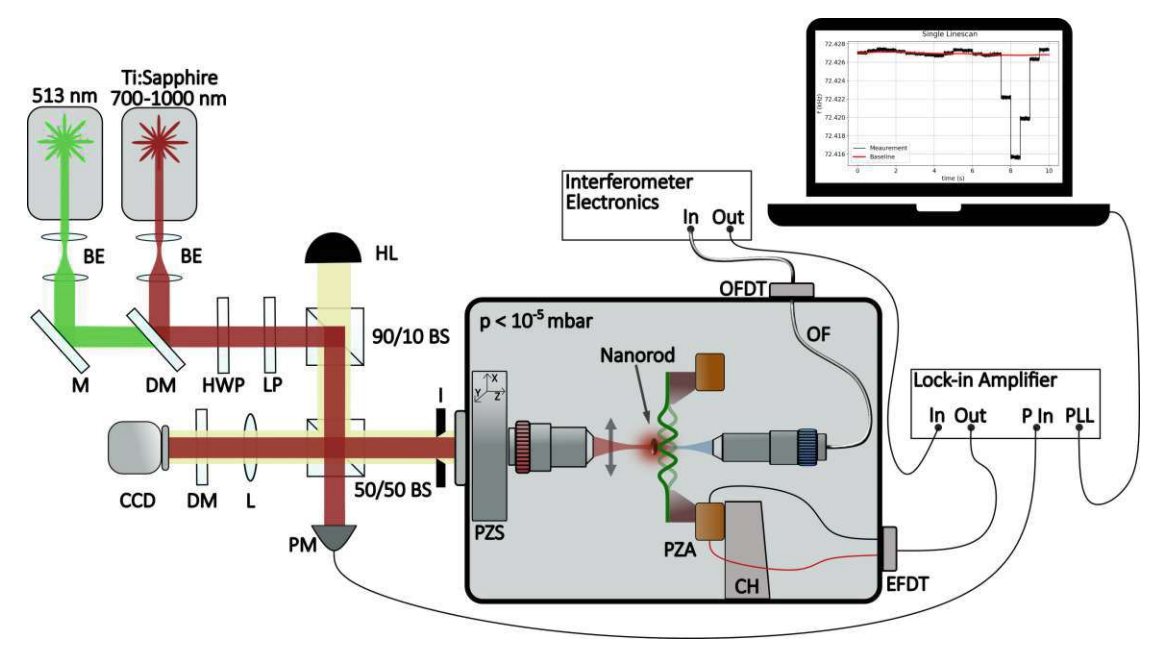


Figure 6.1: Schematics of the operating set-up. The drum resonator is actuated in vacuum  $(p < 10^{-5} \text{ mbar})$  by a piezoshaker (PZA). The displacement is read out by a Fabry-Perot interferometer (blue laser). The interference signal is processed and sent to the lock-in amplifier which records the frequency. The scanning lasers (red and green) are used to generate the photothermal signal by plasmonic excitation of the nanorod. BE: beam expander. BS: beam splitter. CCD: charge-coupled device camera. CH: Chip holder. DM: dichroic mirror. EFDT: Electrical feedthrough. I: iris. L: lens. LP: linear polarizer. HL: halogen lamp. HWP: half-waveplate. M: mirror. OF: Optical fiber. OFDT: Optical feedthrough. PM: Power Meter. PZS: Piezo-stage.

side length, operated at room temperature under high vacuum conditions ( $p < 10^{-5}$ mbar) to reduce both air damping and heat convection [113, 203]. The resonator is fabricated on a  $5 \times 5$  mm<sup>2</sup> chip, mounted on a metallic holder that connects to the vacuum chamber and acts as a thermal sink. A piezoelectric actuator (PA2JEW, Thorlabs, Inc.) is placed between the chip holder and the resonator to excite the mechanical motion. The displacement is detected with a Fabry-Perot interferometer (ISD3010, Attocube Systems AG) operating 1530 nm wavelength (see Chapter 4) [172, 173]. The optical signal is converted in an electrical one, which is subsequently demodulated and phase-locked using a lock-in amplifier (HF2LI, Zurich Instruments) for frequency tracking.

To photothermally probe the LSPR in the NIR and the TSPR in the VIS range of the individual nanorods, the setup is equipped with two continuous-wave (CW) laser sources: a 513 nm green laser (Toptica TopMode), and a Ti:Sapphire laser (M Square SolsTis) with tunable (single-mode) output wavelength in the 700 - 1000 nm range. The latter is pumped by a CW diode laser at 532 nm, delivering up to 8 W of power (Sprout, Lighthouse Photonics). The active lasing medium is a sapphire crystal rod doped with

titanium ions, inside a bow-tie ring cavity. The broad wavelength tuning is enabled by a combination of an optical cavity, a birefrigent filter, an etalon and a piezo-translating cavity mirror. The laser operates with an ultra-narrow linewidth of < 100 kHz, and the wavelength was precisely monitored by coupling a portion of the output light to a spectrometer (Torus Miniature Fiber Optic Spectrometer, Ocean Optics).

For these scanning laser probes, long working distance 50x objectives were used (N.A. = 0.42, M Plan Apo NIR, Mitutoyo in the NIR range; N.A. = 0.55, M Plan Apo, Mitutoyo in the VIS range). The laser's polarization angle is controlled by means of a linear polarizer in the optical beam path. A closed-loop piezoelectric nanopositioning stage (PiMars, Physikinstrumente) enables raster scanning of the sample. The power of the probe laser,  $P_0$ , is continuously monitored using a powermeter (S120C, Thorlabs, Inc.). Prior to each scan, the laser beam waist  $w_0$  is characterized at each wavelength with the knife-edge method [204, 205].

#### 6.1.3Sensor characterization

#### 6.1.3.1Relative Power Responsivity

The drumhead sensor used in this work exhibits a relative power responsivity of  $\mathcal{R}_{P} \approx$  $10^4 \mathrm{\ W^{-1}}$  for the fundemental flexural out-of-plane mode, consistent with the expected value based on the tensile stress of 30 MPa.  $\mathcal{R}_{P}$  has been determined by measuring the frequency detuning of the thermomechanical noise spectral peak of the resonator with the laser Doppler vibrometer (MSA-500, Polytec GmbH) of Setup II (see Chapter 4), operating at a wavelength of 633 nm, for varying input optical powers  $P_0$  (see Fig. 6.2). The extracted responsivity value is based on Fig. 6.2b via Eq. (4.15). For these drumheads, an absorption of  $\alpha(\lambda = 632.8 \text{ nm}) = 0.5\%$  has been measured, in agreement with previously reported results [91].

Interestingly, the sensor's power response to the red laser exhibits nonlinear behavior when the input power exceeds  $P_0 \geq 30 \mu W$ . This nonlinear effect can be attributed to increased thermal radiation emission from the SiN drum resonator, as the temperature T rises above the thermal bath temperature  $T_0$ , leading to higher heat dissipation  $\epsilon_{\rm rad}\sigma_{\rm SB}(T^4-T_0^4)$ . In the range of wavelengths explored with the Ti:Sapphire and interferometry laser in the experimental spectroscopy apparatus, 50 nm thick SiN absorbs less than at 632.8 nm. As a result, the threshold for the nonlinear response increases beyond the 30 µW value, allowing for full exploitation of the sensor's power responsivity. Additionally, operating at 1530 nm for displacement measurements helps reduce photothermal back-action effects [111].

#### Thermal Time Constant 6.1.3.2

The sensor's thermal time constant has been measured to be  $\tau_{\rm th} = 30$  ms with the 90/10method [37]. This value is orders of magnitude larger than the thermal time constant of the nanorod itself, being therefore the limit factor of the scanning speed (see inset of Fig. 6.3). In contrast, the thermal time constant for a nanorod under continuous-wave

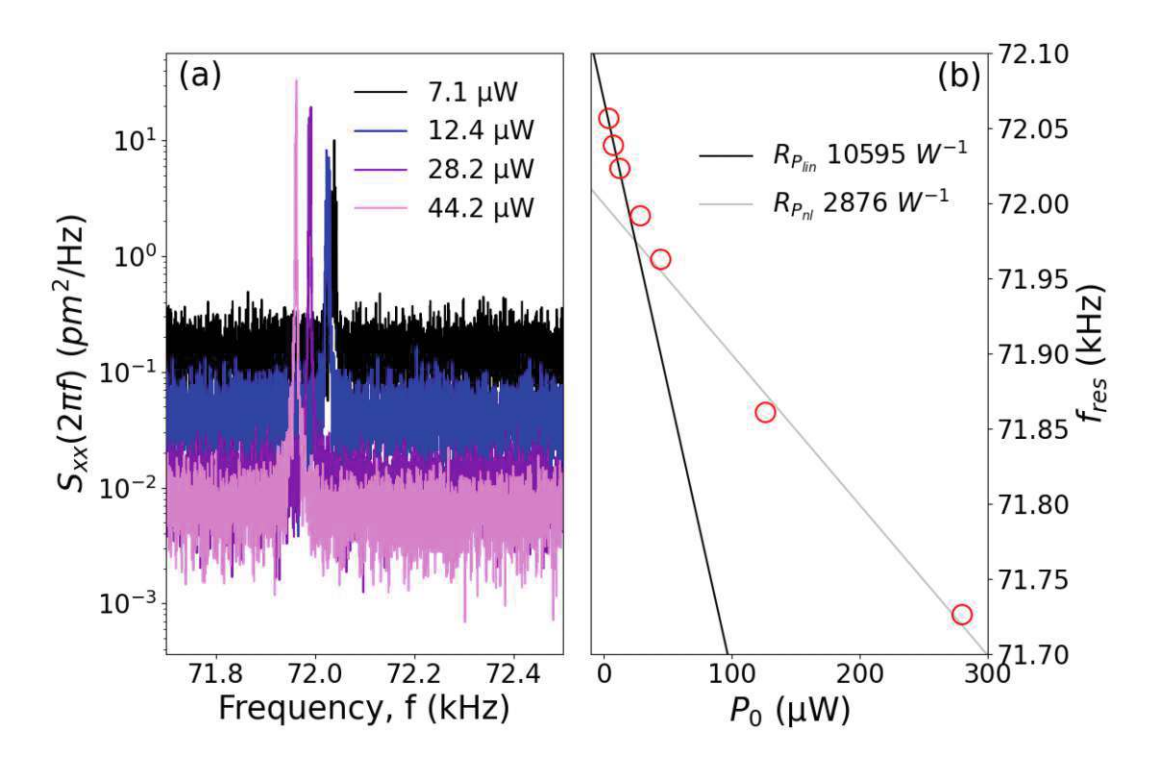


Figure 6.2: Sensor's power responsivity. a. Thermomechanical noise spectra for a drumhead resonator measured with a laser Doppler vibrometer, for four different probing laser power: 7.1, 12.4, 28.2, and 44.2 µW. b. Mechanical resonance frequencies as a function of the input laser power  $P_0$ .

(CW) illumination can be estimated as [206]

$$\tau_{\rm th,nr} \sim r_{\rm eff,nr}^2 \frac{\rho_{\rm nr} c_{\rm p,nr}}{3\kappa_{\rm SiO_2}},$$
(6.4)

where  $r_{\rm eff,nr}$  denotes the effective radius of a spherical nanoparticle of volume equal to the corresponding nanorods' volume,  $\rho_{\rm nr}$  is the mass density of gold (19300 kg/m<sup>3</sup>),  $c_{\rm p,nr}$ is gold specific heat capacity at constant pressure (129 J/(K Kg)), and  $\kappa_{SiO_2}$  thermal conductivity of the silica coating (1.3 W/(K m)).

For individual nanorods, thermal time constants on the order of  $\tau_{\rm th,nr} \simeq 40-60$  ps can be estimated from the volume extracted later in this work, making the nanorods nine orders of magnitude faster than the mechanical resonator to reach the steady-state (see Fig. 6.3).

#### Frequency Stability 6.1.3.3

The frequency stability of the resonator has been characterized in both frequency (Fig. 6.4, left) and time (Fig. 6.4, right). The fractional frequency noise PSD is white in frequency in

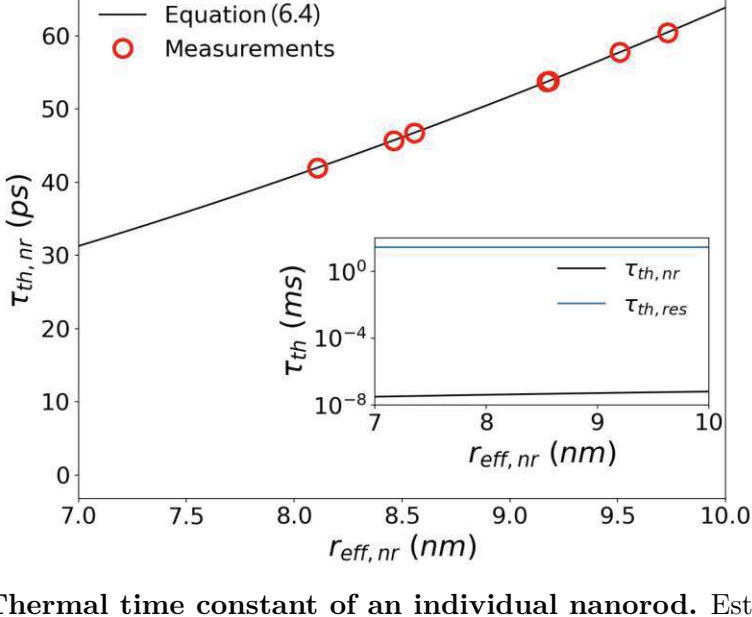


Figure 6.3: Thermal time constant of an individual nanorod. Estimated thermal time constant of the measured individual nanorods (red empty circles) as a function of the effective radius of a sphere of identical volume compared to the corresponding nanorod. (Inset) Comparison between the estimated nanorod thermal time constant and the measured mechanical resonator time constant.

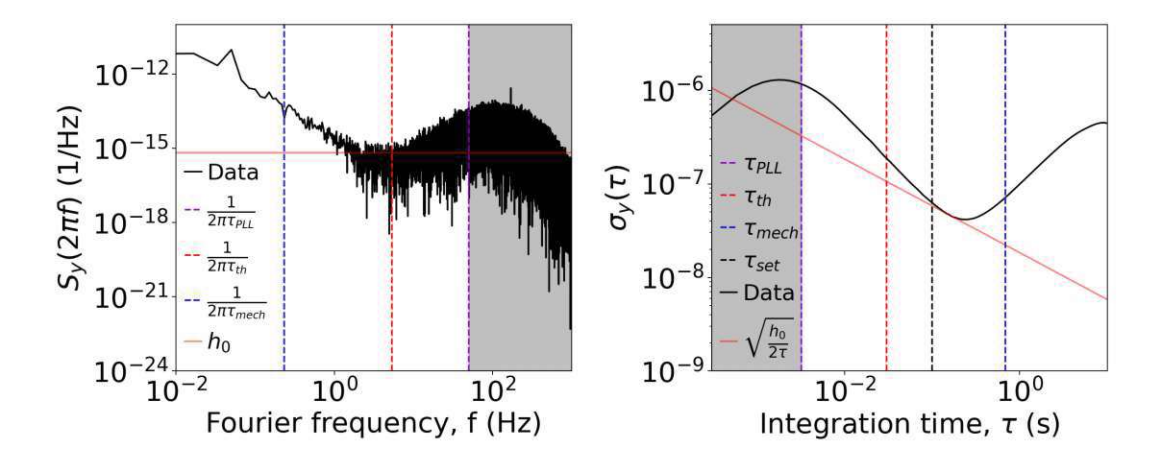


Figure 6.4: Resonator frequency stability. Fractional frequency fluctuations in the Fourier domain (left), where their PSD  $S_u(2\pi f)$  is displayed, and in the time domain (right), where the corresponding Allan deviation is shown.  $\tau_{\rm PLL}$ : PLL time constant.  $\tau_{\rm th}$ : thermal time constant.  $\tau_{\text{mech}}$ : mechanical time constant.  $\tau_{\text{set}}$ : scan settling time.  $h_0$ : white frequency PSD.

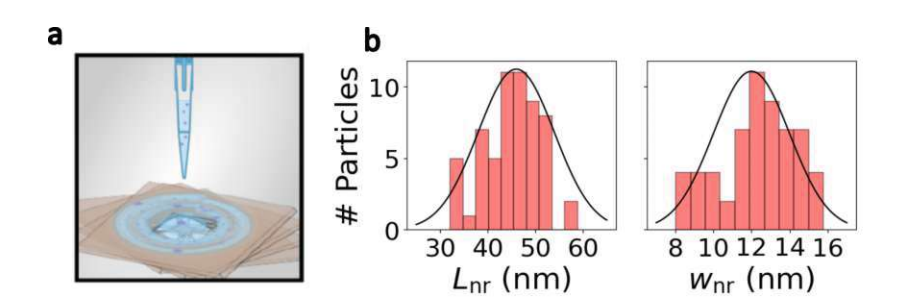


Figure 6.5: Nanorods sampling and size distribution. a. Schematics of the sampling method. Copyright 2023, adapted under a CC-BY 4.0 license, by R. West et al. [61]. b. Nanorod length  $L_{nr}$  (left) and radial diameter  $w_{nr}$  (right) distributions obtained from SEM images.

the range 1–10 Hz (light red horizontal line in Fig. 6.4), with a value  $h_0 \approx 6.76 \cdot 10^{-16} \, \mathrm{Hz}^{-1}$ . which corresponds to the region of minimum frequency fluctuations. This contribution is shown in the Allan deviation, appearing with the characteristic functional form of  $\tau^{-1/2}$  [179]. Based on this analysis, the settling time for the probing laser scans has been chosen to be  $\tau_{\rm set} = 0.1$  s, ensuring both minimal frequency fluctuations and full thermalization of the drumhead ( $\tau_{\rm set} > \tau_{\rm th}$ ).

As a result, the photothermal sensitivity of this specific mechanical resonator is NEP  $\approx$  $2.45 \text{ pW}/\sqrt{\text{Hz}}$ , well below the expected power  $P_{\text{abs}}$  dissipated by an individual nanorod, as it is shown in the following sections.

#### 6.1.4Sampling of the nanorods

Reactant-free silica coated gold nanorods with averaged length of 48 nm and width of 12 nm (silica thickness of 20 nm) dispersed in water (Sigma-Aldrich [207]) were first diluted in Micropur deionized water (18 M $\Omega$ cm, Milli-Q) with a ratio of 1:200 at room temperature. The solution was then spin-coated onto the resonators after being filtered through a 200 nm pore size PTFE membrane syringe filter (Acrodisc, Sigma-Aldrich) to prevent particle aggregation [166] (Fig. 6.5a).

Fig. 6.5b shows the size distributions of the nanorods' length  $L_{nr}$  (left) and radial width  $r_{nr}$  (right), acquired with SEM imaging (Hitachi SU8030). The experimental distributions align with the datasheet's stated mean values but exhibit a slightly larger dispersion [207].

## Photothermal Spectroscopy 6.2

#### 6.2.1Spectral Absorption Cross-section

The nanorods analyzed in this work had lengths  $L_{nr}$  ranging from approximately 38 to 52 nm, radial diameters  $w_{nr}$  between 9.5 and 13.5 nm, and silica coatings with thickness of 18 to 22 nm (Figure 6.5b and inset in Fig. 6.6). Their optical properties in the visible

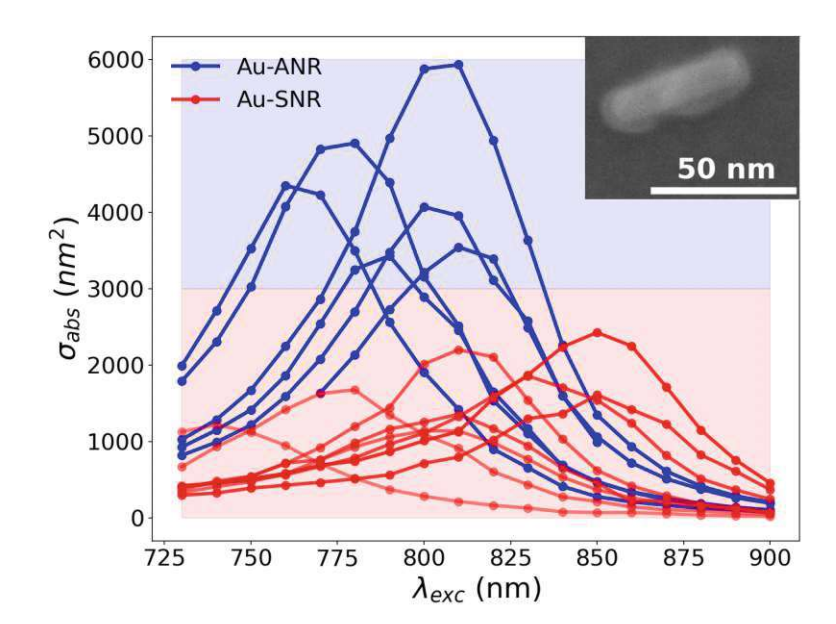


Figure 6.6: Nanomechanical photothermal absorption spectra of gold nanorods. Measured absorption cross-sections spectra of single nanorods (Au-SNR, red curves) and small nanorods aggregations (Au-ANR, blue curves), showing the heterogeneity characterizing these samples, mainly caused by the particle size dispersion. Inset: SEM micrograph of a single silica-coated gold nanorod landing on the drum resonator.

and near-infrared range are characterized by surface plasmon resonances (SPR) — the electromagnetic coupling between an impinging light and the collective motion of the conduction band electrons [54, 208]. Gold nanorods are particularly valuable for their large SPR amplitudes and broad spectral tunability [28, 59, 186–188, 191, 209–216]. When a coating, such as silica, is present, its thickness influences how much the SPR features are affected by the environment. In fact, the plasmonic response is sensitive to its surroundings on the spatial range of the order of the nanorod diameter, the region where the field enhancement takes place [191, 193, 217, 218] (see Fig. 4.11). In this study, the silica coating of roughly 20 nm is thin enough for the SPR to remain sensitive to both the coating and the surrounding medium, albeit at a reduced magnitude [218]. It is also worth noting that the overall extinction cross-section of the nanorods examined here is dominated by absorption,  $\sigma_{\rm ext} = \sigma_{\rm abs} + \sigma_{\rm sca} \approx \sigma_{\rm abs}$ .

The experimental absorption spectra measured with nanomechanical photothermal sensing are shown in Fig. 6.6. Each spectrum was measured with the polarization of the probe beam (here Ti:Sapphire laser) adjusted to maximize the absorption within the wavelength range of 700 - 900 nm. Specifically, these nanorods present maximum absorption in the range of ca. 790 - 830 nm, as measured by the ensemble averaged reference measurement [207] (see also the black curve in Fig. 6.13), due to LSPR excitation

occurring for a laser polarization parallel to the nanorods' long axis.

Absorption signals were recorded for both individual silica-coated gold nanorods (Au-SNR, shown by red curves in Fig. 6.6) and aggregates of a few nanorods (Au-ANR, shown by blue curves). These two cases can be distinguished by their absorption strength at plasmonic resonance  $\sigma_{abs}(\lambda_{LSPR})$  and their resonance peak position  $\lambda_{LSPR}$ . The Au-SNR and Au-ANR subsets show variations in both absorption strength and peak positions. with heterogeneity within the Au-SNR subset largely attributable to size dispersion in the sample, as shown by the SEM data in Fig. 6.5b.

As highlighted in Fig. 6.6, a threshold of  $\sigma_{\rm abs} = 3 \cdot 10^3 \, \rm nm^2$  is used to differentiate individual nanorods from aggregates. The rationale behind this threshold will be explained later. but for now, the focus will remain on the individual nano-absorbers.

#### 6.2.1.1**Individual Nanorods**

The absorption spectra of individual nanorods measured in this work exhibit a Lorentzianlike spectral distribution. To gain insight into their plasmonic-driven optical properties and the relation with the sample size dispersion, their LSPR spectra have been fitted with a quasi-Lorentzian function

$$\sigma_{\rm abs}(\omega) = \Theta \frac{\frac{\Gamma}{2\pi}}{(\omega - \omega_{\rm LSPR})^2 + (\frac{\Gamma}{2})^2},\tag{6.5}$$

which depends on three parameters: the longitudinal surface plasmon resonance energy  $\omega_{\rm LSPR} = \hbar c / \lambda_{\rm LSPR}$  (eV); the overall plasmonic resonance linewidth  $\Gamma$  (eV); the integrated oscillator strength  $\Theta$  (nm<sup>2</sup>) [188, 215]. These are extracted for each nanorod by fitting the measurements with Eq. (6.5), as exemplified with Fig. 6.7.

To properly correlate the extracted parameters to the nanorods' dimensions, their aspect ratio  $AR = L_{\rm nr}/w_{\rm nr}$  and volume  $V_{\rm nr}$  must be determined for each nano-absorber. This can be done exploiting the strong dependence of  $\omega_{LSPR}$  on the aspect ratio, and of  $\Theta$  on the volume, respectively. On the basis of these correlations, it is possible to ultimately quantify the different plasmonic damping mechanisms contributing to the linewidth  $\Gamma$  for each nanoparticle.

Given the complexity of the relationship between  $\omega_{\rm LSPR}$  and  $\Theta$  and the nanorods' dimensions, a two-steps procedure has been employed to extract the corresponding sizes [188, 215]. In the first step, a series of absorption spectra for different nanorod radial diameters  $w_{\rm nr}$  (8 – 16 nm) and aspect ratios AR (2.5 – 5) are calculated using FEM simulations and the T-matrix method (to cross-check the computations) [219]. The latter has been refined by incorporating the effective medium approximation to account for the refractive index of the environment surrounding the nanorod, including the silica coating and surrounding medium [218]. Fig. 6.8 shows how the effective dielectric function  $\epsilon_{\rm EMA}$ varies as a function of the silica thickness  $t_{\rm SiO_2}$ . This trend has been measured for different nanorods in Ref. [218], showing a dependence of the type

$$\epsilon_{\rm EMA} = \epsilon_{\rm c} + (\epsilon_{\rm m} - \epsilon_{\rm c})e^{-bt_{\rm SiO_2}},$$
(6.6)

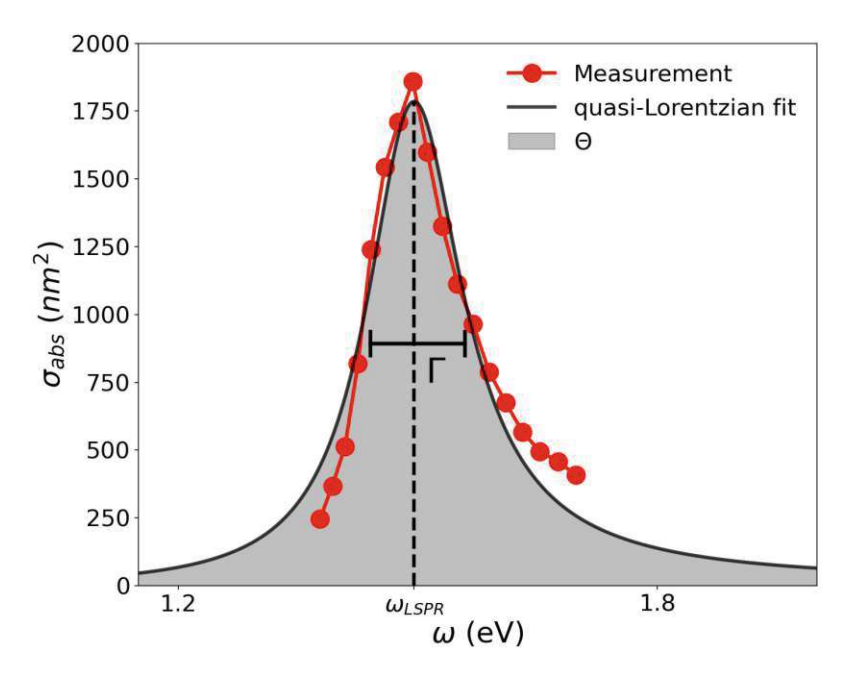


Figure 6.7: Quasi-Lorentzian spectrum of an individual nanorod. Example of fitting of the measured absorption cross-section with a quasi-Lorentzian function (6.5).

with  $\epsilon_{\mathbf{c}} = \epsilon_{\mathrm{SiO}_2}$ , and  $\epsilon_{\mathrm{m}} = \epsilon_{\mathrm{air}}$  denoting the coating and surrounding medium dielectric function, respectively. b is a fitting parameter, which has been found to be  $b = 0.126 \pm 0.004 \text{ nm}^{-1}$  [218]. It is worth noting that the presence of a 20 nm thick coating reduces the sensitivity of the plasmon resonance to both the coating itself and the surrounding medium, effectively screening the plasmons from the environment.

The theoretical spectra computed in the way are then fitted with Eq. (6.5) to extract  $\omega_{\rm LSPR}$  and  $\Theta$ .

In the second step, a calibration surface plot of the nanorod volume is constructed from the simulation results, with the resonance energy  $\omega_{\rm LSPR}$  and integrated oscillator strength  $\Theta$  treated as independent variables. The calibration surface is shown in Fig. 6.9. As expected, the resonance energy shifts to lower frequencies with increasing aspect ratio AR, and also slightly red-shifts with increasing radial diameter  $w_{\rm nr}$ . In contrast, the oscillator strength is highly sensitive to volume and shows a minor dependence on AR. It is important to stress out here that  $\Theta$  is unaffected by the spectral broadening [220], meaning it is independent of the plasmonic damping mechanisms. This independence is crucial for the reliability of the approach used here.

The red crosses in Fig. 6.9 represent the measured individual nanorods, with their coordinates determined by the fitting procedure outlined in Fig. 6.7. For each nano-absorber, both the AR and volume are extracted, allowing for an analysis of the electromagnetic dissipative mechanisms.

Various optical scattering phenomena of conduction band electrons can contribute to the



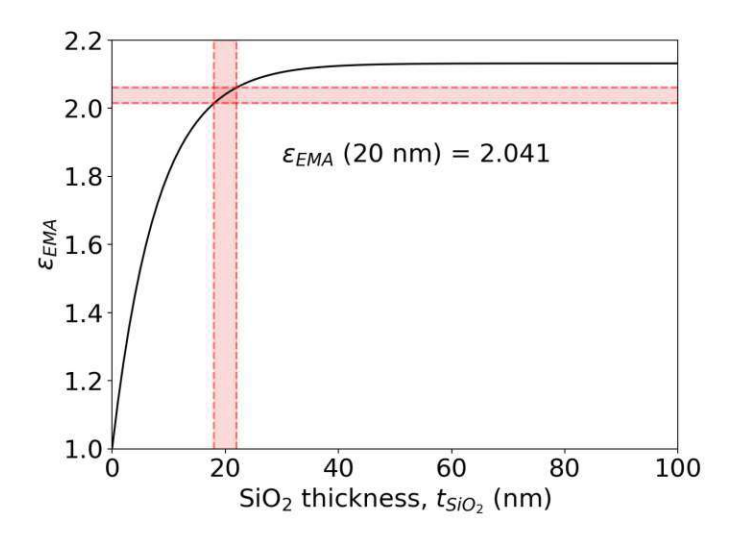


Figure 6.8: Effective medium approximation for the silica coating the gold nanorod. The effective dielectric function varies with the silica thickness in an exponential way. For a silica thickness of  $t_{\mathrm{SiO}_2}=20$  nm, the corresponding effective dielectric constant is  $\epsilon_{\rm EMA} = 2.041$ .

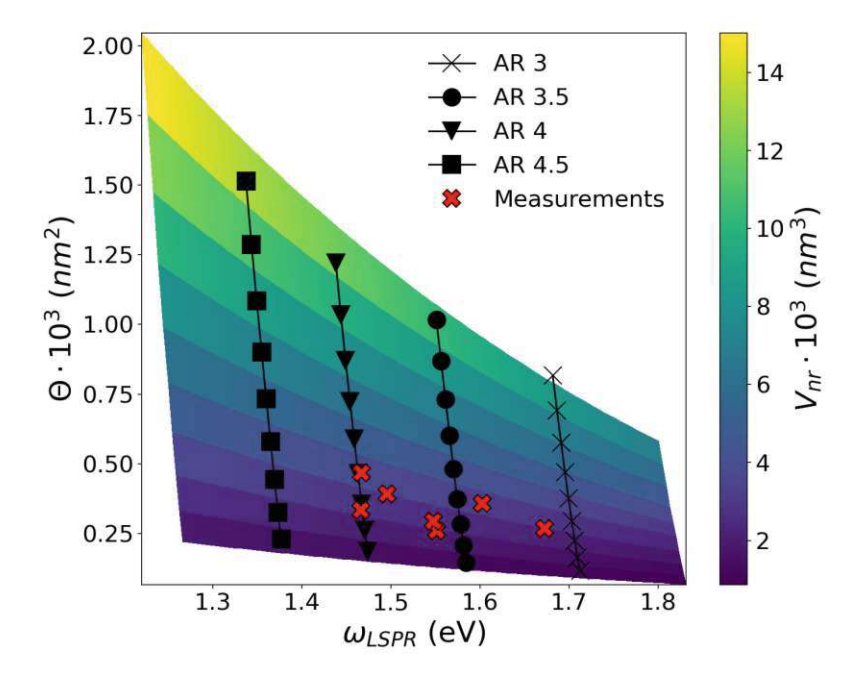


Figure 6.9: Calibration surface plot of the nanorod volume, constructed according to the procedure developed in References [188, 215].

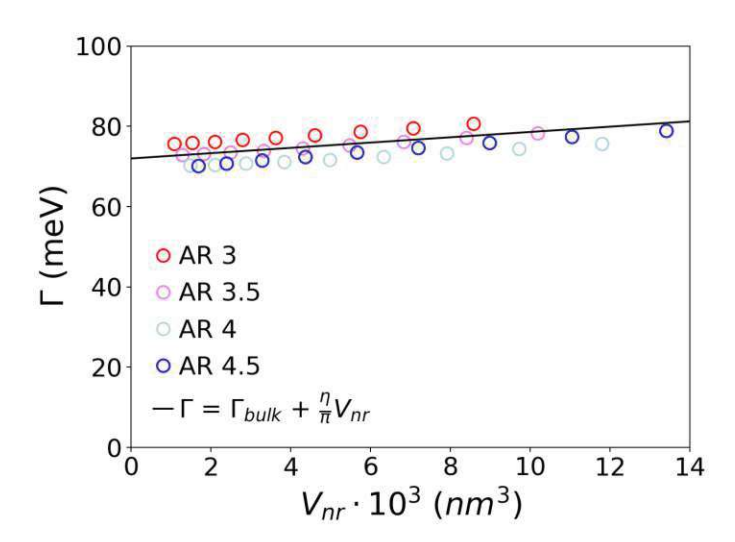


Figure 6.10: Nanorods modelled LSPR linewidths. Simulated LSPR linewidths  $\Gamma$ for different aspect ratios AR as a function of the nanorods volume  $V_{\rm nr}$ . For these results, only the bulk dielectric function for gold [190] was used. The black curve indicates a linear fitting, whose gradient value is  $\eta/\pi = 6.6 \cdot 10^{-7} \text{ eV} \cdot \text{nm}^{-3}$ .

broadening  $\Gamma$  of LSPR resonances in metallic nanorods [188, 215]. The first contribution is electron bulk scattering ( $\Gamma_{\text{bulk}}$ ), which arises from electron-electron, electron-phonon, and electron-defect interaction. This contribution is always present and constant across the spectral range considered here, with  $\Gamma_{\text{bulk}} = 73 \text{ meV}$  for gold.

Part of the absorbed electromagnetic energy can be also re-emitted to the surrounding environment via radiative dissipation ( $\Gamma_{\rm rad}$ ). This mechanism is directly proportional to the absorber's volume  $\Gamma_{\rm rad} = \eta/\pi V_{\rm nr} m$ , where  $\eta/\pi = 6.6 \cdot 10^{-7} \text{ eV} \cdot \text{nm}^{-3}$ . This proportionality constant was derived from fitting FEM-simulated absorption spectra for different AR and volume values, as shown in Fig. 6.10, and is consistent with previously reported values [186, 221].

The experimental LSPR linewidths measured via nanomechanical photothermal sensing are shown in Fig. 6.11a (red crosses), varying in the range 130 – 150 meV. For comparison, the contribution  $\Gamma_{\text{bulk}} + \Gamma_{\text{rad}}$  is also displayed (black curve). A significant discrepancy between the experimental linewidths and these two contributions is evident. Notably, radiative damping is negligible in this case, given the small volume of the nanorods studied, in contrast to what has been observed in spherical gold nanoparticles [221]. To explain these experimental results, quantum confinement effects must be taken into account, i.e., electron surface scattering ( $\Gamma_{\text{surf}}$ ) [186, 188, 215, 222]. Its contribution is evaluated by subtracting the previous electromagnetic losses from the experimental values, yielding  $\Gamma_{\text{surf}} = \Gamma - (\Gamma_{\text{bulk}} + \Gamma_{\text{rad}})$ . The results are presented in Fig. 6.11b. As expected, since quantum confinement effects increase with the surface-to-volume ratio, the surface scattering contribution becomes more pronounced as the nanorod size decreases.

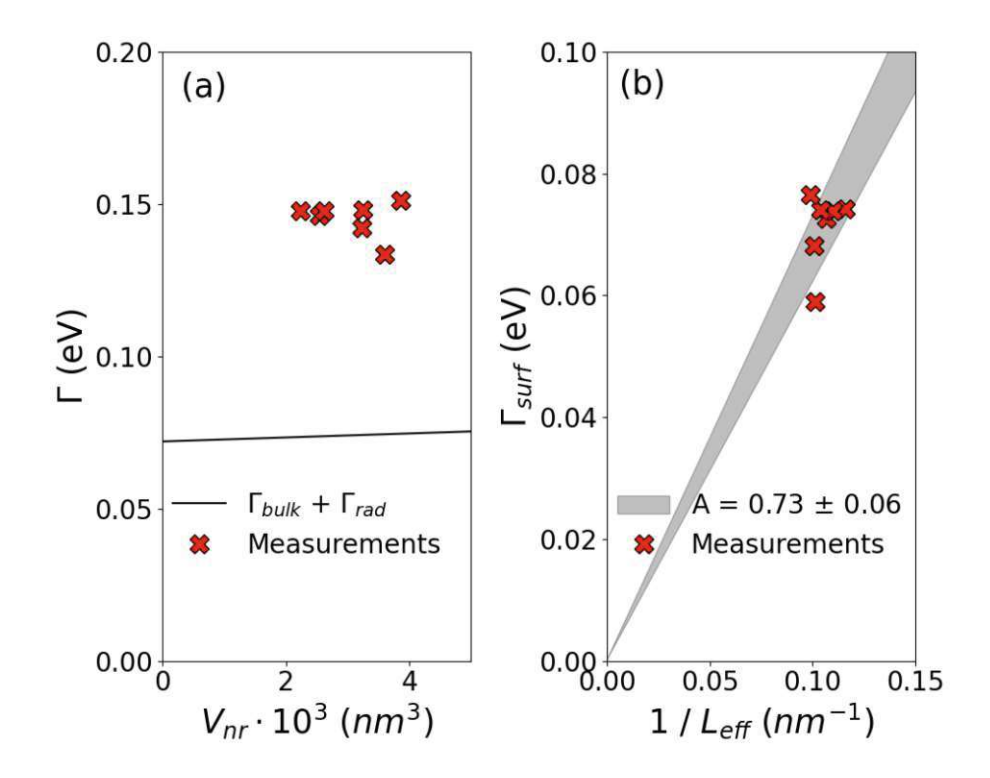


Figure 6.11: Plasmonic damping in individual nanorods. a. Measured LSPR linewidth  $\Gamma$  (red crosses) as a function of the nanorod volume  $V_{nr}$ . For comparison, the contribution  $\Gamma_{bulk} + \Gamma_{rad}$  is plotted (black curve). **b.** Extracted electron surface scattering  $\Gamma_{surf} = \Gamma - (\Gamma_{bulk} + \Gamma_{surf})$  for the measured individual nanorods (red crosses) as s function of the inverse effective length  $1/L_{eff}$ , compared with the theoretical model  $\Gamma_{surf} = v_F A/L_{eff}$ . A value of  $A = 0.73 \pm 0.06$  is found for these nanorods.

In a first approximation, surface scattering can be expressed as  $\Gamma_{\text{surf}} = v_{\text{F}} A / L_{\text{eff}}$ , where  $v_{\rm F} = 1.4 \cdot 10^6$  m/s is the Fermi velocity; A is an experimentally determined proportionality constant, and  $L_{\text{eff}} = 4V_{\text{nr}}/S_{\text{nr}}$  denotes an effective electron path length, which expresses the inverse of the surface-to-volume ratio (introduced in Chapter 4). From the measurements, A was found to be  $0.73 \pm 0.06$ , consistent with previously reported values [188, 215]. This corroborates the evidence that electron surface scattering is a major source of damping in this context, which, indeed, grows with the surface-to-volume ratio

After identification and characterization of the damping mechanisms responsible for the broadening of the LSPR resonances, the approach to distinguish between individual nanorods and aggregates is presented.

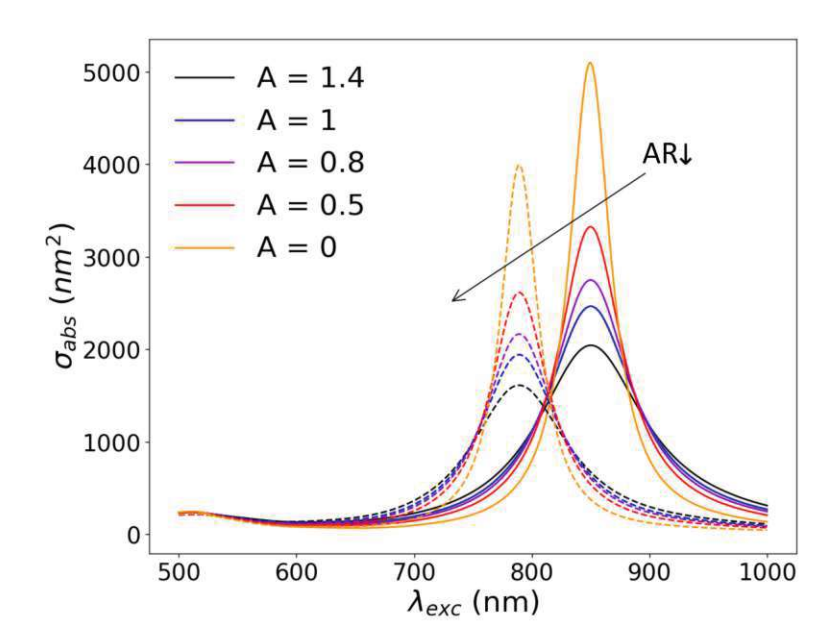


Figure 6.12: Electron surface scattering in individual nanorods. LSPR resonaont absorption spectra calculated with the T-matrix method together with effective medium approximation (EMA), for different value of the parameter A, for two different aspect ratios AR = 3.5 (dashed lines), and 4 (solid lines).

#### 6.2.1.2**Aggregates of Nanorods**

To differentiate between individual and aggregated nanorods based on their plasmonic response, the dependence of the peak absorption amplitude  $\sigma_{abs}$  on the plasmon resonance energy  $\omega_{\rm LSPR}$  and the electron surface scattering  $\Gamma_{\rm surf}$  has been explored.

Using the T-matrix method with an effective medium approximation for the silica coating (as shown in Fig. 6.8), absorption spectra for nanorods with different aspect ratios (AR = 3.5 and 4) and varying electron surface scattering coefficient A were calculated, as shown in Fig. 6.12. As already observed in Fig. 6.9, the resonance energy decreases with the aspect ratio AR, shifting the plasmonic resonance peak towards longer wavelengths  $\lambda_{\rm LSPR}$ . In turn, the absorption cross-section peak  $\sigma_{\rm abs}(\lambda_{\rm LSPR})$  increases as the overlap between the plasmon-assisted resonance and interband electronic transitions diminishes for fixed values of electron surface scattering [214].

For AR = 4 — the highest measured value measured displayed in Fig. 6.9) — the absorption peak reduces considerably as the parameter A is increased. In particular, for A = 0.73, the absorption peak  $\sigma_{\rm abs}(\lambda_{\rm LSPR} \approx 850 \text{ nm}) \approx 3 \cdot 10^3 \text{ nm}^2$  is calculated. Thus, this value sets the threshold for distinguishing individual nanorods from aggregated ones. The strength of single-molecule and particle methods is their ability to unravel the heterogeneity in size, shape, and composition of the system under study. The nanomechanical

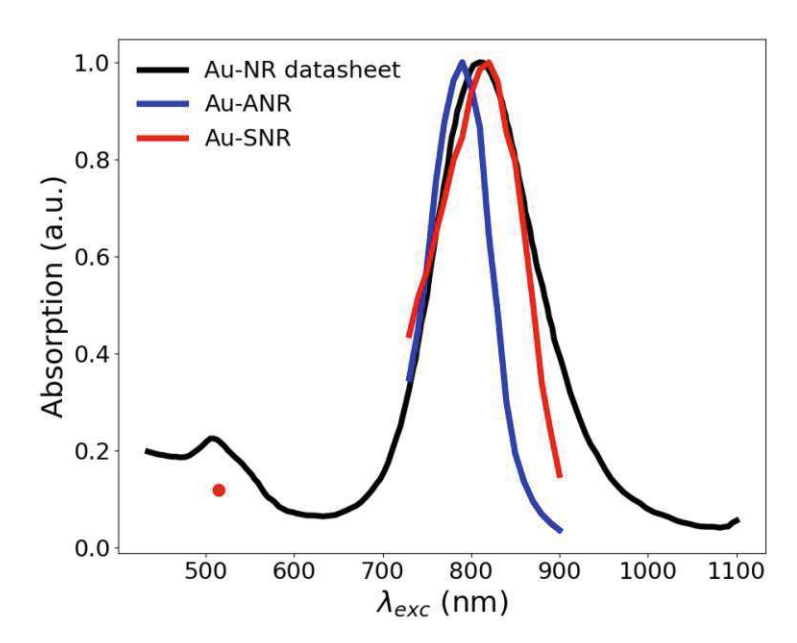


Figure 6.13: Nanorods ensemble spectrum. Red curve and dot: renormalized sum of the measured absorption cross-section spectra of single nanorods (fig. 6.6); blue curve: renormalized sum of the absorption cross-sections of the nanorods aggregation; black curve: ensemble average absorption spectrum given by the datasheet.

photothermal measurements presented in Fig. 6.6 are a demonstration.

The experiments are compared with the ensemble averaged reference spectrum of the nanorods (black curve) in Fig. 6.13. For each subset (single and aggregated nanorods), the individual absorption spectra are summed and normalized. For single nanorods, the renormalized response (red curve) closely aligns with the reference spectrum, recovering a typical ensemble measurement [187, 210]. The central wavelength has been extracted to be  $\lambda_{LSPR} = 809$  nm, in agreement with the nominal value of 808 nm [207].

Conversely, the ensemble Au-ANR (blue curve) shows a central wavelength of 786 nm, corresponding to a blue-shift of 2.8% from the Au-SNR one. A similar blue-shift has been reported by Jain et al. [223]. The study has shown that this shift occurs in nanorod aggregations of two or more units assembled in a side-by-side orientation, for a polarization parallel to their long axis. The corresponding shift strength depends on various parameters, such as the interdistance between the nanorods involved, their aspect ratios, the relative orientational angle, and the number of units considered. For the spectral distribution shown in Fig. 6.13, these signal are expected to originate from side-by-side assembled nanorod aggregations.

Up to this stage, both the experimental and simulated results have been obtained with a 50 nm thick substrate. In the next section, the effect of the resonator on the absorption spectra is investigated.

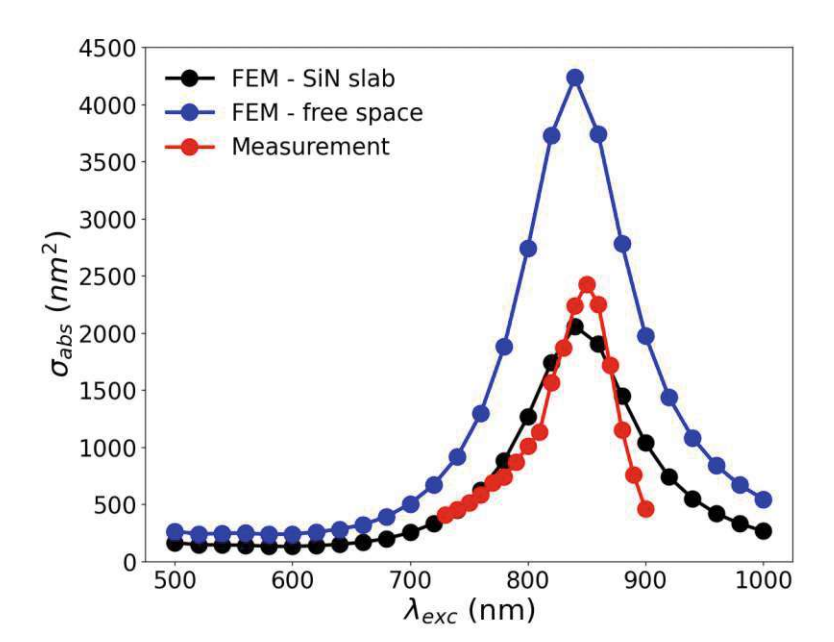


Figure 6.14: FEM - nanomechanical photothermal absorption spectrum comparison. Measured absorption cross-section of a individual nanorod (red dots), compared to FEM simulated absorption spectrum in the presence of the 50 nm thick, silicon nitride substrate (black dot), and in free space (blue dots), obtained for nanorod dimensions of  $L_{\rm nr} = 48$  nm,  $r_{\rm nr} = 6$  nm, with the silica coating thickness of 20 nm.

#### 6.2.2Nanorod-Mechanical Resonator Interaction

The interaction between an individual nanorod and the underlying nanomechanical resonator was further investigated with the aid of FEM simulations.

The results, shown in Fig. 6.14, reveal that The FEM spectrum in the presence of the substrate (black dots) closely matches the experimental absorption spectrum (red dots). In contrast, the FEM analysis conducted in free space, in the absence of the SiN slab, does not (blue dots). More precisely, the absorption cross-section at the plasmon resonance ( $\lambda_{\rm LSPR} = 840$  nm) is reduced from  $\sigma_{\rm abs} \approx 4.2 \cdot 10^{-15}$  m<sup>2</sup> in free space to  $\sigma_{\rm abs} \approx 2 \cdot 10^{-15} \,\mathrm{m}^2$  in the presence of the slab. However, the resonance position  $\lambda_{\rm LSPR}$ and linewidth  $\Gamma$  are only weakly affected by the substrate, with  $\leq 1\%$  variation in both parameters. These slight variations are due to the reduced electromagnetic screening imposed by the substrate.

In general, a dielectric substrate underneath a metal nanoparticle screens the electromagnetic restoring force acting on the plasmon oscillations. This screening can be qualitatively modelled as a nanoparticle image with a reduced number of charges, whose electromagnetic strength is determined by the nanoparticle-substrate interdistance and the slab dielectric permittivity [194]. The weak effect observed in Fig. 6.14 finds its

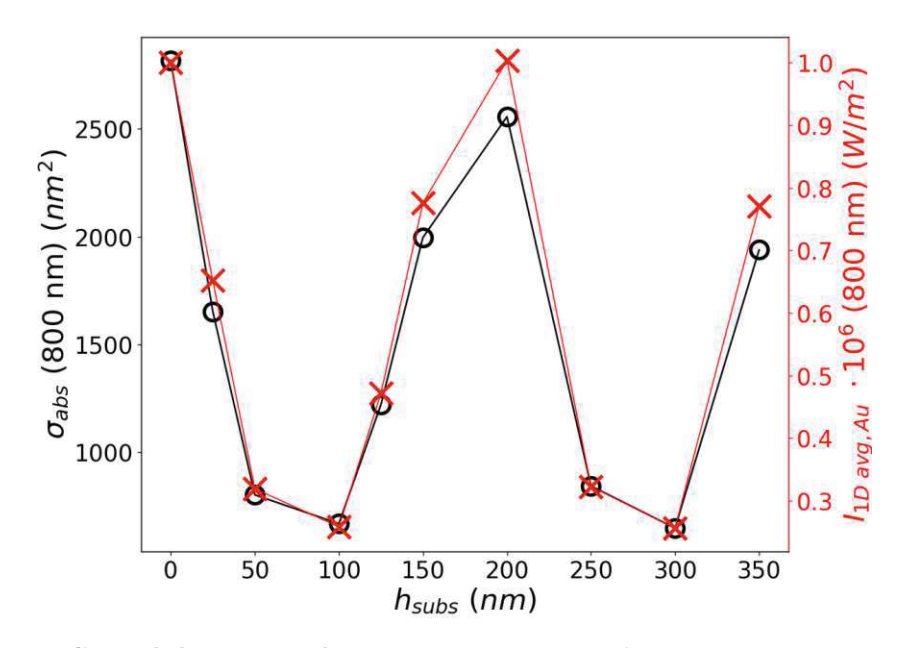


Figure 6.15: SiN slab-nanorod interaction. FEM absorption cross-section at 800 nm wavelength for the same nanorod (black empty dot and solid line), and 1D averaged FEM electromagnetic intensity in the vicinity of the gold core in the presence of the substrate only (red crosses and solid line), for different silicon nitride slab thicknesses.

reason in the relatively large interdistance of 20 nm (due to the thickness of the silica coating) [194, 218] and the relatively low refractive index of low-stress silicon nitride (whose spectral distribution has been taken from Ref. [96]).

To better understand the role played by the SiN slab, additional FEM simulations were conducted at a single wavelength (800 nm) for varying slab thicknesses,  $h_{\text{subs}}$ . The results, displayed in Fig. 6.15, reveal a periodic modulation in the absorption cross-section as the slab thickness increases. This modulation perfectly follows the variation in intensity at the air-SiN interface, in the vicinity of the nanorod, as the electromagnetic losses  $Q_h$  due to absorption are directly proportional to the intensity of the electric field,  $Q_h \propto |\mathbf{E}(\mathbf{r})|^2$ (see Eq. (4.16)). The intensity modulation is due to the interference occurring between the input electric field and the light reflected from the slab, whose magnitude depends on the thickness and refractive index. Here, the calculated intensity value is averaged over the spatial distribution in the proximity of the nanorod, however in the absence of it and with only the presence of the substrate.

In Fig. 6.16, the 1D intensity distribution along the optical axis at  $\lambda = 800$  nm shows how the electric field intensity changes with slab thickness —particularly in the gold core (yellow) region. These intensities are the results of the FEM first step, where the full field formulation has been used in the absence of the nanorod (as explained in Chapter 4). It is interesting to note in both Fig. 6.15 and 6.16 that for a slab thickness of  $h_{\rm subs} = 200$ 

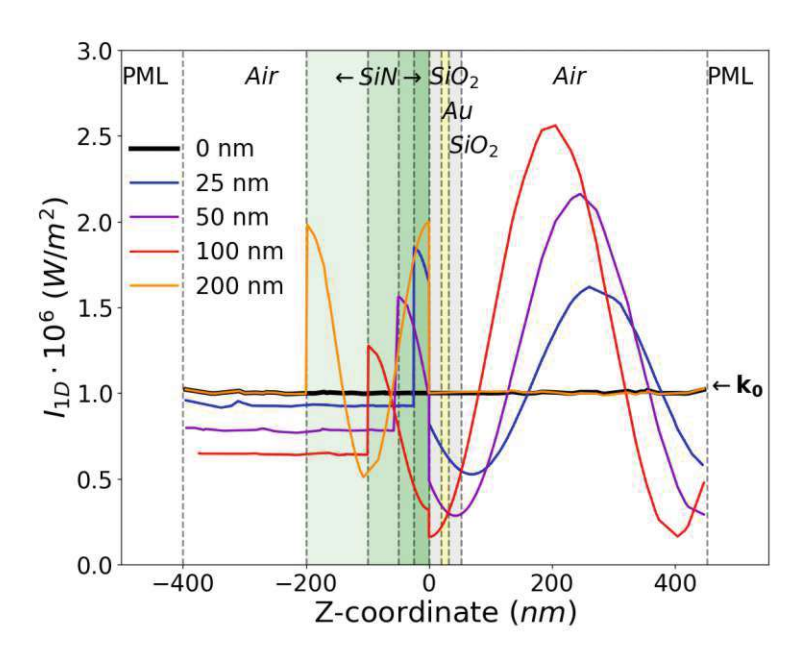


Figure 6.16: **FEM intensity distribution at SiN-air interface.** FEM simulated intensity distribution along a 1D cut line passing in the center of the physical domain at a wavelength of 800 nm, for different silicon nitride slab thicknesses. The intensities are the results to the FEM first step, where only the slab is simulated, without any gold nanorod on top of it. The vertical lines and the relative colors show the positions of each element along the cut line: white, air; grey, silica; yellow, gold; green of different intensities, the different silicon nitride slabs.

nm (orange curve in Fig. 6.16), the intensity outside the slab is identical to the case without any substrate. This occurs due to the optical dispersion of SiN at this excitation wavelength. For a vacuum wavelength of  $\lambda_0 = 800$  nm, the dispersive refractive index of SiN is approximately  $n_{\rm SiN} \approx 2$ , resulting in an effective wavelength within the slab of  $\lambda_{\rm SiN} = \lambda_0 / n_{\rm SiN} \approx 400 \text{ nm} = 2 \cdot h_{\rm subs}.$ 

For the 50 nm thickness used in this work, along with the covered spectral range of 730 - 900 nm and the refractive index of SiN [96], no interference occurs inside the slab. Therefore, the absorption strength modulation in this case is attributed to the interference occurring at the interface between free space and the substrate, differing from what has been reported by Kosaka et al. [224]. There, a 1  $\mu$ m thick silicon cantilever served as an optical cavity for specific wavelengths in the VIS range, modulating the scattering of deposited 100 nm gold nanoparticles. Overall, Both scenarios show that it is possible to tailor the absorption spectrum of individual nano-absorbers by controlling the substrate's refractive index and thickness.

So far, both the experimental and simulated results have focused on the nanorod-ligh interaction for a polarization aligned with the absorber's long axis. Next, it is examined

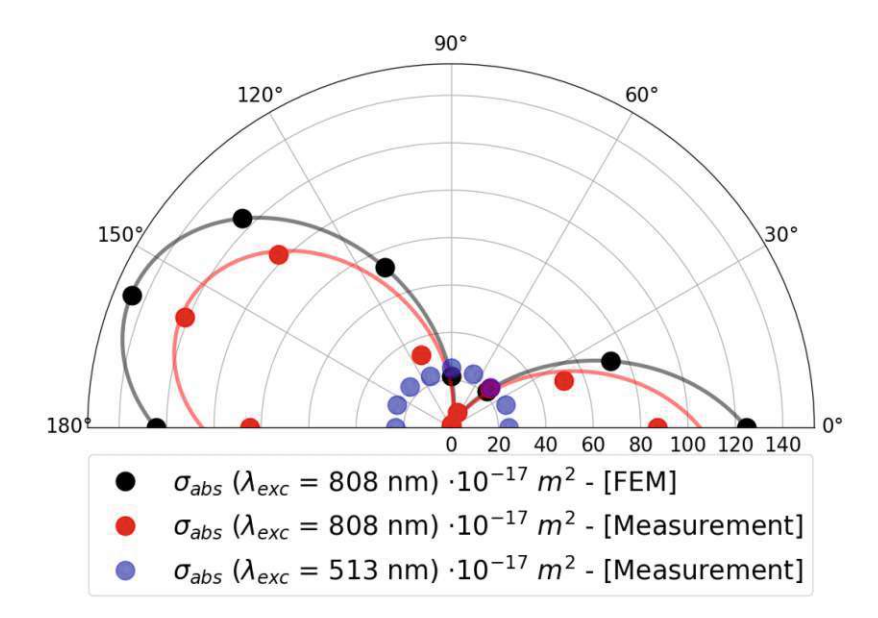


Figure 6.17: Polar plot of the absorption cross-section of an individual nanorod measured at  $\lambda_{\rm exc} = 808$  nm as a function of the polarization angle  $\theta_m athrmpol$  (red dots). The ratio between the absorption cross-section for a polarization parallel to the nanorod long-axis  $(\theta_{\rm pol} \approx 157.5^{\circ})$  and perpendicular to it  $(\theta_{\rm pol} \approx 90^{\circ})$  is roughly  $\sigma_{\rm abs, \parallel}(808~{\rm nm})/\sigma_{\rm abs, \perp}(808~{\rm nm})$ nm)  $\approx 100$ . FEM simulations show good agreement with the measurement (black dots). Both the red and black solid curves represent the  $\cos^2(\theta)$  pattern. Blue dots represent nanomechanical photothermal measurements at  $\lambda_{\rm exc} = 513$  nm.

how polarization influences this interaction.

#### 6.2.3 Polarization Microscopy

As mentioned earlier, the optical response of these non-spherical nanoparticles is highly dependent on the polarization of the electromagnetic field. This is clearly shown in Fig. 6.17 and 6.18.

Fig. 6.17 shows how the absorption cross-section varies with the laser polarization angle for an individual nanorod, with the red dots representing the nanomechanical photothermal measurements at the plasmon resonance ( $\lambda_{LSPR} = 808$  nm). Each data point is obtained by rotating the probe laser polarization in 22.5° increments by means of a half-waveplate (HWP) and a linear polarizer, while keeping the laser input power constant. The absorption cross-section ratio between the polarization aligned with the nanorod's long axis ( $\theta_{\rm pol} \approx 175.5^{\circ}$ ) and perpendicular to it ( $\theta_{\rm pol} \approx 90^{\circ}$ ) is approximately

$$\frac{\sigma_{\rm abs,\parallel}(808~{\rm nm})}{\sigma_{\rm abs,\perp}(808~{\rm nm})} \approx 100. \tag{6.7}$$

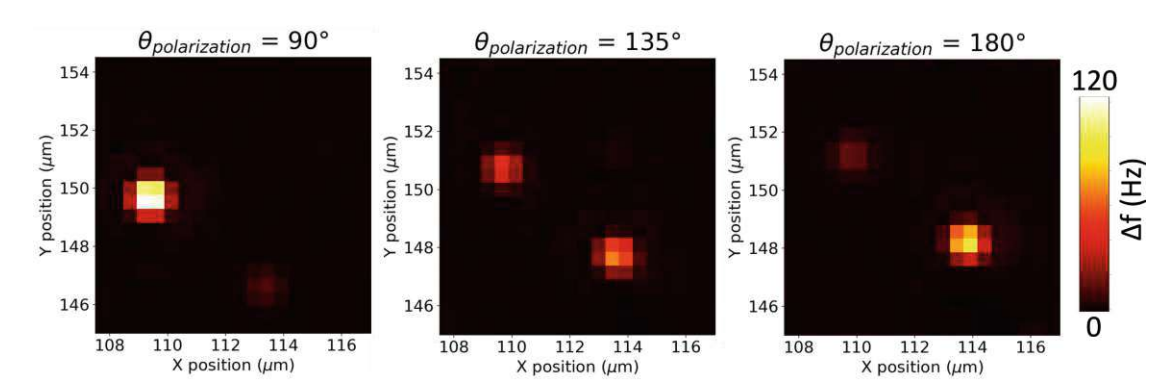


Figure 6.18: **2D polarization microscopy.** 2D maps of the same region at  $\lambda_{\rm exc} = 808$ nm for three different polarization angles  $\theta_{\rm pol}$ : 90°, 135°, 180°. The two responses are from two individual nanorods. For the perpendicular polarizations, 90° and 180°, the absorbers behave in an opposite way, meaning that they are almost perpendicular one to each other, while absorbing almost the same amount of light for the central map  $(\theta_{\rm pol} = 135^{\circ}).$ 

Theis high polarization contrast highlights the strong absorption efficiency control achievable through the incident laser's polarization. The absorption efficiency for the parallel case is  $Q_{\rm abs,\parallel} \approx 3.64$ , while for the perpendicular case it is  $Q_{\rm abs,\perp} \approx 0.03$ , where  $Q_{\rm abs} = \sigma_{\rm abs}/S_{\rm nr}$ , and  $S_{\rm nr} \approx 3.29 \cdot 10^{-16}~{\rm m}^2$  is the surface of the selected nanorod, as extracted with the aid of FEM simulations.

The measurements align well with FEM simulations (black dots), both following the expected  $\sigma_{\rm abs}(\lambda, \theta_{\rm pol}) = \sigma_{\rm abs, \parallel}(\lambda)\cos^2(\theta_{\rm pol})$  pattern characteristic of ideal dipoles [59, 187, 225. For comparison, the polarization response at  $\lambda_{\rm exc} = 513$  nm (blue dots) is also shown. At this wavelength, which excites transversal localized surface plasmons. the polarization contrast is minimal due to the overlap with polarization-independent electronic transitions in gold [190]. For this reason, the plasmonic damping increases, reducing the transverse plasmonic strength compared to the longitudinal one.

Nanomechanical photothermal microscopy also enables the precise determination of the orientation of individual nano-absorbers on the substrate, as demonstrated in Fig. 6.18. 2D maps of the same region on the drumhead are shown for three different polarization angles ( $\theta_{\rm pol} = 90^{\circ}$ , 135°, 180°) at  $\lambda_{\rm exc} = 808$  nm. The two signals correspond to two distinct nanorods, whose absorption amplitudes vary as a function of the laser polarization. In particular, the behavior of the two nanorods is opposite for the perpendicular polarizations (90° and 180°), suggesting that they are nearly perpendicular to each other, while absorbing nearly the same amount of light for the central polarization ( $\theta_{\text{pol}} = 135^{\circ}$ ).

102

#### 6.3 Overview on the State-of-the-Art

This work aimed to show the capabilities of nanomechanical photothermal sensing for single-molecule and particle spectroscopy, as well as polarization microscopy. The analysis presented here has been carried out with an experimental apparatus and through a measurement procedure substantially simpler than other state-of-the-art label-free single molecule techniques [61]. Another key advantage of this platform is its high sensitivity, enabling one of the highest signal-to-noise ratio (SNR) levels in the field. To show that, a comparison between the SNR among various label-free single-molecule techniques is carried out through the following metric [226]

$$SNR_{norm} = \frac{SNR_{exp}}{SNR_0} \frac{P_{heat,0}}{P_{heat,exp}} \sqrt{\frac{\tau_{m,0}}{\tau_{m,exp}}}.$$
 (6.8)

SNR<sub>norm</sub> is defined as the ratio between the experimental SNR of the considered technique (SNR<sub>exp</sub>) and the reference SNR<sub>0</sub> (from this work), accounting for the power absorbed by the sample under study  $P_{\text{heat}}$  and for the measurement time of the experiment  $\tau_{\text{exp}}$ , renormalized.

The compilation of data is presented in Table 6.1 and displayed in Fig. 6.19. The values used as reference correspond to the measurements shown for the individual nanorod in Fig. 6.14 and 6.17 (last dataset of Table 6.1). For the compiled works which do not explicitly give the values, an average is used.

From Fig. 6.19, it is evident that nanomechanical photothermal microscopy described in Ref. [24] (dark red cross) achieves the highest SNR, followed by thermorefractive photothermal with near-critical Xe [231, 232] and the results of the work presented here [31]. The difference in SNR between this study and Ref. [24] is due to the different residual prestress in the dumhead resonator used for the absorption analysis. In Ref. [24], oxygen plasma treatment has been employed to reduce the tensile stress to 0.8 MPa. with the aim to enhance the relative power responsivity  $\mathcal{R}_P$  to detect single Atto 633 molecules. At such low tensile stress,  $\mathcal{R}_P$  is not anymore constant upon photothermal heating, since the stress relaxation is of the same order of magnitude of its initial value. boosting in a positive feedback the thermal response of the sensor.

In the present study, no additional stress engineering was required due to the already high sensitivity of the resonator, which was sufficient for the nanorod detection.

#### Conclusions and Outlook 6.4

In conclusion, this work has explored the capabilities of a nanomechanical photothermal spectroscopy and microscopy platform for single-molecule and particle analysis. The platform demonstrated its ability to image and resolve localized surface plasmon resonances of individual and aggregated gold nanorods in the NIR range. It has been shown that electron bulk and surface scattering are the major sources of plasmonic damping, due to the nanometric sizes of the absorbers. Additionally, the polarization properties of the nanorods were analyzed, showcasing the platform's capability to resolve the sample's

Table 6.1: Parameters of the different techniques for the SNR comparison. SMS: spatial modulation spectroscopy; GSD: ground-state depletion microscopy; PCM: photothermal constrast microscopy; OMM: optical microresonator microscopy; NPM: nanomechanical photothermal microscopy; NPSM: nanomechanical photothermal spectromicroscopy. NG: not given. \*: at the time of publication. \*\*: assumed values.

Technique	Capability*	$\begin{array}{c} \textbf{Pump} \\ \textbf{Intensity} \\ (\textbf{kW/cm}^2) \end{array}$	Sample	$\sigma_{\rm abs}~({\rm m}^2)$	$P_{\text{heat}}$ (pW)	$\tau_{\rm m}  ({\rm ms})$ (avgs)	$SNR_{exp}$
UV-Vis Ex-	Spectro-	NG	Nanorod	NG	1274**	208**	6.38**
tinc. [225]	microscopy						
SMS [227]	Spectro- microscopy	22	Metal cluster	$4.3 \cdot 10^{-16}$	93620	10000*	2000
Extinc. + Bal.Det. [228]	Microscopy	280	TDI dye	$1.8 \cdot 10^{-19}$	508	2 (10x)	5.7
GSD [56]	Microscopy	590	Atto dye	$5 \cdot 10^{-20}$	294	30 (20x)	3.7
IR-PHI [229]	Spectroscopy						
PCM (Glycerol) [58]	Microscopy	9300	BHQ	$4 \cdot 10^{-20}$	1000	300	10
PCM (5CB) [230]	Microscopy	28	Nanosphere	$4.8 \cdot 10^{-16}$	132000	20	78
PCM (Xe) [231]	Microscopy	28	Nanosphere	$4.8 \cdot 10^{-16}$	64	50	9.4
PCM (Xe) [232]	Microscopy	0.45	CP	$4 \cdot 10^{-18}$	64	30	10
OMM [59]	Spectro- microscopy	$2 \cdot 10^{-4}$	Nanorod	$1 \cdot 10^{-14}$	20	1000 (30x)	2
OMM [233]	Spectro- microscopy	522	СР	8 ·10 <sup>-19</sup>	4100	100	4
NPM [24]	Microscopy	35.4	Atto dye	$4.8 \cdot 10^{-20}$	6.3	40	70
NPSM	Spectro- microscopy	4.98	Nanorod	$2.5 \cdot 10^{-15}$	120947	200	30759

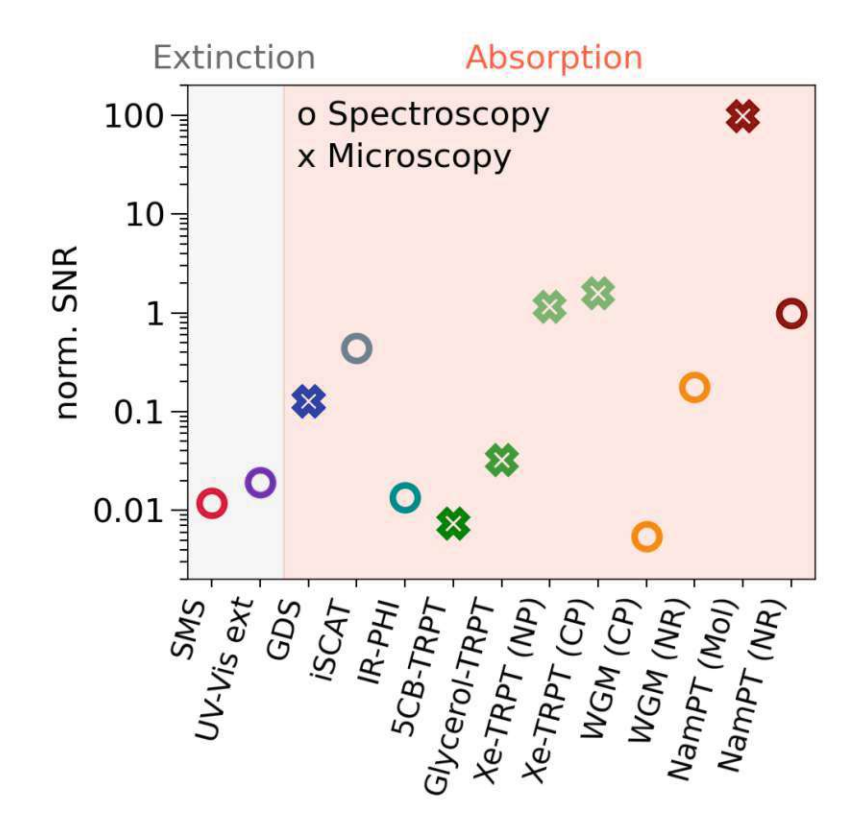


Figure 6.19: SNR comparison between different single-molecule absorption sensing techniques. Red: spatial modulation spectroscopy (SMS) [227]; purple: UV-VIS extinction [225]; blue: ground-state depletion (GSD) [56]; grey: interferometric scattering (iSCAT) [228]; light blue: infrared photothermal heterodyne imaging (IR-PHI) [229]; thermorefractive photothermal (TRPT) microscopy with thermotropic liquid crystals [230] (dark green), with a glycerol medium (green) [58], with a xenon medium at its supercritical point (light green) [231, 232]; orange: whispering gallery mode (WGM) spectroscopy [59, 233]; dark red: nanomechanical photothermal (NamPT) microscopy [24] and spectroscopy [31].

intrinsic heterogeneity, surpassing the limitations of ensemble-averaged spectroscopy techniques.

The interaction between the nano-absorber and the underlying mechanical resonator was also investigated, revealing how the resonator modulates the absorber's strength across a broad spectral range, with minimal influence on the plasmon resonance energy and broadening for silica-coated nanorods.

A comparative analysis of state-of-the-art label-free single-molecule techniques demonstrated that nanomechanical photothermal sensing provides a superior signal-to-noise ratio (SNR) while utilizing a less complex experimental setup and procedure. The results obtained are on par with leading thermorefractive photothermal spectroscopy, even without specific mechanical resonator engineering.

Future improvements in sensor responsivity could be achieved through stress engineering via oxygen plasma treatment, as previously shown in the literature [24]. Alternatively, advancements could be made by patterning the drumhead resonator with a trampoline design [23, 29, 72], which would reduce thermal dissipation, or by using a phononic crystal design where the defect mode enhances the overlap between the mechanical and thermal volumes [133]. However, careful attention must be given to mitigating frequency fluctuations induced by laser intensity variations to further enhance the platform's sensitivity for nanomechanical photothermal single-molecule spectroscopy [111].

# Nanomechanical Photothermal Sensing for Low-loss Material Characterization

In this chapter, nanomechanical photothermal sensing is employed to characterize the optical properties of silicon nitride (SiN), focusing on its extinction coefficient, which is studied as a function of the residual tensile stress at 632.8 nm wavelength. The aim of this work is to investigate the relationship between SiN absorption and its deposition process, as different deposition techniques and recipes are utilized depending on the application [87]. It is demonstrated that the optical extinction of low-pressure chemical vapor deposition (LPCVD) SiN decreases with increasing tensile stress. The experimental results are interpreted within the band-fluctuations framework, linking this trend to a reduction in the energy bandgap, which subsequently lowers the absorption of this widely used material.

The approach introduced here offers a new alternative method for optical characterization of thin films, which can be applied to any material used in nanomechanics and nanophotonics. This method is particularly valuable as it is insensitive to scattering effects that often complicate conventional techniques.

All results and discussions in this chapter are based on Ref. [139].

#### 7.1 Characterization Procedure

#### 7.1.1 Working Principle

The working principle is based on the methods introduced earlier in this work (see Chapter 3). The goal is to determine the absorption coefficient,  $\alpha_{abs}$ , of the thin films by modeling and experimentally characterizing the power response of the patterned thin mechanical structure. Specifically, the direct comparison between the theoretical  $\mathcal{R}_{\rm P}$ and the experimental  $\mathcal{R}_{P_0}$  relative power responsivity of the mechanical resonators used in this work enables the extraction of the absorptance  $\tilde{\alpha}_{abs}(\lambda)$ . This is related to the absorption coefficient  $\alpha_{abs}(\lambda)$ , and the path h travelled by the electromagnetic wave, by

$$\tilde{\alpha}_{abs}(\lambda) = \alpha_{abs}(\lambda) \cdot h \cdot \eta, \tag{7.1}$$

with  $\alpha_{\rm abs}(\lambda)$  with units [dB/m] [234], and  $\tilde{\alpha}_{\rm abs}(\lambda)$  being dimensionless [235]. The factor  $\eta$  is a dimensionless correction for possible interference inside the thin film [74, 235]. For a thin film of thickness h and complex refractive index  $\tilde{n} = n + i\kappa_{\text{ext}}$ , probed at a wavelength  $\lambda$ , the absorptance correction factor is given by [74, 235]

$$\eta = \frac{4n(n^2+1) + (n^2-1)\frac{\lambda}{\pi h}\sin(\frac{4\pi nh}{\lambda})}{1 + 6n^2 + n^4 - (n^2-1)^2\cos(\frac{4\pi nh}{\lambda})}.$$
 (7.2)

As discussed earlier,  $\mathcal{R}_{P}$  represents the relative frequency change per absorbed power  $P(\lambda) = \tilde{\alpha}_{abs}(\lambda)P_0$ , with  $P_0$  being the probe laser input power, and is expressed as [60]

$$\mathcal{R}_{P}(\omega) = \frac{1}{f_0} \frac{\partial f_0}{\partial P} = \frac{\mathcal{R}_{T}}{G} |H_{th}(\omega)|, \qquad (7.3)$$

with  $\mathcal{R}_{\mathrm{T}}$ , G, and  $H_{\mathrm{th}}(\omega) = (1 + i\omega\tau_{\mathrm{th}})^{-1}$  denoting the temperature responsivity, the thermal conductance, and the resonator's thermal response, with a thermal time constant  $\tau_{\rm th}$ , respectively. All measurements have been conducted far from any thermal transient  $(\omega \ll \tau_{\rm th}^{-1})$ , i.e., in the steady state. Therefore, the  $\omega$ -dependence is hereafter dropped. The experimental responsivity  $\mathcal{R}_{P_0}$  is obtained by measuring the relative frequency shift per applied impinging power  $P_0$ , as schematically shown in Fig. 7.1c. The relation between this quantity and  $\mathcal{R}_{P}$  can be easily expressed as

$$\mathcal{R}_{P_0}(\lambda) = \frac{1}{f_0} \frac{\partial f_0}{\partial P_0} = \frac{1}{f_0} \frac{\partial f_0}{\partial P} \frac{\partial P}{\partial P_0} = \tilde{\alpha}_{abs}(\lambda) \ \mathcal{R}_{P}. \tag{7.4}$$

This allows for the direct extraction of the optical absorptance as  $\tilde{\alpha}_{abs} = \mathcal{R}_{P_0}/\mathcal{R}_{P}$ . The optical extinction coefficient  $\kappa_{\text{ext}}$ , which is an intrinsic property of the material, is here the target key parameter. It is related to the absorptance by [234, 235]

$$\kappa_{\text{ext}}(\lambda) = \frac{\lambda \ \tilde{\alpha}_{\text{abs}}(\lambda)}{4\pi \ h \ \eta} = \frac{\lambda \ \alpha_{\text{abs}}(\lambda)}{4\pi}.$$
(7.5)

The second equality represents the theoretical expression of  $\kappa_{\rm ext}(\lambda)$ , where  $\alpha_{\rm abs}(\lambda)$  is evaluated within the framework of the band-fluctuations model [110]. The following sections will define the relevant quantities for the SiN thin films analyzed in this study.

#### Experimental Setup 7.1.2

The thin films are patterned in a string geometry (see Fig. 7.1a), and their fundamental out-of-plane flexural mode is utilized for the optical characterization of SiN. To guarantee



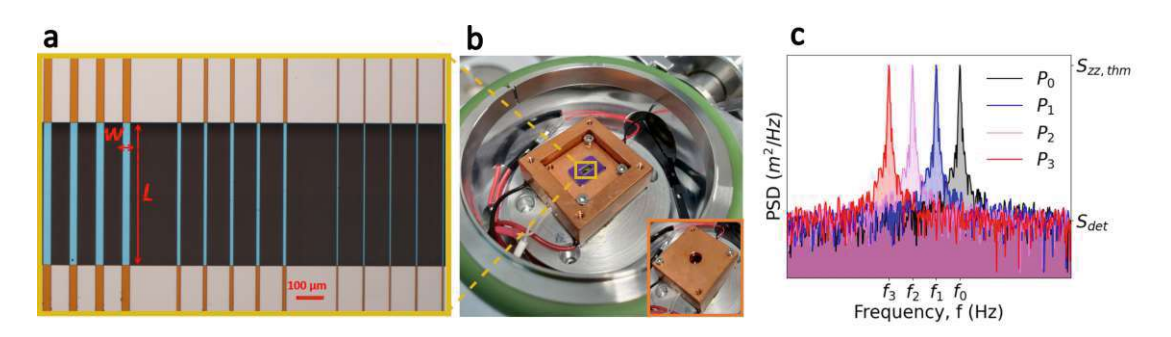


Figure 7.1: Nanomechanical photothermal characterization of optical losses with strings. a. Optical micrograph of the SiN strings used in the present study. Orange/light blue regions are made of SiN; the grey regions are the Si substrate. b. Photo of the cm-scale copper thermal equilibrium chamber used for the characterization of the linear coefficient of thermal expansion (see main text). A thermoelectric module is glued beneath to heat up the whole oven (thick red electrical connections) to guarantee a uniform temperature rise of the chips. The temperature is monitored and kept constant with a PID controller. c. Mechanical frequency detuning measured by monitoring the shift of the thermomechanical noise peak of the string's fundamental mode as a function of  $P_0$ . The peak  $S_{\rm zz,thm}$  is given in terms of displacement power spectral density (PSD) [m<sup>2</sup>/Hz], and is well resolved by the vibrometer ( $S_{\rm zz,thm} \gg S_{\rm det}$ , with  $S_{\rm det}$  denoting the detection noise PSD). In the x-axis,  $f_i = f_{res}(P_i)$ , with i = 1, 2, ..., is the resonance frequency of the fundamental mode at each input laser power  $P_i > P_{i-1}$ .

high photothermal and mechanical performances, the resonators are operated inside a custom-made vacuum chamber at high-vacuum conditions ( $p < 10^{-5}$  mbar) to reduce gas damping and thermal convection losses. In addition, a custom-designed, cm-scale copper oven encloses the resonators and ensures uniform thermal equilibrium between the devices and their environment (details on the oven design and functionality will be discussed later), as illustrated in Fig. 7.1b. The oven is designed to further allow external optical access, as shown in the inset of Fig. 7.1b.

The displacement is transduced optically with a laser-Doppler vibrometer, as outlined in Chapter 4, Setup II. The experimental setup is equipped with a 623.8 nm wavelength laser, with a beam waist of 1.5  $\mu$ m, to both read out the resonator's displacement and probe the optical extinction of the SiN thin films, simplifying the measurement procedure. The frequency shift of the thermomechanical noise peak corresponding to the fundamental resonance mode of each structure is recorded at various optical power levels, ranging from 6 to 120  $\mu$ W, as schematically shown in Fig. 7.1b. During the experiment, the power spectral density (PSD) of the displacement, in units of  $[m^2/Hz]$ , is measured for the undriven fundamental resonance mode. As the optical power increases, the thermomechanical noise peak  $(S_{zz,thm})$  shifts to lower frequencies  $(f_i > f_{i+1})$  for  $P_i < P_{i+1}$ ).

### 7.2LPCVD SiN Thin Films

The SiN thin films were deposited with LPCVD and exhibit varying levels of residual tensile stresses (200 - 850 MPa, see Table 7.1). The rationale behind the choice of a string geometry is the enhanced photothermal responsivity and fast temporal response of this nanomechanical resonator design, as previously shown [111] (see Chapter 3 and 5). The following sections provide a detailed description of the photothermal and mechanical characterization of the string resonators, which is essential for reducing the uncertainties in the experimental determination of the optical extinction of SiN.

#### 7.2.1Theoretical Power Responsivity

For a string resonator, the theoretical relative power responsivity (7.3) is given by [60, 111]

$$\mathcal{R}_{P} = -\frac{\alpha_{\rm th} E}{2\sigma_{0}} \left[ 8 \frac{hw}{L} \kappa + 8Lw \epsilon_{\rm rad} \sigma_{\rm SB} T_{0}^{3} \right]^{-1}, \tag{7.6}$$

with  $\alpha_{\rm th}$ , E,  $\sigma_0$ , h, w, L,  $\kappa$ ,  $\epsilon_{\rm rad}$ ,  $\sigma_{\rm SB}$  and  $T_0$  denoting the resonator's linear coefficient of thermal expansion, Young's modulus, tensile stress, thickness, width, length, thermal conductivity, emissivity, Stefan-Boltzmann constant, and bath temperature, respectively. In Eq. (7.6), the factor outside the brackets is the string's temperature responsivity  $\mathcal{R}_{\rm T} = -\alpha_{\rm th} E/(2\sigma_0)$ ; the terms inside the bracktes account for total thermal conductance G, which includes the thermal dissipation through the surrounding frame  $G_{\text{cond}}$  (first addend), and thermal radiation to the environment  $G_{\text{rad}}$  (second addend) [60, 111]. Since Eq. (7.6) depends on different material parameters, it is crucial to characterize these parameters with precision to accurately assess the optical absorption of the SiN thin films. In particular, the Young's modulus E and the linear coefficient of thermal expansion  $\alpha_{\rm th}$  have been measured to reduce the uncertainty on the estimation of the optical extinction.

#### 7.2.1.1Film Young's Modulus

E has been estimated following the procedure described in Ref. [125]. In this method, the out-of-plane flexural eigenmode spectrum of the string resonator is recorded, and the Young's modulus calculated for each couple of eigenmodes (n,m) (with  $n \neq m$ ) as [125]

$$E = \frac{48L^2\rho}{\pi^2h^2(n^2 - m^2)} \left(\frac{f_n^2}{n^2} - \frac{f_m^2}{m^2}\right),\tag{7.7}$$

where L,  $\rho$ ,  $f_n$ , and  $f_m$  denote the string's length, mass density, and the nth and mth mode resonance frequencies, respectively. An example of such a measurement is shown in Fig. 7.2a, where E is plotted as a function of  $\Delta = |m-n|$ . The experimental results are plotted in Fig. 7.2b and displayed in Table 7.1, with values in the range 170 - 250 GPa, consistent with previously reported data for LPCVD SiN [87, 125]. No stress dependence has been observed for this material parameter.

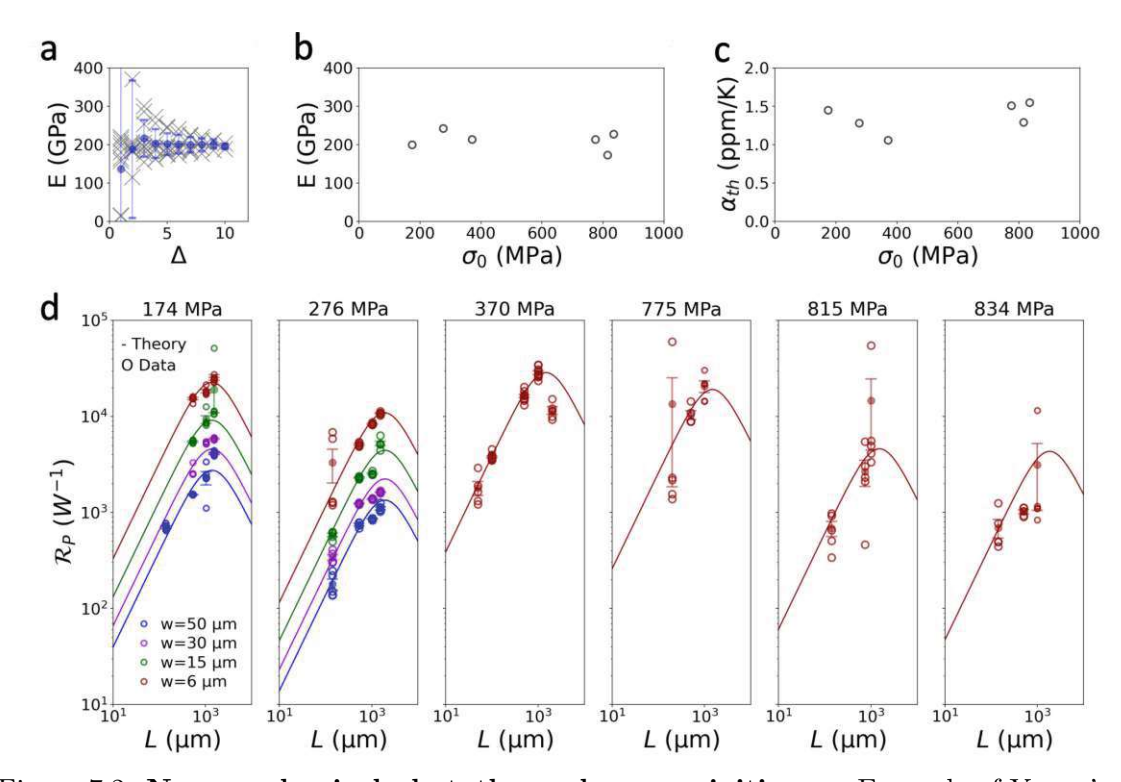


Figure 7.2: Nanomechanical photothermal responsivities. a. Example of Young's modulus estimation, following the procedure of Ref. [125]. b. Experimentall Young's modulus E as a function of the tensile stress  $\sigma_0$ . c. Experimental results for the linear coefficient of thermal expansion  $\alpha_{\rm th}$ , as a function of the residual tensile stress  $\sigma_0$ . d. Relative power responsivity for different SiN string structures. Circles: experimental responsivity (7.4), divided by the corresponding mean absorption coefficient  $\alpha_{abs}$ . Solid curve: theoretical model (7.6). Material parameters used:  $\rho = 3000 \text{ kg/m}^3$ ,  $\kappa = 3 \text{ W/(m}$ K). Emissivity values are calculated from the data reported in Ref. [97]: 0.05 (h = 56nm),  $0.13 \ (h = 157 \ \text{nm}), \ 0.133 \ (h = 177 \ \text{nm}), \ 0.171 \ (h = 312 \ \text{nm}), \ 0.176 \ (h = 340 \ \text{nm}).$ These results are plotted in Fig. 7.3a.

Table 7.1: String resonators' geometrical (h), mechanical  $(\sigma_0, E, \alpha_{th})$ , compositional (Si/N), and optical  $(\eta, \kappa_{\text{ext}}, E_{\text{g}}, \beta^{-1})$  properties.

$\sigma_0$ (MPa)	h (nm)	E (GPa)	$\alpha_{\rm th}~({\rm ppm/K})$	$\eta$	$\kappa_{\rm ext} \ ({\rm ppm})$	Si/N	$E_{\rm g}~({\rm eV})$	$\beta^{-1} \text{ (meV)}$
174	177	200	1.45	1.215	606	0.96	3.23	201
275	340	243	1.28	1.105	588	0.98	3.09	183
370	56	214	1.06	1.022	176	0.89	3.62	212
775	56	214	1.51	1.022	38	0.86	3.90	208
815	157	173	1.29	1.273	20	0.83	4.21	227
834	312	227	1.55	1.268	21	0.84	4.10	217

#### 7.2.1.2Film Linear Coefficient of Thermal Expansion

 $\alpha_{\rm th}$  has been measured by recording the frequency shift of the thermomechanical noise peak as a function of controlled temperature rises ( $\Delta T = 0 - 10$  K), following the approach in Ref. [195]. From these measurements, it is possible to extract the relative temperature responsivity  $\mathcal{R}_{\mathrm{T}}$  of each string, which allows to evaluate the linear coefficient of thermal expansion using the following relationship

$$\alpha_{\rm th,SiN} = \alpha_{\rm th,Si} - \frac{2\sigma_0}{E} \mathcal{R}_{\rm T},$$
(7.8)

where  $\alpha_{\rm th,Si} = 2.6$  ppm/K is the linear coefficient of thermal expansion of the underlying silicon substrate at 300 K [155]. For these measurements, the experimental apparatus consists of a thermoelectric module (GM200-127-10-15, Adaptive Power Management) used to heat the resonators, while monitoring and keeping the temperature at the desired value via a PID controller (TEC-1092, Meerstetter Engineering). The chips have been enclosed inside the cm-scale copper thermal bath of Fig. 7.1b to ensure thermal equilibrium through radiative heat transfer between the strings and their environment. The results are presented in Fig. 7.2c and Table 7.1, showing that  $\alpha_{\rm th}$  (7.8) lies in the range 1-1.6 ppm/K, which is consistent with previously reported values [87, 195]. Similar to the Young's modulus, no stress dependence has been observed for  $\alpha_{\rm th}$ , as shown in Fig. 7.2c.

#### 7.2.2Experimental Power Responsivity

The experimental power responsivity (7.4) across the different residual tensile stress values is displayed in Fig. 7.2d as a function of the resonators' length L (circles), together with the theoretical model (7.6) (solid curves). The scale is given in terms of absorbed power P. A minimum of five resonators was evaluated for each stress and string length. It is worth noting that  $\mathcal{R}_{\mathrm{P}}$  increases for longer strings in the conduction-limited regime (L < 1 mm), since the thermal conductance  $G \approx G_{\text{cond}}$  is inversely proportional to the length L (see Eq. (7.6)), leading to better thermal insulation from the environment [111]. Conversely, increasingly longer resonators (L > 1 mm) enter the radiation-limited regime  $(G \approx G_{\rm rad})$ , leading to a drop of  $\mathcal{R}_{\rm P}$  due to larger radiating areas.

The analyzed resonators have thicknesses of h = 56-340 nm and widths of  $w = 5-50 \mu m$ , ensuring minimal thermal dissipation. As indicated in Eq. (7.6),  $G_{\rm cond} \propto hw$  and  $G_{\rm rad} \propto w$ , making these strings highly responsive to photothermal heating. Furthermore, the length L varies in the range 0.1-2 mm, making the resonators' power response mainly thermal conduction limited [111]. The current experimental approach is, therefore, less influenced by the SiN emissivity, which, according to Kirchhoff's law, equals the optical absorption [127] — the parameter under scrutiny in the present study. Nonetheless, for completeness, the emissivity has been included in the model shown in Fig. 7.2d. The calculations are based on the matrix formalism for a single thin film surrounded by vacuum [234], equivalent to what done in Ref. [124]. The results are shown in Fig. 7.3a. It can be observed that the emissivity increases for thicker materials, as expected for dielectrics [196].

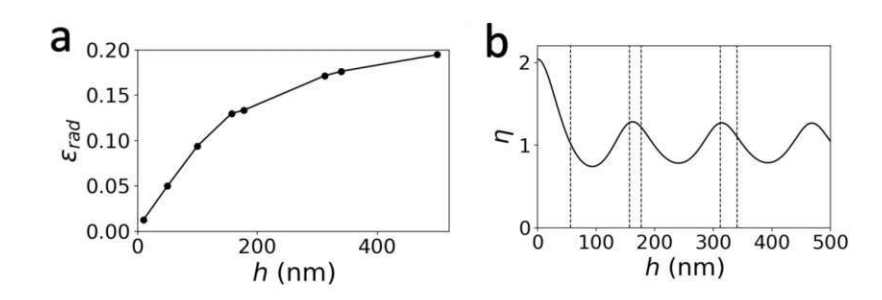


Figure 7.3: SiN emissivity and interference factor. a. Emissivity  $\epsilon_{\rm rad}$  of low-stress SiN as a function of the film thickness h. b. Factor  $\eta$  as a function of the film thickness h at 632.8 nm wavelength. The sold curve is calculated using Eq. (7.2). The dashed vertical lines indicate the thicknesses of the films analyzed in this study.

#### 7.2.3**Interference Correction Factor**

For the evaluation of the extinction coefficient (7.5) of SiN for the different tensile stress values, possible interference effects are taken into account by the absorptance correction factor  $\eta$  (7.2). This depends on the dispersive part of the refractive index n, which has been obtained here from the Sellmeier equation for SiN [236]

$$n(\lambda)^2 = 1 + \frac{3.0249\lambda^2}{\lambda^2 - 135.3406^2} + \frac{40314\lambda^2}{\lambda^2 - 1239842^2},\tag{7.9}$$

with  $\lambda$  given in units [nm]. In the present study, n = 2.04 for  $\lambda = 632.8$  nm.

Fig. 7.3b shows how  $\eta$  varies with the film thickness h at this specific wavelength. The values corresponding to the thicknesses used in this work fall in the range  $\eta = 1 - 1.27$ and are summarized in Table 7.1.

With the various material and geometrical parameters defined, it is possible to extract the extinction coefficient  $\kappa_{\rm ext}$  for the different thin films.

#### 7.3 **Extinction Results**

In this section, the results concerning the optical extinction are discussed, and compared with the state-of-the-art characterization methods. It follows the analysis within the band-fluctuations model, which provides insights into the relationship between optical properties of SiN and the deposition processes involved in its growth.

The extinction coefficient values for each thin film have been extracted from the power responsivity measurements shown in Fig. 7.2 and with the use of Eq. (7.5) (first equality). Fig. 7.4 (black circles) presents the experimental nanomechanical photothermal results of  $\kappa_{\rm ext}$  as a function of the resonators' tensile stress  $\sigma_0$ .

 $\kappa_{\rm ext}$  decreases from  $\approx 10^3$  ppm for the lowest residual tensile stress, down to  $\approx 10^1$ for the highest. These findings are compared with previously reported values of optical extinction for LPCVD (colored circles), as well as plasma-enhanced chemical vapour

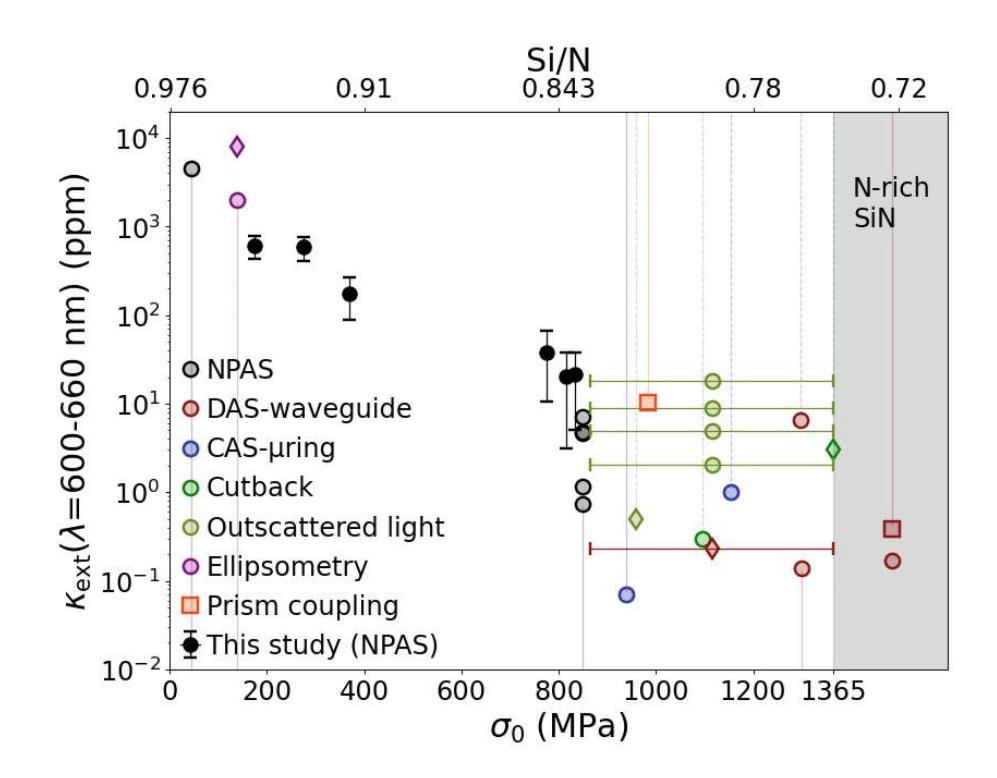


Figure 7.4:  $\kappa_{ext}$  for different SiN string's tensile stresses at an excitation wavelength of  $\lambda =$  $(632.8 \pm 30)$  nm. Characterization techniques included in the figure are: nanomechanical photothermal absorption spectroscopy (NPAS) [74], direct absorption spectroscopy (DAS) in waveguides [237–240], cavity absorption spectroscopy in microrings resonators (CASμring) [75, 241], cutback [99], ellipsometry [91], and prism coupling [105]. Markers refer to LPCVD (circles), plasma-enhanced CVD (PECVD, diamonds), and electron-cyclotron resonance CVD (ECR-CVD, squares) deposited SiN films. For the reported values, the vertical lines indicate a relationship with stress  $\sigma_0$  (intersection with the bottom x-axis) or Si/N (intersection with the top x-axis), explicitly given in (solid lines) or derived from (dashed lines) the original article (for more details see Appendix A). When none of these values could be extracted, a stress error bar has been used ( $\sigma_0 = 865 - 1365 \text{ MPa}$ ).

deposition (PECVD, colored diamonds), and electron cyclotron resonance chemical vapour deposition (ECR-CVD, colored squares) deposited SiN films (for details on their deposition dependencies, see Appendix B). The variance in magnitude among the compiled data for  $\sigma_0 \geq 850$  MPa can be partially attributed also to the inhability of some of the considered techniques to differentiate between true absorption and scattering losses (in particular cutback and outscattered light methods [75]).

Overall, a general trend emerges in Fig. 7.4, with  $\kappa_{\rm ext}$  decreasing for increasingly higher SiN deposition-related tensile stress. These results suggests a correlation of the variations in optical extinction to differences in compositional content among the various thin films under study.

#### **Band-fluctuations Model** 7.3.1

To provide insights on the relationship between the optical extinction and the deposition process, the absorption results (7.1) extracted from the experimental responsivity are analyzed within the framework of the band-fluctuations model [110]. This model accurately describes both the fundamental band-to-band absorption and the Urbach absorption tail, encountered in crystalline, as well as amorphous semiconductors, in a unified way.

Band-to-band absorption occurs between the extended electronic states forming the valence and conduction bands. For the case of amorphous materials like SiN, it follows  $\alpha_{\rm abs}(\hbar\omega) \propto (\hbar\omega - E_{\rm g})^2$ , where  $E_{\rm g}$  denotes the energy bandgap of the material under study in units [eV].

The Urbach tail refers to the absorption occurring between extended states and disorderinduced localized electronic states. This contribution is more pronounced in amorphous materials compared to crystalline ones, due to the increase in disorder-induced density of states (DOS), and follows the relation  $\alpha_{\rm abs}(\hbar\omega) \propto e^{\beta\hbar\omega}$ , where  $\beta^{-1}$  denotes the Urbach energy, with units [eV].

Within this framework, the absorption coefficient (in [dB/m]) for amorphous materials can be written as a function of the excitation energy  $\hbar\omega$  as

$$\alpha_{\rm abs}(\hbar\omega) = \frac{\alpha_0}{\hbar\omega} \frac{1}{\beta^2} \mathcal{J}_{\rm cv}(\beta(\hbar\omega - E_{\rm g})),$$
 (7.10)

with  $\alpha_0$ , and  $\mathcal{J}_{cv}$  denoting a coefficient collecting physical constants in units [m<sup>-1</sup>eV<sup>-1</sup>], and a dimensionless joint DOS, respectively. Fig. 7.5 shows the corresponding functional form: Eq. (7.10) converges to the band-to-band absorption, also called Tauc regime [95], for energy  $\hbar \omega > E_{\rm g}$  (dashed blue curve); for  $\hbar \omega < E_{\rm g}$ , the band-fluctuations model converges to the Urbach regime [110] (dashed red curve).

The model input parameters  $E_{\rm g}$  and  $\beta^{-1}$  are responsible for the dependence of the absorption on the deposition process, notably through the residual tensile stress present in the thin films analyzed here. In turn, this dependence is underpinned by the underlying correlation between stress and the corresponding Si/N content ratio, with the former increasing as the latter is reduced (see Table 7.1), as observed in LPCVD, as well as PECVD and ECR-CVD deposited SiN films [93, 95, 242]. Therefore, the reduction of the optical extinction observed in Fig. 7.4 for increasing tensile stress has to be related

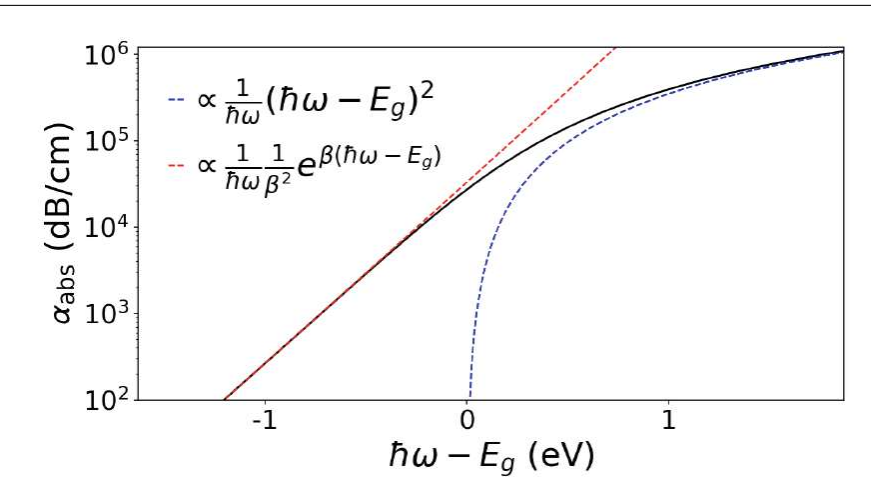


Figure 7.5: Absorption coefficient in the band-fluctuations model. The dashed blue and red curves represent the absorption due to electronic transition between extended states (Tauc regime), and absorption due to disorder-induced localized to extended state transitions (Urbach regime), respectively.

to the difference in chemical composition of the thin films. For this reason, a chemical analysis has been carried out with X-ray photoelectron spectroscopy (XPS).

The Si/N content ratio of each chip has been experimentally characterized with a PHI Versa Probe III-spectrometer, equipped with a monochromator Al- $K_{\alpha}$  X-ray source and a hemispherical analyser. Data analysis was performed using CASA XPS and Multipak software packages. The results are displayed in Table 7.1, and are consistent with those reported in previous works for a similar tensile stress range [95, 98, 242]. For completeness, these values are also shown in the top x-axis of Fig. 7.4 to highlight how SiN extinction coefficient increases with the Si/N ratio. The relationship between energy bandgap  $E_{\rm g}$ and Si/N ratio is considered first.

For each thin film,  $E_{\rm g}$  has been extracted by means of the fitting curve constructed from the compilation of previous works on LPCVD SiN only [75, 93, 95, 243]. The compiled data are shown in Fig. 7.6a, together with the fitting curve (solid black)  $f(x) = ae^{-bx} + c$ , with a = 95.94 eV, b = 4.356, and c = 1.633 eV. The XPS data (dashed vertical lines) are shown for clarity, and fall in the region of strongest dependence on the Si/N ratio. The corresponding energy bandgap has been found to increase from  $\approx 3$  eV, for the highest relative Si concentration, to  $\approx 4.2$  eV, for the lowest. All these values exceed the probing energy used in this work ( $\hbar\omega = 1.96 \text{ eV}$ ), indicating that the absorption results from localized-to-extended electronic transitions of disorder-induced tail states.

Once the energy bandgap has been defined for each thin film, the corresponding Urbach energy  $\beta^{-1}$  has been determined by matching the experimental absorption to the band-fluctuations model. The results are shown in Fig. 7.6b and Table 7.1, and are consistent with the previously reported studies of LPCVD SiN ( $\beta^{-1} \approx 200$  meV), as it can be observed in Fig. 7.7 [75, 243].  $\beta^{-1}$  slightly decreases with increasing Si/N ratios, as it has been observed also for PECVD deposited SiN, but at lower values. Overall,

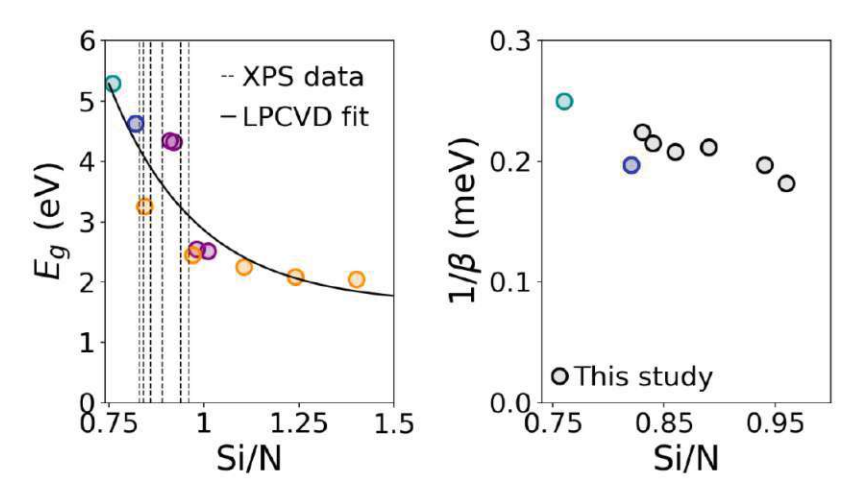


Figure 7.6: Left: Energy bandgap  $E_{\rm g}$  as a function of the Si/N ratio. The solid curve is a fitting function of the displayed reported values of the form  $f(x) = ae^{bx} + c$ , with a = 95.94 eV, b = 4.356, and c = 1.633 eV. Only LPCDV SiN films have been considered. Compilation: darkcyan, Ref. 243; blue, Ref. 75; purple, Ref. 95; orange, Ref. 93. Dashed vertical lines indicate the Si/N ratios measured in this study with XPS. Intersections with the fitting curve are given in Table 7.1. Right: Corresponding Urbach energy  $\beta^{-1}$  of the thin films analyzed in this study (black circles). For comparison, data from Ref. 243 (darkcyan) and Ref. 75 (blues) are displayed.

LPCVD films show a lower Urbach energy than PECVD, meaning that absorption due to electronic transition between disorder-induced localized to extended states is increases in the former.

Hence, lowering the Si/N ratio has the main effect of shifting the bandgap  $E_{\rm g}$  to higher

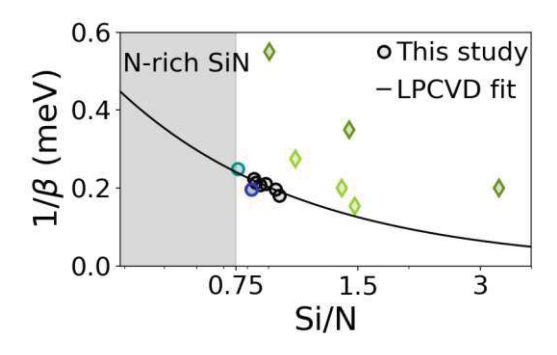


Figure 7.7: Urbach energy  $\beta^{-1}$  as a function of the Si/N ratio, for LPCVD (circles) and PECVD (diamond) SiN films. The compilation of data includes: blue, Ref.75; darkcyan, Ref. 243; dark green, Ref. 244; light green, Ref. 245. The solid curve is a fitting curve of the form  $f(x) = ae^b$  for the LPCVD data only, with a = 0.1843 meV and b = -0.9427.



energies, broadening the SiN transparency window. Conversely, the Urbach energy  $\beta^{-1}$ does not vary significantly among these thin films, indicating that the reduction in extinction coefficient  $\kappa_{\text{ext}}$  is driven by an exponential reduction in the disorder-induced electronic tail DOS at the probing energy of 1.96 eV.

#### 7.4 Conclusions and Outlook

This work has demonstrated that nanomechanical photothermal spectroscopy serves as a highly sensitive, simple, and scattering-free method for the optical characterization of low-loss materials. By employing string resonators made from LPCVD-deposited SiN, this study explored the potential of this platform. Through precise characterization of both mechanical and thermomechanical properties, it was observed that the intrinsic optical extinction coefficient of SiN decreases with increasing tensile stress in the thin films. This reduction in optical extinction is attributed to a blue shift in the energy bandgap, which correlates with the material's composition, specifically the Si/N ratio. The findings highlight that controlling the Si/N ratio offers a tunable approach to adjusting the optical properties of SiN, providing a valuable tool for furthering the understanding of this widely used material. These insights not only enhance knowledge of SiN but also open pathways for optimizing its properties for future applications, where minimizing optical losses is crucial.



# Photothermal back-action

#### **A.1** Experimental evaluation

To quantify the magnitude of the photothermal back-action on the final fractional frequency fluctuations of the resonator, the optical power PSD  $S_P(\omega, \lambda)$  is measured recording the optical power in time  $P_0(t)$  for 1 minute with a silicon photodiode (Thorlabs GmbH S120C,  $1\mu m$  response time) together with a digital power meter console (Thorlabs GmbH PM100D), as shown in Fig. A.1a. The power is then converted in frequency through the use of Eq. (4.15), as shown in Fig. A.1b. The resulting frequency signal is then filtered with a low-pass filter with transfer function  $H_{\rm th}(\omega) = (1 + i\omega \tau_{\rm th})^{-1}$ , to account for the finite time response of the resonator. Fig. A.1c shows the fractional frequency PSD of the signal before (dark red) and after (orange) the filtering. The Allan deviation of the filtered signal is then computed using Eq. (3.40), with an example shown in Fig. A.1d.



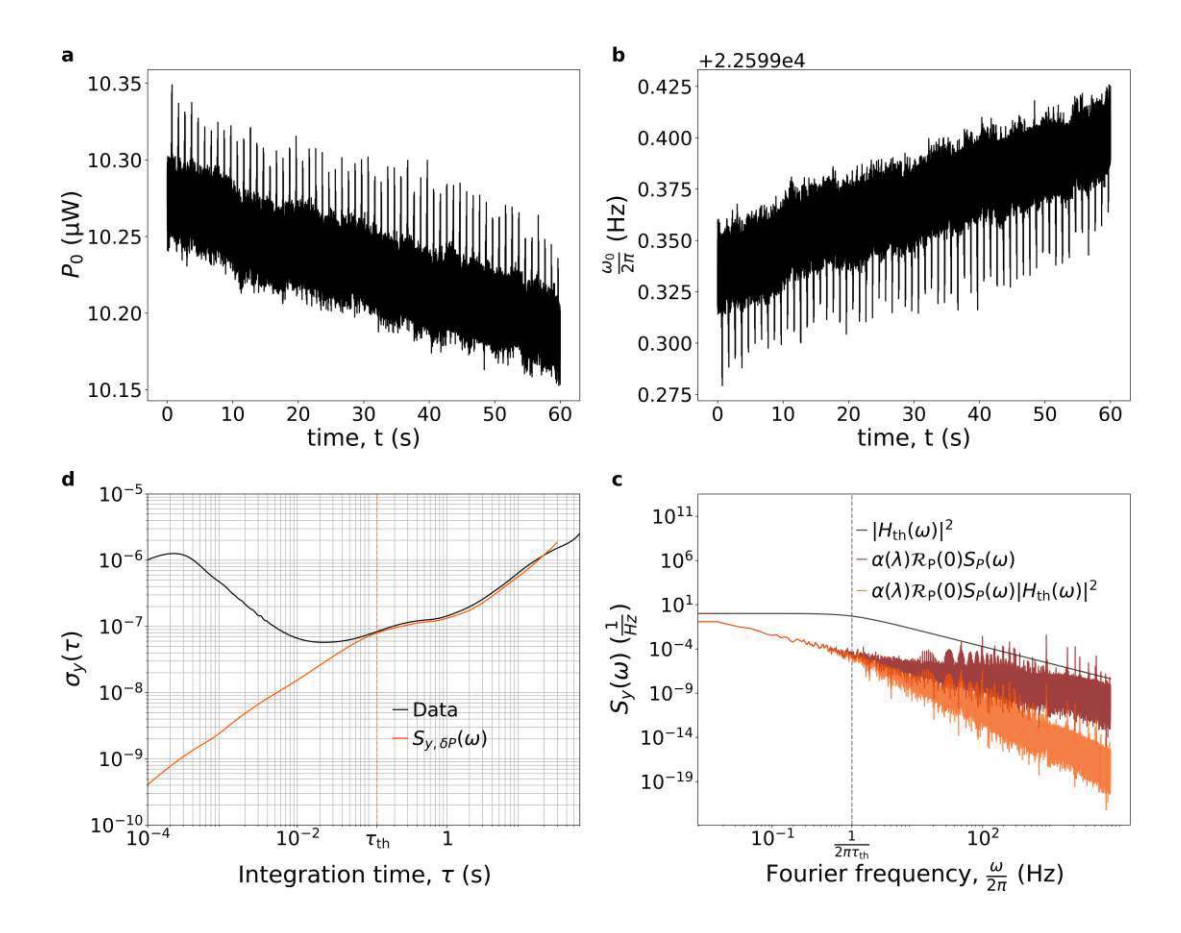


Figure A.1: a Power signal recorded for 1 minute with . b Corresponding frequency signal using Eq. (4.15). c Fractional frequency PSD before (dark red) and after (orange) low-pass filtering with a transfer function  $H_{\mathrm{th}}(\omega)$  (black curve). d Resulting AD (orange), compared to the experimental one (black curve).



# APPENDIX

# Optical characterization of LPCVD SiN - Appendix

### B.1Compilation of state-of-the-art techniques for low-loss absorption characterization

The compiled data shown in Fig. 7.4 relate to various state-of-the-art optical characterization methods for low-loss materials and covered the wavelength range of 600 – 660 nm. The list of the different techniques considered for the comparison is presented in Table B.1. For some of the works included in this analysis, no explicit reference to the tensile stress or Si/N ratio were provided. To account for this, values have been derived exploiting the existing relationship between the dispersive part of the refractive index n and the Si/N ratio, as shown in prior studies [90, 246]. This relationship allows for the estimation of the material composition and/or stress levels from the refractive index

The derivation process for each reference is detailed below where necessary, and is divided into LPCVD and PECVD deposited SiN related categories.

#### Derived Parameters for LPCVD B.1.1

For LPCVD SiN thin films, the measurements carried out in Ref. [90] were used to derived the Si/N ratio from  $n_{LPCVD}$  at 632.8 nm wavelength. Fig. B.1 shows the reported values (circles), together with the corresponding fit. The latter has the form  $f(x) = p_1 x^2 + p_2 x + p_3$ , with  $p_1 = -0.9333$ ,  $p_2 = 2.839$ , and  $p_3 = 0.3608$ .

The works and the corresponding derived values are listed below:

• In Ref. [241], it is reported a value  $n_{\text{LPCVD}} = 2.0115$  for TE mode at 632.8 nm wavelength, resulting in Si/N ratio of 0.783.

Table B.1: List of the extinction values and corresponding parameters used in the main text ( $\lambda = 600 - 660 \text{ nm}$ ).

Reference	Deposition	Method	λ (nm)	$\kappa_{\rm ext} \ ({\rm ppm})$	$\sigma_0 \text{ (MPa)}$	Si/N
74	LPCVD	NPAS	632.8	0.73	850	-
				1.17		
				4.64		
				7.07		
				4.84		
237	LPCVD	DAS-waveguide	630	0.17	-	0.73
	ECR-CVD			0.39		
238	PECVD	DAS-waveguide	632.8	0.23	-	-
75	LPCVD	CAS-pring	644	0.07	-	0.82
241	LPCVD	CAS-µring	632.8	1	-	$0.783^{a}$
99	LPCVD	Cutback	643	0.3	-	$0.794^{a}$
	PECVD			3		$0.751^{b}$
101	LPCVD	Outscattered light	633	18.134	-	-
102	LPCVD	Outscattered light	660	8.98	-	-
100	LPCVD	Outscattered light	630	4.91	-	-
103	LPCVD	Outscattered light	640	2.037	-	-
104	PECVD	Outscattered light	633	0.5	-	$0.817^{b}$
240	LPCVD	DAS-waveguide	648	6.54	-	$0.761^{a}$
91	LPCVD	Ellipsometry	633	2000	137.5	-
	PECVD			8000		
105	ECR-CVD	Prism coupling	632.8	10.15	-	0.813

a Value derived from the dispersive refractive index  $n_{\text{LPCVD}}$  for LPCVD.

<sup>&</sup>lt;sup>b</sup> Value derived from the dispersive refractive index  $n_{\text{PECVD}}$  for PECVD.

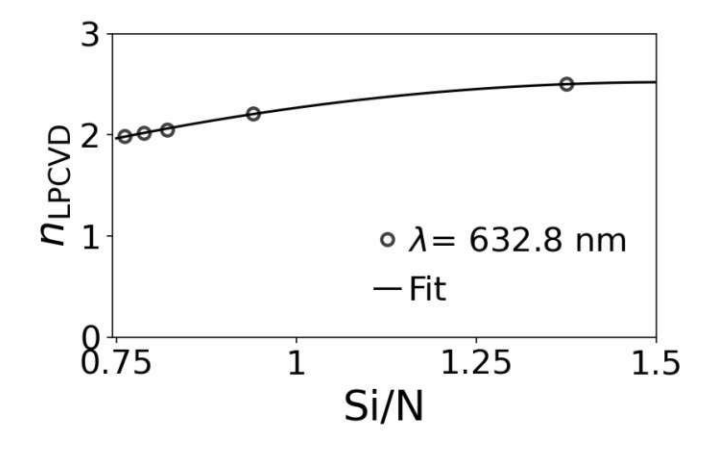


Figure B.1: Refractive index as a function of the Si/N ratio in LPCVD SiN, measured at 632.8 nm wavelength (circles). The solid curve is the fit used to derive the Si/N ratio.

• In Ref. [99], n is obtained upon fitting of the ellipsometric data with the Sellmeier equation

$$n_{\text{LPCVD}} = \sqrt{1 + \frac{2.926\lambda^2}{\lambda^2 - 23.47 \cdot 10^{-15}}},$$
 (B.1)

which results in  $n_{LPCVD}(643 \text{ nm}) = 2.02536$ , resulting in a Si/N ratio of 0.794.

• In Ref. [240], it is reported a value of  $n_{LPCVD}(648 \text{ nm}) = 1.98$ , resulting in a Si/N ratio of 0.761.

#### B.1.2 Derived Parameters for PECVD

For PECVD SiN thin films, the relationship between refractive index and Si/N ratio is derived using the formula from Ref. [246]

$$\frac{\text{Si}}{\text{N}} = \frac{3}{4} \frac{n_{\text{PECVD}} + n_{\text{a-Si:H}} - 2n_{\text{a-Si_3N_4}}}{n_{\text{a-Si:H}} - n_{\text{PECVD}}},$$
(B.2)

with  $n_{\text{PECVD}}$ ,  $n_{\text{a-Si:H}}(632.8 \text{ nm}) = 3.3$ , and  $n_{\text{a-Si;N}_4}(632.8 \text{ nm}) = 1.9$  denoting the measured refractive index, the index for a-Si:H, and for the stoichiometric SiN, respectively

In the following, the list of the PECVD related works and corresponding derived values is presented:

• In Ref. [99], the Sellmeier equation obtained by fitting the ellipsometry results has been given as

$$n_{\text{PECVD}} = \sqrt{1 + \frac{2.503\lambda^2}{\lambda^2 - 17.29 \cdot 10^{-15}}}$$
 (B.3)

Hence,  $n_{\text{PECVD}}(643 \text{ nm}) = 1.9006$ , resulting in a Si/N ratio of 0.751.

• In Ref. [104], it is reported a value  $n_{\text{PECVD}}(633 \text{ nm}) = 1.96$ , resulting in a Si/N ratio of 0.817.

#### **B.2** XPS measurements

All measurements were carried out on a PHI Versa Probe III-spectrometer equipped with a monochromatic Al-K $\alpha$  X-ray source and a hemispherical analyser (acceptance angle:  $\pm 20$ ř). Pass energies of 140 eV and as well as step widths of 0.5 eV were used for survey and detail spectra, respectively. (Excitation energy: 1486.6 eV Beam energy and spot size: 50 W onto 200  $\mu$ m; Mean electron take-off angle: 45° to sample surface normal; Base pressure:  $< 8 \cdot 10^{-10}$  mbar, Pressure during measurements:  $< 1 \cdot 10^{-8}$  mbar). Samples were mounted on double -sided polymer tape. Electronic and ionic charge compensation was used for all measurements (automatized as provided by PHI). The binding energy (BE) scale and intensity were calibrated by using methods described in

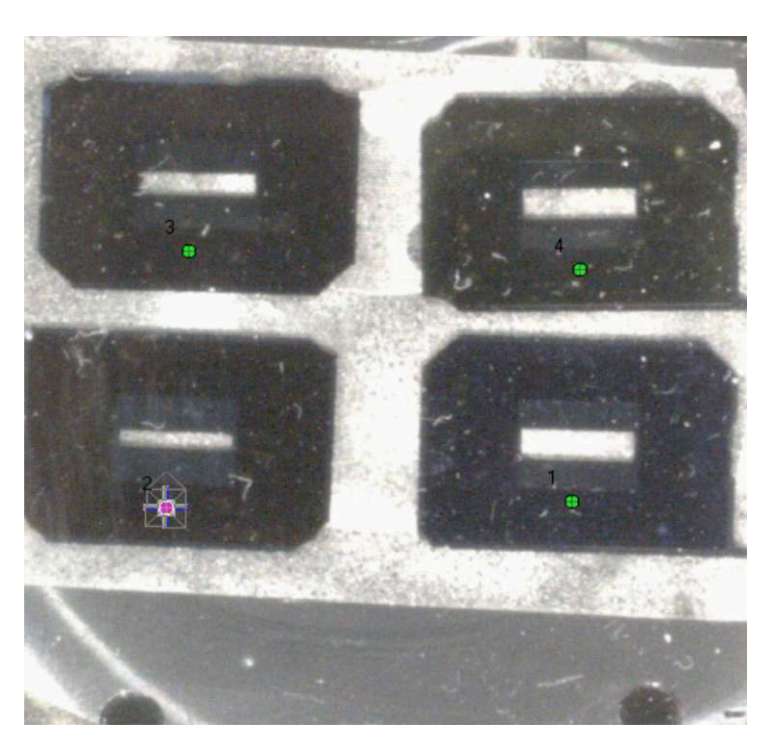


Figure B.2: Chips' regions for the XPS characterization of the Si/N content ratio.

## ISO15472, ISO21270 and ISO24237.

Surface cleaning was carried out using an Ar ion gun (2 kV, 2x2 mm,  $1.3 \mu A$ , 5 min). Data analysis was performed using CASA XPS and Multipak software packages, employing transmission corrections, Shirley/Tougaard backgrounds [247, 248] and customised Wagner sensitivity factors [249].

## **Bibliography**

- [1] Richard P Feynman. Classics there's plenty of room at the bottom an invitation to enter a new field of physics, 2011.
- [2] Arthur Mcgurn. Nanophotonics. Springer Series in Optical Sciences 213, 2018.
- [3] Andrew N. Cleland. Foundations of Nanomechanics. Springer Berlin Heidelberg, 2003.
- [4]Keith C. Schwab and Michael L. Roukes. Putting mechanics into quantum mechanics. Physics Today, 58:36–42, 2005.
- [5]Patricio Arrangoiz-Arriola, E. Alex Wollack, Zhaoyou Wang, Marek Pechal, Wentao Jiang, Timothy P. McKenna, Jeremy D. Witmer, Raphaël Van Laer, and Amir H. Safavi-Naeini. Resolving the energy levels of a nanomechanical oscillator. *Nature*, 571:537–540, 7 2019.
- [6] Lukas Novotny and Bert Hecht. Principles of Nano-Optics. Cambridge University Press, 2 edition, 2012.
- [7]A. N. Cleland and M. L. Roukes. Fabrication of high frequency nanometer scale mechanical resonators from bulk si crystals. Applied Physics Letters, 69:2653–2655. 10 1996.
- [8] David Mason, Junxin Chen, Massimiliano Rossi, Yeghishe Tsaturyan, and Albert Schliesser. Continuous force and displacement measurement below the standard quantum limit. Nature Physics, 15:745–749, 8 2019.
- [9] P. Rabl, S. J. Kolkowitz, F. H.L. Koppens, J. G.E. Harris, P. Zoller, and M. D. Lukin. A quantum spin transducer based on nanoelectromechanical resonator arrays. Nature Physics, 6:602-608, 2010.
- A. K. Naik, M. S. Hanay, W. K. Hiebert, X. L. Feng, and M. L. Roukes. Towards single-molecule nanomechanical mass spectrometry. Nature Nanotechnology, 4:445-450, 2009.



- J. Chaste, A. Eichler, J. Moser, G. Ceballos, R. Rurali, and A. Bachtold. A nanomechanical mass sensor with yoctogram resolution. Nature Nanotechnology, 7:301–304, 2012.
- M. S. Hanay, S. Kelber, A. K. Naik, D. Chi, S. Hentz, E. C. Bullard, E. Colinet, L. Duraffourg, and M. L. Roukes. Single-protein nanomechanical mass spectrometry in real time. Nature Nanotechnology, 7:602–608, 2012.
- John E. Sader, M. Selim Hanay, Adam P. Neumann, and Michael L. Roukes. Mass spectrometry using nanomechanical systems: Beyond the point-mass approximation. Nano Letters, 18:1608–1614, 3 2018.
- Eric Sage, Marc Sansa, Shawn Fostner, Martial Defoort, Marc Gély, Akshay K. Naik, Robert Morel, Laurent Duraffourg, Michael L. Roukes, Thomas Alava, Guillaume Jourdan, Eric Colinet, Christophe Masselon, Ariel Brenac, and Sébastien Hentz. Single-particle mass spectrometry with arrays of frequency-addressed nanomechanical resonators. Nature Communications, 9, 12 2018.
- Marc Sansa, Martial Defoort, Ariel Brenac, Maxime Hermouet, Louise Banniard, Alexandre Fafin, Marc Gely, Christophe Masselon, Ivan Favero, Guillaume Jourdan, and Sébastien Hentz. Optomechanical mass spectrometry. Nature Communications, 11, 12 2020.
- Shoko Yamada, Silvan Schmid, Tom Larsen, Ole Hansen, and Anja Boisen. Pho-[16]to thermal infrared spectroscopy of airborne samples with mechanical string resonators. Analytical Chemistry, 85:10531–10535, 11 2013.
- T. S. Biswas, N. Miriyala, C. Doolin, X. Liu, T. Thundat, and J. P. Davis. Femtogram-scale photothermal spectroscopy of explosive molecules on nanostrings. Analytical Chemistry, 86:11368–11372, 11 2014.
- Sanjukta Bose, Silvan Schmid, Tom Larsen, Stephan S. Keller, Peter Sommer-Larsen, Anja Boisen, and Kristoffer Almdal. Micromechanical string resonators: Analytical tool for thermal characterization of polymers. ACS Macro Letters, 3:55-58, 1 2014.
- Alina J. Andersen, Shoko Yamada, E. K. Pramodkumar, Thomas L. Andresen, Anja Boisen, and Silvan Schmid. Nanomechanical ir spectroscopy for fast analysis of liquid-dispersed engineered nanomaterials. Sensors and Actuators, B: Chemical, 233:667–673, 10 2016.
- Maksymilian Kurek, Matthias Carnoy, Peter E. Larsen, Line H. Nielsen, Ole [20]Hansen, Thomas Rades, Silvan Schmid, and Anja Boisen. Nanomechanical infrared spectroscopy with vibrating filters for pharmaceutical analysis. Angewandte Chemie - International Edition, 56:3901–3905, 3 2017.

- Maximilian Karl, Peter E. Larsen, Varadarajan P. Rangacharya, En Te Hwu, Jukka Rantanen, Anja Boisen, and Thomas Rades. Ultrasensitive microstring resonators for solid state thermomechanical analysis of small and large molecules. Journal of the American Chemical Society, 140:17522–17531, 12 2018.
- Maximilian Karl, Lasse H.E. Thamdrup, Jukka Rantanen, Anja Boisen, and Thomas Rades. Temperature-modulated micromechanical thermal analysis with microstring resonators detects multiple coherent features of small molecule glass transition. Sensors (Switzerland), 20, 2 2020.
- Niklas Luhmann, Robert G. West, Josiane P. Lafleur, and Silvan Schmid. Nanoelec-[23]tromechanical infrared spectroscopy with in situ separation by thermal desorption: Nems-ir-td. ACS Sensors, 8:1462–1470, 4 2023.
- Miao Hsuan Chien, Mario Brameshuber, Benedikt K. Rossboth, Gerhard J. Schütz, and Silvan Schmid. Single-molecule optical absorption imaging by nanomechanical photothermal sensing. Proceedings of the National Academy of Sciences of the United States of America, 115:11150–11155, 10 2018.
- Tom Larsen, Silvan Schmid, Luis G. Villanueva, and Anja Boisen. Photothermal [25]analysis of individual nanoparticulate samples using micromechanical resonators. ACS Nano, 7:6188–6193, 7 2013.
- Silvan Schmid, Kaiyu Wu, Peter Emil Larsen, Tomas Rindzevicius, and Anja Boisen. Low-power photothermal probing of single plasmonic nanostructures with nanomechanical string resonators. Nano Letters, 14:2318–2321, 5 2014.
- Daniel Ramos, Oscar Malvar, Zachary J. Davis, Javier Tamayo, and Montserrat Calleja. Nanomechanical plasmon spectroscopy of single gold nanoparticles. Nano Letters, 18:7165–7170, 11 2018.
- Varadarajan Padmanabhan Rangacharya, Kaiyu Wu, Peter Emil Larsen, Lasse Højlund Eklund Thamdrup, Oleksii Ilchenko, En Te Hwu, Tomas Rindzevicius, and Anja Boisen. Quantifying optical absorption of single plasmonic nanoparticles and nanoparticle dimers using microstring resonators. ACS Sensors, 5:2067–2075, 7 2020.
- Miao Hsuan Chien and Silvan Schmid. Nanoelectromechanical photothermal polarization microscopy with 3 Å localization precision. Journal of Applied Physics, 128, 10 2020.
- Miao Hsuan Chien, Mostafa M. Shawrav, Kurt Hingerl, Philipp Taus, Markus Schinnerl, Heinz D. Wanzenboeck, and Silvan Schmid. Analysis of carbon content in direct-write plasmonic au structures by nanomechanical scanning absorption microscopy. Journal of Applied Physics, 129, 2 2021.

- Kostas Kanellopulos, Robert G. West, and Silvan Schmid. Nanomechanical photo thermal near infrared spectromicroscopy of individual nanorods. ACS Photonics, 10:3730–3739, 10 2023.
- Jan N. Kirchhof, Yuefeng Yu, Gabriel Antheaume, Georgy Gordeev, Denis Yagodkin, Peter Elliott, Daniel B. De Araújo, Sangeeta Sharma, Stephanie Reich, and Kirill I. Bolotin. Nanomechanical spectroscopy of 2d materials. Nano Letters, 22:8037–8044, 10 2022.
- Jan N. Kirchhof, Yuefeng Yu, Denis Yagodkin, Nele Stetzuhn, Daniel B. de Araújo, Kostas Kanellopulos, Samuel Manas-Valero, Eugenio Coronado, Herre van der Zant, Stephanie Reich, Silvan Schmid, and Kirill I. Bolotin. Nanomechanical absorption spectroscopy of 2d materials with femtowatt sensitivity. 2D Materials, 10, 7 2023.
- Fatemeh Samaeifar, Andrea Casci Ceccacci, Sanjukta Bose Goswami, Line Hagner Nielsen, Ahmad Afifi, Kinga Zór, and Anja Boisen. Evaluation of the solid state form of tadalafil in sub-micron thin films using nanomechanical infrared spectroscopy. International Journal of Pharmaceutics, 565:227–232, 6 2019.
- Andrea Casci Ceccacci, Alberto Cagliani, Paolo Marizza, Silvan Schmid, and Anja Boisen. Thin film analysis by nanomechanical infrared spectroscopy. ACS Omega, 4:7628-7635, 4 2019.
- X. C. Zhang, E. B. Myers, J. E. Sader, and M. L. Roukes. Nanomechanical torsional resonators for frequency-shift infrared thermal sensing. Nano Letters, 13:1528–1534, 4 2013.
- Laurent Duraffourg, Ludovic Laurent, Jean Sébastien Moulet, Julien Arcamone, and Jean Jacques Yon. Array of resonant electromechanical nanosystems: A technological breakthrough for uncooled infrared imaging. *Micromachines*, 9, 8 2018.
- Andrew Blaikie, David Miller, and Benjamín J. Alemán. A fast and sensitive room-temperature graphene nanomechanical bolometer. Nature Communications, 10, 12 2019.
- Leonardo Vicarelli, Alessandro Tredicucci, and Alessandro Pitanti. Micromechanical bolometers for subterahertz detection at room temperature. ACS Photonics, 9:360-367, 2 2022.
- Markus Piller, Johannes Hiesberger, Elisabeth Wistrela, Paolo Martini, Niklas Luhmann, and Silvan Schmid. Thermal ir detection with nanoelectromechanical silicon nitride trampoline resonators. IEEE Sensors Journal, 23:1066–1071, 1 2023.
- Chao Li, Ya Zhang, and Kazuhiko Hirakawa. Terahertz detectors using microelectromechanical system resonators. Sensors, 23, 7 2023.

- Chang Zhang, Eeswar K Yalavarthi, Mathieu Giroux, Wei Cui, Michel Stephan, Ali [42]Maleki, Arnaud Weck, Jean-Michel Ménard, and Raphael St-Gelais. High detectivity terahertz radiation sensing using frequency-noise-optimized nanomechanical resonators, 2024.
- W. E. Moerner. Viewpoint: Single molecules at 31: What's next? Nano Letters, 20:8427-8429, 12 2020.
- Nidhi Chauhan, Kirti Saxena, and Utkarsh Jain. Single molecule detection; from microscopy to sensors. International Journal of Biological Macromolecules, 209:1389– 1401, 6 2022.
- Subhasis Adhikari and Michel Orrit. Progress and perspectives in single-molecule optical spectroscopy. Journal of Chemical Physics, 156, 4 2022.
- Grant J. Simpson, Víctor García-López, A. Daniel Boese, James M. Tour, and Leonhard Grill. How to control single-molecule rotation. Nature Communications, 10, 12 2019.
- Lisanne Sellies, Raffael Spachtholz, Sonja Bleher, Jakob Eckrich, Philipp Scheuerer, and Jascha Repp. Single-molecule electron spin resonance by means of atomic force microscopy. Nature, 624:64-68, 12 2023.
- Lee Priest, Jack S. Peters, and Philipp Kukura. Scattering-based light microscopy: From metal nanoparticles to single proteins. Chemical Reviews, 121:11937–11970, 10 2021.
- W. E. Moerner and L. Kador. Optical detection and spectroscopy of single molecules in a solid. Physical Review Letters, 62:2535–2538, 1989.
- M Orrit. Single pentacene molecules detected by fluorescence excitation in a p-terphenyl crystal. Physical Review Letters, 65, 1990.
- [51]Leonhard Möckl and W. E. Moerner. Super-resolution microscopy with single molecules in biology and beyond-essentials, current trends, and future challenges. Journal of the American Chemical Society, 142:17828–17844, 10 2020.
- Jaime Ortega Arroyo and Philipp Kukura. Non-fluorescent schemes for singlemolecule detection, imaging and spectroscopy. Nature Photonics, 10:11–17, 1 2016.
- Warwick Bowen, Frank Vollmer, and Reuven Gordon. Single Molecule Sensing [53]Beyond Fluorescence. Springer Cham, 2022.
- Craig F. Bohren and Donald R. Huffman. Absorption and scattering of light by small particles. Wiley, 1983.

- Judith Langer et al. Present and future of surface-enhanced raman scattering. ACS Nano, 14:28–117, 1 2020.
- [56]Shasha Chong, Wei Min, and X. Sunney Xie. Ground-state depletion microscopy: Detection sensitivity of single-molecule optical absorption at room temperature. Journal of Physical Chemistry Letters, 1:3316–3322, 12 2010.
- [57]Subhasis Adhikari, Patrick Spaeth, Ashish Kar, Martin Dieter Baaske, Saumyakanti Khatua, and Michel Orrit. Photothermal microscopy: Imaging the optical absorption of single nanoparticles and single molecules. ACS Nano, 14:16414–16445, 12
- A. Gaiduk, M. Yorulmaz, P.V. Ruijgrok, and Michel Orrit. Room-temperature detection of a single molecule's absorption by photothermal contrast. Science, 330:353–356, 10 2010.
- Kevin D. Hevlman, Niket Thakkar, Erik H. Horak, Steven C. Quillin, Charles Cherqui, Kassandra A. Knapper, David J. Masiello, and Randall H. Goldsmith. Optical microresonators as single-particle absorption spectrometers. Nature Photonics, 10:788-795, 11 2016.
- Silvan Schmid, Luis Guillermo Villanueva, and Michael Lee Roukes. Fundamentals of Nanomechanical Resonators. Springer International Publishing, 2023.
- Robert G. West, Kostas Kanellopulos, and Silvan Schmid. Photothermal microscopy and spectroscopy with nanomechanical resonators. The Journal of Physical Chemistry C, 127:21915–21929, 11 2023.
- [62]Antoni Rogalski. Infrared and Terahertz Detectors, volume 3rd Edition. CRC Press, 2019.
- Markus Piller, Niklas Luhmann, Miao-Hsuan Chien, and Silvan Schmid. Nanoelectromechanical infrared detector. Proc. of SPIE, 11088:1, 9 2019.
- [64]Hamza Shakeel, Haoyan Wei, and J. M. Pomeroy. Measurements of enthalpy of sublimation of ne, n2, o2, ar, co2, kr, xe, and h2o using a double paddle oscillator. Journal of Chemical Thermodynamics, 118:127–138, 3 2018.
- Mathieu Giroux, Chang Zhang, Nikaya Snell, Gengyang Mu, Michel Stephan, and Raphael St-Gelais. High resolution measurement of near-field radiative heat transfer enabled by nanomechanical resonators. Applied Physics Letters, 119, 10 2021.
- [66]Mathieu Giroux, Michel Stephan, Maxime Brazeau, Sean Molesky, Alejandro W. Rodriguez, Jacob J. Krich, Karin Hinzer, and Raphael St-Gelais. Measurement of near-field radiative heat transfer at deep sub-wavelength distances using nanomechanical resonators. Nano Letters, 23:8490–8497, 9 2023.

- King Yan Fong, Hao Kun Li, Rongkuo Zhao, Sui Yang, Yuan Wang, and Xiang Zhang. Phonon heat transfer across a vacuum through quantum fluctuations. Nature, 576:243–247, 12 2019.
- [68]Chang Zhang and Raphael St-Gelais. Demonstration of frequency stability limited by thermal fluctuation noise in silicon nitride nanomechanical resonators. Appl. Phys. Lett., 122:193501, 5 2023.
- Pedram Sadeghi, Manuel Tanzer, Niklas Luhmann, Markus Piller, Miao Hsuan Chien, and Silvan Schmid. Thermal transport and frequency response of localized modes on low-stress nanomechanical silicon nitride drums featuring a phononicband-gap structure. Phys. Rev. Appl., 14:024068, 8 2020.
- Y. Tsaturyan, A. Barg, E. S. Polzik, and A. Schliesser. Ultracoherent nanomechanical resonators via soft clamping and dissipation dilution. Nature Nanotechnology, 12:776–783, 8 2017.
- Niklas Luhmann, Dennis Høj, Markus Piller, Hendrik Kähler, Miao Hsuan Chien, Robert G. West, Ulrik Lund Andersen, and Silvan Schmid. Ultrathin 2 nm gold as impedance-matched absorber for infrared light. Nature Communications, 11, 12 2020.
- Miao Hsuan Chien, Johannes Steurer, Pedram Sadeghi, Nicolas Cazier, and Silvan Schmid. Nanoelectromechanical position-sensitive detector with picometer resolution. ACS Photonics, 7:2197–2203, 8 2020.
- Christian M. Pluchar, Aman R. Agrawal, Edward Schenk, and Dalziel J. Wilson. [73]Towards cavity-free ground-state cooling of an acoustic-frequency silicon nitride membrane. Applied Optics, 59:G107, 8 2020.
- Andrew T. Land, Mitul Dey Chowdhury, Aman R. Agrawal, and Dalziel J. Wilson. Sub-ppm nanomechanical absorption spectroscopy of silicon nitride. Nano Letters, 5 2024.
- Mateus Corato-Zanarella, Xingchen Ji, Aseema Mohanty, and Michal Lipson. Absorption and scattering limits of silicon nitride integrated photonics in the visible spectrum. Optics Express, 32:5718, 2 2024.
- [76]Galan Moody et al. 2022 roadmap on integrated quantum photonics. JPhys Photonics, 4, 1 2022.
- Nitesh Chauhan, Jiawei Wang, Debapam Bose, Kaikai Liu, R. L. Compton, C. Fertig, C. W. Hoyt, and Daniel J. Blumenthal. Ultra-low loss visible light waveguides for integrated atomic, molecular, and quantum photonics. Optics Express, 30:6960, 2 2022.

- Laurent C. Moreaux, Dimitri Yatsenko, Wesley D. Sacher, Jaebin Choi, Changhyuk Lee, Nicole J. Kubat, R. James Cotton, Edward S. Boyden, Michael Z. Lin, Lin Tian, Andreas S. Tolias, Joyce K.S. Poon, Kenneth L. Shepard, and Michael L. Roukes. Integrated neurophotonics: Toward dense volumetric interrogation of brain circuit activity—at depth and in real time. Neuron, 108:66–92, 10 2020.
- Aseema Mohanty, Qian Li, Mohammad Amin Tadayon, Samantha P. Roberts, Gaurang R. Bhatt, Euijae Shim, Xingchen Ji, Jaime Cardenas, Steven A. Miller, Adam Kepecs, and Michal Lipson. Reconfigurable nanophotonic silicon probes for sub-millisecond deep-brain optical stimulation. Nature Biomedical Engineering, 4:223-231, 2 2020.
- Dalziel Joseph Wilson. Cavity Optomechanics with High-Stress Silicon Nitride Films. California Institute of Technology, 2012. Ph.D. Dissertation.
- Christoph Reinhardt, Tina Müller, Alexandre Bourassa, and Jack C. Sankey. [81]Ultralow-noise sin trampoline resonators for sensing and optomechanics. Physical Review X, 6, 2016.
- [82]Claus Gärtner, João P. Moura, Wouter Haaxman, Richard A. Norte, and Simon Gröblacher. Integrated optomechanical arrays of two high reflectivity sin membranes. Nano Letters, 18:7171–7175, 11 2018.
- Guanhao Huang, Alberto Beccari, Nils J. Engelsen, and Tobias J. Kippenberg. Room-temperature quantum optomechanics using an ultralow noise cavity. Nature, 626:512-516, 2 2024.
- Constanze Metzger, Max Ludwig, Clemens Neuenhahn, Alexander Ortlieb, Ivan [84]Favero, Khaled Karrai, and Florian Marquardt. Self-induced oscillations in an optomechanical system driven by bolometric backaction. Physical Review Letters, 101, 9 2008.
- K An, B A Sones, C Fang-Yen, R R Dasari, and M S Feld. Optical bistability induced by mirror absorption: measurement of absorption coefficients at the sub-ppm level. OPTICS LETTERS, 22:1433, 1997.
- Nikaya Snell, Chang Zhang, Gengyang Mu, Alexandre Bouchard, and Raphael [86]St-Gelais. Heat transport in silicon nitride drum resonators and its influence on thermal fluctuation-induced frequency noise. Physical Review Applied, 17, 4 2022.
- Alain E. Kaloyeros, Youlin Pan, Jonathan Goff, and Barry Arkles. Review—silicon [87]nitride and silicon nitride-rich thin film technologies: State-of-the-art processing technologies, properties, and applications. ECS Journal of Solid State Science and Technology, 9:063006, 1 2020.
- Xingchen Ji, Yoshitomo Okawachi, Andres Gil-Molina, Mateus Corato-Zanarella, Samantha Roberts, Alexander L. Gaeta, and Michal Lipson. Ultra-low-loss silicon

- nitride photonics based on deposited films compatible with foundries. Laser and Photonics Reviews, 17, 3 2023.
- Daniel J. Blumenthal, René Heideman, Douwe Geuzebroek, Arne Leinse, and Chris Roeloffzen. Silicon nitride in silicon photonics. Proceedings of the IEEE, 106:2209-2231, 12 2018.
- [90] Takahiro Makino. Composition and structure control by source gas ratio in lpcvd sinx. J. Electrochem. Soc., 130(2):450, feb 1983.
- Daniel P Poenar and Reinoud F Wolffenbuttel. Optical properties of thin-film silicon-compatible materials. Appl. Opt., 36:5122, 7 1997.
- Pao Tai Lin, Vivek Singh, Hao Yu Greg Lin, Tom Tiwald, Lionel C. Kimerling, and Anuradha Murthy Agarwal. Low-stress silicon nitride platform for mid-infrared broadband and monolithically integrated microphotonics. Adv. Opt. Mater., 1:732-739, 10 2013.
- [93]Clemens J. Krückel, Attila Fülöp, Zhichao Ye, Peter A. Andrekson, and Victor Torres-Company. Optical bandgap engineering in nonlinear silicon nitride waveguides. Opt. Express, 25:15370, 6 2017.
- Joao Resende, David Fuard, Delphine Le Cunff, Jean-Herve Tortai, and Bernard Pelissier. Hybridization of ellipsometry and energy loss spectra from xps for bandgap and optical constants determination in sion thin films. Mater. Chem. Phys., 259:124000, 2021.
- Leonid Yu. Beliaev, Evgeniy Shkondin, Andrei V. Lavrinenko, and Osamu Takayama. Optical, structural and composition properties of silicon nitride films deposited by reactive radio-frequency sputtering, low pressure and plasma-enhanced chemical vapor deposition. Thin Solid Films, 763:139568, 2022.
- Herbert R. Philipp. Optical properties of silicon nitride. J. Electrochem. Soc., 120(2):295, feb 1973.
- Giuseppe Cataldo, James A. Beall, Hsiao-Mei Cho, Brendan McAndrew, Michael D. [97]Niemack, and Edward J. Wollack. Infrared dielectric properties of low-stress silicon nitride. Opt. Lett., 37(20):4200-4202, Oct 2012.
- Chris Yang and John Pham. Characteristic study of silicon nitride films deposited [98]by lpcvd and pecvd. Silicon, 10:2561–2567, 11 2018.
- Cheryl Sorace-Agaskar, Dave Kharas, Siva Yegnanarayanan, Ryan T. Maxson, Gavin N. West, William Loh, Suraj Bramhavar, Rajeev J. Ram, John Chiaverini, Jeremy Sage, and Paul Juodawlkis. Versatile silicon nitride and alumina integrated photonic platforms for the ultraviolet to short-wave infrared. IEEE J. Sel. Top. Quantum Electron., 25(5):1–15, 2019.



- [100] Jack A. Smith, Henry Francis, Gabriele Navickaite, and Michael J. Strain. Sin foundry platform for high performance visible light integrated photonics. Opt. Mater. Express, 13:458, 2 2023.
- [101] Marçal Blasco-Solvas, Berta Fernández-Vior, Jad Sabek, Adrián Fernández-Gavela, Thalía Domínguez-Bucio, Frederic Y. Gardes, Carlos Domínguez-Horna, and Joaquín Faneca. Silicon nitride building blocks in the visible range of the spectrum. J. Light. Technol., pages 1–10, 2024.
- [102] Marcin Lelit, Mateusz Słowikowski, Maciej Filipiak, Marcin Juchniewicz, Bartłomiej Stonio, Bartosz Michalak, Krystian Pavłov, Marcin Myśliwiec, Piotr Wiśniewski, Andrzej Kaźmierczak, Krzysztof Anders, Stanisław Stopiński, Romuald B. Beck, and Ryszard Piramidowicz. Passive photonic integrated circuits elements fabricated on a silicon nitride platform. Materials, 15(4), 2022.
- [103] Alireza Tabatabaei Mashayekh, Thomas Klos, Douwe Geuzebroek, Edwin Klein, Theo Veenstra, Martin Büscher, Florian Merget, Patrick Leisching, and Jeremy Witzens. Silicon nitride pic-based multi-color laser engines for life science applications. Opt. Express, 29:8635, 3 2021.
- [104] A. Gorin, A. Jaouad, E. Grondin, V. Aimez, and P. Charette. Fabrication of silicon nitride waveguides for visible-light using pecvd: a study of the effect of plasma frequency on optical properties. Opt. Express, 16(18):13509–13516, Sep 2008.
- [105] Dawson B. Bonneville, Jeremy W. Miller, Caitlin Smyth, Peter Mascher, and Jonathan D.B. Bradley. Low-temperature and low-pressure silicon nitride deposition by ecr-pecvd for optical waveguides. Appl. Sci. (Switzerland), 11:1–11, 3 2021.
- [106] Luc Museur, Andreas Zerr, and Andrei Kanaev. Photoluminescence and electronic transitions in cubic silicon nitride. Sci. Rep., 6:18523, 1 2016.
- [107] Jessica Steinlechner, Christoph Krüger, Iain W. Martin, Angus Bell, Jim Hough, Henning Kaufer, Sheila Rowan, Roman Schnabel, and Sebastian Steinlechner. Optical absorption of silicon nitride membranes at 1064 nm and at 1550 nm. Phys. Rev. D, 96:022007, 7 2017.
- [108] Corey Stambaugh, Mathieu Durand, Utku Kemiktarak, and John Lawall. Cavityenhanced measurements for determining dielectric-membrane thickness and complex index of refraction. Appl. Opt., 53:4930, 8 2014.
- [109] Maodong Gao, Qi Fan Yang, Qing Xin Ji, Heming Wang, Lue Wu, Boqiang Shen, Junqiu Liu, Guanhao Huang, Lin Chang, Weiqiang Xie, Su Peng Yu, Scott B. Papp, John E. Bowers, Tobias J. Kippenberg, and Kerry J. Vahala. Probing material absorption and optical nonlinearity of integrated photonic materials. Nature Communications, 13, 12 2022.

- [110] J. A. Guerra, A. Tejada, J. A. Töfflinger, R. Grieseler, and L. Korte. Bandfluctuations model for the fundamental absorption of crystalline and amorphous semiconductors: A dimensionless joint density of states analysis. Journal of Physics D: Applied Physics, 52, 1 2019.
- [111] Kostas Kanellopulos, Friedrich Ladinig, Stefan Emminger, Paolo Martini, Robert G. West, and Silvan Schmid. Comparative analysis of nanomechanical resonators: Sensitivity, response time, and practical considerations in photothermal sensing. arXiv, 2024. Submitted.
- [112] L. D. Landau and E. M. Lifshitz. Theory of Elasticity, volume 7, Course of Theoretical Physics. Pergamon Press Oxford, 3 edition, 1986.
- [113] Scott S. Verbridge, Rob Ilic, H. G. Craighead, and Jeevak M. Parpia. Size and frequency dependent gas damping of nanomechanical resonators. Applied Physics Letters, 93, 2008.
- [114] RG Christian. The theory of oscillating-vane vacuum gauges. Vacuum, 16(4):175– 178, 1966.
- [115] S. Schmid, K. D. Jensen, K. H. Nielsen, and A. Boisen. Damping mechanisms in high-q micro and nanomechanical string resonators. Physical Review B - Condensed Matter and Materials Physics, 84, 10 2011.
- [116] A. N. Cleland and M. L. Roukes. Noise processes in nanomechanical resonators. Journal of Applied Physics, 92:2758–2769, 9 2002.
- [117] A.S. Nowick and B.S. Berry. Anelastic Relaxation In Crystalline Solids. Materials science and technology. Elsevier Science, 1972.
- [118] Kevin Y Yasumura, Timothy D Stowe, Eugene M Chow, Timothy Pfafman, Thomas W Kenny, Barry C Stipe, and Daniel Rugar. Quality factors in micron-and submicron-thick cantilevers. JOURNAL OF MICROELECTROMECHANICAL SYSTEMS, 9:117, 2000.
- [119] L. G. Villanueva and S. Schmid. Evidence of surface loss as ubiquitous limiting damping mechanism in sin micro- and nanomechanical resonators. Physical Review Letters, 113, 11 2014.
- [120] Nils Johan Engelsen, Alberto Beccari, and Tobias Jan Kippenberg. Ultrahighquality-factor micro- and nanomechanical resonators using dissipation dilution. Nature Nanotechnology, 3 2024.
- [121] S. A. Fedorov, N. J. Engelsen, A. H. Ghadimi, M. J. Bereyhi, R. Schilling, D. J. Wilson, and T. J. Kippenberg. Generalized dissipation dilution in strained mechanical resonators. Physical Review B, 99, 2 2019.

- [122] Eduard Ventsel and Theodor. Krauthammer. Thin plates and shells: theory, analysis, and applications. Marcel Dekker, 2001.
- [123] Paul W. Kruse and David D. Skatrud. Uncooled Infrared Imaging Arrays and Systems, volume 47. Academic Press, 2001.
- [124] Chang Zhang, Mathieu Giroux, Thea Abdul Nour, and Raphael St-Gelais. Radiative heat transfer in freestanding silicon nitride membranes. Physical Review Applied, 14, 8 2020.
- [125] Yannick S. Klaß, Juliane Doster, Maximilian Bückle, Rémy Braive, and Eva M. Weig. Determining young's modulus via the eigenmode spectrum of a nanomechanical string resonator. Applied Physics Letters, 121, 8 2022.
- [126] Carlos H Mastrangelo, Yu-Chong Tai, and Richard S Muller. Thermophysical properties of low-residual stress, silicon-rich, lpcvd silicon nitride films. Sensors and Actuators, pages 856–860, 1990.
- [127] T. L. Bergman, Adrienne. Lavine, and Frank P. Incropera. Fundamentals of heat and mass transfer. John Wiley & Sons, 2017.
- [128] Markus Piller, Pedram Sadeghi, Robert G. West, Niklas Luhmann, Paolo Martini, Ole Hansen, and Silvan Schmid. Thermal radiation dominated heat transfer in nanomechanical silicon nitride drum resonators. Applied Physics Letters, 117, 7 2020.
- [129] S. Yamada. Analyzing Engineered Nanoparticles using Photothermal Infrared Spectroscopy. Technical University of Denmark, 2016. Ph.D. Dissertation.
- [130] Alper Demir. Understanding fundamental trade-offs in nanomechanical resonant sensors. Journal of Applied Physics, 129, 1 2021.
- [131] Hajrudin Bešić, Alper Demir, Johannes Steurer, Niklas Luhmann, and Silvan Schmid. Schemes for tracking resonance frequency for micro- and nanomechanical resonators. Physical Review Applied, 20, 8 2023.
- [132] David W Allan. Statistics of atomic frequency standards. Proc. IEEE, 54:221–230, 1966.
- [133] Pedram Sadeghi, Alper Demir, Luis Guillermo Villanueva, Hendrik Kahler, and Silvan Schmid. Frequency fluctuations in nanomechanical silicon nitride string resonators. Phys. Rev. B, 102:214106, 12 2020.
- [134] Tomás Manzaneque, Murali K. Ghatkesar, Farbod Alijani, Minxing Xu, Richard A. Norte, and Peter G. Steeneken. Resolution limits of resonant sensors. Phys. Rev. Appl., 19:054074, 4 2023.

- [135] John R Vig and Yoonkee Kim. Noise in microelectromechanical system resonators. T-UFFC, 46:1558–1565, 1999.
- [136] Paul.W. Kruse. A comparison of the limits to the performance of thermal and photon detector imaging arrays. Infrared Physics & Technology, 36(5):869–882, 1995.
- [137] Pasquale. Maddaloni, Marco Bellini, and Paolo. De Natale. Laser-based measurements for time and frequency domain applications: a handbook. CRC Press/Taylor & Francis, 2013.
- [138] Avik Dutt, Aseema Mohanty, Alexander L. Gaeta, and Michal Lipson. Nonlinear and quantum photonics using integrated optical materials. Nature Reviews Materials, 9:321-346, 5 2024.
- [139] Kostas Kanellopulos, Robert G. West, Stefan Emminger, Paolo Martini, Markus Sauer, Annette Foelske, and Silvan Schmid. Stress-dependent optical extinction in low-pressure chemical vapor deposition silicon nitride measured by nanomechanical photothermal sensing. Nano Letters, 24(36):11262–11268, 2024. PMID: 39213585.
- [140] Jiacheng Xie, Mohan Shen, Yuntao Xu, Wei Fu, Likai Yang, and Hong X. Tang. Sub-terahertz electromechanics. Nature Electronics, 6:301–306, 4 2023.
- [141] Ken-Ichi Fujii, Mitsuru Tanaka, Yoshiaki Nezu, Kan Nakayama, and Ryohei Masui. Accurate determination of the density of a crystal silicon sphere. *IEEE* TRANSACTIONS ON INSTRUMENTATION AND MEASUREMENT, 42:395, 1993.
- [142] E. J. Boyd, V. Nock, X. Li, and D. Uttamchandani. Density measurement of thin-films for micro-electromechanical systems using micro-cantilever structures. Thin Solid Films, 519:7932–7935, 9 2011.
- [143] Shuhua Yao, Jiyang Wang, Hong Liu, Xiaobo Hu, Haijin Zhang, Xiufeng Cheng, and Zongcheng Ling. Growth, optical and thermal properties of near-stoichiometric linbo3 single crystal. Journal of Alloys and Compounds, 455:501–505, 5 2008.
- [144] Michael E. Levinshtein, Sergey L. Rumyantsev, and Michael S. Shur. Properties of Advanced Semiconductor Materials: GaN, AlN, InN, BN, SiC, SiGe. John Wiley & Sons, 2001.
- [145] Alex Masolin, Pierre Olivier Bouchard, Roberto Martini, and Marc Bernacki. Thermo-mechanical and fracture properties in single-crystal silicon. Journal of Materials Science, 48:979–988, 2 2013.
- [146] G. L. Harris. Properties of Silicon Carbide. INSPEC, the Institution of Electrical Engineers, London, 1995.

- [147] M. Gruber, A. Leitner, D. Kiener, P. Supancic, and R. Bermejo. Effect of crystal orientation on the hardness and strength of piezoelectric linbo3 substrates for microelectronic applications. Materials and Design, 213, 1 2022.
- [148] D Gerlich, S L Dole, and Andg A Slack. Elastic properties of alumi m nitride. J Phys Chem Sohds, 47:4374, 1986.
- [149] Peng Chai, Shujuan Li, Yan Li, Lie Liang, and Xincheng Yin. Mechanical behavior investigation of 4h-sic single crystal at the micro-nano scale. Micromachines, 11, 1 2020.
- [150] Hossein Ftouni, Christophe Blanc, Dimitri Tainoff, Andrew D. Fefferman, Martial Defoort, Kunal J. Lulla, Jacques Richard, Eddy Collin, and Olivier Bourgeois. Thermal conductivity of silicon nitride membranes is not sensitive to stress. *Physical* Review B - Condensed Matter and Materials Physics, 92, 9 2015.
- [151] Eiji Yamasue, Masahiro Susa, Hiroyuki Fukuyama, and Kazuhiro Nagata. Thermal conductivities of silicon and germanium in solid and liquid states measured by non-stationary hot wire method with silica coated probe. Journal of Crystal Growth, 234:121–131, 2002.
- [152] Rusheng Wei, Sheng Song, Kun Yang, Yingxin Cui, Yan Peng, Xiufang Chen, Xiaobo Hu, and Xiangang Xu. Thermal conductivity of 4h-sic single crystals. Journal of Applied Physics, 113, 2 2013.
- [153] Huanyou Wang, Gui Jin, and Qiaolai Tan. Thermal expansion and specific heat capacity of wurtzite aln. In Proceedings - 2020 3rd International Conference on Electron Device and Mechanical Engineering, ICEDME 2020, pages 406–409. Institute of Electrical and Electronics Engineers Inc., 5 2020.
- [154] Yvete Toivola, Jeremy Thurn, Robert F. Cook, Greg Cibuzar, and Kevin Roberts. Influence of deposition conditions on mechanical properties of low-pressure chemical vapor deposited low-stress silicon nitride films. Journal of Applied Physics, 94:6915– 6922, 11 2003.
- [155] Yasumasa Okada and Yozo Tokumaru. Precise determination of lattice parameter and thermal expansion coefficient of silicon between 300 and 1500 k. Journal of Applied Physics, 56:314–320, 1984.
- [156] D. N. Talwar and Joseph C. Sherbondy. Thermal expansion coefficient of 3c-sic. Applied Physics Letters, 67:3301, 1995.
- [157] Mahmoud M. Abouellell and Fred J. Leonberger. Waveguides in lithium niobate. Journal of the American Ceramic Society, 72:1311–1321, 1989.
- [158] W. M. Yim and R. J. Paff. Thermal expansion of aln, sapphire, and silicon. Journal of Applied Physics, 45:1456–1457, 1974.

- [159] Wen Hsien Chuang, Thomas Luger, Rainer K. Fettig, and Reza Ghodssi. Mechanical property characterization of lpcvd silicon nitride thin films at cryogenic temperatures. Journal of Microelectromechanical Systems, 13:870–879, 2004.
- [160] Akhilesh K. Swarnakar, Omer Van der Biest, and Jan Vanhellemont. Determination of the si young's modulus between room and melt temperature using the impulse excitation technique. Physica Status Solidi (C) Current Topics in Solid State Physics, 11:150–155, 1 2014.
- [161] J. Dong and A.-B. Chen. Fundamental Properties of SiC: Crystal Structure, Bonding Energy, Band Structure, and Lattice Vibrations, pages 63–87. Springer Berlin Heidelberg, Berlin, Heidelberg, 2004.
- [162] Songbin Gong and Gianluca Piazza. Design and analysis of lithium-niobate-based high electromechanical coupling rf-mems resonators for wideband filtering. In IEEE Transactions on Microwave Theory and Techniques, volume 61, pages 403–414, 2013.
- [163] R S Weis and T K Gaylord. Lithium niobate: Summary of physical properties and crystal structure. Appl. Phys. A, 37:191–203, 1985.
- [164] C. M. Lueng, H. L.W. Chan, C. Surya, and C. L. Choy. Piezoelectric coefficient of aluminum nitride and gallium nitride. Journal of Applied Physics, 88:5360–5363, 11 2000.
- [165] A. Boretti, Q. Li, and S. Castelletto. Pioneering the future with silicon carbide integrated photonics. Optics and Laser Technology, 181, 2 2025.
- [166] Miao-Hsuan Chien. Nanoelectromechanical photothermal microscopy and spectroscopy for single-molecule detection and imaging at room temperature. Technische Universität Wien, 2021. Ph.D. Dissertation.
- [167] Pedram Sadeghi. Study of high-Q nanomechanical silicon nitride resonators. Technische Universität Wien, 2021. Ph.D. Dissertation.
- [168] Minhang Bao. Analysis and Design Principles of MEMS Devices. Elsevier, 2095.
- [169] Andreas Barg, Yeghishe Tsaturyan, Erik Belhage, William H.P. Nielsen, Christoffer B. Møller, and Albert Schliesser. Measuring and imaging nanomechanical motion with laser light. Applied Physics B: Lasers and Optics, 123, 1 2017.
- [170] B. P. Abbott et al. Observation of gravitational waves from a binary black hole merger. Physical Review Letters, 116, 2 2016.
- [171] Georg A. Reider. *Photonics: An Introduction*. Springer Cham, 2016.
- [172] Klaus Thurner, Pierre François Braun, and Khaled Karrai. Fabry-pérot interferometry for long range displacement sensing. Review of Scientific Instruments, 84, 9 2013.



- [173] Klaus Thurner, Francesca Paola Quacquarelli, Pierre-François Braun, Claudio Dal Savio, and Khaled Karrai. Fiber-based distance sensing interferometry. Applied Optics, 54:3051, 4 2015.
- [174] Klaus Thurner. Position sensing using a fiber-optic Fabry-Perót interferometer. Technische Universität München, 2016. Ph.D. Dissertation.
- [175] Alper Demir and M. Selim Hanay. Fundamental sensitivity limitations of nanomechanical resonant sensors due to thermomechanical noise. IEEE Sensors Journal, 20:1947-1961, 2 2020.
- [176] Selim Olcum, Nathan Cermak, Steven C. Wasserman, and Scott R. Manalis. Highspeed multiple-mode mass-sensing resolves dynamic nanoscale mass distributions. Nature Communications, 6, 5 2015.
- [177] S. Schmid, P. Senn, and C. Hierold. Electrostatically actuated nonconductive polymer microresonators in gaseous and aqueous environment. Sensors and Actuators, A: Physical, 145-146:442-448, 7 2008.
- [178] L. Guillermo Villanueva, Rassul B. Karabalin, Matthew H. Matheny, Eyal Kenig, Michael C. Cross, and Michael L. Roukes. A nanoscale parametric feedback oscillator. Nano Letters, 11:5054-5059, 11 2011.
- [179] Enrico Rubiola. Phase noise and frequency stability in oscillators. Cambridge University Press, 2009.
- [180] J. Parsons, C. P. Burrows, J. R. Sambles, and W. L. Barnes. A comparison of techniques used to simulate the scattering of electromagnetic radiation by metallic nanostructures. Journal of Modern Optics, 57:356–365, 3 2010.
- [181] V. L.Y. Loke, G. M. Huda, E. U. Donev, V. Schmidt, J. T. Hastings, M. Pinar Mengüç, and T. Wriedt. Comparison between discrete dipole approximation and other modelling methods for the plasmonic response of gold nanospheres. Applied Physics B: Lasers and Optics, 115:237–246, 2014.
- [182] Zeid A. Nima, Yevgeniy R. Davletshin, Fumyia Watanabe, Karrar M. Alghazali, J. Carl Kumaradas, and Alexandru S. Biris. Bimetallic gold core-silver shell nanorod performance for surface enhanced raman spectroscopy. RSC Advances, 7:53164-53171, 2017.
- [183] Juan Manuel Núñez-Levva, Eleazar Samuel Kolosovas-Machuca, John Sánchez, Edgar Guevara, Alexander Cuadrado, Javier Alda, and Francisco Javier González. Computational and experimental analysis of gold nanorods in terms of their morphology: Spectral absorption and local field enhancement. Nanomaterials, 11, 7 2021.
- [184] https://www.comsol.com/model/scatterer-on-substrate-14699, 2022.

- [185] Johan Grand and Eric C. Le Ru. Practical implementation of accurate finiteelement calculations for electromagnetic scattering by nanoparticles. *Plasmonics*, 15:109–121, 2 2020.
- [186] Carolina Novo, Daniel Gomez, Jorge Perez-Juste, Zhenyuan Zhang, Hristina Petrova, Maximilian Reismann, Paul Mulvaney, and Gregory V. Hartland. Contributions from radiation damping and surface scattering to the linewidth of the longitudinal plasmon band of gold nanorods: A single particle study. Physical Chemistry Chemical Physics, 8:3540–3546, 2006.
- [187] Otto L. Muskens, Guillaume Bachelier, Natalia Del Fatti, Fabrice Vallée, Arnaud Brioude, Xuchuan Jiang, and Marie Paule Pileni. Quantitative absorption spectroscopy of a single gold nanorod. Journal of Physical Chemistry C, 112:8917–8921, 6 2008.
- [188] Vincent Juvé, M. Fernanda Cardinal, Anna Lombardi, Aurélien Crut, Paolo Maioli, Jorge Pérez-Juste, Luis M. Liz-Marzán, Natalia Del Fatti, and Fabrice Vallée. Sizedependent surface plasmon resonance broadening in nonspherical nanoparticles: Single gold nanorods. Nano Letters, 13:2234–2240, 5 2013.
- [189] Kyeong Seok Lee and Mostafa A. El-Sayed. Dependence of the enhanced optical scattering efficiency relative to that of absorption for gold metal nanorods on aspect ratio, size, end-cap shape, and medium refractive index. Journal of Physical Chemistry B, 109:20331–20338, 11 2005.
- [190] P.B. Johnson and R.W. Christy. Optical-constants of noble-metals phys. rev. b 6(12), 4370–4379 (1972). Physical Review B, 1318:4370–4379, 1972.
- [191] Yevgeniy R. Davletshin, Anna Lombardi, M. Fernanda Cardinal, Vincent Juvé, Aurélien Crut, Paolo Maioli, Luis M. Liz-Marzán, Fabrice Vallée, Natalia Del Fatti. and J. Carl Kumaradas. A quantitative study of the environmental effects on the optical response of gold nanorods. ACS Nano, 6:8183–8193, 9 2012.
- [192] Eduardo A. Coronado and George C. Schatz. Surface plasmon broadening for arbitrary shape nanoparticles: A geometrical probability approach. Journal of Chemical Physics, 119:3926-3934, 8 2003.
- [193] Limei Tian, Enze Chen, Naveen Gandra, Abdennour Abbas, and Srikanth Singamaneni. Gold nanorods as plasmonic nanotransducers: Distance-dependent refractive index sensitivity. Langmuir, 28:17435–17442, 12 2012.
- [194] Mark W. Knight, Yanpeng Wu, J. Britt Lassiter, Peter Nordlander, and Naomi J. Halas. Substrates matter: influence of an adjacent dielectric on an individual plasmonic nanoparticle. Nano Letters, 9:2188-2192, 5 2009.
- [195] T. Larsen, S. Schmid, L. Grönberg, A. O. Niskanen, J. Hassel, S. Dohn, and A. Boisen. Ultrasensitive string-based temperature sensors. Applied Physics Letters, 98, 3 2011.

- [196] Sheila Edalatpour and Mathieu Francoeur. Size effect on the emissivity of thin films. Journal of Quantitative Spectroscopy and Radiative Transfer, 118:75–85, 3 2013.
- [197] R. Tufan Erdogan, Mohammed Alkhaled, Batuhan E. Kaynak, Hashim Alhmoud, Hadi Sedaghat Pisheh, Mehmet Kelleci, Ilbey Karakurt, Cenk Yanik, Zehra Betül Sen, Burak Sari, Ahmet M. Yagci, Aykut Özkul, and M. Selim Hanay. Atmospheric pressure mass spectrometry of single viruses and nanoparticles by nanoelectromechanical systems. ACS Nano, 16:3821–3833, 3 2022.
- [198] James W Wagner and James B Spicer. Theoretical noise-limited sensitivity of classical interferometry. J. Opt. Soc. Am. B, 4, 1987.
- [199] N. R. Isenor. Polarization and mode hopping in a gas laser. J. Appl. Phys., 38:417-418, 1967.
- [200] John Lawall and Ernest Kessler. Michelson interferometry with 10 pm accuracy. Rev. Sci. Instrum., 71:2669–2676, 2000.
- [201] Vincent Dumont, Jiaxing Ma, Eamon Egan, and Jack C. Sankey. High-power quantum-limited 35 mhz photodiode and classical laser noise suppression. Review of Scientific Instruments, 94, 12 2023.
- [202] Antoni Rogalski. Infrared and terahertz detectors. CRC press, 2019.
- [203] H. Wu, S. Grabarnik, A. Emadi, G. De Graaf, and R. F. Wolffenbuttel. Characterization of thermal cross-talk in a mems-based thermopile detector array. Journal of Micromechanics and Microengineering, 19, 2009.
- [204] John M. Khosrofian and Bruce A. Garetz. Measurement of a gaussian laser beam diameter through the direct inversion of knife-edge data. Appl. Opt., 22(21):3406-3410, Nov 1983.
- [205] Wesley J. Marshall. Two methods for measuring laser beam diameter. Journal of Laser Applications, 22:132–136, 11 2010.
- [206] Guillaume Baffou and Romain Quidant. Thermo-plasmonics: Using metallic nanostructures as nano-sources of heat. Laser and Photonics Reviews, 7:171–187, 3 2013.
- [207] Sigma-Aldrich. Gold nanorods 10 nm diameter, silica coated, absorption/808 nm, dispersion in H2O. PRD.0.ZQ5.10000047270.
- [208] Stefan A. Maier. Plasmonics: fundamentals and applications. Springer, 2007.
- [209] Viktor Myroshnychenko, Jessica Rodríguez-Fernández, Isabel Pastoriza-Santos, Alison M. Funston, Carolina Novo, Paul Mulvaney, Luis M. Liz-Marzán, and F. Javier García de Abajo. Modelling the optical response of gold nanoparticles. Chemical Society Reviews, 37:1792–1805, 8 2008.

- [210] Wei Shun Chang, Ji Won Ha, Liane S. Slaughter, and Stephan Link. Plasmonic nanorod absorbers as orientation sensors. Proceedings of the National Academy of Sciences of the United States of America, 107:2781–2786, 2 2010.
- [211] Yun Sheng Chen, Wolfgang Frey, Seungsoo Kim, Pieter Kruizinga, Kimberly Homan, and Stanislav Emelianov. Silica-coated gold nanorods as photoacoustic signal nanoamplifiers. Nano Letters, 11:348–354, 2 2011.
- [212] Aurélien Crut, Paolo Maioli, Natalia Del Fatti, and Fabrice Vallée. Optical absorption and scattering spectroscopies of single nano-objects, 6 2014.
- [213] Attilio Zilli, Wolfgang Langbein, and Paola Borri. Quantitative measurement of the optical cross sections of single nano-objects by correlative transmission and scattering microspectroscopy. ACS Photonics, 6:2149–2160, 8 2019.
- [214] A. Brioude, X. C. Jiang, and M. P. Pileni. Optical properties of gold nanorods: Dda simulations supported by experiments. Journal of Physical Chemistry B, 109:13138-13142, 7 2005.
- [215] Zhongming Li, Weizhi Mao, Mary Sajini Devadas, and Gregory V. Hartland. Absorption spectroscopy of single optically trapped gold nanorods. Nano Letters, 15:7731–7735, 11 2015.
- [216] Guillaume Baffou, Frank Cichos, and Romain Quidant. Applications and challenges of thermoplasmonics. Nature Materials, 19:946–958, 9 2020.
- [217] Luis M. Liz-Marzán, Jorge Pérez-Juste, and Isabel Pastoriza-Santos. Plasmonics of gold nanorods, considerations for biosensing. In Michael Giersig and Gennady B. Khomutov, editors, Nanomaterials for Application in Medicine and Biology, pages 103-111, Springer, Dordrecht, 2008. Springer Netherlands.
- [218] David B. Lioi, Sarah N. Izor, Vikas Varshney, Hugh M. DeJarnette, Pedro A. Derosa, and W. Joshua Kennedy. Effective medium approximation for the dielectric environment of coated gold nanorods. Optical Materials Express, 12:3577, 9 2022.
- [219] Thomas A. Germer. pyscatmech: A python interface to the scatmech library. https://pages.nist.gov/pySCATMECH/index.html. (accessed 2023-09-06).
- [220] Anna Lombardi, Matthieu Loumaigne, Aurélien Crut, Paolo Maioli, Natalia Del Fatti, Fabrice Vallée, Miguel Spuch-Calvar, Julien Burgin, Jérôme Majimel, and Mona Tréguer-Delapierre. Surface plasmon resonance properties of single elongated nano-objects: Gold nanobipyramids and nanorods. Langmuir, 28:9027–9033, 6 2012.
- [221] C. Sönnichsen, T. Franzl, T. Wilk, G. von Plessen, J. Feldmann, O. Wilson, and P. Mulvaney. Drastic reduction of plasmon damping in gold nanorods. *Physical* Review Letters, 88:774021-774024, 2 2002.

- [222] Arisato Kawabata and Ryogo Kubo. Electronic properties of fine metallic particles. ii. plasma resonance absorption. J. Phys. Soc. Jpn., 1966.
- [223] Prashant K. Jain, Susie Eustis, and Mostafa A. El-Sayed. Plasmon coupling in nanorod assemblies: Optical absorption, discrete dipole approximation simulation, and exciton-coupling model. Journal of Physical Chemistry B, 110:18243-18253, 9 2006.
- [224] P. M. Kosaka, V. Pini, J. J. Ruz, R. A. Da Silva, M. U. González, D. Ramos, M. Calleja, and J. Tamayo. Detection of cancer biomarkers in serum using a hybrid mechanical and optoplasmonic nanosensor. Nature Nanotechnology, 9:1047–1053, 1 2014.
- [225] Tian Ming, Lei Zhao, Zhi Yang, Huanjun Chen, Lingdong Sun, Jianfang Wang, and Chunhua Yan. Strong polarization dependence of plasmon-enhanced fluorescence on single gold nanorods. Nano Letters, 9:3896–3903, 12 2009.
- [226] Goldsmith, R. Optical microresonators as single-molecule spectrometers. (accessed 2023-07-15).
- [227] A. Arbouet, D. Christofilos, N. Del Fatti, F. Vallée, J. R. Huntzinger, L. Arnaud, P. Billaud, and M. Broyer. Direct measurement of the single-metal-cluster optical absorption. Physical Review Letters, 93, 9 2004.
- [228] Michele Celebrano, Philipp Kukura, Alois Renn, and Vahid Sandoghdar. Singlemolecule imaging by optical absorption. Nature Photonics, 5:95–98, 2011.
- [229] Zhongming Li, Kyle Aleshire, Masaru Kuno, and Gregory V. Hartland. Superresolution far-field infrared imaging by photothermal heterodyne imaging. Journal of Physical Chemistry B, 121:8838–8846, 9 2017.
- [230] Wei Shun Chang and Stephan Link. Enhancing the sensitivity of single-particle photothermal imaging with thermotropic liquid crystals. Journal of Physical Chemistry Letters, 3:1393–1399, 5 2012.
- [231] Tina X. Ding, Lei Hou, Harmen Van Der Meer, A. Paul Alivisatos, and Michel Orrit. Hundreds-fold sensitivity enhancement of photothermal microscopy in near-critical xenon. Journal of Physical Chemistry Letters, 7:2524–2529, 7 2016.
- [232] Lei Hou, Subhasis Adhikari, Yuxi Tian, Ivan G. Scheblykin, and Michel Orrit. Absorption and quantum yield of single conjugated polymer poly 2-methoxy-5-(2ethylhexyloxy)-1,4-phenylenevinylene] (meh-ppv) molecules. Nano Letters, 17:1575-1581, 3 2017.
- [233] Erik H. Horak, Morgan T. Rea, Kevin D. Heylman, David Gelbwaser-Klimovsky, Semion K. Saikin, Blaise J. Thompson, Daniel D. Kohler, Kassandra A. Knapper, Wei Wei, Feng Pan, Padma Gopalan, John C. Wright, Alán Aspuru-Guzik, and

- Randall H. Goldsmith. Exploring electronic structure and order in polymers via single-particle microresonator spectroscopy. Nano Letters, 18:1600–1607, 3 2018.
- [234] H. Angus Macleod. Thin-Film Optical Filters. CRC Press, 2010.
- [235] Achim Bubenzer and Peter Koidl. Exact expressions for calculating thin-film absorption coefficients from laser calorimetric data. Appl. Opt., 23(17):2886–2891, Sep 1984.
- [236] Kevin Luke, Yoshitomo Okawachi, Michael R.E. Lamont, Alexander L. Gaeta, and Michal Lipson. Broadband mid-infrared frequency comb generation in a si3n4 microresonator. Optics Letters, 2015-August, 8 2015.
- [237] Takashi Inukai Takashi Inukai and Ken'ichi Ono Ken'ichi Ono. Optical characteristics of amorphous silicon nitride thin films prepared by electron cyclotron resonance plasma chemical vapor deposition. Jpn. J. Appl. Phys., 33(5R):2593, may 1994.
- [238] D.A.P. Bulla, B.V. Borges, M.A. Romero, N.I. Morimoto, L.G. Neto, and A.L. Cortes. Design and fabrication of sio/sub 2//si/sub 3/n/sub 4/ cvd optical waveguides. In 1999 SBMO/IEEE MTT-S International Microwave and Optoelectronics Conference, volume 2, pages 454–457 vol. 2, 1999.
- [239] N. Daldosso, M. Melchiorri, F. Riboli, F. Sbrana, L. Pavesi, G. Pucker, C. Kompocholis, M. Crivellari, P. Bellutti, and A. Lui. Fabrication and optical characterization of thin two-dimensional si 3n4 waveguides. Mater. Sci. Semicond. Process., 7:453-458, 2004.
- [240] Wesley D. Sacher, Xianshu Luo, Yisu Yang, Fu-Der Chen, Thomas Lordello, Jason C. C. Mak, Xinyu Liu, Ting Hu, Tianyuan Xue, Patrick Guo-Qiang Lo, Michael L. Roukes, and Joyce K. S. Poon. Visible-light silicon nitride waveguide devices and implantable neurophotonic probes on thinned 200 mm silicon wafers. Opt. Express, 27:37400, 12 2019.
- [241] Kerstin Worhoff, Edwin Klein, Gamar Hussein, and Alfred Driessen. Silicon oxynitride based photonics. In 2008 10th Anniversary International Conference on Transparent Optical Networks, volume 3, pages 266–269, 2008.
- [242] P. Temple-Boyer, C. Rossi, E. Saint-Etienne, and E. Scheid. Residual stress in low pressure chemical vapor deposition sinx films deposited from silane and ammonia. Journal of Vacuum Science & Technology A: Vacuum, Surfaces, and Films, 16:2003–2007, 7 1998.
- [243] J. Bauer. Optical properties, band gap, and surface roughness of si3n4. physica status solidi (a), 39:411–418, 1977.
- [244] S. Garcia, D. Bravo, M. Fernandez, I. Martil, and F. J. López. Role of oxygen on the dangling bond configuration of low oxygen content sinx: h films deposited at room temperature. Applied Physics Letters, 67:3263, 1995.

- [245] Hiromitsu Kato, Norihide Kashio, Yoshimichi Ohki, Kwang Soo Seol, and Takashi Noma. Band-tail photoluminescence in hydrogenated amorphous silicon oxynitride and silicon nitride films. Journal of Applied Physics, 93:239–244, 1 2003.
- [246] H. MäcKel and R. Lüdemann. Detailed study of the composition of hydrogenated sin x layers for high-quality silicon surface passivation. J. Appl. Phys., 92:2602–2609, 9 2002.
- [247] D. A. Shirley. High-resolution x-ray photoemission spectrum of the valence bands of gold. Phys. Rev. B, 5:4709–4714, Jun 1972.
- [248] Sven Tougaard. Universality classes of inelastic electron scattering cross-sections. Surf. Interface Anal., 25(3):137–154, 1997.
- [249] C.D. Wagner. Sensitivity factors for xps analysis of surface atoms. J. Electron Spectr. Rel. Phenom., 32:99-102, 1983.